UNIVERSITY OF SOUTHAMPTON

NOVEL SOLID STATE MODULATOR FOR THE INFRARED: THE GERMANIUM CHOPPER

Peter Douglas Fairley

Doctor of Philosophy

FACULTY OF ENGINEERING AND APPLIED SCIENCE
DEPARTMENT OF ELECTRONICS AND COMPUTER SCIENCE

June 2000

UNIVERSITY OF SOUTHAMPTON

ABSTRACT

FACULTY OF ENGINEERING AND APPLIED SCIENCE
DEPARTMENT OF ELECTRONICS AND COMPUTER SCIENCE
Doctor of Philosophy

NOVEL SOLID STATE MODULATOR FOR THE INFRARED: THE GERMANIUM CHOPPER

by Peter Douglas Fairley

Uncooled thermal imaging cameras in the 8 to 14 μm band use pyroelectric array detectors as the preferred technology. The systems advantages offered by these uncooled detectors are those of reduced cost, complexity and power consumption. The price paid for this uncooled technology is that the image must be modulated in order to generate a change in signal intensity on the detector. Currently this is achieved using a rotating chopper blade, which introduces moving parts to the system, and has the drawbacks of size and image degradation as camera motion changes the blade's rotational speed.

A need has existed for considerable time for solid state broad optical bandwidth modulation in the infrared. The application requires modulation of the 8 to 14 μm band with high 'on' state transmission, although not necessarily a very low 'off' state transmission. Crucially this must be over a relatively large (1 cm^2) aperture. The modulator should be insensitive to polarisation since this would halve the image intensity from a randomly polarised scene, reducing the system signal to noise ratio. Low power consumption, compactness, and the incorporation into a low f-number optical system are the systems requirements for this application. The specification is eased only by the moderate chopping frequencies (<100 Hz) characteristic of pyroelectric detector operation.

Adequate modulation using a novel method has been achieved in the 8 to 14 μm region by introducing moderate levels of excess carriers to suitably prepared germanium by excitation from a diode laser source. The process utilises inter valence band transitions from the light-hole to heavy-hole band, requiring excitation power densities in the order of Watts cm^{-2}. This has been exploited by the construction of the first solid state modulator satisfying the requirements of thermal imaging cameras in the 8 to 14 μm band. A depth of modulation of from 95.4% (AR coated) to 4.7% transmission at 10μm using a total power density of $5.6Wcm^{-2}$ from 980nm diode lasers has been achieved in the centre of a $1cm^2$ aperture. The 'on' state loss at this wavelength is limited by the single-layer quarter-wavelength AR coating properties, and may be eliminated through use of a multilayer coating. There is presently no solid state modulator in the required thermal image band that even approaches this performance.

The possibility of using electrical pumping to generate the required holes for the induced absorption is investigated. The design of an electrical-injection area-based modulator, modulating radiation perpendicular to the junction plane is affected by the conflicting requirements of uniform absorption across the aperture and high 'on' state transmission. A design for such a device is outlined. Modulation of a beam of radiation parallel to the junction plane is demonstrated by a reconfigured p-n junction diode to illustrate the principle.

Contents

List of Figures

List of Tables

Acknowledgements

This solid-state solution to the inherent requirement for image modulation in pyroelectric-based thermal imaging cameras was proposed by Harvey Rutt after examination of the specifications for germanium in optical systems.

Firstly I must thank Harvey for giving me the opportunity to work on this idea. Your guidance, enthusiasm and support over the past few years has given me the energy necessary to complete the project.

This project would not have been possible on this scale without the continual support from DERA Malvern, the sponsors of this work. I would like to thank Rex Watton for initially posing the requirement for a solid state modulator, and Paul Manning and Paul Donohue for their management of the project thereafter. Your time and valuable discussions are very much appreciated, as were the many pieces of borrowed equipment.

Thanks are also due to Eugene Haller of California University for the loan of the first germanium sample that was to show the effect, and to Mo Taghizadeh of Heriot Watt University for the use of reactive ion etching equipment.

Finally, thank you to Nicky Marsh, Lucy Peake, Ceri Morgan and Clare Trudgeon for your friendship and support over these tricky years, and thank you to my family, in particular Priscilla and Anne for your encouragement and support, and to George for giving me the determination to see this work through.

Chapter 1

Introduction

1.1 Background: why is a modulator required?

Uncooled thermal imaging cameras in the 8 to $14\mu m$ band use pyroelectric array detectors as the preferred technology. The systems advantages offered by these uncooled detectors are those of reduced cost, complexity and power consumption. The price paid for this uncooled technology is that the image must be modulated in order to generate a change in signal intensity on the detector. Currently this is achieved using a rotating chopper blade, which introduces moving parts to the system, and has the drawbacks of size and image degradation as camera motion changes the blade's rotational speed.

A need has existed for considerable time for solid state broad optical bandwidth modulation in the infrared. The application requires modulation of the 8 to $14\mu m$ band with high 'on' state transmission, although not necessarily a very low 'off' state transmission. Crucially this must be over a relatively large ($1cm^2$) aperture. The modulator should be insensitive to polarisation since this would halve the image intensity from a randomly polarised scene, reducing the system signal to noise ratio. Low power consumption, compactness, and the incorporation into a low f-number optical system are the systems requirements for this application. The specification is eased only by the moderate chopping frequencies (< 100 Hz) characteristic of pyroelectric detector operation.

Well-documented methods of modulating infrared beams include the acousto-optic [1] [2] [3] [4] effect in crystals, electro-optic effect [5] [6] [7] [8] [9], and free carrier absorption using the plasma effect [10] [11] [12] [13] [14] [15] [16] [17] [18] in semiconductors. These methods however have limitations and are primarily restricted to modulation of small apertures or beams of radiation where a distortion-free image, and low power consumption by the switching process are not primary requirements. Both the acousto-optic and electro-optic effects have a characteristic narrow band of polarisation-dependent modulated wavelengths with high f-number requirement rendering them of little use in this application. Free carrier absorption using the plasma effect can be used to induce severe absorption over a wide spectral region, but generation of this effect in the $10\mu m$ region requires an immense power density. Liquid crystals have also been investigated for their application to infrared modulation [19] [20]. Although modulation has been achieved over a narrow band in the $5\mu m$ region [19], little success has been achieved at longer wavelengths. The inherent polarisation-dependence of this form of modulation makes it unattractive.

Adequate modulation using a novel method has been achieved in the 8 to $14\mu m$ region by introducing moderate levels of excess carriers to suitably prepared germanium [21] [22] by excitation from a diode laser source. The process utilises inter valence band transitions from the light-hole to heavy-hole band, requiring excitation power densities in the order of $Watts\ cm^{-2}$. A depth of modulation of from 95.4% (AR coated) to 4.7% transmission at $10\mu m$ using a total power density of $5.6W\ cm^{-2}$ from $980nm$ diode lasers has been achieved in the centre of a $1cm^2$ aperture. The 'on' state loss at this wavelength is limited by the single-layer quarter-wavelength AR coating properties, and may be eliminated through use of a multilayer coating.

1.2 Intervalence band transitions in germanium: the history

The modulator absorption process uses intervalence band transitions in germanium to induce a high level of absorption in the 8 to $14\mu m$ region. These hole transitions were first observed [23] in germanium in 1952 by Briggs and Fletcher through the differences in absorption spectra of n and p doped samples. N doped germanium exhibits a structureless λ^2 absorption dependence beyond the bandgap, whereas p germanium shows bands of absorption. In 1953 Kaiser, Collins and Fan [24] suggested that the absorption in p-type germanium could only be due to hole transitions within the valence band; only suppositions as to the band structure existed at that date. Later [25] Kahn developed the theory of infrared absorption in germanium, attributing the observed absorption to intervalence band transitions in connection with results from cyclotron resonance experiments, and calculated transition strengths between these bands. In 1956, Kane [26] calculated the valence band structure in germanium using the data from cyclotron resonance experiments. This forms the basis of today's understanding of the band structure.

Later in the 1960's germanium became the most popular semiconductor with the development of the transistor, until it was superseded by silicon.

Germanium has however had a continued application in infrared optical components with its long wavelength cutoff at $18\mu m$, low-dispersion and ease of machining. It was through the specification of these optical components [21] that the long-forgotten inter-valence band absorption process was revived. The specification for germanium optical components is generally low n-doped material [27] (or ν-type). This gives a combination of low optical absorption at $10\mu m$ and a low temperature coefficient of absorption. 10 to $40\Omega cm$ is the preferred range for this spectral region [28]. Since $n \cdot p = n_i^2$ at constant temperature, n-type doping suppresses the hole concentration (p) with its higher absorption cross section in this region. However, too high an electron density causes λ^2 free electron absorption to dominate. Intrinsic material cannot be used in high power CO_2 lasers, for example in welding, since a small amount of absorbed power in the long wavelength region due to hole inter-valence band absorption causes heating of the lens and further carrier generation. This leads to thermal runaway in the lens and its eventual destruction.

1.3 This work

Initial results [21] showed that strong absorption could be temporally induced in the 8 to $14\mu m$ region using the light- to heavy-hole transition in germanium. The holes were optically generated by an $808nm$ diode laser. This demonstrated the potential of the absorption process. This thesis shows the application of earlier knowledge on germanium and its processing in the development and optimisation of the inter-valence band absorption process in a solid state modulator. A modulator has been developed through an understanding of the interband absorption process, by modelling and the experimental validation of related effects. The final aim of this work was to design and construct an optimised modulator for use in pyroelectric thermal imaging cameras.

The layout of the thesis is as follows. Chapter 2 reviews the semiconductor absorption processes that might be of use in a modulator. These conclude that inter-valence band transitions offer the highest potential in the application. Other materials are then considered in which this absorption process might be observed, and germanium is justified as the sole semiconductor of interest. Chapter 3 investigates the properties of germanium relevant to modulator design and optimisation at both a physics and a systems level. Chapter 4 details the theory of modulator operation at a carrier diffusion level, highlighting the dominant electrical parameters governing operation, and giving target values for their optimisation. Chapters 5 and 6 form the bulk of the experimental results in the thesis, with Chapter 5 validating the theory and predictions of Chapter 4. Chapter 6 considers optimisation of the modulator performance, which is used in the design of an optically-pumped modulator in Chapter 7. Chapter 8 considers how electrical excitation might be used to generate the holes required for the induced absorption. Chapter 9 concludes the work, highlighting future areas of development for this interesting project.

Chapter 2

Absorption processes in semiconductors

This Chapter reviews the semiconductor energy-band structure and the possible optical transitions that arise. Several optical transition mechanisms are examined as to their relevance in the modulation of infrared radiation, and methods of utilising their absorption in an infrared modulator are detailed.

2.1 Energy band structure of semiconductors

The states in which an electron or hole can exist in a semiconductor lattice are described by the energy-momentum or E-k diagram. This diagram is generally drawn for a particular crystal direction in which the bandgap, or minimum energy separation between conduction band minimum and valence band maximum, exists, having considered all crystal directions. Among other factors, the minimum conduction-valence band energy separation depends on the physical separation between adjacent atoms, and increases as the separation is reduced. Depending on the crystal symmetry, along different directions in the crystal the interatomic separation is different, thus the energy separation is directionally-dependent. A typical E-k diagram for an indirect semiconductor is shown in Figure 2.1, in this case for gallium phosphide [29].

The E-k diagram represents the range of energy and momentum that an electron within the lattice can have, and is conventionally drawn with electron energy increasing in the upward vertical direction. Hole energy increases in the downward vertical direction. A hole exists temporarily in the valence band when an electron has been removed from the valence band to the conduction band, or permanently if the semiconductor is p-

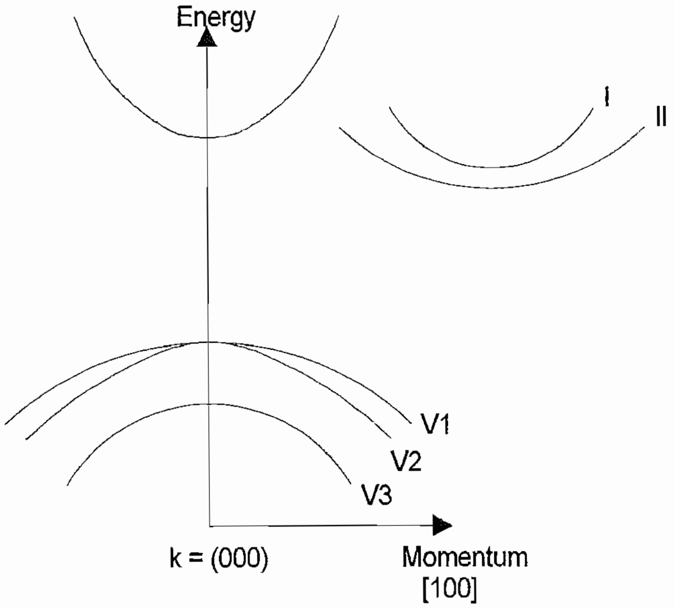

Figure 2.1: Generalised energy band E-k diagram for an indirect gap semiconductor

doped. Both holes and electrons can undergo transitions described by the E-k diagram, providing there is a free state into which the carrier can move.

In addition to the conduction and valence bands, there is the often-neglected spin orbit band (V3), which exists below and separate from the valence band. Due to spin-orbit interaction, the valence band in most semiconductors splits into two bands, a light-hole band and a heavy-hole band. Hole states exist in all three of these bands although holes are usually confined to the upper valence bands due to the large energy separation of the spin-orbit.

The E-k diagram shows that for an electron at a given energy, there are several values that its momentum in that band can have. Electron or hole transitions that occur between the conduction and valence bands (interband transitions), or within the conduction or valence band (also interband transitions) can either be vertical, undergoing only a change in energy, or diagonal, undergoing a change in both energy and momentum. In either case, energy and momentum must be conserved by the participants in the transition. In order for a transition to take place, it must be permitted by various selection rules, one of which is the Pauli exclusion principle which states that a maximum of two like-carriers can exist in the same state at any one time, accounting for spin-up and spin-down. Thus if the valence band is full of electrons, no holes exist in this band, and transitions by holes between the valence sub-bands cannot take place. These transitions only become possible when an electron has been removed from the valence band to free-up an energy level into which the hole can move. Depopulation of the electrons in the valence band is achieved temporarily by electron excitation, or permanently by p-doping. Different transitions therefore take place at different levels of conduction and valence band filling. These transitions determine the semiconductor's absorption spectrum, which therefore depends on the band's population.

The maximum momentum described by the E-k diagram is defined as the edge of the first Brillouin zone. An electron within the crystal is subject to E-k functions which are periodic in momentum-space. The E-k diagram is a function representing the reduced values of momentum which lead to physically different behaviour. In a simplified energy band model the electron energy E is related to its momentum k by the relationship:

$$E_k = \frac{\hbar^2}{2m^*}k^2 \tag{2.1}$$

In this simplified model the energy bands are known as 'parabolic' with momentum, k. $\hbar$ is the reduced Planck's constant $(h/2\pi)$. The effective mass m^* is the constant of proportionality defined by rearranging this equation, giving:

$$m^* = \hbar^2 \Big/ \frac{d^2E}{dk^2} \tag{2.2}$$

The carrier effective mass is therefore related to the band curvature with k; steeply curving bands having a lower effective mass than more gradually curving bands. This is the origin of the light (V2) and heavy hole (V1) bands in Figure 2.1. For most purposes, providing the energy variation is not too far from the minimum energy in that band, the parabolic energy assumption is sufficiently accurate, and the energy E will be proportional to $(k - k_0)^2$ where k_0 is the wave vector at the band centre.

Despite the one-dimensional E-k diagram above, crystal momentum is three dimensional and the carrier effective mass in a particular band is directionally-dependent. This is seen by plotting a curve of constant energy for the conduction or valence band near the band centre. Considering the two-dimensional case first; the E-k diagram is obtained by rotating the 1-d diagram about the $k = 0$ axis to give a contour of constant energy. If the momentum distribution is equal (same lattice spacing) in the two directions this results in a circular contour of constant momentum at that energy for the band. If the lattice spacing is different in the two directions the diagram shows an ellipse.

In three dimensions the model can be plotted to give a surface of constant energy; a sphere of constant energy giving rise to an isotropic mass. Plotting the three dimensional surfaces of constant energy in two dimensions for a given plane in k-space shows the degree of anisotropy, as shown in Figure 2.2 from [30]. For both silicon and germanium the constant energy surfaces of the valence band are [30] warped spheres centred at $k = 0$. This requires calculations using the effective mass for a particular band to either be in a known direction, or averaged over all directions. In germanium the warping is greater for the heavy hole band, although the effective mass anisotropy in either band is not very great [31]. To a good approximation each band can be treated as having a single effective mass, given by the light hole mass or heavy hole mass accordingly. Only about 5% of the free holes [31] occupy the light hole band at room temperature, affecting calculations involving hole transport. The edge of the conduction band in germanium occurs in four crystallographically equivalent positions, and in silicon the edges occur in six equivalent positions along the [100] axes. In Figure 2.2, the germanium conduction band edges are shown by dots, which occur on the boundary of the Brillouin zone in the ⟨111⟩ directions. The other half of the conduction band valley in this direction is provided by the crystallographically equivalent opposite arm of the diagram. The conduction band electrons are distributed among these equivalent-energy valleys. The constant energy surfaces of each valley of the conduction bands of silicon and germanium are prolate ellipsoids, characterised by a transverse and a longitudinal mass. In the minor (x and y) or 'transverse' axes directions the effective mass is isotropic and the energy varies rapidly with k, giving a low transverse mass ($m_\perp$). In the 'longitudinal' (z) direction the energy varies relatively slowly, giving a large $m_{||}$. The energy distribution with vector momentum k_x, k_y and k_z, for a given valley with a band centre at k_{0x}, k_{0y}, k_{0z} is therefore [30] given by Equation 2.3.

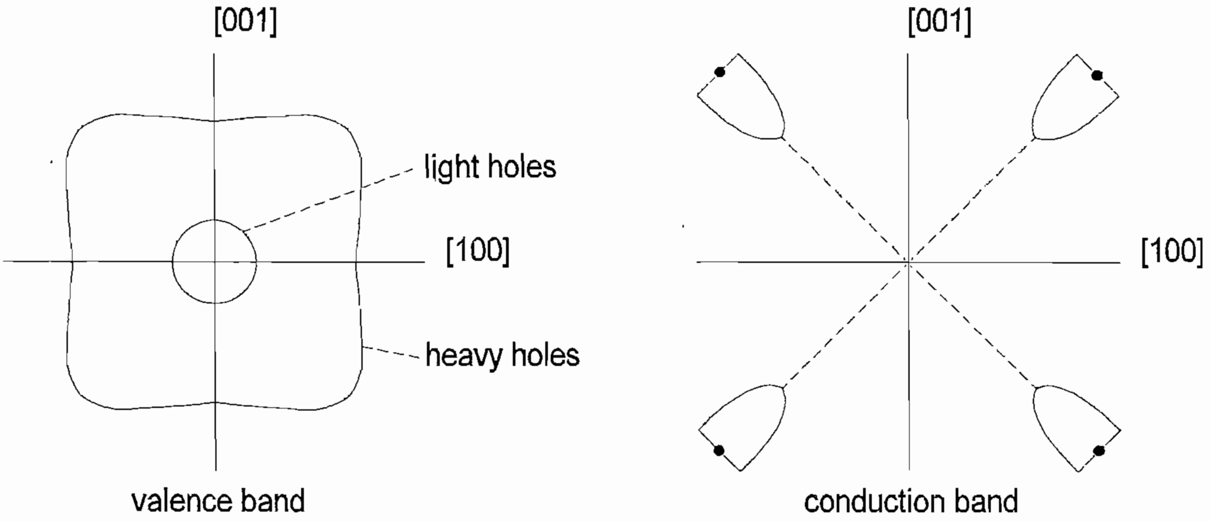

Figure 2.2: Constant energy contours near the conduction and valence band edges projected on the (010) plane in k space for germanium

$$E(k) = \frac{h^2}{2\pi}\left[\frac{(k_x - k_{0x})^2 + (k_y - k_{0y})^2}{2m_\perp} + \frac{(k_z - k_{0z})^2}{2m_{||}}\right] \tag{2.3}$$

The effects of this are considered in more detail for germanium in Chapter 3. At this stage it is important that the energy-momentum relationship for small energy perturbations from the band edge is to a good approximation, parabolic, and that due to the warped energy spheres or elliptical surfaces of constant energy, the carrier effective mass in a particular band must be averaged over all directions when carriers are not constrained to motion in a particular direction. Such unconstrained motion occurs during optical excitation in the absence of electric and magnetic fields. Having outlined the semiconductor band structure, the possible transitions between these bands are considered for their relevance in an infrared modulator.

2.1.1 Fundamental direct and indirect transitions

The fundamental absorption refers to the transition of an electron between the valence and the conduction band. This process is of concern during optical excitation of a semiconductor, and can also be used to modulate infrared radiation as a subsidiary effect. If the bandgap transition does not require a change in momentum, the semiconductor has a direct bandgap, otherwise it is an indirect-gap material. Transitions between any bands in the semiconductor must conserve energy and momentum, and at above absolute-zero temperature, phonons may be involved in the excitation transition.

Phonons are a quantum of lattice vibration having a small amount of energy and a large amount of momentum, and one or more phonons can take part in the transition process if they have the required amount of momentum and energy. Six types of phonons exist: two transverse optical (TO), two transverse acoustic (TA), one longitudinal optical (LO) and one longitudinal acoustic (LA). Optical phonons have a high characteristic range of vibrational frequencies. In a lattice with ions of opposite sign these produce a polarisation that interacts with light waves. Acoustical phonons have a lower characteristic range of vibrational frequencies. The number of phonons n_ν at a frequency ν and temperature T follows [31] Planck's law, and is given by $n_\nu = (exp(\frac{h\nu}{kT}) - 1)^{-1}$. Thus at room temperature there is a higher number of low frequency (long wavelength), acoustical phonons with which a free carrier may interact, than optical phonons. A phonon involved in the fundamental absorption process must have the same momentum vector as the direction in which this fundamental transition exists, the [111] direction in germanium. In this direction the two TO modes are degenerate, as are the two TA modes, leaving four different modes. Crystal symmetry dictates [32] that all four modes with this k vector (TO, LO, LA, TA) contribute to the fundamental absorption if the conduction band minima lies within the Brillouin zone but only the acoustic modes are permitted by selection rules if the conduction band minima are at the edge of the zone. In germanium there are actually eight conduction band minima, each extending to the edge of the Brillouin zone. However, each of the minima only contributes half a valley to the four conduction band valleys. Therefore it is only the acoustic mode phonons that take part in the fundamental absorption. The energies of these phonons have been determined experimentally [33] as $7.76meV$ and $27.58meV$. Transitions involving phonons (indirect) are less probable than those which do not require phonons (direct) due to the reduced number of participants. This absorption process is different from that at the long wavelength lattice absorption region in germanium, where phonons from both the optical and acoustic modes contribute to the multiphonon absorption 'combination' bands.

With direct transitions, the absorption spectrum shows no increase with photon energy until the photon energy reaches the direct bandgap, at which point the absorption increases steeply with photon energy. With indirect transitions the absorption initially shows a very gradual initial increase starting at an energy E_p below the bandgap. The energy deficit is provided through the absorption of phonons of energy E_p, and whose momentum is essential in making the transition to the indirect valley. A gradual increase is seen due to the low transition probability since the process requires both the electron and a phonon. Further increase in photon energy shows a steeper increase in absorption starting at an energy E_p above the bandgap. This absorption corresponds to the more probable emission of a phonon during the absorption. This slope is maintained until the photon energy is sufficient to take the carrier vertically into the direct valley. From here onward the absorption is even steeper, since no phonons are required by absorbing transitions at these energies. The fundamental absorption spectrum of an indirect semiconductor therefore shows characteristics of both indirect and direct transitions as photon energy is increased.

Once an electron has undergone a fundamental transition it can take several paths before recombining with a valence band hole. At this stage a band - band transition is assumed for the latter transition as opposed to via intermediary levels, which are considered in Chapter 3. If the electron has been excited to a point above the minimum of the conduction band it will lose energy and momentum through collisions with the lattice (phonon emission), returning to the minimum in the conduction band, before recombining with a hole via a band-to-band transition. Whilst in the conduction band the electron is 'free', and can undergo secondary absorption processes, such as band-band transitions or free carrier absorption, which take it to higher permitted energy levels.

The mean time the electron spends out of the valence band is defined as the bulk carrier lifetime. In direct bandgap semiconductors this is characteristically very short, typically nanoseconds. In indirect bandgap semiconductors the lifetime is much longer because carrier recombination through a simple band to band process requires phonon emission to permit the electron transition back to the top of the valence band. Excitation of equal bandgap semiconductors with the same absorbed power therefore results in a higher carrier density in the excited band in an indirect bandgap semiconductor compared to a direct bandgap semiconductor due to the lower carrier loss rate to the valence band.

2.1.2 Interband transitions within the conduction or valence band

The previous subsection considered transitions between the conduction and valence bands. This section considers transitions between the sub-bands of a given band, interband transitions. The sub-band absorption is dependent on the occupancy of the conduction and valence bands, and hence can be used to modulate radiation. The valence band of most semiconductors is split into three subbands due to spin orbit interaction, hole interband transitions being possible between these bands. Detail of the band splitting in germanium is shown in Figure 2.3.

With this band structure, hole transitions are possible between (a) the heavy hole (HH) band and the spin orbit splitoff (SO) band, (b) the light hole (LH) band and the spin orbit splitoff band, and (c) the heavy hole band and light hole band. To enable these transitions a hole must exist in the valence band. However, in many semiconductors the transition (a) occurs at too short a wavelength and is masked by the fundamental absorption, and transitions (b) and (c) occur at too long a wavelength where they are masked by free carrier or multiphonon absorption. In germanium these three transitions are all observed within the optical passband of the lattice, as illustrated by the transmission spectra in Figure 2.4 for a $0.536cm$ p-doped germanium sample with resistivity $1.2\Omega cm$ and hole doping density of $2.9 \times 10^{15} cm^{-3}$. The area carrier density associated with this absorption is $1.55 \times 10^{15} cm^{-2}$.

Figure 2.4 for intrinsic germanium shows no absorption bands within the lattice

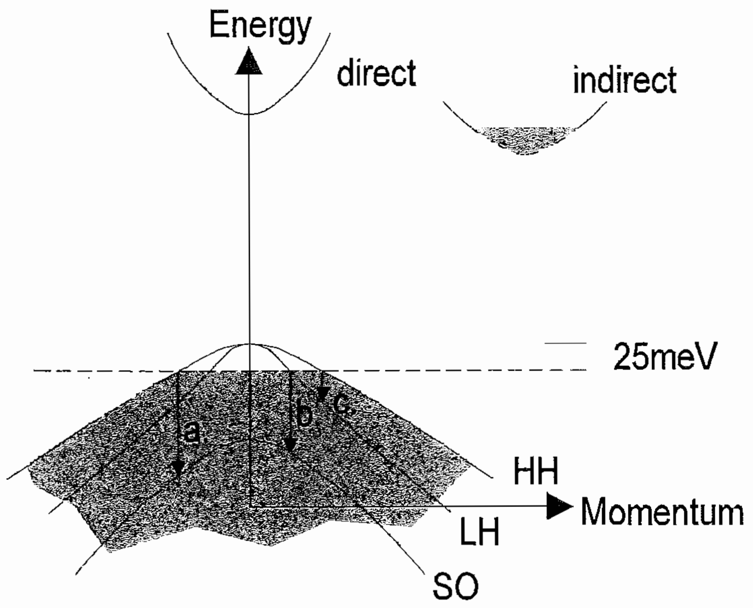

Figure 2.3: Detail of the split valence band in germanium showing possible hole transitions during optical excitation. Electrons are represented by the shaded region

passband of 1.8 to $18\mu m$. The transmission is practically constant with wavelength over this region. In contrast, the p-doped germanium spectra is marked by three distinct absorption bands centred at $3.3\mu m$, $4.5\mu m$ and a third broader band at around $10\mu m$. These correspond to the above transitions (a), (b) and (c) respectively. Ubiquitous fluctuations in room CO_2 concentration cause the band at around $4.2\mu m$. To temporarily increase the absorption, the semiconductor must be near-intrinsic, or low-doped so as to provide low absorption in the 'on' state. Carrier excitation moves electrons to the conduction band, increasing this absorption. This increases the free hole density in the valence band hole, hence increasing the number of holes making transitions between the split levels in the valence band. Termination of the excitation restores the transmission to that beforehand, after the excited electrons have recombined with holes in the valence band. This is illustrated by Figure 2.5.

The absorption bands seen in the lower graph of Figure 2.5 are almost entirely due to hole absorption, and disappear when the germanium is made n-type. Temporally inducing this strong absorption will later be seen to be the operating mechanism behind the modulator.

In addition to being a valence band absorption process, interband absorption takes place between conduction band valleys. In some semiconductors, such as gallium phosphide [34], the conduction band has a low-lying second valley above the conduction band minimum, and direct transitions are possible between these valleys. For this transition to permit significant absorption the semiconductor must have a significant electron density

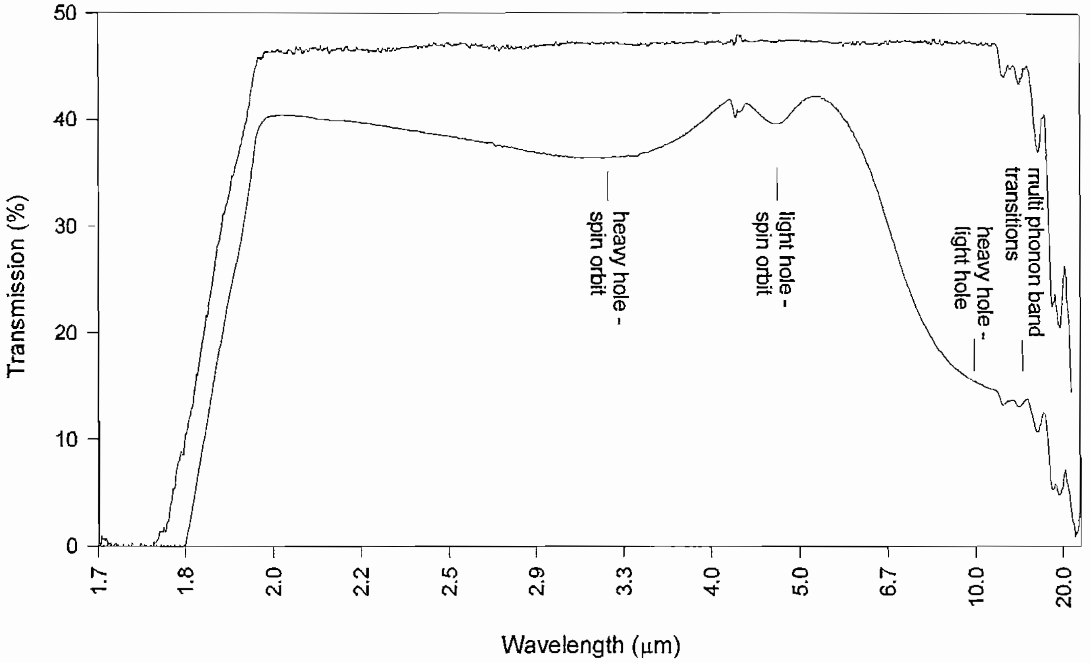

Figure 2.4: Transmission spectra of intrinsic germanium (upper) and $1.2\Omega cm$ p-type germanium, with respective thickness $0.31cm$ and $0.54cm$

in the conduction band. Many semiconductors have these higher-lying conduction band minima, which could in principle be used to modulate radiation, although frequently the energies involved in transitions between these valleys are so large that the absorption is masked by the fundamental absorption.

2.1.3 Free carrier transitions

Free carriers are carriers that are free to move within a band. Free carrier (hole or electron) absorption arises [30] through the excitation of a free carrier to a higher energy level within the same band. This requires a change in energy (which is provided by the absorbed photon) and a change in momentum, which is provided by interaction with the lattice through phonons or by scattering from ionized impurities. Free carrier absorption increases with carrier density, showing a smooth increase with wavelength with a spectral dependence λ^r where r ranges from 1.5 to 3.5 depending on the scattering process. Classical Drude Zener free carrier absorption assumes an electron is driven by an oscillating electric field, and results in an damping factor that increases as λ^2, giving an absorption coefficient [35]:

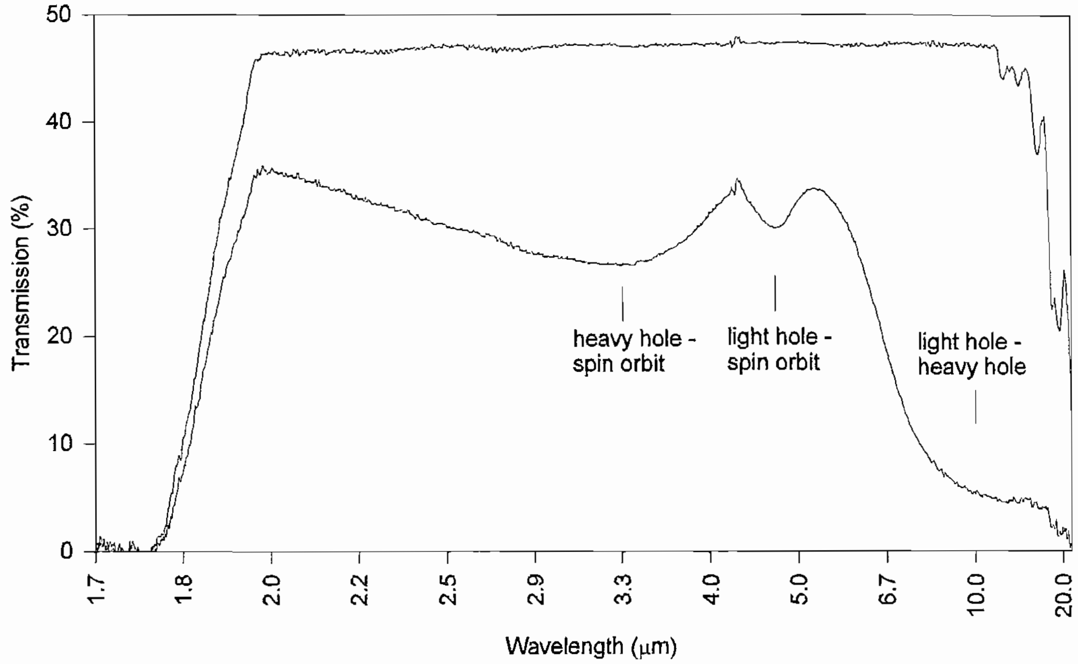

Figure 2.5: Transmission spectra of unexcited intrinsic germanium (upper) and germanium optically excited by $9.6 W\ cm^{-2}$ at $980 nm$

$$\alpha_{fc} = \frac{\lambda^2 q^3}{4\pi^2 c^3 n^* \epsilon_0}\left[\frac{n}{m_n^2 \mu_n} + \frac{p}{m_p^2 \mu_p}\right] \tag{2.4}$$

Where n^* is the refractive index, n and p are the electron and hole densities, m_n is the electron mass and μ_n is the electron mobility. Scattering [36] via acoustic phonons leads to a $\lambda^{1.5}$ absorption dependence, optical phonon scattering gives a $\lambda^{2.5}$, and scattering via ionized impurities leads to a λ^3 or $\lambda^{3.5}$ dependence. In practice all three of these processes may exist, although one may dominate depending on the impurity concentration. The combined absorption tends toward λ^r, where r increases with doping. In n-doped germanium $r \cong 2$ and the Drude-Zener model is adequate in modelling free carrier absorption.

Unlike inter-valence band absorption, free carrier absorption shows no sharp absorption peak. The absorption spectra arising from free carrier absorption is shown by the lower graph in Figure 2.6, the transmission spectrum of a very heavily n-doped germanium sample. This is in contrast with the transmission spectrum of p-doped germanium in Figure 2.4.

Figure 2.6 clearly shows a λ^2 absorption process due to free carriers. The free electron

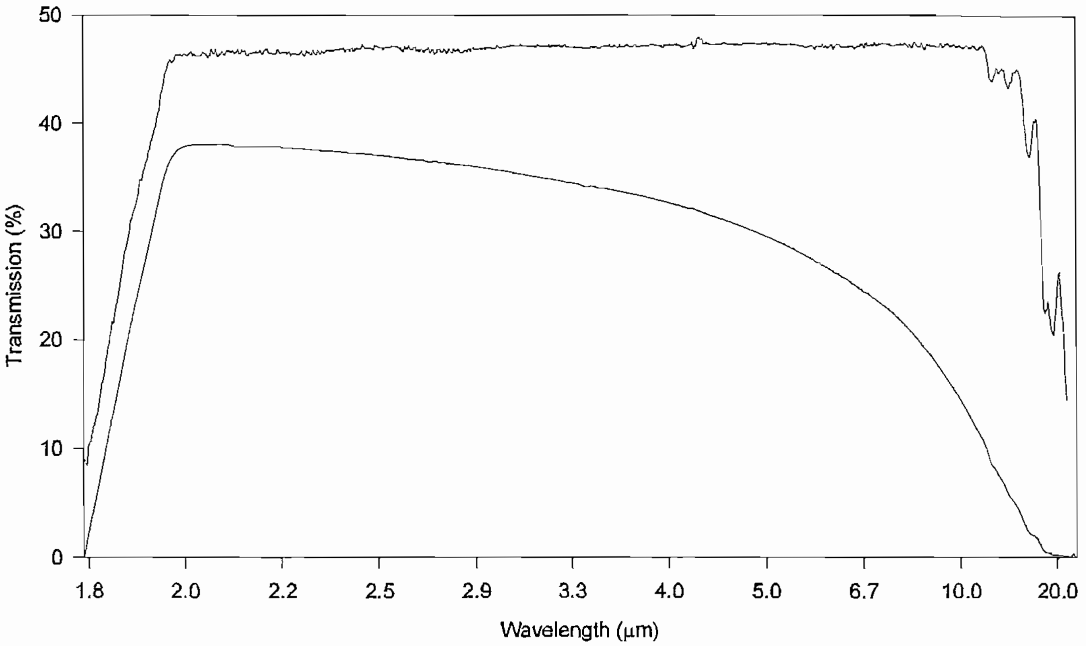

Figure 2.6: Transmission spectra of an intrinsic germanium sample (upper) and a heavily n-doped germanium sample with resistivity $0.03\Omega cm$, with respective thickness $0.31cm$ and $0.47cm$

density associated with this $0.03\Omega cm$ sample is $5.3 \times 10^{16} cm^{-3}$, and the sample thickness is $0.468cm$, giving an area carrier density of $2.48 \times 10^{16} cm^{-2}$. Comparison to the hole dominated inter-valence band absorption process in Figure 2.4 is given in Table 2.1.

doping	**Figure**	**thickness**(cm)	**T** (%)**at** 10.0μm	**area carrier density** (cm^{-2})
n	2.6	0.468	14.49	2.48×10^{16}
p	2.4	0.536	14.97	1.55×10^{15}

Table 2.1: Comparison of absorption in n and p doped germanium

Similar levels of transmission (and hence absorption) are seen in the two doped samples which are of similar thickness. However to induce the same level of absorption in the n-doped sample requires 16 times the area carrier density. This is expected since the hole absorption cross section at $10.6\mu m$ is 15.7 times that for electrons.

2.2 Modulation mechanisms in the infrared

Modulation in the infrared requires a controllable infrared absorbing transition process. $10.0\mu m$ corresponds to a photon energy of $0.124eV$, and the transition must be sufficiently broad to cover the 8 to $14\mu m$ band for use in the application. The absorption must be switchable, enabling a rapid change in semiconductor absorption from a low 'on' state value to a high 'off' state value through a strong increase in absorption or reflection. This section considers methods of achieving this through the previously described mechanisms, detailing their application in an infrared modulator.

For a practical modulator in portable applications, a high level of switchable absorption at low power consumption over 1 : 1 duty cycle operation is a primary requirement. The absorption cross section σ is defined as the ratio of the absorption coefficient at a given wavelength to the free carrier density, having units cm^2. This can be envisaged as the physical area around an electron or hole within which a passing photon will be absorbed. The absorption coefficient measured at a given wavelength is the total resulting from free carrier absorption, absorption within the subbands of the conduction and valence bands, lattice scattering through phonon emission, impurity absorption and fundamental absorption. The strength of these components is wavelength-dependent. A modulator using an 'induced' absorption process must have low 'on' state absorption, and a controlled process must be used that enables large numbers of transitions in a high absorption cross section absorption process to take place during the modulator's absorbing 'off' state. Low 'on' state absorption is achieved using a semiconductor in a region spectrally remote from the bandgap or lattice absorption.

2.2.1 Absorption via shifting the fundamental absorption edge

In a heavily-doped or strongly optically-excited semiconductor, one important effect of transitions into a direct or indirect valley is the observed shift of the bandgap toward shorter wavelength. This occurs when the conduction band starts to fill significantly with electrons. This 'Moss-Burstein' shift [37] occurs when conduction band electrons prevent transitions from the valence band to these occupied levels. Only higher-energy electrons are capable of making the transition to unfilled states. This progressive apparent band-edge shift toward shorter wavelengths is most significant in semiconductors having a steeply curved conduction band with momentum, since the band fills quickly with a low electron density.

The Moss-Burstein shift could be used to modulate in the infrared. At wavelengths just short of the bandgap a semiconductor is strongly absorbing. In principle, strong optical excitation of a low effective mass semiconductor rapidly fills the conduction and valence bands with electrons and holes respectively. Optical transitions that were possible before the excitation are then no longer permitted, and the absorption just short of the semiconductor's unexcited bandgap falls considerably. The stronger the optical excitation, the further the bandgap is shifted toward shorter wavelength. Such an area-based optical shutter has been demonstrated [38], at around $10\mu m$ in $Pb_{0.63}Sn_{0.37}Te$. Here a $100kW\ cm^{-2}$ probe beam at $10.6\mu m$ ($10meV$ from the absorption edge) was switched by a $300kW\ cm^{-2}$ pump beam at $9.3\mu m$ (a further $16meV$ from the absorption edge). The sample thickness was $5\mu m$ with an unexcited absorption coefficient at $10.6\mu m$ of $5 \times 10^3 cm^{-1}$, which was cooled to $77K$. At $500kW\ cm^{-2}$ pump intensity the probe beam transmission was increased by a factor of 5, although the absorption is nonlinear with power due to the shape of the absorption edge.

In practice, generating significant changes in absorption using the Moss-Burstein shift requires a semiconductor with a very low effective mass conduction band. Some direct bandgap semiconductors such as InSb show the effect, but their inherent short bulk carrier lifetime requires high power to sustain an adequate electron density. If available, an indirect bandgap semiconductor with a similarly narrow momentum-width conduction or valence band valley would require much lower power to produce this reduction in absorption. The process is also limited to modulation over a narrow spectral region close to the semiconductor bandgap, and few semiconductors exist with a bandgap in the $10\mu m$ region. In addition to the high power required to exploit this absorption process, the pump beam is also an issue. If this requires CO_2 laser excitation it would imply a large modulator system, and at such high power in a portable device would limit operation to low repetition rate applications. Much shorter wavelength diode lasers could generate the required electron-hole pairs in the material, but at reduced efficiency since there are more photons per Watt of optical power at longer wavelength; requiring immense power from diode lasers. Unless a suitable indirect bandgap semiconductor exists, this method of modulation is restricted to applications requiring narrow spectral width modulation where physical space and power consumption are not design constraints.

2.2.2 Free carrier absorption

Free carrier absorption can be used to modulate in the infrared following the temporary generation of electron-hole pairs. This requires a near-intrinsic semiconductor with long-wavelength cutoff beyond the range of wavelengths requiring modulation. In the unexcited state the electron and hole densities n and p in Equation 2.4 are low, giving a low absorption coefficient. Free carriers generated temporarily by above-bandgap optical excitation or through electrical injection in a p-n junction diode-type structure increase the absorption coefficient. The absorption increases smoothly with wavelength, having λ^r dependence where r lies from1.5 to 3.5. Modulation using this mechanism is therefore favourable at long wavelengths where the absorption is stronger.

Free carrier absorption is generally dominated by one particular charge carrier. Equation 2.4 above requires the effective mass of the electrons and holes, which is an average over the crystal directions. For silicon and germanium the electron effective mass is averaged over the longitudinal and transverse axes of the ellipsoidal conduction band constant-energy surface [25], giving the average effective electron mass as:

$$\frac{1}{\langle m^* \rangle} = \frac{1}{3}\left(\frac{1}{m_l^*} + \frac{2}{m_t^*}\right) \tag{2.5}$$

For holes the heavy hole mass is used in the absence of a magnetic field [39] in calculations of average effects over times much longer than picoseconds. Since the hole relaxation is so short (picoseconds), holes spend most of their time in the heavy hole band. For most semiconductors [40] the hole constant energy surfaces are sufficiently close to spherical that the hole longitudinal and transverse effective masses are about the same. For germanium an average electron mass of $0.12m_0$ and an average hole mass of $0.28m_0$ are found. These values are in agreement within experimental error with those determined by microwave techniques [41]. The electron and hole mobilities at room temperature in germanium are $\mu_e = 3900cm^2/Vs$ and $\mu_h = 1900cm^2/Vs$ [42]. In germanium this gives $m_p^2\mu_p = 2.7 \times m_n^2\mu_n$. From Equation 2.4, this shows the Drude-Zener absorption in intrinsic germanium is dominated by free electron absorption. Using these parameters, the absorption coefficient due to free carriers alone in n type and p type germanium is computed in Figure 2.7.

In practice, measurement of the free carrier absorption at $10\mu m$ is possible in n-type germanium, but in p-type germanium it is masked by the much stronger absorption from hole inter-valence band transitions (Section 2.2.5). Based on the above calculations, to reduce the transmission at $10.0\mu m$ from 100% to 50% in a $0.5cm$ thick modulator using free carrier absorption requires a uniform free carrier density of $4.3 \times 10^{16}cm^{-3}$ when only free carrier absorption is considered.

Several such free-carrier induced-absorption modulators have been demonstrated [43] [44] [45] [46], in which carriers were injected into a diode-type structure or were optically excited. One such device [44] uses a silicon tunnel MIS diode to inject carriers

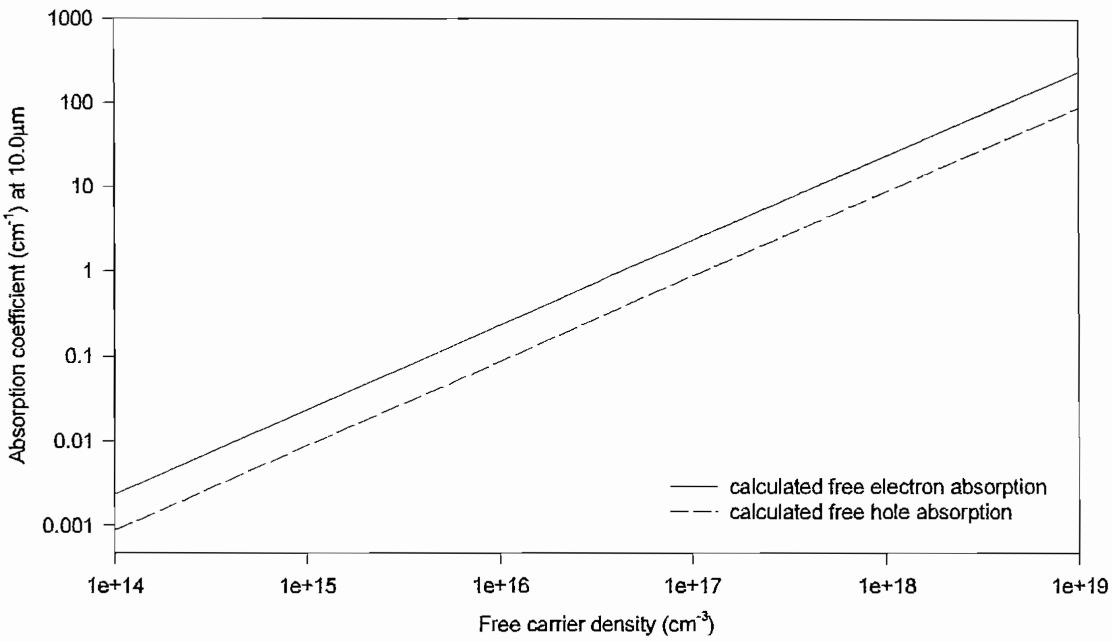

Figure 2.7: Absorption coefficient due to free carrier absorption in germanium at $10.0\mu m$ from Equation 2.4

into a ridge-type optical waveguide and modulate a $10.6\mu m$ CO_2 laser beam. A depth of modulation of 62% was achieved using a current of $63A\ cm^{-2}$ and the waveguide cross section was $30 \times 400\mu m$. The modulation is parallel to the junction plane in this structure, restricting modulation to that of a beam of waveguided radiation, in contrast with the required area-modulator. In principle, area-modulation using free carrier absorption with the probe beam perpendicular to the junction plane could be achieved, providing sufficient current could be passed through the structure, and providing this level of current injection could be achieved using infrared-transparent contacts. This is discussed in Section 8.1.

2.2.3 Plasma switching

With the previously-reviewed modulation mechanisms the real part of the refractive index of the semiconductor has been assumed constant during optical excitation. Plasma switching involves exciting the semiconductor to generate an immense carrier density, to the point where the real part of the refractive index is no longer constant. The plasma frequency in a solid is given [47] by:

$$\omega_p = \sqrt{\frac{nq^2}{m^*\epsilon}} \tag{2.6}$$

where m^* is the effective mass, ϵ is the dielectric constant and n is the carrier density. The plasma frequency is defined as the frequency below which the refractive index becomes imaginary and this lies in the far-infrared for most unexcited semiconductors. It can be though of as the resonant frequency of the excited carrier plasma.

Well above the plasma frequency the semiconductor is transparent, and below the plasma frequency the semiconductor is reflecting. It is the electrons with their low effective mass that are responsible for the modulation using plasma switching. Optical excitation is used to move the plasma frequency toward shorter wavelengths, shifting the point at which the reflectivity increases. This technique has been widely used to modulate in the infrared [10] [11] [12] [13] [14] [15] [16] [17] [18] in applications where high optical excitation power is available.

In the examples cited the optical switch is configured as a high contrast reflection device, so that the semiconductor, such as germanium, is usually aligned [10] [11] at the Brewster angle so it has a low reflectivity in the unexcited state at the wavelengths requiring modulation. At free space wavelengths shorter than the plasma frequency the semiconductor is transmitting, and at wavelengths beyond the plasma frequency the semiconductor's reflectivity approaches unity. In the unexcited state n is low, the plasma frequency is low, and so the wavelength at which the plasma-induced absorption occurs will be long and the semiconductor's reflectivity in the modulated band will also be low. Increasing the carrier density n via optical illumination reduces the free space wavelength corresponding to the plasma frequency in the excited semiconductor, and renders the semiconductor reflecting at the desired, modulated, wavelength.

Modulation of the plasma frequency in a semiconductor can be used to modulate in the infrared, although its Brewsters-angle alignment makes it polarisation-sensitive. In principle such a device could be configured at normal incidence, eliminating polarisation-sensitivity, and used as a transmission modulator. However, the power densities required to shift the plasma frequency to the $10\mu m$ region in germanium are in the order of $10MW\ cm^{-2}$ when using a Q-switched $1.06\mu m$ excitation source [10] [18]. This power density renders the plasma-switching modulator unsuitable for low power devices, and limited to short-pulse low repetition-rate applications. Also it would be difficult to design such a system for low f-number optics and Brewster's angle alignment due to astigmatism. The large Brewster angle of germanium (76°) also requires very large optical components.

2.2.4 Hot-electron assisted absorption

With indirect fundamental transitions it is possible to absorb photons of energies just lower than the bandgap, where the additional energy and momentum increment required is provided by a phonon. With hot electron assisted absorption a similar mechanism takes place, but the additional energy increase required is provided by a free carrier. In the hot-electron assisted absorption process a photon with energy just below the bandgap excites an electron from the valence band to a virtual state just below the conduction band. From here the electron is given the final energy boost to take it to the conduction band, by a phonon emitted by a 'hot' electron in the conduction band. 'Hot' electrons are obtained by applying a small electric field so as to increase the electron temperature.

The process is not usually observed in indirect bandgap materials since the large momentum required to complete the electron transition to the valence band is too great to be supplied by the phonon from an electron. This effect exists at long wavelengths and is not negligible. Calculations [36] [48] show that for an electron density of $10^{16} cm^{-3}$ and an electron temperature of $kT_e = 0.01eV$ the absorption coefficient at an energy deficit of $0.01eV$ is $6cm^{-1}$, and reduces as the energy deficit increases. However, this process is easily masked by transitions between impurity levels and by sub-band transitions, and therefore is only observed in relatively pure, direct gap materials.

The effects of hot electrons on the absorption have been observed [49] in the infrared at $17\mu m$, although the excitation power density required to observe these transitions was $14MW\ cm^{-2}$. This, combined with the absence of the effect in indirect-gap materials suggests that the process would have little use in an application in which excitation power is a design constraint.

2.2.5 Comparison of modulation mechanisms

All the modulation mechanisms reviewed have potential in the modulation of infrared radiation. Their spectral dependence, level of absorption and power required to induce the infrared-absorbing transitions are of primary concern in a portable modulator system. These modulation mechanisms rely on the population of conduction and valence bands with carriers, and modulation of the infrared is achieved through a secondary process of enabling or preventing infrared transitions. Following the carrier excitation required to populate these bands, the level of absorption is dependent on the carrier density in the conduction and valence bands. The duration of the absorbing period of the modulation can therefore only be in the order of the carrier recombination time, unless excess excitation power is used to compensate for the recombining carriers. Direct bandgap semiconductors with characteristic nanosecond carrier recombination times can therefore sustain induced absorption over this period, but require an excessive excitation power to sustain high excited carrier densities over longer periods. At the low modulation frequencies and long (tens of milliseconds) absorbing duration associated with the application, an indirect bandgap semiconductor must therefore be used.

Hot-electron assisted absorption is therefore of little use. Free carrier absorption offers potential since indirect bandgap semiconductors may be used by the process, but the low free carrier absorption cross section in comparison to inter-valence band absorption requires higher excitation power. Even higher excitation power is required with plasma switching to shift the plasma frequency to the $10\mu m$ region. The Moss-Burstein absorption-edge shift process is also restricted to high power applications when modulating over the required spectral band. This also involves finding a suitable semiconductor with a bandgap in the $10\mu m$ region. Such semiconductor compounds may be created with the added complications of complete material-characterisation and costly development. The characteristics of these absorption mechanisms are summarised in Table 2.2.

modulation mechanism	**power density**	**available in indirect gap material?**	**range of modulated wavelengths**
Moss Burstein	$300kW\ cm^{-2}$	mainly direct	very narrow
Free carrier	$160W\ cm^{-2}$	yes	broad
Plasma switching	$10MW\ cm^{-2}$	yes	broad
Hot electron	$14MW\ cm^{-2}$	no	narrow
Light hole-heavy hole	$10W\ cm^{-2}$	yes	broad bands

Table 2.2: Summary of the modulation mechanisms reviewed

Of these processes the light - heavy hole inter-valence band absorption process, in particular in germanium, offers the highest level of induced absorption at a reasonable excitation power density. This process is now discussed in detail.

2.3 Intervalence band transitions: the modulator mechanism

The split valence band in germanium is shown in Figure 2.8 where V1 and V2 are the heavy- and light-hole bands, and V3 is the Spin Orbit band. The mean thermal energy of free holes in near-intrinsic germanium is shown by the dotted line corresponding to $25meV$ at $300K$. The spin orbit splitting is $0.28eV$ [25] so the spin orbit band is not hole-populated at room temperature.

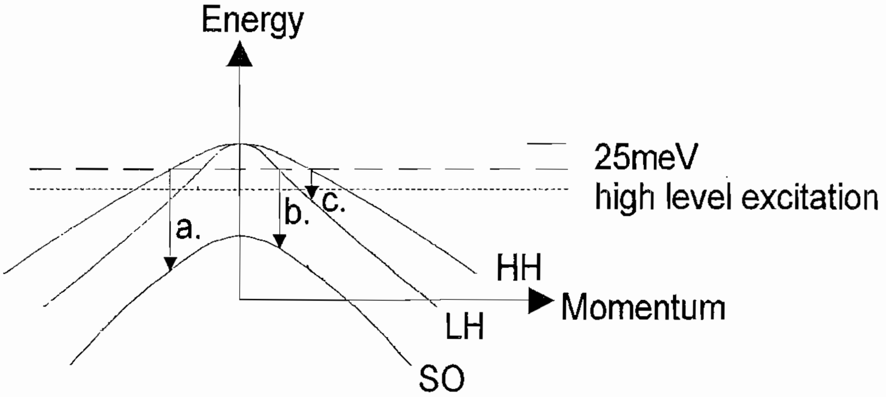

Figure 2.8: Schematic valence band structure near the top of the valence band in germanium showing inter-valence band transitions

Figure 2.8 shows that photon-absorbing hole transitions V1 to V3, V2 to V3 and V1 to V2 are possible. These correspond to absorption bands centred at $3.3\mu m$, $4.5\mu m$ and a third broader band centred at around $10\mu m$. These transitions are direct, involving only photon absorption. At $k = 0$ these transitions are not permitted due to selection rules [25], but at $k \neq 0$ the selection rule breaks-down. At high values of hole energy (and hence k) the Maxwellian hole distribution function means that fewer holes are present to make the transitions. This explains the 'bands' of absorbed radiation. After a photon has been absorbed by this process, the excited hole in the light hole or spin orbit band rapidly scatters back (within picoseconds) to the heavy hole band, losing momentum and energy through lattice collisions (phonon emission) and may then absorb another photon. This rapid scattering process means that only at MW absorbed radiation power levels [50] [51] [52] [53] does the heavy hole band become depleted of holes and the absorption from these three bands saturate.

Temporary hole generation, and the subsequent induced absorption required by the modulator, is achieved using near-intrinsic germanium as the starting material. The Fermi level is situated close to the middle of the germanium bandgap. Above-bandgap excitation temporarily moves electrons to the conduction band, generating the same number of holes in the valence band. High level excitation (excess carrier density > intrinsic carrier density) causes the Fermi level to split into two quasi Fermi levels, one for electrons and one for holes. The quasi Fermi levels move toward their respective bands with increased optical excitation. At very high hole densities, achieved through p-doping or optical excitation, the hole quasi Fermi level moves into the valence band and the semiconductor becomes degenerate, as shown by the lower dotted line (higher mean hole energy) in Figure 2.3. In this case the depopulation of valence band electrons permits hole occupation from the top of the valence band to the lower dotted line. However, typical excitation levels used in the modulator are just below the limit of degeneracy (which is discussed in Chapter 3), the Fermi levels remain within the bandgap and the mean room-temperature hole energy is described by the upper dashed line. Increasing the optical excitation increases the density of holes with this mean energy. At higher hole energies than shown by this line the free hole density tails-off to zero. In correspondence with the tailing-off hole density, the electron population tails-off in the upper vertical direction over the same kT spread of thermal energy. Vertical transitions from all lower-energy hole states are now possible that terminate on bands V2 and V3, although the majority of these take place from the vicinity of the intersection of the $25meV$ line and the relevant band. This is due to the combination of a higher hole population in the starting heavy or light hole bands, and a higher state density in the terminating (light or spin orbit) band.

During moderate-level excitation the hole quasi Fermi level is situated between the intrinsic Fermi level and the valence band edge. The mean hole energy is denoted by the upper dotted line, at a lower energy than kink in the V2 light hole band. This kink occurs at hole energies considerably higher than kT, and after this point the gradient of the V2 band becomes less steep, thereafter becoming nearly-parallel with the V1 band [26]. At the point where the bands become nearly parallel, transitions occurring over the thermal (kT) spread in hole energy about the mean hole energy in the starting band, undergo vertical transitions of similar energies. This gives the narrow absorption band at around $10\mu m$. Near-parallel bands in the E-k momentum diagram have a high transition probability, giving a high absorption coefficient in this region. The transitions V1 to V3 and V2 to V3 are considerably broader due to the bigger difference in gradients of the respective bands over a kT spread in energy about the Fermi level at this point. The V1 to V3 transition is extremely broad in frequency terms for this reason.

Further increase in valence band hole density through higher level excitation moves the Fermi level into the valence band (lower dotted line). Figure 2.3 shows the effect of this is to move the peak of the V1 to V3 transition toward higher energies, the V2 to V3 peak moves toward lower energies, and the low energy edge (long wavelength cutoff) of the V1 to V2 transition moves toward higher energies. Spectra of optically excited near-intrinsic germanium are shown in Figure 2.9, but these effects are small and difficult to observe as degeneracy is not encountered. The V1-V3 transition is too broad to define an exact minimum, and the long wavelength cutoff of the V1 to V2 transition is masked by the lattice absorption. However, the spectrally narrower V2 to V3 shift toward lower energies is observed.

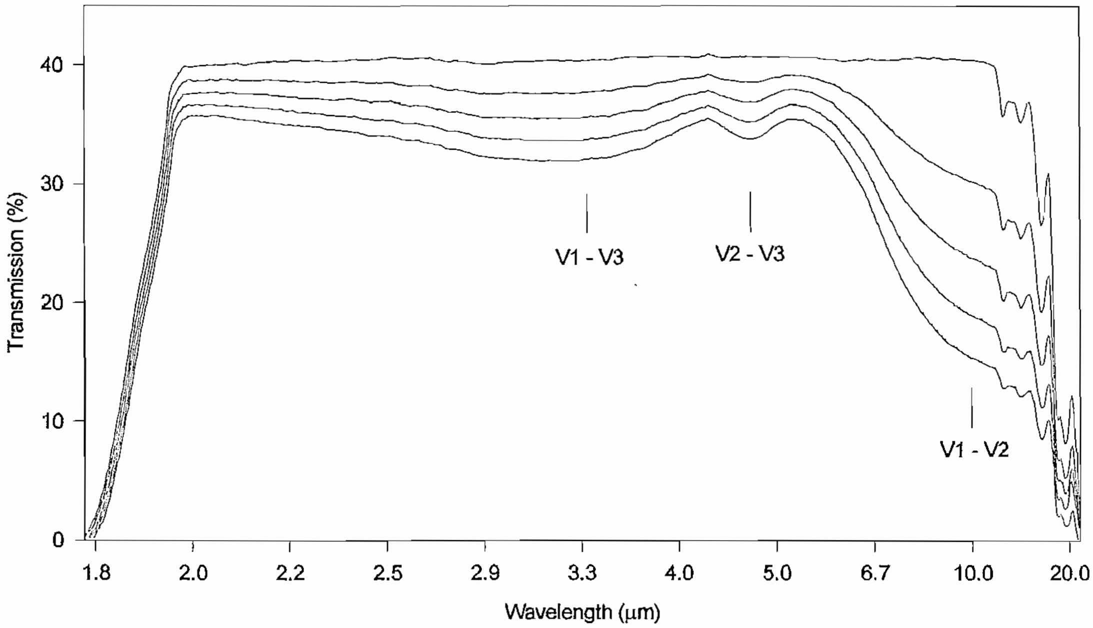

Figure 2.9: Transmission spectra of germanium excited at 0, 4, 8, 12 and 16$W\ cm^{-2}$ showing shift of absorption peaks with excitation power

To complete the description of the absorption process, changes in absorption with reduced temperature are now detailed. The low temperature range considered is not encountered during the modulator's usual operation. Operation will be confined to the military temperature range of $300K \pm 50K$. A temperature dependence of the absorption spectra is expected from the temperature-dependent hole population. As temperature is reduced the Fermi level moves upward in Figure 2.8 and the kT mean hole thermal energy over which its population tails off, reduces. This shifts the vertical hole transitions from the light and heavy hole bands toward lower momentum values, also reducing the momentum range over which these transitions take place. This causes the transitions to narrow spectrally. Specifically this means the absorption peaks from the V1 to V2 and the V1 to V3 transitions will move toward longer wavelength, whilst the absorption from the V2 to V3 transition moves toward shorter wavelength. The measured transmission spectra for p-germanium as a function of temperature is shown in Figure 2.10.

Figure 2.10 shows both the V1 to V2 transition (centred at $10\mu m$) and the V1 to V3

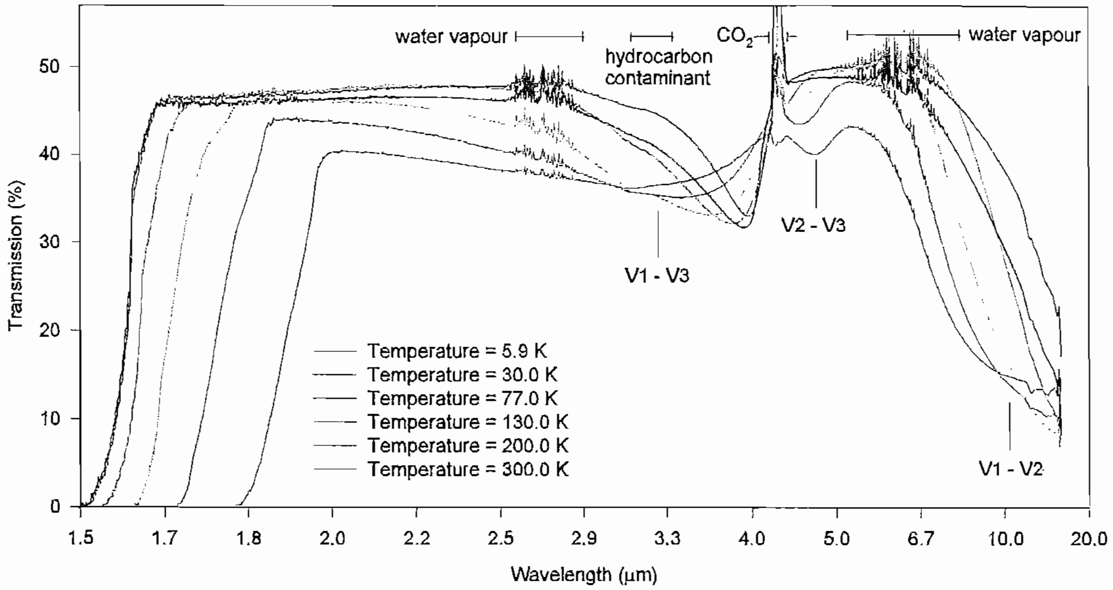

Figure 2.10: Absorption due to inter-valence band transitions in $0.04\Omega cm$ p-type germanium

transition (centred at around $3.3\mu m$) moving toward longer wavelength with reduced temperature as predicted. The spectral width of the V1 to V3 transition narrows as expected, whilst that for the V1 to V2 transition is masked by lattice absorption. The V2 to V3 transition (centred at $4.5\mu m$) moves toward shorter wavelength as predicted. By $77K$ the V1 to V3 and the V2 to V3 bands have overlapped, further reduction in temperature causing the combined band to narrow even more. The general form of the spectra is also seen to change. Movement of the fundamental absorption edge toward shorter wavelength is seen, and the transmission in the $6\mu m$ region increases due to a reduction in Drude-Zener free hole absorption as holes freeze-out onto acceptor states. At $0K$ one would expect the transmission spectra become flat over the entire passband, characteristic of intrinsic germanium, all free holes having frozen-out. At $5.9K$ there still appears to be a significant hole population. However, the FTIR spectrophotometer used to measure the transmission causes the power from the entire hot source spectrum sampled to be incident on the cooled sample during measurement. This complicates the measured spectrum since optical carrier generation occurs continually. This optical excitation occurs not only from fundamental transitions but more importantly from excitation from the acceptor states situated at the Fermi level which is within the bandgap at these temperatures. Therefore the spectrum detail is affected at low temperatures. This may explain why the transmission at $30K$ and $5.9K$ in the $10\mu m$ region is lower than the trend might suggest. The anomalous increase in transmission of the combined V1 to V3 and V2 to V3 band at $30K$ may also be due to this effect. Ubiquitous fluctuations in room CO_2 and water vapour concentration causing the marked bands should be ignored. The rogue hydrocarbon contaminant centred at $3.1\mu m$ ($3230cm^{-1}$) featured in many low temperature spectra with this cryostat. However, the important features described by the analysis are clearly present, although repeating measurements with a dispersive spectrophotometer would clarify the optical generation issue. Over the operating temperature range of the modulator (close to room temperature), shifts in the absorption peaks are minimal. Movement of the peak centred at $10\mu m$ therefore has no influence on modulator design.

For use in our application the particular transition of interest in germanium is the heavy hole to light hole transition centred at $10\mu m$. At this wavelength a minimal contribution to the hole absorption cross section σ_h is also given by free hole absorption. The total absorption coefficient due to both electrons and holes is given [27] by α_{total} with units cm^{-1}.

$$\alpha_{total} = \sigma_e n + \sigma_h p + K_{phonon} \tag{2.7}$$

n and p represent the electron and hole concentrations (cm^{-3}), and the carrier absorption cross sections are given by σ_e and σ_h. K_{phonon} is the phonon absorption arising from lattice vibrations. The electron absorption cross section in the $10\mu m$ region is much lower than that due to holes since absorption by electrons, being indirect, is less probable than the vertical, direct hole transitions. At $10.6\mu m$ these parameters have been measured [28] as $\sigma_e = 0.34 \times 10^{-16} cm^2$ $\sigma_h = 5.33 \times 10^{-16} cm^2$ and $K_{phonon} = 0.0073 cm^{-1}$. This gives the ratio of hole to electron absorption cross section as 15.7. In intrinsic germanium ($n = p = 2.4 \times 10^{13} cm^{-3}$) hole absorption therefore dominates the absorption. This does not contradict Section 2.2.2, which calculated only the free carrier absorption, and did not account for inter-valence band absorption processes. However, the absorption by electrons in the two situations should be similar, since the electrons do not undergo sub-band transitions. The Drude Zener absorption in Equation 2.4 predicts an absorption by electrons in intrinsic germanium of $0.632 \times 10^{-3} cm^{-1}$, and Equation 2.7 gives an absorption of $0.816 \times 10^{-3} cm^{-1}$, a discrepancy of 30%. The reason behind this discrepancy between the theory of Equation 2.4 and the measured value used in Equation 2.7 may be due to slight deviation from the λ^2 Drude Zener dependence assumed in Section 2.2.2. A slightly different exponent from 2 could easily generate an error of 30% by $10\mu m$. In modelling the absorption in later chapters the measured absorption cross section is used.

In the modulator application, low absorption is required in the transmitting 'on' state; a high level of absorption being generated in the absorbing 'off' state. At constant temperature in unexcited germanium the product of the electron and hole densities $(n \cdot p)$ is constant (n_i^2). In the 'on' state it is therefore preferable to have a slight excess of electrons, suppressing the hole concentration with its higher absorption cross section, so slightly n-doped germanium is preferable. In the absorbing 'off' state, holes are generated through excitation that moves electrons to the conduction band, thereby creating holes in the valence band which may undergo the heavy hole to light hole transitions.

In order to compare the other modulation schemes reviewed, the carrier density required to induce moderate inter-valence band absorption is calculated. Ignoring multiple reflections, the transmission (T_1) of a germanium sample of thickness (x) is given by Equation 2.8.

$$T_1 = T_0 e^{-\alpha_{total} \cdot x} \tag{2.8}$$

T_0 is the sample transmission in the unexcited state. To reduce the sample transmission by a factor of 0.14 requires $\alpha_{total} \cdot x = 2.0$, requiring (Equation 2.7) an area carrier density of $3.75 \times 10^{15} cm^{-2}$. If these carriers are produced by above-bandgap excitation with a laser wavelength $\lambda_{exc} = 980nm$ at an absorbed power density P_{Excabs} $(W\ cm^{-2})$, and if carriers have a recombination rate of $(1/\tau)$ where τ is the carrier lifetime, the area carrier density at any time in a constantly-illuminated sample is given by:

$$Carriers(cm^{-2}) = \frac{P_{Excabs} \cdot \lambda_{exc} \cdot \tau}{h \cdot c} \tag{2.9}$$

Where h is Planck's constant and c is the speed of light. If a carrier lifetime of $1ms$ in germanium is assumed, this carrier density is achieved by an absorbed power density of $0.76W\ cm^{-2}$. This power requirement is much lower than that of any other induced absorption process reviewed. Later it will be seen that generating this level of absorption using heavy hole to light hole interband absorption requires $\sim$ 10 times this power density due to other loss mechanisms. This is still much lower than any of the other induced absorption processes (which are also be subject to these loss mechanisms) and offers induced absorption over the entire 8 to $14\mu m$ band.

2.3.1 Materials for use as a modulator

Whilst the required induced absorption is known to exist in germanium, an extensive materials study was undertaken to investigate alternatives in which suitable characteristics might exist. This revealed few alternatives, and none whose combination of characteristics are comparable to those of germanium. To be a successful modulator, the material requires: i) infrared transparency of the lattice in the 8 to $14\mu m$ region, ii) a sub-band transition overlapping the 8 to $14\mu m$ region, and iii) the possibility of long bulk carrier lifetime.

Gallium antimonide exhibits strong interband absorption in both the conduction and valence bands. The room temperature intrinsic band-edge occurs at $1.8\mu m$, and the long-wavelength cutoff occurs at around $10\mu m$. In n-type material an absorption band extends from about $2\mu m$ to $5\mu m$ with a peak at $3.3\mu m$, and beyond about $5\mu m$ the absorption increases smoothly as a function of wavelength [54]. The band is due to electron interband transitions between the conduction band minimum and higher-lying minima. The smoothly-varying absorption beyond $5\mu m$ is due to free carrier absorption. In p-type GaSb the absorption increases rapidly beyond about $2\mu m$, and is due to the intervalence band transitions. However, the limited infrared lattice transparency of GaSb, combined with its direct-bandgap nature, make it an unsuitable modulator material.

Indium antimonide is infrared transparent from 7 to $17\mu m$ [55], although relatively high residual absorption in this region limits the maximum transmission. In n-type material free carrier absorption increases [56] with λ^2. P-type material does not show λ^2 free carrier absorption dependence. Its direct bandgap structure has a split valence band, within which interband transitions have been observed between light and heavy hole bands beyond about $6\mu m$ [57]. In heavily-doped InSb the Urbach absorption tail on the fundamental absorption edge is particularly pronounced. The direct bandgap of InSb makes it unsuitable for this application.

Gallium arsenide is a direct bandgap semiconductor with lattice transparency [55] from its room-temperature bandgap at $0.87\mu m$ to $16\mu m$. Its valence band is split into light and heavy hole bands, and transitions are possible between these and the spin orbit band. Intervalence band transitions have been observed [36] at $2.95\mu m$ (spin orbit to heavy hole), $4.0\mu m$ (spin orbit to light-hole), and $8.3\mu m$ (light hole to heavy hole). The hole absorption cross section at the $8.3\mu m$ band is free-carrier density dependent due to the shift of the light-hole to heavy-hole transition toward shorter wavelengths with increased free carrier density. The hole absorption cross section, arising from both free carrier and sub-band processes, is [36] $3.1 \times 10^{-16} cm^2$ at $8.3\mu m$, similar to that of germanium in this region. However, since Gallium Arsenide is a direct-gap semiconductor it is of no use in this application.

Indium arsenide is a direct gap semiconductor with a split valence band. The lattice is infrared transmitting from $3.8\mu m$ to $> 7.0\mu m$ [55]. Its valence band is split into a light hole band and two heavy hole bands [58]. In p-type InAs two absorption regions are observed [59] [58], a peak at $7.3\mu m$, and a steady rise beyond $11.8\mu m$ which is due to free carrier absorption. The peak at $7.3\mu m$ is due to light hole to heavy-hole transitions, and is not observed in n-type material. The transitions between the spin orbit and light- and heavy-hole bands are not resolved. These are masked by the intrinsic absorption edge due to the large spin-orbit splitting. Being a direct bandgap semiconductor, Indium arsenide is of no use in this application.

Aluminium antimonide is an indirect-gap semiconductor with its band edge at $0.93\mu m$ [60]. In n-type AlSb an inter-conduction band transition is observed at $300K$ at $4.3\mu m$, and beyond $10\mu m$ free carrier absorption dominates with λ^2 dependence. Several lattice absorption bands are present [60] at 11.2, 13.5, 16.5, 22.9, 27.8 and $29.8\mu m$. AlSb is relatively easy to grow [30], although it is difficult to grow high purity crystals. AlSb is susceptible to oxidation under humid conditions, eventually crumbling to a powder [61]. In p-type material an absorption band has been identified at $1.6\mu m$, and is suggested [61] as being due to transitions to an acceptor level resulting from antimony vacancies. Although this indirect semiconductor has a split valence band, suggesting inter-valence band transitions should occur, little literature exists [62] on this material due to difficulty in its growth without surface layers, and no literature has been found to confirm observation of the transitions. The observed band at $1.6\mu m$ may however be due to one of these. The unstable nature of this semiconductor makes it unsuitable for the modulator application.

Silicon has an indirect bandgap, a similar energy band structure to germanium, and a split valence band. Intrinsic silicon is infrared transparent from $1.13\mu m$ to around $10\mu m$, although multiphonon absorption increases significantly for wavelengths $> 7\mu m$, interrupting the transmission. In n-type silicon the absorption for wavelengths $> 6\mu m$, shows a smooth increase with wavelength [63], characteristic of free carrier absorption. The splitting of the light and heavy hole bands in silicon is very gradual, much less than in germanium, hence the hole inter-valence band transitions occur at much longer wavelengths than in germanium. However, none of these transitions have been observed in p-type material since at these wavelengths their absorption is masked by free hole absorption [30]. The maximum absorption of the heavy-hole to light-hole transition is predicted [25] to occur in p-silicon at $25\mu m$ at $300K$, and then diminish rapidly toward shorter wavelength. The heavy-hole to spin obit and light-hole to spin orbit transitions are predicted to occur near $33\mu m$, but are too weak to be distinguished from free hole absorption. Since these transitions occur beyond the region of required modulation, and significant lattice absorption exists in this region, silicon is an unsuitable modulator material.

Gallium phosphide is an indirect bandgap material with infrared lattice transparency from its band-edge at $0.55\mu m$ [64] to $12.5\mu m$. From $12.5\mu m$ to $24\mu m$ multiphonon combination bands give significant absorption. The hole and electron lifetimes are considerably different [65], with electron lifetimes from 1 to $20ns$ and hole lifetimes from 0.1 to $2\mu s$. This is due to the presence of deep hole traps which are filled via an Auger mechanism. N-type GaP shows a broad absorption band in the 1 to $4\mu m$ region [34], beyond which the absorption increases with wavelength and free carrier concentration. The 1 to $4\mu m$ absorption does not occur in p-type material and is due to electron inter-conduction band transitions between two sets of conduction band minima with $0.3eV$ separation. This is superimposed on the absorption due to free carriers, which has a $\lambda^{1.8}$ wavelength dependence [65]. In p-type material the absorption is primarily due to free carriers, and has a $\lambda^{1.7}$ dependence. The contribution from intervalence band absorption is minimal. The ratio of hole to electron absorption cross section in GaP is usually less than unity, although beyond $5\mu m$ the ratio of the two increases to 0.9.

In unexcited high purity compensated bulk GaP the absorption coefficient is $< 1cm^{-1}$ in the region from the band edge to $\lambda < 10\mu m$. When optically excited, electron-hole pairs are generated and the induced absorption coefficient increases, starting at about $2\mu m$, and is primarily due to free hole absorption [66]. The absorption spectra does not show [66] the contribution from electrons as the electron lifetime is so much shorter than the hole lifetime. The hole absorption cross section at $10\mu m$ in GaP [65] is $3 \times 10^{-16} cm^2$, approximately half that of germanium. Additionally the large bandgap of GaP requires costly green excitation illumination, and the lifetime is much shorter than in germanium.

Germanium is an indirect-bandgap semiconductor with intrinsic transmission from its room-temperature band edge at $1.8\mu m$ to $18\mu m$. Multiphonon absorption bands starting at around $18\mu m$ limit the long wavelength absorption in intrinsic material. The valence band in germanium is split [25] into the light-hole and heavy-hole bands due to spin orbit interaction. The conduction band does not have overlapping band minima, so electron inter-conduction band transitions are not possible. In n-type germanium [67] the absorption increases smoothly with wavelength as λ^2, characteristic of free carrier absorption. In p-type germanium, inter-valence band absorption structure is observed [24] [68] for energies less than the bandgap, with two weak bands at $2.9\mu m$ and $4.55\mu m$, and a third, stronger band starting at around $5.6\mu m$. Whilst in many of the semiconductors examined so far the spin orbit splitting is too great for the transitions to the spin orbit to be observed, in germanium the spin orbit splitting at $k = 0$ is only $0.28eV$. Since this is below the $0.67eV$ bandgap, transitions to this band are not masked by the fundamental absorption. The broad light hole to heavy hole transition, centred roughly at $10\mu m$ is in the correct wavelength region for use in the modulator.

2.3.2 Selection of modulator material

The indirect-bandgap requirement leaves only aluminium antimonide, silicon, gallium phosphide and germanium as candidates for the modulator material. Inter-valence band transitions in Aluminium antimonide in the required region have not been observed, if they exist. Silicon is of no use as the inter-valence band transitions are incorrectly placed and masked by free hole absorption. This leaves only gallium phosphide and germanium as modulator candidates.

In principle, absorption in the 8 to $12\mu m$ band could be used in an optically-excited GaP modulator. This is a spectrally narrower modulated band than that preferred by the application, and would result in loss of information from the modulated image scene at the long-wavelength (lower-temperature) region. The room-temperature induced absorption would be almost entirely due to holes with the biggest contribution from the intervalence absorption processes. The hole lifetime, controlled mainly by trapping, is much shorter than that in germanium, and would have to be increased considerably in order to provide an efficient device. The costly excitation, limited availability in large-volume samples required by an area-modulator, and inefficiency of optically-exciting such a wide bandgap material make GaP an inferior alternative to germanium. Germanium, with its narrower bandgap offers the possibility of longer wavelength excitation where cheaper near-infrared diode lasers exist. Additionally, the hole induced-absorption coefficient at $10\mu m$ in germanium is roughly twice that of holes in GaP, giving a more-efficient device.

Germanium is the ideal modulator material. The combination of heavy-hole to light-hole transitions in the required spectral region, the possibility of long carrier lifetime in this indirect semiconductor, the availability of moderately-priced diode lasers at wavelengths suitable for above-bandgap excitation, and the infrared transparency of the lattice from 1.8 to 18μm in a readily-available material that is routinely optically fabricated is extremely fortuitous. No other material aside from germanium appears to possess the required properties for the modulator.

Chapter 3

Electrical and optical properties of germanium

3.1 Introduction

This Chapter reviews the properties of germanium to enable adequate specification of the material and processing conditions, and to define the physical properties which are appropriate to the operating regime of the modulator.

Germanium materials processing technology has advanced considerably since initial transistor work in the 1960's, primarily through its application in nuclear radiation detectors, and is now one of the most electrically-pure semiconductors. A mid-gap electrically-active impurity density of $10^{10} cm^{-3}$ is relatively common. Its ease of single-crystal growth, through the Bridgman or Czochralski technique permits reduction of the impurity concentration through differences in impurity segregation coefficient. Much of the high purity single-crystal germanium [69] [70] used in nuclear detectors is grown by the Czochralski technique. Subsequent zone-refining and discarding of the lower part of the crystal, reduces the concentration of the main electrically active impurity elements Ga, Al, As and P by a factor of 10 or more [70]. Two zone-refining stages are generally used, after which little further reduction in impurity concentration is achieved.

Semiconductor grade single-crystal germanium is specified by its conductivity type, electrically active impurity density and resistivity range, whereas optical grade germanium may include specification of its refractive index, refractive index temperature coefficient, transmittance, optical absorption and fracture stress [71]. The modulator's electrical and optical system design requires a combination of these parameters to describe its operation. This requires specification of the conductivity type, electrically active impurity density, resistivity, transmittance and optical absorption. Optimising the induced absorption requires maximisation of the bulk carrier lifetime; therefore only single crystal germanium will be used in the modulator. The germanium used in this work fell into three categories: optical grade, semiconductor grade, and nuclear detector grade, in order of increasing purity and hence bulk carrier lifetime. The primary material grade which is used in this work is nuclear detector grade, high purity germanium (HPGe), which deserves a brief overview.

HPGe is grown [69] by the Czochralski technique in a SiO_2 crucible in a H_2 ambient. SiO_2 has an advantage over graphite, acting as an effective aluminium getter. A maximum boule diameter of $90mm$ is currently produced using this technique. HPGe requires an electrically active impurity density $|N_a - N_d|$ in the order of $10^{10}cm^{-3}$, which is achieved through subsequent zone refining and rejection of the lower part of the crystal. Germanium is well-suited to this process as most of its electrically active impurities have distribution coefficients much lower than unity. The growth process requires a broadly-controlled dislocation density in the range $10^2 - 10^4cm^{-2}$. Too low a dislocation density means that excess vacancies cannot be annihilated during normal cooling after solidification and they then form hole trapping centres. Too high a dislocation density permits significant charge trapping by the dislocations themselves. Following crystal growth the axial conductivity is measured before the crystal is diced and the resistivity and Hall coefficient are measured. One important, yet (usually) electrically inactive impurity is hydrogen, incorporated at approximately $10^{15}cm^{-3}$ from the growth atmosphere. This passivates some defects, and is stable at room temperature. If the crystal is heated to $> 300°C$ and rapidly cooled, the hydrogen may dissociate, forming metastable electrically-active complexes.

The suppliers of samples used in this work and purity level (if this information was available from the supplier) are summarised in Table 3.1.

3.2 Electrical properties of germanium

This section investigates the carrier lifetime and the diffusion of carriers, both of which affect the level of induced absorption in the modulator and the rate at which this can be switched. The dependence of these parameters on material properties is investigated to enable their use in the modelling and hence optimisation of the induced absorption in Chapter 4.

Following the generation of (Δn_0) excess electron-hole pairs in a semiconductor, the

sample reference	supplier	electrically active impurity density
EGG1...	E. G & G Instruments, UK	$< 3 \cdot 10^{10} cm^{-3}$
EGG2... (incl. cube 1,2)	E. G & G Instruments, UK	$< 10^{10} cm^{-3}$
Haller	Prof. E. E. Haller, University of California, USA	n-type wafer ref. S-60-15.5
148a,b/ 149a,b	Oxford Instruments, UK	nuclear detector grade
EX... / ABC...	Exotic Materials Inc.	no information available
K6...	Eagle Picher Technologies	optical grade

Table 3.1: Table of samples used in this work and their suppliers

rate at which these carriers decay toward equilibrium is defined by the reciprocal of the effective carrier lifetime $\tau_{effective}$, giving the excess carrier density (Δn) as a function of time as:

$$\Delta n(t) = \Delta n_0 e^{-\frac{t}{\tau_{effective}}} \tag{3.1}$$

The effective carrier lifetime comprises recombination due to all processes, and under certain conditions can be treated as time-invariant. Generally, this requires the initial excitation to be small compared to equilibrium carrier densities, that the surface carrier recombination rate is negligible, and that carrier trapping is insignificant. The single time constant under these conditions is important in modelling electrical device operation. The effective carrier lifetime is however affected by carrier recombination at both the surface of the germanium and in the bulk, and is generally defined as:

$$\frac{1}{\tau_{effective}} = \frac{1}{\tau_{bulk}} + \frac{1}{\tau_{surface}} \tag{3.2}$$

τ_{bulk} and $\tau_{surface}$ represent the carrier lifetime in the bulk and the effect of the surface on lifetime respectively. The surface recombination velocity (which exists on real surfaces) determines the effect of the surface on carrier lifetime, and is frequently much shorter than that in the bulk. Although the bulk carrier lifetime remains constant for small excess carrier densities, recombination of carriers at the surface complicates Equation 3.2 since its contribution to the effective lifetime depends on the carrier distribution in its vicinity. It is therefore incorrect to define a constant effective lifetime when significant surface recombination exists since the spatial evolution of the carrier profile changes $\tau_{effective}$ with time. The temporal dependence of the effective lifetime is particularly pronounced in the case of optical excitation, which produces an exponential carrier distribution decaying with distance from the surface. In this case the carrier density at a point in the germanium may be represented as a function of time during carrier decay by a series of exponential functions in the form of Equation 3.1. During the decay the faster, higher order terms rapidly die away, and then a fundamental decay constant remains. The faster decaying terms are due to the high carrier concentration close to the surface. The fundamental decay constant governs decay when the distribution of the carriers reaches a steady shape, carriers close to the surface having recombined. The importance of the fundamental decay constant will be shown in Chapter 4, affecting the switching rate of the absorption, and at this stage the individual components contributing to the separate bulk and surface lifetimes are detailed.

3.2.1 Bulk carrier recombination in germanium

During continuous carrier generation in the modulator by an external stimulus, a short time after the initial stimulus, carriers will be in a non-equilibrium steady state. After the stimulus is removed, carriers return to equilibrium conditions. If carrier decay is exponential, a decay constant can be calculated, the reciprocal of which is the mean time for which an electron-hole pair exists. Within the semiconductor bulk this time is defined as the bulk carrier lifetime, and is distinguished from that occurring at the surface (Section 3.2.2). In the modulator this affects the hole population and hence 'off' state absorption, and the rate at which the absorption returns to equilibrium after the stimulus is removed. The processes which affect carrier lifetime by providing a path for recombining electrons as they lose energy and recombine with holes are described by this section. These enable accurate modelling of carrier decay through the bulk lifetime by determining conditions for its validity. If excited with sufficient energy ($> 0.8eV$), an electron will be in the direct valley, and will rapidly scatter into the indirect valley, from which most recombination paths commence. The processes considered will be band-to-band recombination, recombination via impurity levels within the bandgap (Shockley-Read-Hall recombination), trapping, and Auger recombination.

The simplest electron-hole recombination process is through a band-to-band transition which is direct or indirect. Despite the picosecond scattering time for an electron from the direct to indirect conduction band and subsequently low electron population, an electron in the direct conduction band valley may undergo a direct transition. However, if direct, since the absorption coefficient at $0.8eV$ is approximately $10^3 cm^{-1}$, unless the transition takes place very close to the surface the photon will be reabsorbed by the germanium where it is more likely that the subsequently generated electron will scatter to the indirect valley as described above. The recombination of an electron in the indirect valley may be radiative, emitting a photon of energy close to $0.67eV$ accompanied by phonon emission, or solely through multiple phonon emission. The highest-energy phonons in germanium have approximately an order of magnitude lower energy than that required by a recombination [30]. Recombination solely through phonon emission is therefore improbable, requiring > 10 phonons. The emission of a photon of close to $0.67eV$ and the required phonons is more probable. Measurements of the recombination radiation emitted from thin ($120\mu m$) samples [72] show a higher emission intensity at $0.67eV$ than that $0.8eV$. This is due to the lower absorption coefficient ($\sim 10cm^{-1}$) at the longer emission wavelength, so more of this radiation escapes from the sample, and also due to the lower electron population in the direct conduction band. Pyroelectric detectors are sensitive to this emission, which must be filtered unless a low carrier density exists at the modulator surface facing the detector.

The recombination rates for direct and indirect band-to-band recombination in germanium have been determined [73] as $\sim 10^{-8}cm^3s^{-1}$, and $\sim 10^{-15}cm^3s^{-1}$, accounting for reabsorption. However, direct recombination does not affect the lifetime observed in germanium due to the low electron density in the (higher) direct minimum valley. The long indirect lifetime ($20.8s$ in intrinsic germanium) does not affect the bulk lifetime, which is determined by faster recombination processes. The main contributor to this is via recombination centres within the bandgap.

Recombination through a single type of centre in the bandgap is described by the Shockley-Read-Hall model [74]. This assumes a single energy level (or centre) exists within the bandgap at an energy E_t, which may take either of two charge states. This is illustrated by Figure 3.1

Figure 3.1 illustrates four processes a) the capture of an electron from the conduction band b) the emission of an electron to the conduction band c) the capture of a hole by the valence band and d) the emission of a hole to the valence band. For recombination to take place an electron must undergo the transition to the initially uncharged centre (a), next the negatively charged centre must trap a hole (c) which results in mutual annihilation of the electron and hole. After the electron has been captured, it is possible that before a hole is able to make the transition to the negatively charged centre, the electron will be emitted back to the conduction band (process b). This particular case is known as trapping, and is considered later in this section. At this point only recombination processes are considered.

The probability of recombination at a centre depends on the total density of recom-

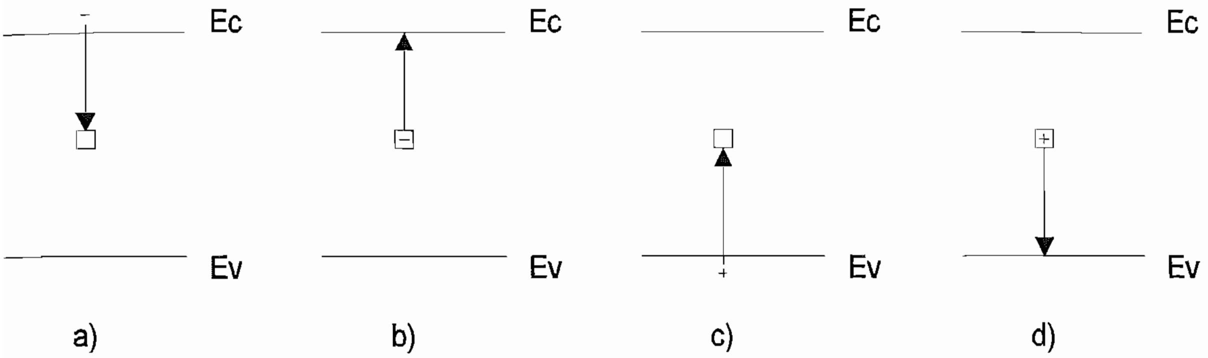

Figure 3.1: Processes involved in carrier recombination through a single centre

bination centres in the semiconductor, the density of recombination centres that are usually filled under equilibrium conditions, the capture probability of the recombination centres, and the free carrier density. The effect of these conditions on the carrier lifetime is now examined.

The Shockley-Read-Hall (SRH) recombination model [74] gives the carrier lifetime (τ) in a semiconductor in the presence of recombination centres at a single energy level. When an equal number of excess electrons (Δn) and holes (Δp) are introduced to the semiconductor this gives:

$$\tau = \frac{\tau_{p0} \cdot (n_0 + n_1 + \Delta n) + \tau_{n0} \cdot (p_0 + p_1 + \Delta n)}{n_0 + p_0 + \Delta n} \tag{3.3}$$

n_1 and p_1 are the equilibrium electron and hole densities corresponding to a Fermi level at E_t, and are given by:

$$n_1 = N_c \cdot exp\left(\frac{E_t - E_c}{kT}\right) \tag{3.4}$$

$$p_1 = N_v \cdot exp\left(\frac{E_v - E_t}{kT}\right) \tag{3.5}$$

E_t is the energy level of the recombination centres. Under conditions of low level excitation ($\Delta n << n_0 + p_0$) and the 'low-level' lifetime becomes τ_0:

$$\tau_0 = \frac{\tau_{p0} \cdot (n_0 + n_1) + \tau_{n0} \cdot (p_0 + p_1)}{n_0 + p_0} \tag{3.6}$$

τ_0 is therefore independent of the excess carrier density ($\Delta n = \Delta p$) and excess carriers recombine at a rate proportional to Δn, with a time constant τ_0.

The density of recombination centres is N_t, which is related to the limiting values of the carrier lifetime in heavily doped material τ_{n0} and τ_{p0}. τ_{n0} is the mean time for an empty recombination centre to capture an electron, and τ_{p0} is the average time for a negatively charged centre to capture a hole.

$$\tau_{n0} = \frac{1}{N_t \cdot \langle v \cdot A_n \rangle} \tag{3.7}$$

$$\tau_{p0} = \frac{1}{N_t \cdot \langle v \cdot A_p \rangle} \tag{3.8}$$

$\langle v \cdot A \rangle$ is the average of the product of electron thermal velocity and capture cross section of an electron by an empty recombination centre (A_n), or capture cross section for a hole by a filled centre (A_p). Typically A is in the range 10^{-22} to $10^{-13} cm^2$, with most reported values in the order of $10^{-15} cm^2$. This is expected as it is the order of the physical dimension of an atom or ion [75]. $\langle v \cdot A \rangle$ is the average probability per unit time that a carrier makes the transition to the level. An increased capture cross section or density of recombination centres therefore reduces the total lifetime. Changing the equilibrium electron or hole densities, n_0 or p_0, through doping moves the position of the Fermi level within the bandgap, changing the occupancy of the recombination centres. If these centres are assumed to exist between the intrinsic fermi level and conduction band ($E_c > E_t > E_i$), then in n-doped material $n_0 >> (p_0 + p_1)$ in Equation 3.6 and the lifetime becomes:

$$\tau_0 = \tau_{p0} \cdot \left(1 + \frac{n_1}{n_0}\right) \tag{3.9}$$

In heavily n-doped material the lifetime becomes $\tau = \tau_{p0}$. In this case the Fermi level is close to the conduction band; the recombination centres are nearly full of electrons and recombination is limited by the rate of capture of a hole by the negatively charged centre, τ_{p0}. Conversely in heavily p-doped material the lifetime becomes τ_{n0}. Now the Fermi level is close to the valence band so the capture of a hole by a negatively charged centre is highly probable, and recombination is limited by the requirement for the uncharged centre to initially capture an electron. When the Fermi level is near the centre of the bandgap, in near-intrinsic germanium the lifetime is a maximum. The exact position of the Fermi level required for maximum lifetime depends on the relative values of (τ_{n0}) and (τ_{p0}).

The effect of the position of the recombination centre energy level (E_t) within the bandgap is now considered. The transition probability of a carrier transition to a recombination centre is dependent on the difference in energy required to make the transition. A higher transition probability is therefore found when recombination centres are close to either the conduction or valence bands. However, this transition only involves one type of carrier. In this situation, these shallow-lying energy levels within the bandgap act as donors or acceptors, contributing to the conduction process. The recombination rate through shallow levels is inefficient, requiring a less-probable larger-energy transition by the opposite type of carrier to enable recombination at the centre. When recombination centre energy levels are near the middle of the bandgap, both electrons and holes have higher transition probabilities to the recombination centre, and so a higher recombination rate results. The exact energy level of the recombination centre for maximum recombination rate is dependent on the relative values of τ_{p0} and τ_{n0}, and n_0 and p_0. Assuming intrinsic germanium, and assuming $\tau_{p0} = \tau_{n0}$, then differentiation of Equation 3.3 gives a minimum lifetime at $E_t =\sim (E_c + E_v)/2$. In practice this is still valid for a wide range of τ_{p0} and τ_{n0}.

Therefore to maximise the bulk carrier lifetime in germanium and hence the excited state carrier density the energy levels of recombination centres must be remote from the middle of the bandgap, and also near-intrinsic germanium should be used. These recombination centres exist in germanium due to the presence of impurity atoms or due to imperfections in the crystal introduced during growth or subsequent processing. Recombination centres introduced by impurities and those introduced through crystal imperfections have the same effect on carrier lifetime. Rapid heat treatment is one method by which lifetime-reducing defects are introduced to germanium. Generally, germanium can be heated to about $900°C$ and retain its room temperature lifetime of several hundred microseconds if it is cooled slowly ($100°C$ per minute) and contamination is avoided [75]. The risk of contamination during any heating process is particularly severe for impurities which introduce recombination centres near the middle of the bandgap.

Dislocations, introduced during growth or subsequent heat treatment also reduce carrier lifetime. This occurs when a carrier is trapped by a dislocation, and the charged centre is subsequently annihilated by the capture of an opposite carrier. In n-type germanium [30] the dislocation density affects room-temperature lifetime τ in n-type material as:

$$\tau = 2.5 \cdot N_d^{-1} \tag{3.10}$$

where N_d is the dislocation density (cm^{-2}). For millisecond bulk carrier lifetime material to not be affected by the dislocation density, $N_d < 10^3 cm^{-2}$ is required. This is within the HPGe specification, justifying the statement that at above $10^4 cm^{-2}$ charge trapping becomes important in long bulk carrier lifetime material. Under the above assumptions, bulk carrier recombination in the millisecond bulk carrier lifetime HPGe used in this work is dominated by that due to impurities. Whereas the impurities which are used to dope germanium have low ionisation energies [76] and come from group III or V of the periodic table, the impurities which are likely to have mid-gap recombination centres in germanium have large ionisation energies, and are mainly the transition metals in the periodic table. Some impurities such as copper and gold introduce multiple levels within the bandgap, and these act as stepping-stones for electrons on their path from the conduction to valence band, enhancing the recombination rate due to a higher transition probability existing for each of the smaller energy steps. Impurities with a high diffusion coefficient that come into contact with the germanium after crystal growth are also damaging, although a high diffusion coefficient is not a prerequisite for danger to the bulk carrier lifetime if incorporated during the growth phase. These impurities are now detailed to highlight their incompatibility with processes involved in the modulator's construction. The impurity diffusion coefficient D_i at temperature T is given by:

$$D_i = D_0 exp\left(-\frac{\Delta H}{R \cdot T}\right) \tag{3.11}$$

where D_0, ΔH (the activation energy in $Jmol^{-1}$) and the diffusion coefficient at $850°C$ are given in Table 3.2. R is the gas constant ($8.314 Jmol^{-1}K^{-1}$).

Having considered low level excitation of germanium, the other extreme is now considered. Under conditions of high level excitation, $\Delta n >> p_0 + n_0 + p_1 + n_1$, the limiting case of the carrier lifetime from Equation 3.3 becomes:

$$\tau_{high} = \tau_{p0} + \tau_{n0} \tag{3.12}$$

Here the 'high level' lifetime (as with the low level lifetime) is independent of the excess carrier density ($\Delta n = \Delta p$). The excess carrier recombination rate is proportional to Δn, having a time constant $1/\tau_{high}$. Therefore in both high level and low level excitation cases, SRH recombination through a recombination centre at a single energy level leads to a recombination rate which is proportional to the excess carrier density, and carriers decay with a single time constant.

For medium excitation levels the carrier lifetime is dependent on the excess carrier density. This statement is now justified and its effect on intrinsic germanium is deter-

impurity	**distribution coefficient**	$E_t - E_i$ eV	A_e A^2	A_h A^2	D_0 cm^2s^{-1}	ΔH kJ	$D_i(850°C)$ cm^2s^{-1}	**Ref**
Copper	2×10^{-5}	3^- at 0.135	0.1	1.0	4.2×10^{-4}	21	4.5×10^{-5}	[77]
		2^- at -0.065						[78]
		1^- at -0.355						[30]
Gold	3×10^{-5}	3^- at 0.355			12.6	218	9.9×10^{-10}	[79]
		2^- at 0.195						[77]
		1^- at -0.235						[30]
		1^+ at -0.345						
Nickel	5×10^{-6}	2^- at 0.095	0.8	> 40	0.8	88	6.6×10^{-5}	[78]
		1^- at -0.175						[79]
								[77]
								[30]
Iron	3×10^{-5}	?2^- at 0.025			0.13	105	1.8×10^{-6}	[35]
		?1^- at 0.045						[30]

Table 3.2: Table of impurities likely to degrade the lifetime in germanium

mined semi-quantitatively. Measurements of the capture cross section of an electron by an empty recombination centre A_n, and capture cross section for a hole by a filled centre A_p show [75] that for germanium $A_p >> A_n$ is always reported. Following this, Equation 3.8 and Equation 3.7 gives $\tau_{n0} >> \tau_{p0}$, so it takes longer for an uncharged centre to capture an electron than it does a negatively charged centre to capture a hole. Under these conditions the low level lifetime (for intrinsic germanium with $n_0 = p_0 = n_i$) becomes:

$$\tau_{0(Intrinsic\,Ge)} \cong \tau_{no} \cdot \left(\frac{n_i + p_1}{2n_i}\right) \tag{3.13}$$

If the recombination centres are assumed to exist only within ($E_c > E_t > E_i$) then $p_1 << n_i$ and Equation 3.13 for the low level lifetime becomes:

$$\tau_{0(Intrinsic\,Ge)} \cong \frac{\tau_{no}}{2} \tag{3.14}$$

The high level lifetime becomes (since $\Delta n >> p_0 + n_0$):

$$\tau_{high(Intrinsic\,Ge)} = \tau_{no} \cdot \left(\frac{p_0 + p_1 + \Delta n}{n_0 + p_0 + \Delta n}\right) \cong \tau_{no} \tag{3.15}$$

This doubling of the carrier lifetime with the change from low level to high level excitation also shows that between low and high level excitation an intermediate lifetime, dependent on Δn is obtained. The intermediate situation is understood [75], but no literature could be found to support the prediction for lifetime-dependence on the carrier density in intrinsic germanium as this requires knowledge of the nature of the recombination centres. It is predicted [75] that in heavily n-doped germanium with nickel recombination centres that the lifetime should increase by a factor of 10 from low level to high level excitation, agreeing with more recent literature [80]. In heavily-doped p-type germanium no variation in lifetime has been reported with excess carrier concentration [75]. In near-intrinsic p-type germanium a decrease in lifetime by a factor of 3 with increasing excess carrier density has been observed, although again, precise interpretation of these results is not possible due to the energy level and capture cross sections of the recombination centres being unknown. Since these factors are required to give a meaningful dependence of lifetime on excess carrier density, at this stage the low level excitation lifetime will be assumed and this is independent of the carrier concentration. Later chapters will show that the excitation used in experiments spans both low and high levels, complicating the analysis of effects involving the lifetime. The effect of this on the decay of a large carrier density is to give an initial exponential decay rate with one time constant, then a non-exponential decay constant when the carrier density is medium-level, and then a faster exponential carrier decay rate when the carrier density is low-level. The above calculation for intrinsic germanium predicts that providing the recombination centres are located in the upper half of the bandgap, that the difference in lifetime at high and low level excitation is a factor of 2. For the laser-excitation used in practical areas of this work, the exponential dependence of carrier density on displacement from the surface causes carriers close to the surface decay rapidly due to a high surface recombination (Section 3.2.2). The remaining carrier profile has a density closer to the low-level excitation case. This suggests that the error introduced by the assumption of a constant bulk lifetime for all carrier concentrations should not be too great.

A special case of the SRH recombination process is trapping. This occurs at both the surface and in the bulk of the germanium but is independent of the surface recombination velocity (Section 3.2.2). Trapping is illustrated in Figure 3.1 when the uncharged recombination centre captures a carrier, and before the oppositely-charged carrier has a chance to be captured by the (now charged) centre, the initial carrier is emitted back to its previous (conduction or valence) band. Now the centre is known as a 'trap'. Whilst the carrier is in the trap it is immobilised and no longer a free carrier. The trapping process therefore leads to unequal excess (over the equilibrium values) numbers of free electrons and holes. This is caused by significantly different carrier capture times (τ_{p0}

and τ_{n0} in above Equations), and is also affected by the position of the centres within the bandgap. In practice the trapping process occurs whilst other carriers in the material are recombining. However it is only discernible if the number of trapped carriers is significant in comparison to the number of free carriers of that type. Unlike the recombination process, trapping gives a non-exponential decay rate, causing a long tail in the carrier decay. Photoconductive current decay in a material possessing traps shows a fast initial drop due to recombination processes, followed by a slowly-decaying tail as the traps slowly release their trapped carriers.

The probability of trapping is determined by the ratio of the probability per unit time of capture of a charge carrier, to the probability per unit time of it being returned to its previous band or recombining at the centre. This is determined by the density of the recombination centres (N_t) and also the ratio of the capture cross section of an electron by an uncharged centre (A_n) to the capture cross section of a hole by a negatively charges centre (A_p). HPGe has a very low density of recombination centres, and the (A_n/A_p) ratio is responsible for the observed trapping [81] [75]. To observe trapping [81] the germanium had to be cooled to $200K$ to see the characteristic non-exponential carrier decay. It is suggested [81] that the absence of trapping in germanium at room temperature is due to the exponentially increasing probability of the initial carrier that made the transition to the trap level being returned to its previous band with increasing temperature. Recombination centres such as nickel and copper act as traps in germanium, although at room temperature in HPGe their effect is rarely observed. It is suggested that many types of recombination centres at room temperature act as traps at low temperature [30]. This work involves HPGe at close to room temperature so the effect of traps is insignificant and is not considered by the bulk lifetime model.

In addition to band-to-band transitions through photon and or phonon emission, the Auger process permits non-radiative band to band recombination. Here the energy and momentum of an excited carrier (A) is transferred to another excited carrier (B) (not necessarily the same carrier type). Carrier A recombines non-radiatively through a band to band transition and carrier B is excited with the momentum and energy of carrier A. Carrier A then loses energy and momentum through phonon emission. Crucially, the band-to-band Auger process depends on the existence of three carriers (two to recombine and one to transport-away the energy and possibly momentum), so the resulting recombination rate depends on the cube of the free carrier density. The decay constant (reciprocal lifetime) therefore depends on the square of the carrier density, assuming equal electron and hole concentrations at these high carrier densities.

The Auger process is most significant at high free carrier densities and is considered since it leads to a carrier-density-dependent bulk lifetime. The carrier density at which this becomes significant must be investigated to see if it is important within the modulator's operating regime, and whether modelling must account for a density-dependent bulk carrier lifetime. If significant, this would provide a severe carrier-loss mechanism, and may reveal an upper carrier density above which modulator operation is impractical.

In addition to being a band-to-band process, Auger recombination can also involve centres within the bandgap. Figure 3.2 illustrates the possible Auger processes.

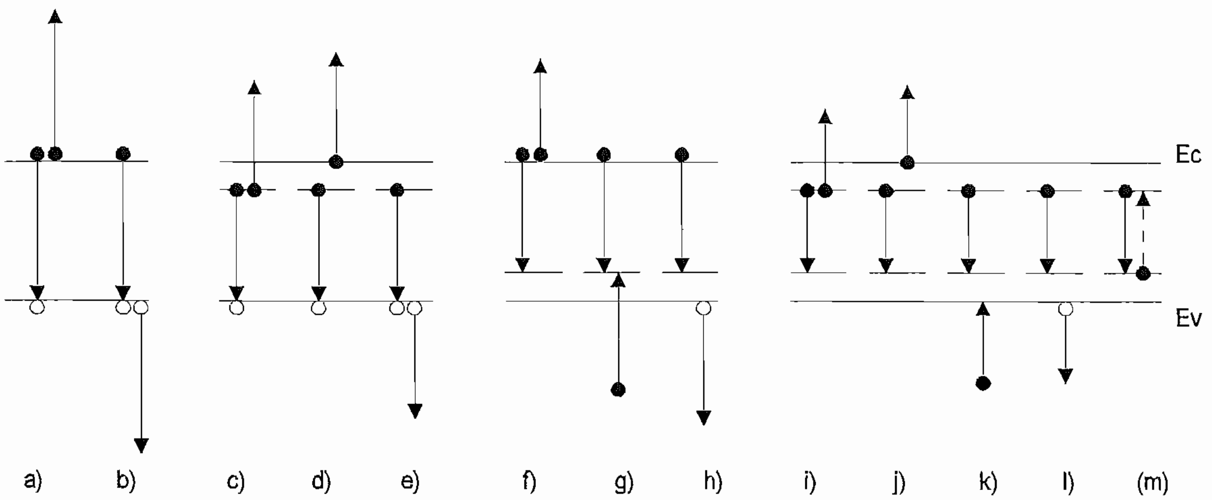

Figure 3.2: Possible Auger-assisted recombination processes in a semiconductor

The probability of the recombining carrier A giving its energy to another carrier B is dependent on the density of carrier B. For this reason, recombining electrons tend to dissipate energy to the majority carrier rather than the minority one. In Figure 3.2 a) and b) represent band to band transitions in n type and p type material respectively. In a) the conduction band electron gives its energy to another electron as it recombines, in p-type material in b) the excited (upper) electron gives its energy to a hole which is then excited deep into the valence band. Recombination transitions from donor levels to the valence band are also possible (c-e) and the energy is transferred to an electron in the conduction band (d) or to a hole in the valence band (e) if the hole density is high. Transitions from the conduction band to the acceptor level are also possible (f-h), and transitions from donor to acceptor levels can take place (i-k). Process (m) is 'resonant absorption' and is not an Auger process as the second electron may dissipate its energy radiatively.

Auger recombination is mainly of importance in very narrow bandgap semiconductors [35] such as InSb, in which the electron and hole effective masses are considerably different. High Auger recombination rates are seen in these materials since an electron at the bottom of the conduction band (with zero momentum) can give its energy to another electron with little increase in its own momentum (steeply curved conduction band). The less-steeply curved valence band offers a large number of holes with the required energy but over a wide range of momentum, with which the electron can recombine. This, combined with the low energy gap increases the transition probability. In these narrow gap materials the carrier concentration and hence Auger recombination rate is strongly temperature-dependent. In wider bandgap materials it is only of concern in heavily-doped or strongly excited semiconductors. The coefficient for Auger recombination, γ_3 is given in the following Auger recombination rate equation:

$$\frac{dn}{dt} = -\gamma_3 n^3 \tag{3.16}$$

Auger recombination processes are represented by γ_3. Some discrepancy exists in the literature [82] [83] [84] [85], spanning more than thirty years, as to the value of γ_3 in germanium and its possible dependence on impurity density. Its measurement is complicated by the presence of SRH recombination, a finite surface recombination velocity which must be accounted for, and also the exact nature of the energy level of the centres made analysis difficult. Additionally it varies depending on the position of the quasi Fermi level within the conduction or valence bands in strongly excited germanium [84].

In near-intrinsic germanium the room temperature coefficient for Auger band-to-band recombination has been determined experimentally from the decay of an initially degenerate excited carrier density [84] as $\gamma_3 = 1.1 \times 10^{-31} cm^6 s^{-1}$. The initial decay constant following optical excitation is given by $1/\tau = \gamma_3 \cdot n_0^2$ where n_0 is the initial carrier density. At a carrier density of $9.5 \times 10^{16} cm^{-3}$ this gives a decay lifetime $\tau = 1ms$, so unless this carrier density is attained, decay processes with lifetimes shorter than $1ms$ will dominate the recombination process. In the results cited, the coefficient was determined at a density of $10^{20} cm^{-3}$ and is expected to rise with reducing carrier density (the Fermi levels still being within the conduction and valence bands). When the Fermi levels are within the conduction and valence bands the number of final states that excited carriers may occupy is reduced. This reduces the probability of an Auger process. Theoretical predictions [82] give $\gamma_3 = 7 \times 10^{-33} cm^6 s^{-1}$ in germanium although this discrepancy may be due [84] to the difference in position of the Fermi levels within the conduction and valence bands.

The onset of degeneracy represents the transition between (independent-particle) Maxwell-Boltzmann statistics (at low carrier concentration) and Fermi-Dirac statistics, although the transition is in fact continuous. The condition for degeneracy of a band is that the Fermi level should be no lower than kT below the band edge [30]. The carrier density (n) at which this occurs is given by:

$$kT_{deg} = \frac{h^2}{8m^{(N)}} n_{deg}^{2/3} \tag{3.17}$$

In germanium the conduction and valence bands becomes degenerate at $300K$ at electron and hole densities of $0.75 \times 10^{18} cm^{-3}$ and $2.7 \times 10^{18} cm^{-3}$ respectively. At much greater carrier densities than this the Auger coefficient is germanium is therefore expected to drop due to reduced electron state availability in the conduction band.

Earlier experimental results [85] gave an estimated coefficient of $\gamma_3 = 10^{-31} cm^6 s^{-1}$ in p-type germanium for carrier densities up to $10^{19} cm^{-3}$. More recent results [83] suggest that both band-to-band Auger recombination processes and Auger recombination through centres within the bandgap (Figure 3.2) take place in heavily doped germanium, leading to a decay involving two contributions to γ_3. In relatively pure germanium (recombination centre density $< 10^{11} cm^{-3}$) band to band Auger recombination processes dominate the Auger recombination and a coefficient $\gamma_3 = 10^{-32} cm^6 s^{-1}$ exists. At higher impurity densities, contributions to γ_3 from the Auger recombination through the centres becomes significant. Additionally the diffusion of carriers to the recombination centres may be limited by the impurity density, and this may even increase the bulk carrier lifetime [83]. Under the condition of high impurity density ($> 10^{11} cm^{-3}$) the decay constant therefore no longer depends on the square of the free carrier density. This explains some of the earlier discrepancies in the reported results, which are likely to have used germanium with a significant impurity density. Assuming the use of HPGe and an Auger coefficient of $\gamma_3 = 10^{-32} cm^6 s^{-1}$ suggests Auger recombination only becomes significant in comparison to recombination processes with a lifetime of $1ms$, at a carrier density of $> 3.2 \times 10^{17} cm^{-3}$. Therefore in material with a $1ms$ SRH-limited lifetime, Auger recombination does not need to be accounted for unless this carrier density is exceeded, and the carrier-density dependent recombination rate associated with the Auger process does not provide a barrier to achieving high 'off' state absorption in the modulator.

The recombination processes reviewed lead to a generalised rate equation for the decay of carriers in the bulk, given by Equation 3.18.

$$\frac{dn}{dt} = -\gamma_1 n - \gamma_2 n^2 - \gamma_3 n^3 \tag{3.18}$$

The effects of non-radiative Shockley Read Hall recombination through recombination centres are given by γ_1 for both low and high level excitation, although γ_1 changes slightly for these two conditions as described earlier. γ_2 is the recombination rate for two-body collision processes, representing the effect of radiative recombination, requiring both an electron and a hole for the recombination process. γ_3 represents the effect of Auger band-to-band recombination and Auger recombination involving a recombination centre, both processes involving three bodies. Equation 3.18 gives a decay constant which is the sum of the contributions from these processes, given by:

$$\frac{1}{\tau_{bulk}} = \gamma_1 + n\gamma_2 + n^2\gamma_3 \tag{3.19}$$

The contributions from each of these processes depend on the carrier density and transition probability as discussed earlier. Generally in HPGe the contribution from radiative processes is negligible, and providing the carrier density does not exceed $10^{17} cm^{-3}$, the contribution from Auger processes is also negligible, and only the former SRH process need be considered.

The effect of temperature on the bulk carrier lifetime is now considered theoretically, since this will be an important factor in determining the operating temperature range of the modulator. Following the above argument, the SRH process is assumed to dominate recombination. The predicted variation in bulk lifetime in the military $220 - 320°C$ temperature range has been found to be small for both high and low level excitation. The equations governing the temperature dependence of the lifetime are 3.3 to 3.12. The lifetime is found to be dependent on the doping type, the energy level of the recombination centre in relation to the intrinsic Fermi level, and the density of the recombination centres. To provide meaningful results the dependence of the lifetime is summarised for a low density of recombination centres ($N_t = 10^{11} cm^{-2}$) in Table 3.3, for intrinsic germanium under low and high level excitation conditions.

Additional assumptions in the analysis are that $\tau_{no} >> \tau_{po}$, which is reported in the literature and described earlier, and that the capture cross section is temperature-independent. This is also reported over the temperature range $77K$ to $350K$ [81] [75]. The bulk carrier lifetime in the above table always decreases with increasing temperature. This might be intuitive from an argument of a reduced collision rate with the

excitation **intensity**	**mid b'gap centres** $E_t = E_i$	**upper b'gap centres** $E_t - E_i = 0.1kT/q$	**lower b'gap centres** $E_t - E_i = -0.1kT/q$
low level	$\propto \frac{1}{\sqrt{T}}$	$\propto \frac{e^{-(E_c - E_t - 0.3925) \cdot \frac{q}{kT}}}{\sqrt{T}}$	$\propto \frac{e^{-(E_t - E_v - 0.3925) \cdot \frac{q}{kT}}}{\sqrt{T}}$
high level	$\propto \frac{1}{\sqrt{T}}$	$\propto \frac{1}{\sqrt{T}}$	$\propto \frac{1}{\sqrt{T}}$

Table 3.3: Predicted bulk carrier lifetime dependence on temperature for intrinsic germanium

recombination centres at lower temperatures. The probability of a transition to the recombination level is given by the product of the carrier thermal velocity and the recombination centre's capture cross section. The factor $1/\sqrt{T}$ is due to this fact, and results from the electron thermal velocity. Where present, the exponential term increases with increasing T, but the presence of $1/\sqrt{T}$ dominates over the temperature range of practical interest, the net effect in these cases being to decrease the lifetime with increasing T. Similar expressions exist for heavily p and n doped germanium although the predicted lifetime was always found proportional to $1/\sqrt{T}$, decreasing with increasing temperature in n-type germanium. For low-level excitation in p-germanium a lifetime minimum was found at around $280K$, increasing either side of this.

Practical evidence confirming the above predictions is sparse. Much of the early work used germanium with high impurity densities, and multiple types of impurities. Characterisation of the impurities would therefore be required to confirm agreement with these ideas. In the literature, evidence exists for both an increase [86] in lifetime with reduced temperature for low p-doped material with copper impurities, and also an increase in lifetime with decreasing temperature for p and n doped material [81]. The lifetimes found in the older literature generally decrease with decreasing temperature [87], although high impurity densities are likely to have existed in these materials as indicated by the moderately low room temperature lifetime. Using the theory behind one of these results [81], and extending it from the heavily doped material used in the experiments, to intrinsic material of interest in this work, the variation in equilibrium carrier density with temperature becomes important, changing the sign of the temperature dependence of lifetime, agreeing with the conclusions in this work. More recent results [83] for heavily p- and n-doped germanium show slight temperature dependence, with lifetimes varying no more than 50% in the range $80 - 300^{o}K$, over which $1/\sqrt{T}$ would differ by less than a factor of two.

In the absence of more accurate data on the measured temperature dependence of lifetime and the energy levels of recombination centres present, the predicted lifetime dependence under most conditions for near-intrinsic germanium approximates to $1/\sqrt{T}$. Over the modulator's likely operational temperature range, $10°C$ either side of room temperature, the variation in bulk lifetime is in the order of a few %. For most purposes this is negligible in terms of its effect on system operation.

Measurements of the recombination rate during heavy injection into near-intrinsic germanium [88] show that for a wide range of temperature and concentration, the recombination rate varies linearly with carrier concentration. This is proof that the recombination takes place largely through recombination centres within the germanium bandgap, and not through Auger or direct transitions. Auger and direct transitions at high excess carrier densities show a recombination rate dependence on the cube and square of the excess carrier concentration respectively. The presence of traps has been established at reduced temperature, although in moderately pure germanium at room temperature the effects of these are not usually observed. Providing the excitation is not too high-level, and the density of impurities is low, and the temperature in the device remains within about $10°C$ of room temperature then use of a single bulk carrier lifetime for modelling carrier decay is valid. Over a military temperature range of $-50°C$ to $+50°C$ the factor $1/\sqrt{T}$ varies by a factor 0.8, the bulk carrier lifetime reducing with increased temperature. The effect of the resulting 20% drop in induced absorption over this temperature range on the modulator's 'off' state transmission becomes negligible at high levels of induced-absorption.

3.2.2 Surface carrier recombination in germanium

Having considered carrier recombination in the bulk material, recombination at the surface is now investigated. Suitable optical excitation sources for the modulator have a high absorption coefficient and typically their absorption depths are in the order of $1\mu m$. Following optical excitation a high carrier density therefore exists in the vicinity of the surface, which is therefore strongly affected by surface recombination. Surface recombination acts to reduce the lifetime of carriers, which is frequently much lower than that in the bulk. This is important in the modulator, reducing the excess carrier density for a given excitation level, and hence the system's efficiency. This section outlines the theory of surface recombination and how its rate can be reduced.

Due to the discontinuity of the lattice at the surface and the requirement for dangling germanium bonds to be terminated, the germanium bonds interlink and a surface oxide layer forms. This disruption to the regular lattice structure and alteration of the bonding, changes the surface energy band structure surface by introducing energy levels within the bandgap and by bending the energy bands. Recombination at the surface proceeds through these intermediate surface states as with indirect bulk recombination. The effect of these levels on the recombination of carriers is characterised by the surface recombination velocity (SRV). The SRV is defined by S, the ratio of the recombination rate per unit area (U_s) to the excess carrier concentration close to the surface (Δn):

$$S = U_s / \Delta n \tag{3.20}$$

The recombination rate U_s can be visualised as a carrier density Δn drifting with an average velocity S toward the surface, where all the carriers recombine. The band diagram at the surface is affected by the surface potential, which is a function of the surface environment and the species terminating the surface bonds. Surface states in the oxide layer trap charge, giving rise to a space charge layer near the surface, and a potential barrier. The value of the potential is such that the excess charge in the oxide layer is balanced by that of the ionised impurities and free carriers in the space charge layer. This is shown in Figure 3.3.

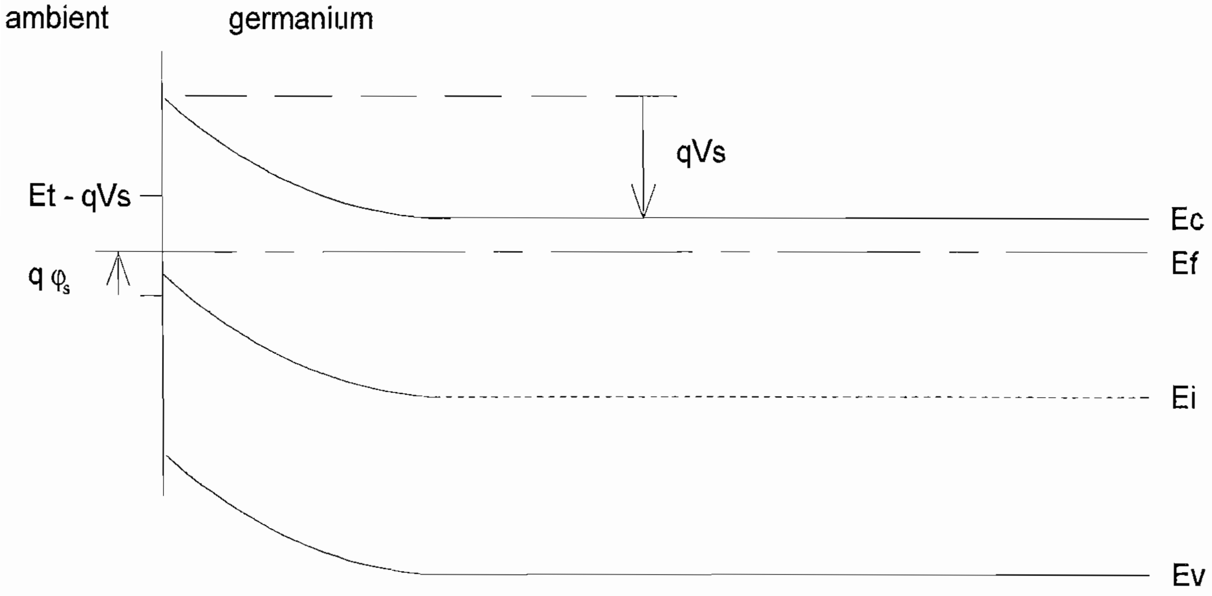

Figure 3.3: Energy band diagram at the surface of low n-doped germanium

The surface states are categorised as 'fast' surface states, with a decay lifetime in the order of $1 \mu s$; and 'slow' surface states with a decay constant in the order of hours. Fast surface states, or interface states, have good electrical contact with the semiconductor surface, and are associated with the surface treatment prior to oxidation, such as the presence of cracks and dislocations. Slow surface states, or interface states, exist in the oxide film or in higher proportions at the oxide-gas interface, requiring a long time to pass charge through the oxide layer. Typical densities for these states are approximately $10^{12} cm^{-2}$, and $10^{11} - 10^{13} cm^{-2}$ for the fast and slow states respectively [30]. Surface recombination is attributed to fast (interface) states.

The surface recombination velocity S due to recombination at a single centre at energy E_t, with a centre density N_t per cm^2 is given by:

$$S = \frac{N_t \langle vA_p \rangle \langle vA_n \rangle (p_0 + n_0)}{2n_i exp(q\phi_0/kT)[cosh(\frac{E_t - \phi_i - q\phi_0}{kT}) + cosh(\frac{\phi_s - \phi_0}{kT})]} \tag{3.21}$$

$$q\phi_0 = kT/2ln(A_p/A_n) \tag{3.22}$$

Parameters have meanings as in Equations 3.3 to 3.6. ϕ_s is the surface potential:

$$q\phi_s = \phi - \phi_i + qV_s \tag{3.23}$$

Positive ϕ_s indicates an excess of electrons over holes at the surface. Following Equation 3.21, the surface recombination velocity is symmetric around $\phi_s - \phi_0$. S is constant here, falling off for large $|\phi_s - \phi_0|$. Values of A_p , A_n and N_t of $10^{-14} cm^2$, $10^{-15} cm^2$ and $10^{11} cm^{-2}$ respectively have been found [75], giving the dependence of S on ϕ_s in Figure 3.4.

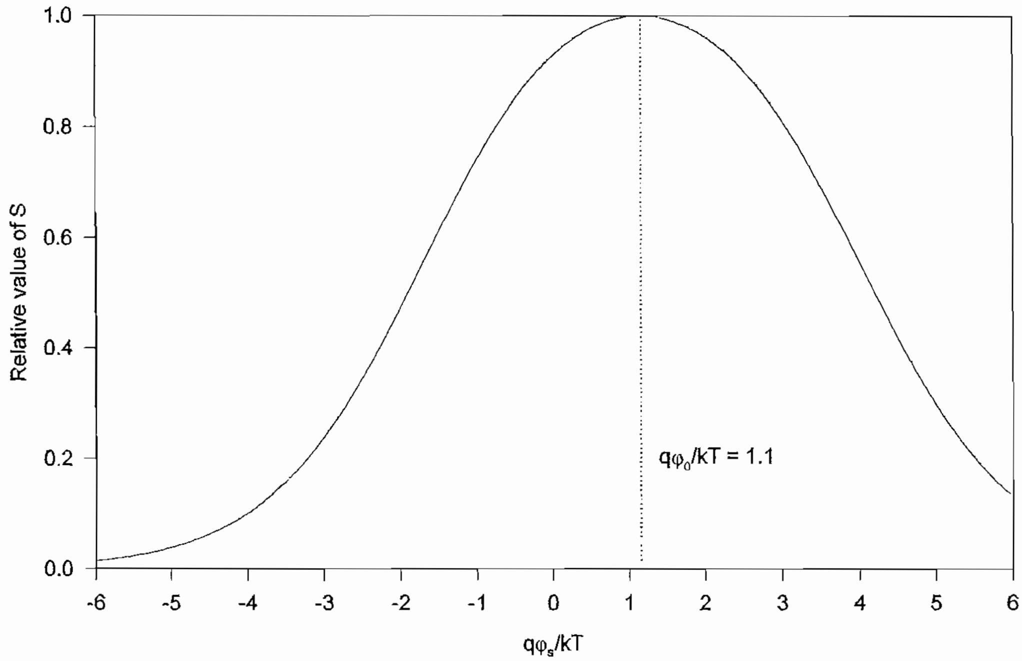

Figure 3.4: Theoretical variation in surface recombination velocity with surface potential

Figure 3.4 shows that to minimise the surface recombination velocity, $|\phi_s - \phi_0|$ should be maximised. Variation of the surface potential and hence surface recombination velocity is achieved by changing the gaseous ambient [89] or through application of an electric field normal to the surface [90]. In germanium ϕ_0 is usually positive since $A_p > A_n$. In n-type or intrinsic germanium in a wet ambient, V_s and hence ϕ_s is more positive, and in the dry ambient more negative, so the surface recombination velocity drops in a wetter ambient, following S to the right of the line $\phi_s = \phi_0$ in Figure 3.4. This demonstrates the environmental dependence of S, showing that species adsorbed to the surface alter the surface potential V_s. Reduction of the density of fast surface states (N_t) is achieved in practice through etching the germanium, which reduces the density of surface cracks and dislocations. Additionally, the etchant composition terminates the surface with a particular species. This also reduces the surface recombination velocity by increasing the surface potential ϕ_s, and is considered further in Section 6.1.

Typically the surface recombination velocity varies from tens of cms^{-1} for an etched surface to $10^5 cms^{-1}$ [79]. Etching therefore offers a significant increase in the effective carrier lifetime (Equation 3.1) of electron-hole pairs close to the surface.

3.2.3 Carrier diffusion

When the modulator is optically-excited, the equilibrium carrier distribution at a point in the crystal is disturbed and carriers diffuse in the homogeneous semiconductor until the carrier density is everywhere equal, providing there is no electric field. Carrier diffusion therefore affects the absorption across the modulator's aperture. To accurately model carrier diffusion in Chapter 4, the validity of its usual treatment as a constant material parameter is determined in this section.

The vector current density (J_x) driving the change in carrier distribution is determined by the diffusion coefficient (D_x) and the carrier density gradient (dn/dx), for a particular direction, by the relationship:

$$J_x = D_x q \frac{dn}{dx} \tag{3.24}$$

Following such a disturbance, diffusion currents are generated in the x y and z directions. Assuming homogeneous diffusion, the electron and hole diffusion coefficients are treated as the scalar values D_n and D_p respectively. Providing trapping does not occur, the densities of free electrons and holes must be equal in an optically-excited intrinsic semiconductor. The diffusion coefficients for electrons and holes are given by the Einstein relationship:

$$D_{n,p} = \mu_{n,p}kT/q \tag{3.25}$$

The mobilities of electrons and holes in germanium of 3900 and $1900cm^2/Vs$ respectively at $300^\circ K$ give different diffusion coefficients of $D_n = 100.8cm^2s^{-1}$ and $D_p = 49.1cm^2s^{-1}$. However, the excited electron-hole plasma must remain electrically neutral. As the electrons try to diffuse faster than the holes, the attractive forces between holes and electrons restrict their maximum spatial separation and the whole electron-hole plasma diffuses with a combined diffusion coefficient. This is defined by the ambipolar diffusion coefficient [47] in Equation 3.26.

$$D_a = \frac{(n+p)D_nD_p}{nD_n + pD_p} \tag{3.26}$$

For low-level excitation in n doped germanium ($n >> p$) this approximates to D_p and diffusion is limited by the minority carrier, holes. In near-intrinsic germanium under moderate optical excitation, $n = p$, and Equation 3.26 reduces to:

$$D_a = \frac{2 \cdot D_nD_p}{D_n + D_p} \tag{3.27}$$

The electron-hole plasma therefore diffuses in all directions with diffusion coefficient D_a and this is assumed henceforth since the conditions of no trapping, moderate level excitation and near-intrinsic starting germanium prevail. At $300^\circ K$ the ambipolar diffusion coefficient for germanium is $66.03cm^2s^{-1}$.

The diffusion length L_d is defined in accordance with the bulk carrier lifetime (τ_{bulk}) and the ambipolar diffusion coefficient D_a and is given by:

$$L_d = \sqrt{D_a\tau_{bulk}} \tag{3.28}$$

This represents the physical distance over which the electron-hole plasma density falls to $1/e$ of its maximum. Typically, high purity germanium has a bulk carrier lifetime of approximately $1ms$, which, using the above ambipolar diffusion coefficient gives a diffusion length of $2.6mm$.

However, the plasma can only be treated as having a combined, ambipolar diffusion coefficient if the electron diffusion with higher D_n does not lead the hole diffusion by too-large a distance. This constraint requires that the plasma remains electrically neutral over a distance whose minimum is short compared to the distance over which carriers decay, L_d. The neutral region around an ion is now calculated.

The radius of a sphere around an impurity ion within which electrical neutrality is maintained is defined as the Debye length (L_{Debye}). For a semiconductor of uniform impurity concentration and bulk characteristics this is given [47] by:

$$L_{Debye} = \sqrt{D_n \tau_d} = \sqrt{k_B T / q^2} \cdot \sqrt{\epsilon_r \epsilon_0 / n} \tag{3.29}$$

Here ϵ_0 is the permittivity of free space and ϵ_r is the relative dielectric constant. For intrinsic germanium at 300°K, $L_{Debye} \cong 1\mu m$. At excess carrier densities of 10^{16} and $10^{16} cm^{-3}$ the Debye length reduces to $48nm$ and $15nm$ respectively. If degenerate, a correction factor must be applied which, at higher carrier densities, causes a lower rate of reduction of L_{Debye} with carrier concentration, although L_{Debye} still reduces with increasing carrier concentration.

Even in (relatively impure) optical grade germanium with $\tau_{bulk} \cong 1\mu s$ the corresponding diffusion length of $8\mu m$ is much longer than the Debye length. Charge neutrality is still maintained over an electron-hole pair separation whose minimum is short compared to the distance over which the carrier population decays. On average, electrons can only lead the diffusion process by a Debye length, and since this is short compared to the mean distance that electrons and holes diffuse, the entire plasma can be treated as moving with one combined (ambipolar) diffusion coefficient.

The temperature and carrier concentration dependence of the diffusion coefficients D_n and D_p are now considered. The diffusion coefficient for a non-degenerate semiconductor is linked to the drift mobility through the Einstein relationship in Equation 3.25. This was a specific form of the generalised diffusion coefficient equations, Equation 3.30 and Equation 3.31 [42], which include the degenerate case.

$$D_n = 2 \cdot \left(\frac{kT}{q}\mu_n\right) F_{1/2}\left(\frac{E_F - E_C}{kT}\right) \Big/ F_{-1/2}\left(\frac{E_F - E_C}{kT}\right) \tag{3.30}$$

$$D_p = 2 \cdot \left(\frac{kT}{q}\mu_p\right) F_{1/2}\left(\frac{E_V - E_F}{kT}\right) \Big/ F_{-1/2}\left(\frac{E_V - E_F}{kT}\right) \tag{3.31}$$

Where $F_{1/2}$ is the Fermi-Dirac integral. These simplify to Equation 3.25 in the non-degenerate case. The temperature dependence of the mobility depends on the temperature range and doping density. Close to room temperature the mobility in n-type and p-type germanium follows a $T^{-1.66}$ and a $T^{-2.33}$ law [91] respectively and is restricted by lattice scattering. At low temperatures the mobility is restricted by impurity scattering but this region is not of interest in the modulator. The effect of this on a temperature increase of 10°K from 300°K is small, reducing the ambipolar mobility from $66.03 cm^2/Vs$ to $63.69 cm^2/Vs$.

During optical excitation, carrier diffusion is treated with the ambipolar diffusion coefficient, but this has been found to be carrier-density dependent [40] [92] [93] [94]. Evidence also suggests that the diffusion coefficient remains constant up to densities of 10^{19} to $10^{20} cm^{-3}$ [13]. Consideration of carrier kinetics [40] suggests that after the onset of carrier degeneracy, at about $10^{19} cm^{-3}$ the ambipolar diffusion coefficient increases monotonically with carrier density due to the increase in carrier energy. This follows from Equations 3.30 and 3.31 and is considered later. Below this carrier density, however it is also suggested that the diffusion coefficient may be lower than its low-level value due to a reduction in the bandgap at the optically-excited surface of the germanium. This is also considered later.

Since optical carrier generation at around $980nm$ has an absorption depth in the order of $1\mu m$, carriers are generated very close to the surface, giving a high initial carrier density. Subsequent carrier decay through bulk and surface recombination, causes the diffusion coefficient to act over a wide range of carrier densities. In practice the effect of any change in the ambipolar diffusion coefficient is dependent on both the carrier density during excitation, and the timescale of interest in the experiment.

At this point it is important to distinguish the carrier mobility of interest here, from the drift mobility measured in the presence of an electric field, the effects of which are described in semiconductor device literature. The drift mobility shows a strong reduction in the presence of an electric field due to carrier-carrier scattering [95], dropping from its low density value for carrier densities in excess of $10^{17} cm^{-3}$. However, for excited carriers in the absence of an electric field, this reduction is unlikely to take place since electrons and holes travel in the same directions, in contrast to the drift case. The drift mobility is not thought to affect the diffusion coefficient of the diffusing plasma of interest in this work [40]. The mobility used to calculate the diffusion coefficient used in this work is therefore assumed constant at fixed temperature.

The cited bandgap reduction with increased surface carrier density is caused by a high carrier temperature compared to the lattice temperature in the presence of an increased carrier density close to the surface [40] [92], or by a high lattice temperature. However, carrier-carrier scattering takes place in the order of $10^{-14}s$, and carrier-lattice coupling takes place in the order of $10^{-12}s$ [93], whilst only diffusion over the $1ms$ excitation and carrier decay period is of importance in this work. Since carrier- and lattice-temperature equilibrium is reached over a much shorter timescale than the carrier excitation period, these effects do not affect the diffusion coefficient of interest in this work, and are only of importance during high energy, short pulse excitation.

However, the increase in ambipolar diffusion coefficient due to degeneracy, occurring at carrier densities of $>\sim 10^{19} cm^{-3}$ at room temperature [40], will occur in the present work if these carrier densities are encountered. This increase is predicted (Equations 3.30 and 3.31) by the increased kinetic energy of the electrons and holes which occurs for independent particles after the onset of degeneracy, and is not restricted by the timescale of its action. Below this carrier density the ambipolar diffusion coefficient will be treated as a constant at a given temperature, which, at room temperature is $66.03 cm^2/Vs$.

3.3 Optical properties of germanium

The optical properties of germanium that facilitate its use in infrared optics are its low dispersion and wide optical passband. Its high refractive index of 4.004 at $10.0\mu m$ necessitates antireflection coatings to eliminate the Fresnel loss. The induced infrared absorption characteristics have already been considered, and this section determines the additional links with the electrical properties that are important in characterising germanium for the modulator.

The optical absorption of germanium was shown in Chapter 2 to depend on the density and type of charge carrier present. The spectral dependence of the absorption depends on these parameters, and whether particular transitions are permitted due to band filling criteria. The optical absorption in the modulator's $10\mu m$ operating region, and its dependence on carrier type and density are now considered. Equation 2.7 gave the absorption coefficient (α_{total}) at fixed wavelength as:

$$\alpha_{total} = \sigma_e n + \sigma_h p + K_{phonon} \tag{3.32}$$

The effect of the resistivity ρ on the absorption is given by Equation 3.33, which is plotted in Figure 3.5 at three temperatures.

$$\rho = \frac{1}{\sigma} = \frac{1}{nq\mu_n + pq\mu_h} \tag{3.33}$$

From Figure 3.5 the resistivity of intrinsic germanium is $47.6\Omega cm$ at $300^\circ K$. The maximum resistivity at this temperature is $51.6\Omega cm$, which occurs for slightly p-type material with a hole density of $1.6 \times 10^{16} cm^{-3}$. Increasing the carrier concentration through n-doping reduces the resistivity (lower portion of graph) and the absorption initially falls due to suppression of the hole concentration with its higher absorption cross section. Along this region the absorption is very low, the minimum occurring in the range $10 - 40\Omega cm$, and hence this is the usual specification of infrared optics [28]. For

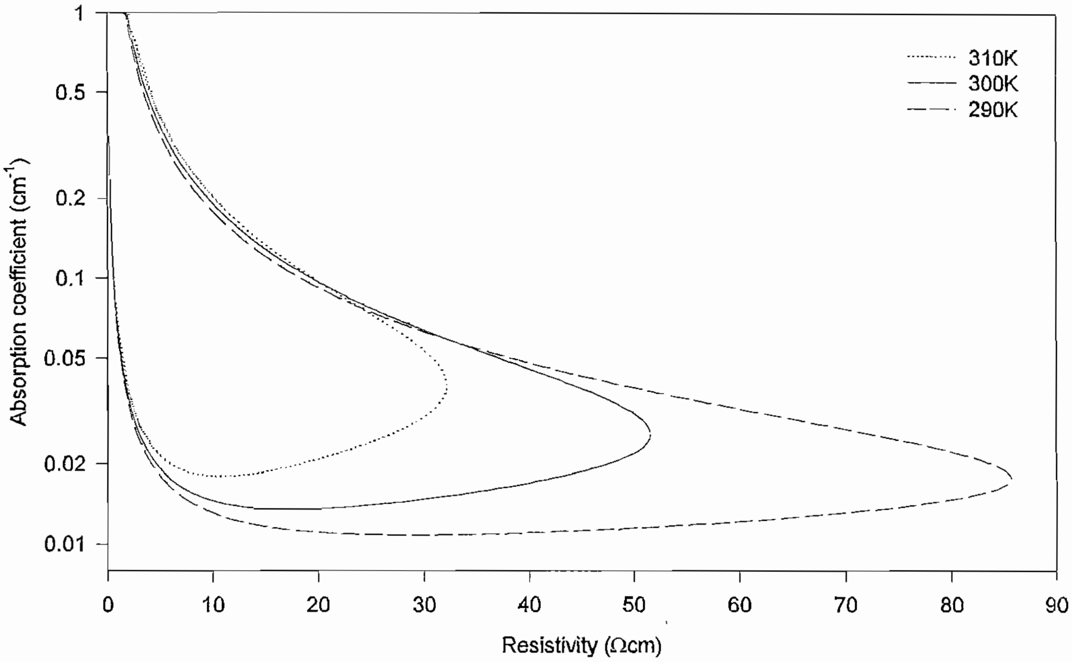

Figure 3.5: Absorption coefficient (α_{total}) vs resistivity for germanium; $\sigma_e = 0.34 \times 10^{-16} cm^2$, $\sigma_p = 5.33 \times 10^{-16} cm^2$,$K_{phonon} = 0.0073 cm^{-1}$

very low resistivity n-type material the absorption increases since electron absorption dominates the total absorption. The phonon absorption of $0.0073cm^{-1}$ sets a minimum for the n-doped absorption. Doping the germanium p-type follows the upper half of the curve in Figure 3.5. Absorption by holes dominates the absorption, which increases proportionately. The effect of temperature is also predicted by the figure, which accounts for the temperature-dependence of both the mobility and equilibrium electron hole population [96]. This shows the significant effect of temperature on the absorption coefficient, and that to obtain both low absorption and a low temperature dependence of absorption, the most suitable material is lower resistivity n-doped of about $10\Omega cm$. To ensure low absorption in the modulator's 'on' state the material should therefore be n-type with this resistivity. In practice the high purity, long bulk carrier lifetime material which is available due to nuclear detector applications is almost exclusively near-intrinsic, and is used almost entirely throughout this work. The implication of a temperature increase of $10°K$ from $300°K$ for an unexcited $0.5cm$ intrinsic sample is an increase in absorption coefficient from 0.021 to 0.03, corresponding to a 0.5% decrease in transmission. Decreasing the temperature to $290°K$ reduces the absorption coefficient to 0.015, increasing the transmission by 1.78%.

The absorption coefficient is linked to the refractive index through its imaginary term, the extinction coefficient. The complex refractive index (n_c) is given by:

$$n_c = n_{ge} - ik \tag{3.34}$$

where the complex part or extinction coefficient k at wavelength λ_0 is given by:

$$k = \alpha_{total} \cdot \frac{\lambda_0}{4\pi} \tag{3.35}$$

Usually for polished germanium at $10\mu m$ n_c is real and the imaginary part is insignificant. Intrinsic germanium at $300°K$ has $\alpha_{total} = 0.044cm^{-1}$ from Figure 3.5, giving $k = 35 \times 10^{-9}$ at $10\mu m$. During the modulator's 'off' state the absorption coefficient is intentionally high due to the induced inter-valence band absorption, with $\alpha_{total} \cong 6$. The effect of this on the refractive index is still insignificant at $10\mu m$, justifying the earlier statement that absorption using this process does not significantly modify the real part of the refractive index.

Accounting for multiple reflections, the intensity transmission of a sample of thickness d, absorption coefficient α (cm^{-1}) and refractive index n, is given by Equation 3.36.

$$T = \frac{(1-r)^2 \cdot e^{-\alpha d}}{1 - r^2 e^{-2\alpha d}} \tag{3.36}$$

Equation 3.36 gives the average transmission across a fringe in the case of a coherent source, and is used in this situation since the source is incoherent (sample thickness >> coherence length of source). The reflection coefficient r per surface is given at normal incidence by:

$$r = \frac{(n_{ge} - 1)^2 + k^2}{(n_{ge} + 1)^2 + k^2} \tag{3.37}$$

For a $0.5cm$ thick intrinsic germanium sample at $300°K$ this gives $T = 45.74\%$ at $10.0\mu m$. Care must be taken when considering the transmission of a sample at a fixed wavelength, or using a spectrometer when the fringe separation is resolved. Interference fringes occur in transmission spectra, giving reflection minima when the sample thickness is an odd number of quarter wavelengths. This has implications for later experiments in Chapter 5 and in the design of antireflection coatings (Section 6.3). At this stage the Fresnel loss, giving a maximum transmission of 45.74% at around $10\mu m$ is noted. The germanium has low dispersion at around this wavelength, and toward shorter wavelengths until about $3\mu m$. On approaching the bandgap from a longer wavelength the characteristic increase in real refractive index is seen, and this becomes significant before the pump wavelength (of approximately $980nm$) is reached. Most optical applications do not involve the refractive index of germanium over such a wide spectral range, but for this application it is important, and dispersion must be considered. The dispersion is shown by Figure 3.6, which plots the real part of the refractive index, n_{ge}, and the extinction coefficient k vs wavelength [97].

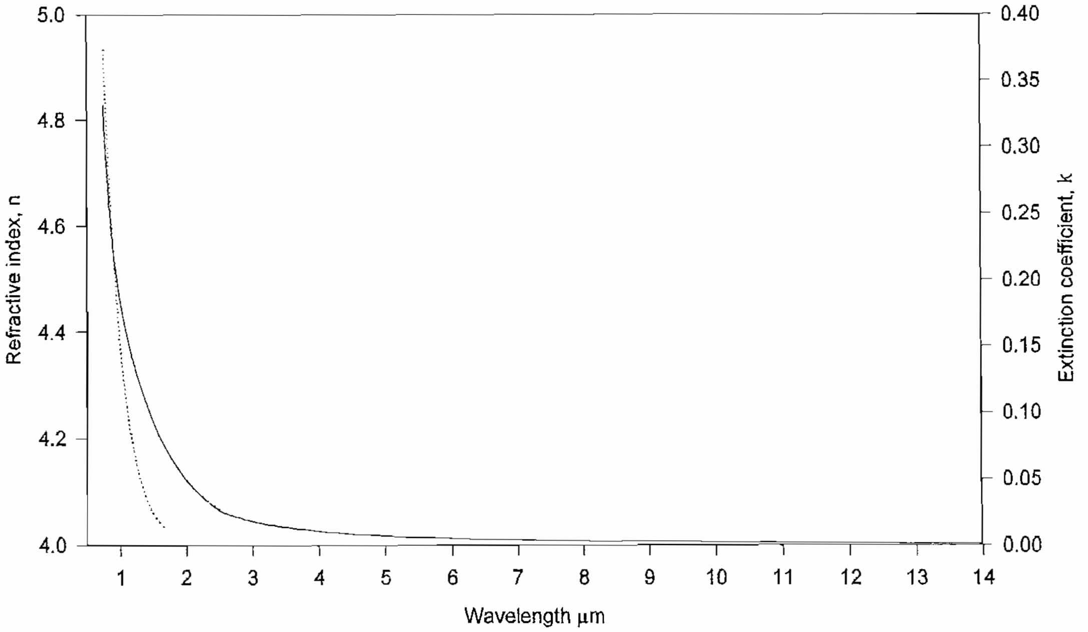

Figure 3.6: n_{ge} (solid) and k (dotted) vs wavelength for Ge showing the effect of dispersion

To a good approximation, dispersion can be ignored at longer wavelengths, although this is not valid in calculations at shorter wavelength involving the pump beam wavelength or antireflection film properties. At $10.0\mu m$ and at $980nm$ the refractive index is 4.004 and $4.473+0.161i$ respectively. At $980nm$ for example the reflectance of the pump beam is 40.3% per surface accounting for dispersion; and 36.1% if only a real refractive index of 4.004 were assumed.

The absorption edge of germanium is of particular importance since this determines the required optical excitation wavelength and the initial spatial carrier distribution following optical excitation. The temperature dependence of the absorption coefficient at the absorption edge strongly affects the absorption coefficient for small temperature changes. The absorption spectra is given [68] in Figure 3.7.

At high photon energy the high absorption coefficient varies slowly with photon

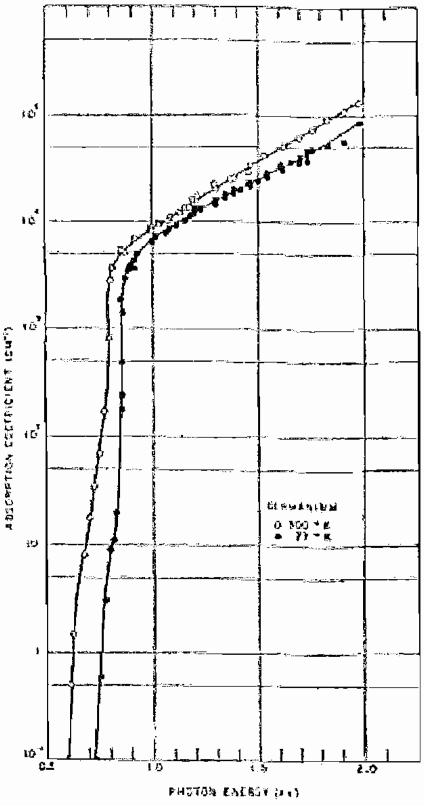

Figure 3.7: Absorption spectra of single crystal germanium at $77^\circ K$ and $300^\circ K$

energy. Carriers are excited beyond the minimum of the direct valley and the slowly increasing density of states with photon energy causes this low spectral dependence. On approaching the direct gap energy, as the photon energy is reduced the absorption coefficient has strong spectral dependence due to the high-probability direct optical transitions. Toward lower photon energy the indirect bandgap is reached and a lower spectral dependence of the phonon-assisted transitions is observed in the range $<\sim 0.8eV$ to $0.67eV$ at $300^\circ K$.

Ideally the excitation wavelength for electron-hole pair generation in the modulator should be as long as possible, where more photons per watt of optical power are available. Too long a wavelength is undesirable due to the reduced absorption coefficient, risking the excitation passing straight through the germanium. Wavelengths close to the direct gap are unsuitable, giving a strong wavelength-dependence of the absorption coefficient. The temperature dependence of the position of the (indirect) bandgap is $-4.4 \times 10^{-4} eV/^\circ K$, and that for the direct gap is $-3 \times 10^{-4} eV/^\circ K$ [68].

Following optical excitation the carriers decay, mainly through non-radiative SRH recombination. A very low transition probability for radiative recombination exists, although photon emission has been observed [98]. Approximately 1% of the recombination is radiative, depending on the other recombination mechanisms present [39]. This was observed only in very thin samples approximately an absorption depth thick. In the modulator this radiative recombination is undesirable, appearing as a parasitic NIR signal during the 'off' state. If present, this radiation would have to be filtered to avoid detection by the wide optical bandwidth pyroelectric detector. Alternatively, the sample should be sufficiently thick to ensure its re-absorption. The absorption coefficient is $7.6cm^{-1}$ at the indirect bandgap ($0.67eV$) (Figure 3.7) so to ensure re-absorption of the radiative emission the modulator thickness should be at least three absorption depths ($0.39cm$) thick.

3.3.1 Optical properties of germanium and their effect on the modulator

The hole density required for reasonable 'off' state absorption is now calculated to determine its effect on carrier lifetime and diffusion. Ignoring multiple reflections the 'off state' sample transmission is given by Equations 3.38 and 3.39. T_0 is the 'on' state transmission, A is the product of the hole absorption cross section σ_h and the excited-state area carrier density, and η is the absorption efficiency.

$$T = T_0 e^{-A\eta} \tag{3.38}$$

$$A \cong \frac{\tau_{effective} P_{Excabs} \lambda_{exc} \sigma_h}{hc} \tag{3.39}$$

$\tau_{effective}$ is given by Equation 3.1, P_{Excabs} is the absorbed excitation power at wavelength λ_{exc}, h is Planck's constant and c is the speed of light. The excitation wavelength must be above-bandgap, and ideally as long as possible to take advantage of the higher photon per Watt ratio. At the longer wavelength a lower absorption coefficient exists, so carriers are generated further from the excited surface at which surface recombination occurs. However, unless carriers are generated more than a diffusion length from the surface the effective carrier lifetime will still be affected by the surface recombination velocity. A diffusion length of $2.6mm$ in high purity germanium was calculated above, and a corresponding absorption depth is available by excitation at approximately $1.8\mu m$. However, a modulator element several absorption depths thick is required to ensure none of the excitation power reaches the detector, requiring an unreasonably thick germanium sample. Less critically, a modulator element several diffusion lengths thick is required to ensure a low carrier density exists at the sample's back surface to avoid additional filtering. This is less critical since only $\sim 1\%$ of the carriers recombine radiatively, and a finite surface recombination velocity on the back surface reduces the carrier concentration there. Additionally the decrease in absorption coefficient close to $1.8\mu m$ with reduced temperature (Figure 3.7) risks the excitation passing through the germanium and onto the pyroelectric detector if the temperature were to drop. Excitation of the germanium is therefore preferable at shorter wavelengths where the effect of the temperature-dependent absorption coefficient is unimportant. Economics and the availability of laser diodes dictate the excitation wavelength used in the application, restricting it to close to $810nm$ or $980nm$ or $1480nm$ where pump lasers are more easily available. High power is only currently available at moderate cost close to $810nm$ and $980nm$, $980nm$ being preferable due to the higher photon per Watt ratio.

Assuming an induced absorption coefficient of 2 is required in Equation 3.39 to give reasonable absorption, and assuming an effective carrier lifetime of $1ms$, a power density of $0.76W\ cm^{-2}$ at an excitation wavelength of $980nm$ with an absorption efficiency $\eta = 1$ is required to reduce the transmission by a factor of 0.14. In practice it will be seen that the loss due to Fresnel reflection of the pump excitation wavelength, (60% reflection at $980nm$) combined with the effects of surface and bulk recombination on reducing $\tau_{effective}$ make this prediction too low by a factor of about 10.

The refractive index of 4.0 in the low dispersion region around $10\mu m$ means that AR coatings are required at the image wavelength to maximise the 'on' state transmission. Section 6.3 considers optimisation of modulator performance through use of AR coatings at the pump and image wavelengths.

From Equation 3.32, an area carrier density of A/σ_h is required for the above absorption. If the carriers are produced by an instantaneous pulse, giving an initial carrier distribution determined only by optical absorption, before carrier diffusion takes place, then if the excitation produces a carrier profile $N(x)$ (cm^{-3}), given by:

$$N(x) = N_0 e^{-\alpha_{ill} x} \tag{3.40}$$

where N_0 is the surface carrier distribution (cm^{-3}) then the initial area carrier density is given by N_0/α_{ill}. For an optical excitation absorption coefficient of $\alpha_{ill} = 10^4 cm^{-1}$ this gives a surface carrier density of $N_0 = 3.75 \times 10^{19} cm^{-3}$. This is much higher than the predicted ($\sim 10^{17} cm^{-3}$) density at which Auger recombination becomes significant. It is also in the region where degeneracy starts to become important and an increase in the ambipolar diffusion coefficient is predicted to occur. Although this calculation is only for moderate absorption, it ignores surface recombination which significantly reduces the surface carrier density, and the calculated value may never be attained. In order to determine the actual carrier densities encountered and the processes which are significant, the evolution of the electron-hole plasma must be modelled, accounting for this, and this is the subject of Chapter 4.

Chapter 4

Theory of modulator operation: carrier diffusion

4.1 Introduction

Methods of generating the electron-hole plasma required for the induced absorption include electrical injection, electron-beam irradiation, and above-bandgap optical excitation. The two former methods are considered in Chapter 8 on the electrically-modulated device. Much insight into system operation is given through the generation of electron-hole pairs through the easier method of laser illumination with a near-infrared pulse of above-bandgap radiation. This avoids fabrication complications of producing infrared-transparent carrier-injecting contacts, and the source is easier to characterise and control than an electron beam.

In the understanding, design and optimisation of the modulator, modelling of the spatial carrier density, during and after optical excitation is required to determine how the absorption changes with time. Modelling of the carrier distribution in the static and dynamic situations is necessary to predict the required optical power for a given absorption, and also to determine the rate at which this can be switched. This chapter details the diffusion equation models which have been developed to understand the dominant parameters affecting the induced absorption, and gives reasonable values which must be attained experimentally to optimise the modulator. The initial one-dimensional models are later developed into two and three-dimensional models to predict the spatial carrier distribution following excitation of the surface with a non-uniform illumination function. In addition to the primary application of producing uniform absorption across the aperture there is a need to produce an absorbing pattern on the germanium aperture to reproduce the scanning effects of present-technology mechanical choppers. The feasibility of this is investigated through the lateral extent of carrier diffusion.

Following the development of carrier diffusion models, their validation is also required. Validation of the main diffusion equation model is given in Chapter 5 through experiments measuring the effects of spatial and temporal carrier decay. This is subsequently developed to model the microwave reflectance of an excited sample and is used in combination with experimental results to distinguish between bulk and surface effects.

Chapter 3 investigated the carrier recombination processes and concluded that providing the carrier density is not too high, the use of fixed values for the bulk carrier lifetime, surface recombination velocity and the ambipolar diffusion coefficient is valid. The thinking in this chapter is to assume these values are constants in the models and to verify these assumptions using carrier-density predictions and experimental results. The starting point for each of these models is the one-dimensional general diffusion equation given [91] for electrons by Equation 4.1.

$$\frac{\partial n(x,t)}{\partial t} = n(x,t)\mu_n\frac{\partial \varepsilon}{\partial x} + \varepsilon\mu_n\frac{\partial n(x,t)}{\partial x} + D_n\frac{\partial^2 n(x,t)}{\partial x^2} + G_g(x,t) - \frac{n(x,t)}{\tau_{bulk}} \tag{4.1}$$

n is the excess carrier density (cm^{-3}), t is time, μ_n is the electron (minority carrier) mobility, ε is the applied electric field, x is displacement into the germanium as given in Figure 4.1, D_n is the electron (minority carrier) diffusion coefficient, G_g is the spatial carrier generation ($cm^{-3}s^{-1}$) term and τ_{bulk} is the bulk carrier lifetime. Equation 4.1 is for a generalised doped semiconductor where diffusion is limited by minority carriers. All models considered here assume zero electric field and equal numbers of electrons and holes, as is the case in optically-excited near intrinsic germanium with no trapping. Equation 4.1 now reduces to Equation 4.2.

$$\frac{\partial n(x,t)}{\partial t} = D_a\frac{\partial^2 n(x,t)}{\partial x^2} + G_g(x,t) - \frac{n(x,t)}{\tau_{bulk}} \tag{4.2}$$

In Equation 4.2 the electron diffusion coefficient is replaced by the ambipolar diffusion coefficient due to the presence of equal densities of electrons (n) and holes, as discussed in Chapter 3. This one-dimensional diffusion equation model forms the basis for this chapter. Solutions to this equation are developed under the conditions of non-equilibrium steady state, and non-equilibrium decay, for the boundary conditions of semi-infinite x and finite x, for various source generation functions in one, two and three dimensions, to understand the diffusion process. The parameters used during the modelling process that are common to most stages of the modelling are given in Table 4.1.

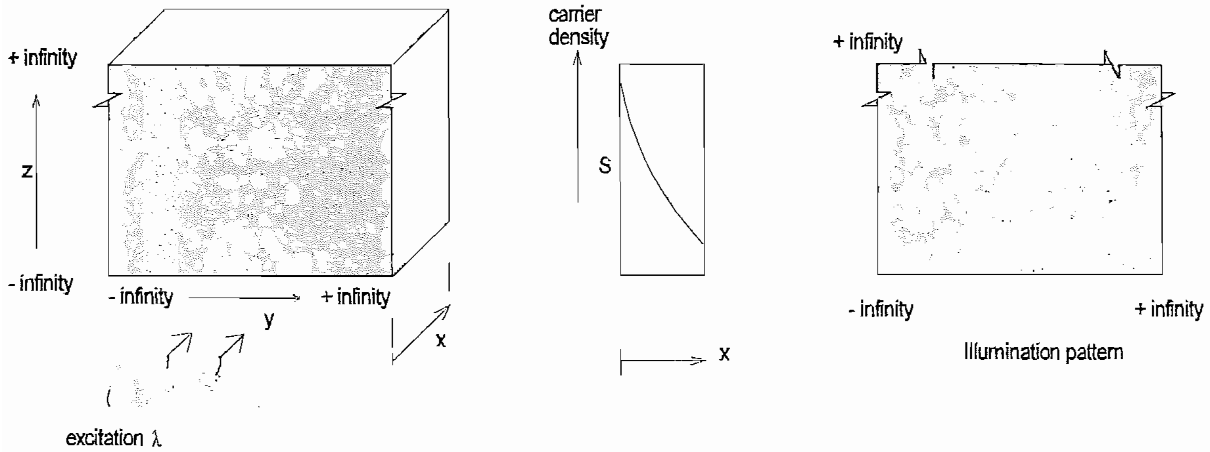

Figure 4.1: Germanium sample geometry used in the modelling process

4.2 One-dimensional carrier diffusion model: Steady state excitation

Initially much information on the diffusion process is given by a one-dimensional steady state model. This assumes continuous illumination of the sample's front surface, which is infinite in lateral extent and semi-infinite (Section 4.1.1) or finite (Section 4.1.2) in the x direction. This gives the non-equilibrium steady state solution for the carrier distribution as a function of x. Under steady state conditions, the $\partial n/\partial t$ term in Equation 4.2 is zero and the equation becomes:

$$0 = D_a \frac{d^2 n(x)}{dx^2} + G_g(x) - \frac{n(x)}{\tau_{bulk}} \tag{4.3}$$

If the optical generation term G_g is given by Equation 4.4:

$$G_g(x) = N_0 e^{-\alpha_{ill} x} \tag{4.4}$$

where α_{ill} is the absorption coefficient at the excitation wavelength and N_0 is the volume generation rate at the surface, which is given by integration as:

parameter	symbol	value	units
Ambipolar diffusion coefficient	D_a	66.04	cm^2s^{-1}
Bulk carrier lifetime	τ_{bulk}	1.0	ms
Surface recombination velocity	S	1	ms^{-1}
Excitation wavelength	λ_{exc}	980	nm
Excitation absorption coefficient	α_{ill}	1.9×10^4	cm^{-1}

Table 4.1: Parameters and their values in the modelling process

$$N_0 = \frac{\alpha_{ill} P_{Excabs} \lambda_{exc}}{hc} \tag{4.5}$$

where P_{Excabs} is the absorbed excitation power, λ_{exc} is the excitation wavelength, h is Planck's constant and c is the speed of light.

4.2.1 Steady state semi-infinite germanium

The solution to Equation 4.3 for a semi-infinite sample with surface recombination velocity S at the front surface where carriers are generated is subject to the boundary conditions:

$$n(x \to \infty) = 0 \tag{4.6}$$

$$D_a \frac{dn}{dx}\bigg|_{x=0} = S \cdot n(x=0) \tag{4.7}$$

Giving the solution:

$$n(x) = \frac{N_0 \cdot \tau_{bulk}}{1 - \alpha_{ill}^2 L_a^2} \cdot \left[e^{-\alpha_{ill} \cdot x} - \frac{L_a \cdot (S + D_a \alpha_{ill}) \cdot e^{-\frac{x}{L_a}}}{S L_a + D_a} \right] \tag{4.8}$$

where $L_a = \sqrt{D_a \tau_a}$ is the ambipolar diffusion length. This is plotted in Figure 4.2 for a range of surface recombination velocity and bulk carrier lifetime parameters.

Figure 4.2 shows the expected reduction in steady state carrier density with increased S or reduced τ_{bulk}. Also if a long bulk carrier lifetime and low surface recombination are present, a significant carrier density at the back surface of a thin sample exists, so surface recombination here becomes important. At the front surface, on a scale too small to be shown in Figure 4.2, diffusion causes a positive carrier density gradient due

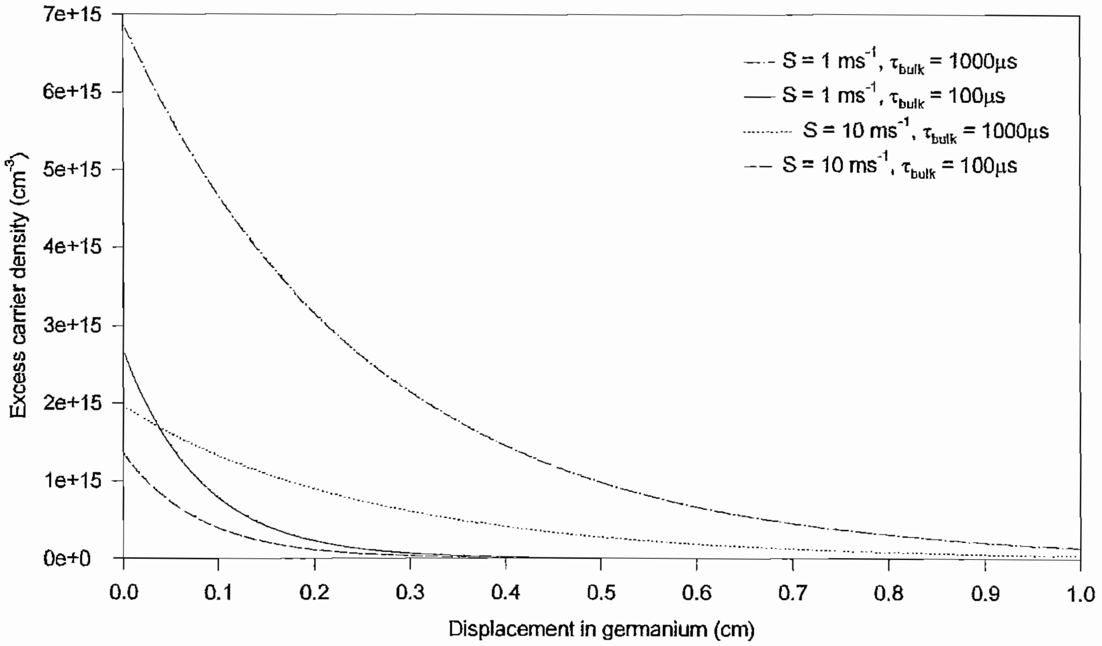

Figure 4.2: Excess carrier distribution (cm^{-3}) during non-equilibrium steady state excitation for an absorbed power of $0.5W\ cm^{-2}$

to the finite surface recombination velocity. This is shown in Figure 4.3 over reduced displacement (x) for the same parameters as Figure 4.2, the carrier density gradient satisfying Equation 4.7.

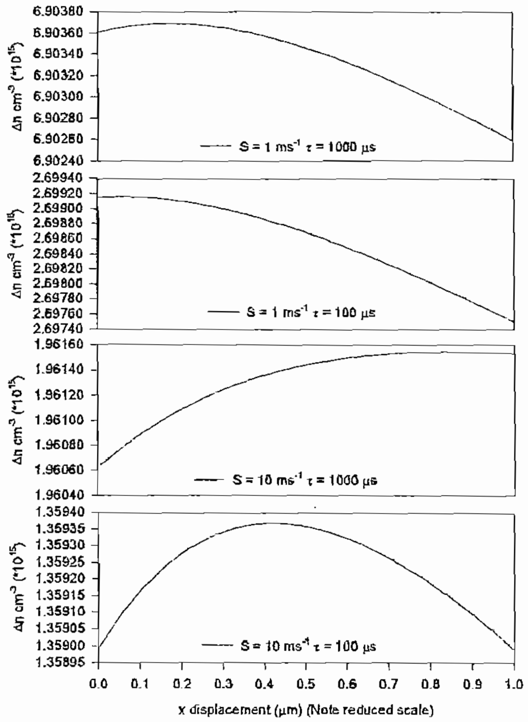

Figure 4.3: Excess carrier distribution (cm^{-3}) at the excited surface showing positive carrier density gradient supplying surface recombination current

The total induced absorption coefficient in the modulator's 'off' state is proportional to the hole density per unit area (Equation 3.32, Chapter 3), with the hole absorption cross section as the constant of proportionality. The sensitivity of the total absorption to the surface recombination velocity S, is now determined by calculating the excited-state area carrier density. Integration of Equation 4.8 over x gives the area carrier density (cm^{-2}) as:

$$\int_0^\infty n(x)dx = \frac{\frac{\alpha_{ill} P_{Excabs} \lambda_{exc} \tau_{bulk}}{hc}}{1-\alpha_{ill}^2 L_a^2} \cdot \left[\frac{1}{\alpha_{ill}} - \frac{L_a^2 \cdot (S + D_a \alpha_{ill})}{S L_a + D_a}\right] \tag{4.9}$$

The effect of the surface recombination velocity on the total absorption coefficient is determined by comparing this equation for finite S to the situation with $S = 0$, giving the normalised area carrier density as:

$$\frac{\int_0^\infty n(x)dx|_{S=S}}{\int_0^\infty n(x)dx|_{S=0}} = \frac{1 - \frac{\alpha_{ill} D_a \tau_{bulk}(S + D_a \alpha_{ill})}{D_a + S\sqrt{D_a \tau_{bulk}}}}{1 - \alpha_{ill}^2 D_a \tau_{bulk}} \tag{4.10}$$

This is plotted as a function of S for a bulk carrier lifetime of $1ms$ and $100\mu s$ in Figure 4.4.

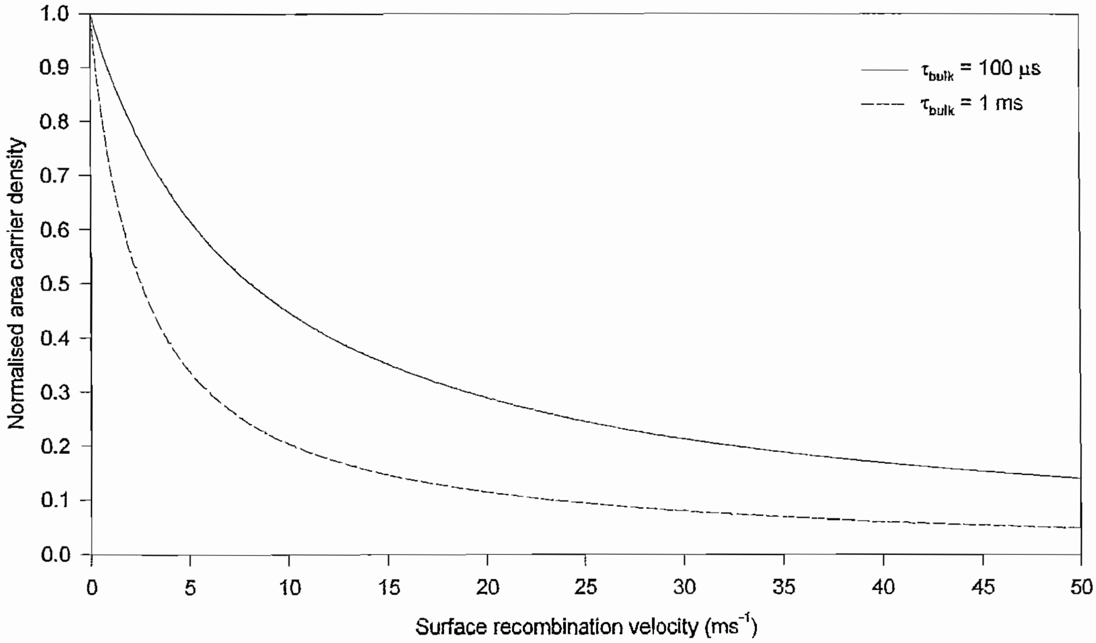

Figure 4.4: Steady state area carrier density in presence of surface recombination velocity S normalised to zero surface recombination case

$S = 0$ in Figure 4.4 represents a perfect surface and gives a ratio of unity. As S increases, more carriers recombine at the front surface and the ratio and hence induced absorption reduce. As S tends toward infinity the relative absorption tends toward $1/(1 + \alpha_{ill}\sqrt{D_a\tau_{bulk}})$ as few carriers still escape from the surface. Figure 4.4 shows that a value of $S \sim< 3ms^{-1}$ is required to obtain efficient induced absorption (0.8 in Figure 4.4) for $\tau_{bulk} = 100\mu s$. As S is reduced further the magnitude of the gradient of the ratio increases, showing a stronger dependence of the ratio on S. To maintain a constant depth of modulation over long periods of time, more time-stable S surfaces are required at low values of S than at high S. Increasing the bulk carrier lifetime increases the dependence of the induced absorption on the surface recombination velocity since the maximum induced absorption is less restricted by the bulk carrier lifetime. This is shown by the greater magnitude of the gradient for $\tau_{bulk} = 1ms$ compared to that for $\tau_{bulk} = 100\mu s$ at fixed S. Consequently, lower values of S are required to optimise the induced absorption when a long bulk carrier lifetime exists. This prediction of the required surface recombination velocity is within experimental possibility; sandblasted surfaces have $S = \sim 100 ms^{-1}$ [30], and chemically etched surfaces have values in the order of cms^{-1}.

4.2.2 Steady state model for a finite sample thickness

The previous section showed that a sufficiently low surface recombination velocity for optimisation of the induced absorption could be achieved. However, S was assumed to act only at the front surface. Although this is where the initial carrier density is highest, long diffusion lengths were seen to give a substantial carrier density a few mm from the front surface (Figure 4.2). Ideally the modulator element should be as thin as possible $(1 - 2mm)$ from the aspects of required space and economics of the costly high purity germanium. However, at this thickness a long bulk carrier lifetime and low front surface recombination velocity gives a significant back-surface carrier density. Back-surface recombination must therefore be accounted for, and a reasonable modulator thickness determined for which its effect is negligible, carriers instead recombining in the bulk. The excitation geometry is shown in Figure 4.5, where S acts at both the front and back surfaces.

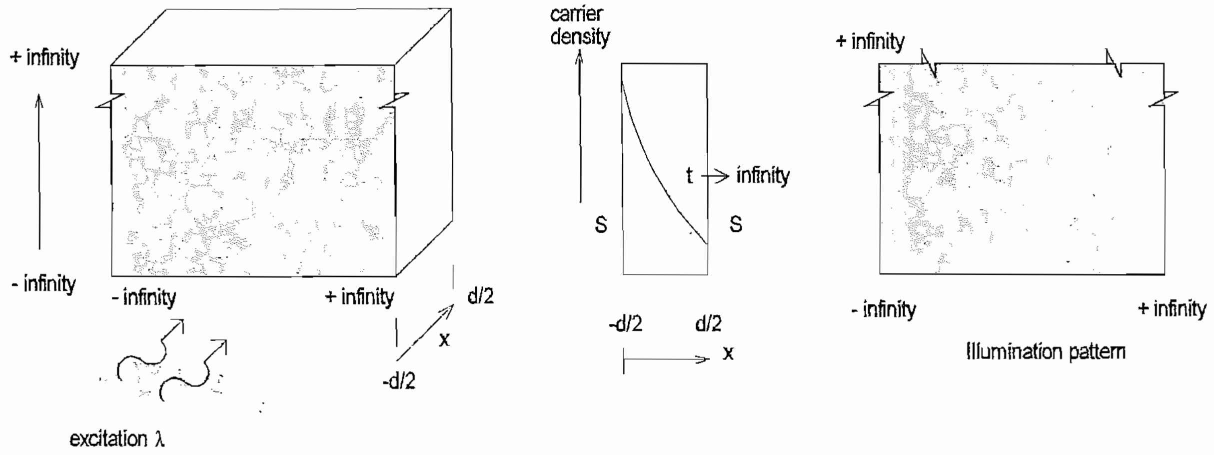

Figure 4.5: Excitation geometry for finite length samples

The boundary conditions for the front and back surfaces now become:

$$D_a \frac{dn}{dx}\bigg|_{x=-\frac{d}{2}} = S \cdot n\left(x = -\frac{d}{2}\right) \tag{4.11}$$

$$D_a \frac{dn}{dx}\bigg|_{x=\frac{d}{2}} = -S \cdot n\left(x = \frac{d}{2}\right) \tag{4.12}$$

The source term must be changed for the new coordinate system to:

$$G_g(x) = N_0 e^{-\alpha_{ill}\cdot\left(x+\frac{d}{2}\right)} \tag{4.13}$$

The steady state solution under these boundary conditions was determined using the complementary function and particular integral, giving:

$$n(x) = \frac{N_0 L_a^2 e^{-\alpha_{ill} d/2}}{D_a(1-\alpha_{ill}^2 L_a^2)} \cdot \left[\frac{a1 \cdot e^{x/L_a} + a2 \cdot e^{-x/L_a}}{[(D_a - SL_a)^2 e^{-d/L_a} - (D_a + SL_a)^2 e^{d/L_a}]} + e^{-\alpha_{ill} x}\right] \tag{4.14}$$

where $a1$ and $a2$ are given respectively by:

$$a1 = L_a \cdot \left[e^{-d(\frac{\alpha_{ill}}{2}-\frac{1}{2L_a})} \cdot [S - D_a\alpha_{ill}][D_a + SL_a] + e^{d(\frac{\alpha_{ill}}{2}-\frac{1}{2L_a})} \cdot [D_a\alpha_{ill} + S][D_a - SL_a]\right] \tag{4.15}$$

$$a2 = L_a \cdot \left[e^{d(\frac{\alpha_{ill}}{2}+\frac{1}{2L_a})} \cdot [S + D_a\alpha_{ill}][D_a + SL_a] + e^{-d(\frac{\alpha_{ill}}{2}+\frac{1}{2L_a})} \cdot [D_a - SL_a][S - \alpha_{ill}D_a]\right] \tag{4.16}$$

This is plotted in Figure 4.6 for a range of S values.

As in Figure 4.3, the carrier density gradient in Figure 4.6 at both front and back surfaces satisfies the surface recombination velocity boundary conditions, although this detail is too small to be shown in the above figure.

Integration of Equation 4.14 gives the area carrier density in the sample. The induced absorption coefficient is proportional to the area carrier density. The effect of back-surface recombination on the area density is now determined, and conditions are imposed on the modulator thickness to make its effect negligible. Figures 4.7 and 4.8 show the area carrier density (cm^{-2}) as a function of S and sample thickness d for $\tau_{bulk} = 100\mu s$ and $1ms$ respectively, for continuous excitation with $1W\ cm^{-2}$ of $980nm$. Note the difference in vertical scales in these figures.

Figure 4.7 shows the area carrier density reducing with increased surface recombination velocity or reduced sample thickness. As sample thickness is reduced, the back

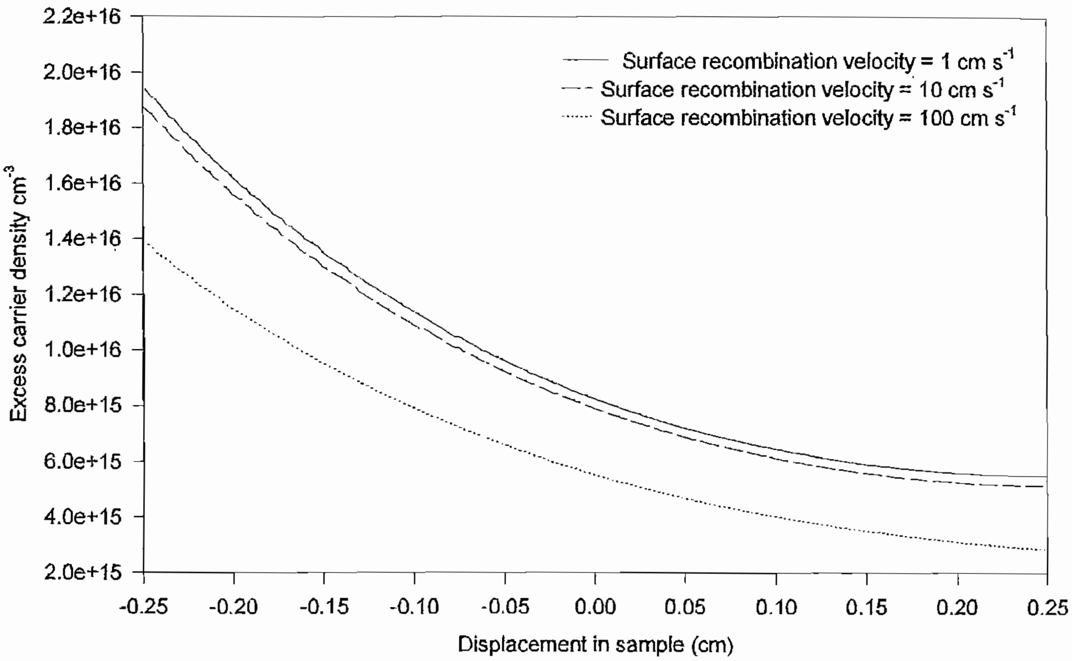

Figure 4.6: Steady state carrier distribution vs displacement in the excited sample for given S at both surfaces; $\tau_{bulk} = 1ms$, absorbed power $= 1W\ cm^{-2}$

surface carrier density and hence effect of back-surface recombination become more significant. For a given S, at sufficient sample thickness the effect of back surface recombination becomes negligible after the start of the plateau along the 'sample thickness' axis. The modulator's thickness should conform to this to improve the system efficiency. A reduced dependence on S is seen (lower gradient of dn_{area}/dS) for thick samples for this reason.

The effect of an increase in bulk carrier lifetime is shown by the higher maximum area carrier density in Figure 4.8. The change in n_{area} with sample thickness is much more gradual, and no definite plateau is reached over the plotted range. Despite the higher area carrier density due to the longer lifetime, Figure 4.8 shows a much stronger dependence on S, for low S, than the previous figure. At these higher carrier densities the effect of S is more significant, following its definition in Equation 3.20. Therefore, optimising the induced absorption in the presence of a long bulk carrier lifetime requires lower values of S than in the presence of low τ_{bulk}. The asymptotes of the area carrier density are given by Equations 4.17 to 4.20.

$$n_{area}\Big|_{d\to 0} = 0 \tag{4.17}$$

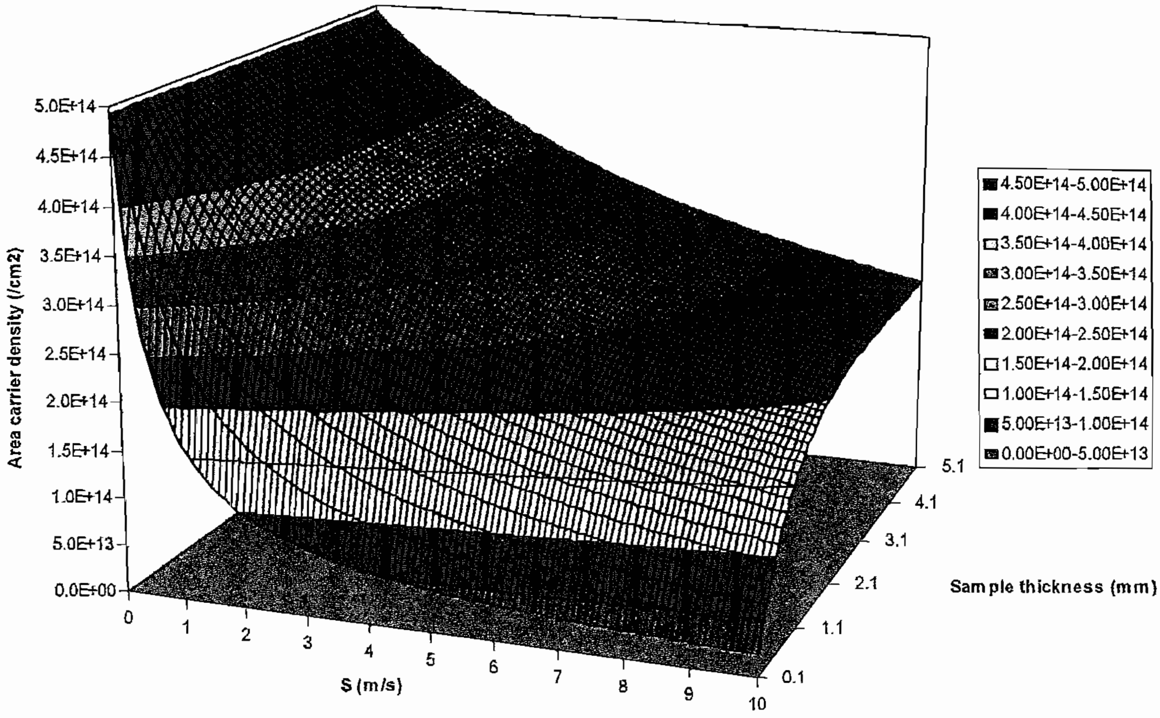

Figure 4.7: Area carrier density in germanium vs S and sample thickness for $\tau_{bulk} = 100\mu s$

$$n_{area}\Big|_{d\to\infty} = \frac{P_{Excabs}\lambda_{exc}\tau_{bulk}}{hc}\cdot\frac{1}{1-\alpha_{ill}^2L_n^2}\cdot\left[1-\frac{\tau_{bulk}\alpha_{ill}(\alpha_{ill}D_a+S)(D_a+SL_n)}{(D_a+S^2\tau_{bulk})+2SL_n}\right] \quad (4.18)$$

$$n_{area}\Big|_{S\to 0} = \frac{P_{Excabs}\lambda_{exc}\tau_{bulk}}{hc}\cdot\left[1-e^{-\alpha_{ill}d}\right] \quad (4.19)$$

$$n_{area}\Big|_{S\to\infty} = \frac{P_{Excabs}\lambda_{exc}\tau_{bulk}}{hc}\cdot\frac{2e^{-\frac{\alpha_{ill}d}{2}}}{1-\alpha_{ill}^2L_n^2}\cdot\left[sinh(\alpha_{ill}d/2)+\frac{\alpha_{ill}L_n cosh(\alpha_{ill}d/2)(1-cosh(d/L_n))}{sinh(d/L_n)}\right] \quad (4.20)$$

The designs used in this work used samples $5mm$ thick since for low τ_{bulk} little was gained in terms of reduced effect of S at the back surface, and for long τ_{bulk} ($1ms$) the slow variation in n_{area} with S required an unreasonable sample thickness of $\sim 10mm$ to significantly increase n_{area}. With typical values of $\tau_{bulk} = 1ms$ and $S = 3ms^{-1}$ an area carrier density of $1.93 \times 10^{15} cm^{-2}$ per $W\ cm^{-2}$ is predicted by Figure 4.8, giving an 'off' state transmission of 35.7%. This is in the order of that reported in the introduction. If surface recombination were zero in the above calculation, an area carrier density of 4.93×10^{15} would be attained, the above calculation being 39.1% of this maximum.

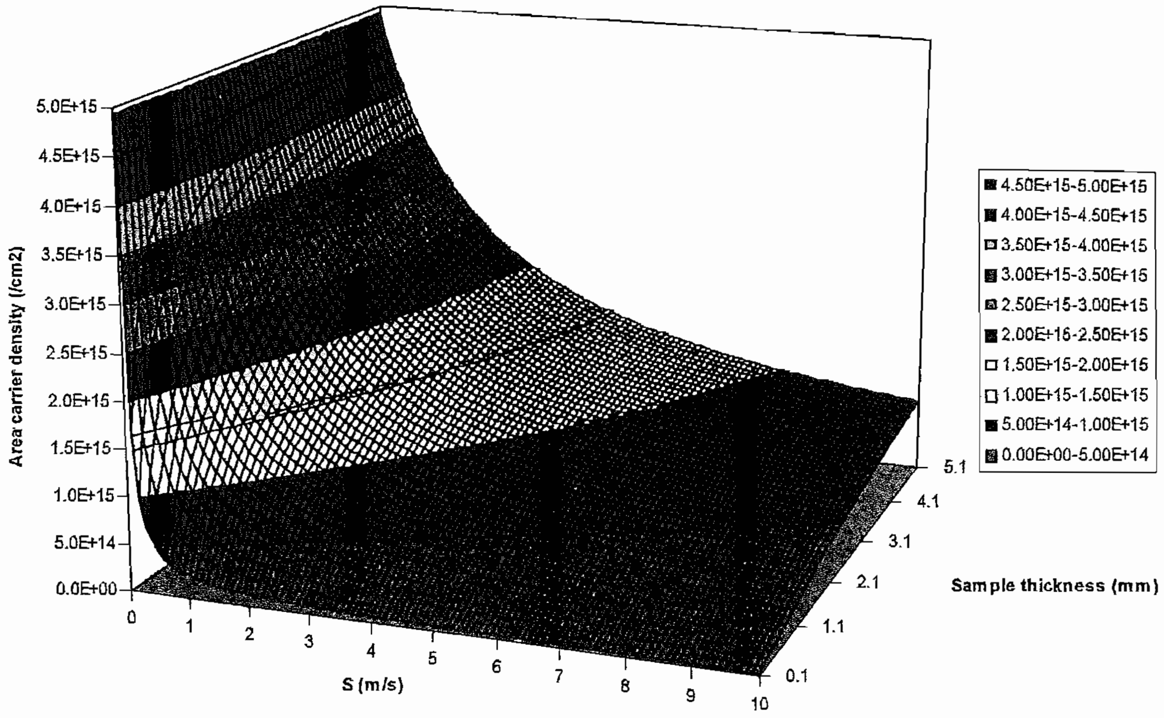

Figure 4.8: Area carrier density in germanium vs S and sample thickness for $\tau_{bulk} = 1ms$

4.3 One dimensional carrier diffusion: Transient excitation

Having modelled the steady state carrier distribution, the dynamic case is now considered. The temporal carrier decay is important in determining the switching speed of the induced absorption, and also in validating the experimental results of Section 5.4. Initially the excitation is assumed (as beforehand) to be uniform and infinite in lateral extent, so that only diffusion in the x-direction need be considered. Later, excitation functions are considered where the power varies spatially on the germanium surface, and diffusion must be considered in two and three spatial directions as a function of time.

4.3.1 Square-pulse excitation

This section solves the continuity equation for the case of a temporally square pulse of infrared excitation. From Equation 4.2 the continuity equation is given by:

$$\frac{\partial n(x,t)}{\partial t} = D_a \frac{\partial^2 n(x,t)}{\partial x^2} - \frac{n(x,t)}{\tau_{bulk}} \tag{4.21}$$

The carrier generation term G_g is no longer in Equation 4.21, and is instead assumed to act as an impulse function which causes an initial condition. Solution of Equation 4.21 gives the impulse response. The response following a temporally square pulse of illumination, as required by the physical situation, is then found by convolving the impulse response with a square pulse function. The generation term therefore becomes:

$$G_i(x,t) = N_0 \cdot \left[e^{-\alpha_{ill}\left(x+\frac{d}{2}\right)}\right]\delta(t) \tag{4.22}$$

and the initial carrier distribution is given by:

$$n(x,t=0) = N_0 \cdot \left[e^{-\alpha_{ill}\left(x+\frac{d}{2}\right)}\right] \tag{4.23}$$

N_0 is given by Equation 4.5 as before, and the boundary conditions for the surface recombination velocity are given by Equations 4.11 and 4.12. Solution of this equation is given by the separation of variables method, for example [99], [100]. See Appendix A for the complete solution. If the solution is assumed to be of the form:

$$n(x,t) = X(x) \cdot T(t) \tag{4.24}$$

then substitution into Equation 4.21 gives:

$$\frac{1}{T}\frac{dT}{dt} + \frac{1}{\tau_{bulk}} = \frac{D}{X}\frac{d^2X}{dx^2} = \psi \tag{4.25}$$

in which ψ must be a constant, giving the following separated differential equations:

$$D\frac{d^2X}{dx^2} - \psi X = 0 \tag{4.26}$$

$$\frac{dT}{dt} = T\left(\frac{1}{\tau_{bulk}} - \psi\right) = 0 \tag{4.27}$$

From Equations 4.26 and 4.27, one such solution is:

$$n(x,t) = e^{-\frac{t}{\tau_{bulk}}} \cdot [Ae^{-D_a\alpha_1^2 t}cos(\alpha_1 x) + Be^{-D_a\beta_1^2 t}sin(\beta_1 x)] \tag{4.28}$$

thus a linear superposition of such solutions satisfies the diffusion equation, and is required to satisfy the boundary conditions. This is given by:

$$n(x,t) = e^{-\frac{t}{\tau_{bulk}}} \sum_n [A_n e^{-D_a\alpha_n^2 t}cos(\alpha_n x) + B_n e^{-D_a\beta_n^2 t}sin(\beta_n x)] \tag{4.29}$$

The separate substitution of the n^{th} sine and cosine terms in Equation 4.11 solves for the α_n and β_n coefficients respectively, given by the periodic series:

$$cot\left(\frac{\alpha_n d}{2}\right) = \frac{D_a \alpha_n}{S} \tag{4.30}$$

$$tan\left(\frac{\beta_n d}{2}\right) = -\frac{D_a \beta_n}{S} \tag{4.31}$$

which also satisfy the second boundary condition, Equation 4.12. The A_n and B_n coefficients are then determined by substitution of the initial condition Equation 4.23 into Equation 4.28, giving:

$$A_n = \frac{2N_0 \alpha_n}{(\alpha_n d + sin(\alpha_n d))(\alpha_{ill}^2 + \alpha_n^2)} \cdot \left[\alpha_{ill} cos\left(\frac{\alpha_n d}{2}\right) \cdot (1 - e^{-\alpha_{ill} d}) + \alpha_n sin\left(\frac{\alpha_n d}{2}\right) \cdot (1 + e^{-\alpha_{ill} d})\right] \tag{4.32}$$

$$B_n = \frac{2N_0 \beta_n}{(\beta_n d - sin(\beta_n d))(\alpha_{ill}^2 + \beta_n^2)} \cdot \left[\beta_n cos\left(\frac{\beta_n d}{2}\right) \cdot (1 - e^{-\alpha_{ill} d}) - \alpha_{ill} sin\left(\frac{\beta_n d}{2}\right) \cdot (1 + e^{-\alpha_{ill} d})\right] \tag{4.33}$$

which, with Equations 4.29, 4.30, and 4.31 give the solution for impulse excitation. The effect of square pulse excitation (or any shape pulse) is given by convolution of the impulse response with the excitation pulse function. For a square pulse of period T, two solutions are given, one for during and one for after the optical pulse, given respectively by:

$$\begin{aligned} n(x,t) = \frac{1}{T}\sum_n \quad & \bigg[\frac{A_n \cdot cos(\alpha_n x)}{(D_a \alpha_n^2 + \frac{1}{\tau_{bulk}})} \cdot \bigg(1 - exp\bigg[-(D_a \alpha_n^2 + \frac{1}{\tau_{bulk}})t\bigg]\bigg) + \\ & \frac{B_n \cdot sin(\beta_n x)}{(D_a \beta_n^2 + \frac{1}{\tau_{bulk}})} \cdot \bigg(1 - exp\bigg[-(D_a \beta_n^2 + \frac{1}{\tau_{bulk}})t)\bigg]\bigg)\bigg] \end{aligned} \tag{4.34}$$

$$\begin{aligned} n(x,t) = \frac{1}{T}\sum_n \quad & \left[\frac{A_n \cdot cos(\alpha_n x)}{(D_a \alpha_n^2 + \frac{1}{\tau_{bulk}})} \cdot \left[exp\left(-\left[D_a \alpha_n^2 + \frac{1}{\tau_{bulk}}\right]t\right)\right]\left[exp\left[D_a \alpha_n^2 + \frac{1}{\tau_{bulk}}\right]T - 1\right] + \right. \\ & \left. \frac{B_n \cdot sin(\beta_n x)}{(D_a \beta_n^2 + \frac{1}{\tau_{bulk}})} \cdot \left[exp\left(-\left[D_a \beta_n^2 + \frac{1}{\tau_{bulk}}\right]t\right)\right]\left[exp\left[D_a \beta_n^2 + \frac{1}{\tau_{bulk}}\right]T - 1\right]\right] \end{aligned} \tag{4.35}$$

and N_0 is now given by:

$$N_0 = \frac{\alpha_{ill} P_{Excabs} \lambda_{exc} T}{hc} \tag{4.36}$$

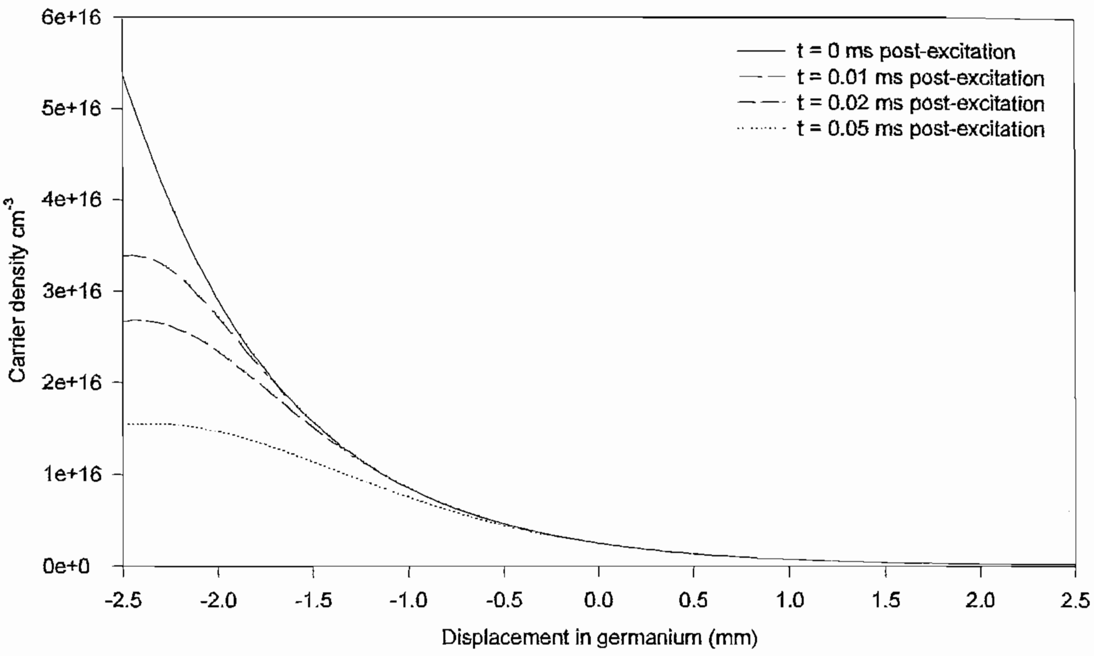

Figure 4.9: Carrier decay vs displacement in sample for $\tau_{bulk} = 1ms$ and $S = 1ms^{-1}$ following square pulse excitation with period $T = 1.0ms$

Carrier decay is of particular interest in this application in determining the recovery time of the induced absorption, given by the effective carrier lifetime. This is shown for the decay period ($t \geq T$) in Figure 4.9

The effect of a finite surface recombination velocity in the above simulation is more apparent over the plotted displacement range for $t > T$ than in Figure 4.6 as here the generation term is removed. The spatial carrier distribution in this figure is strongly dependent on the τ_{bulk} and S parameters, and this will be shown in Section 4.3.2 to affect the microwave reflectivity measurements.

The absorption seen along the x-direction during carrier decay is obtained by integrating the carrier volume density (Equation 4.35 over the range $-d/2 \leq x \leq d/2$ and determining the area carrier density. Only the cosine x terms need be integrated due to symmetry, giving:

$$n_{area}(t) = \frac{2}{T} \cdot \sum_{n} \frac{A_n sin\left(\frac{\alpha_n d}{2}\right)}{\alpha_n \left(D_a \alpha_n^2 + \frac{1}{\tau_{bulk}}\right)} \cdot \left[e^{\left(D_a \alpha_n^2 + \frac{1}{\tau_{bulk}}\right)T} - 1\right] \cdot e^{-\left(D_a \alpha_n^2 + \frac{1}{\tau_{bulk}}\right)t} \qquad (4.37)$$

The transmission of a probe beam at $10.6\mu m$ in a test sample that is not AR coated must account for multiple reflections, and is given by Equation 3.36, with $\alpha d = n_{area}\sigma_h$ and $r = 0.36$. The modulator element in a real device the would however be AR coated, giving $r = 0$. The predicted transmission of a test sample during carrier decay is plotted in Figure 4.10 for two values of surface recombination velocity. Also plotted in Figure 4.10 is the product of area carrier density and hole absorption cross section, $n_{area} \cdot \sigma_h$. If carriers are assumed to decay with a lifetime $\tau_{effective}$ (Equation 3.2), the decay of the area carrier density is given by Equation 4.39. $-t/\tau_{effective}$, given by $ln(n_{area} \cdot \sigma_h)$ is also plotted in Figure 4.10, the slope of which gives the net carrier decay constant $-1/\tau_{effective}$.

$$T = \frac{(1-r)^2 \cdot e^{-n_{area} \cdot \sigma_h}}{1 - r^2 \cdot e^{-2 \cdot n_{area} \cdot \sigma_h}} \tag{4.38}$$

$$n(t) = n_0 e^{-\frac{t}{\tau_{effective}}} \tag{4.39}$$

Figure 4.10 shows that for low S, and a long bulk carrier lifetime, surface recombination is negligible and the decay constant is constant with time. Higher values of S which give a comparable recombination rates to that in the bulk, give a time-dependent decay constant

Figure 4.10 gives the transmission at a fixed wavelength. The effects of surface and bulk recombination are combined into an 'effective' lifetime as discussed in Chapter 3. Initially the carrier decay is fast since most carriers are generated within an absorption depth ($\sim 1\mu m$) of the surface, and are affected by the surface recombination velocity. Later the carrier distribution reaches a stable shape and the decay constant becomes constant with time. This is seen by the initial steep gradient of the $-t/\tau_{effective}$ curve above, which is steeper for the higher S curve. Subsequently, both curves reduce to a constant decay lifetime once the carrier distributions have reached stable shapes.

The limiting value of the decay constant for large time is affected by the surface recombination velocity and is not purely the bulk lifetime. Inspection of the area carrier density in Equation 4.37 shows that the decay constant is a combination of n decay constants of the form τ'_n :

$$\frac{1}{\tau'_n} = \frac{1}{\tau_{bulk}} + D_a \alpha_n^2 \tag{4.40}$$

This is analogous to Equation 3.2, where the effect of surface recombination is to give an apparent surface lifetime, represented by $\tau_{surface} = 1/D_a\alpha_n^2$. The α_n solutions increase with n, contributing less and less to the surface lifetime with increasing n due

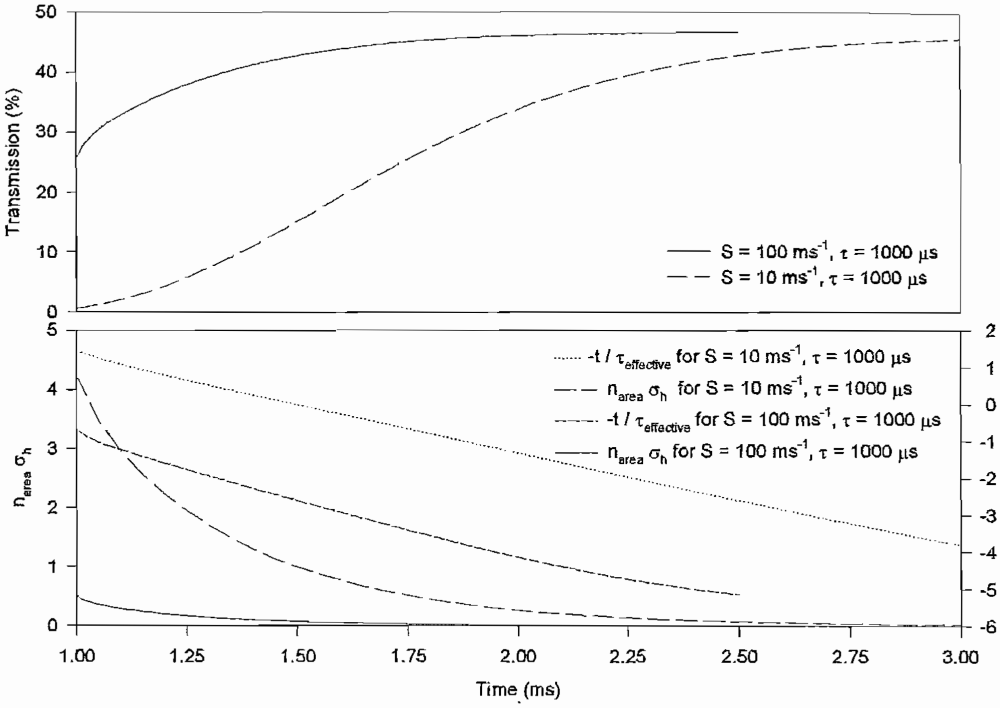

Figure 4.10: Transmission and absorption at $10.6\mu m$ following carrier decay from $1W\ cm^{-2}$ absorbed pulse at $980nm$

to its square dependence. The exponential form of this sum can be shown to depend on approximately 100 terms of α_n for $t << T$, and for $t >\sim 1/D_a\alpha_1^2$ the decay constant depends, to a good approximation on the first term, α_1 only. The poor convergence is a characteristic of the Fourier series solution close to a discontinuity in the first derivative of $n(t)$. The implication for this on the decay is that for $t >\sim 1/D_a\alpha_1^2$ the decay constant is given to a good approximation by:

$$\frac{1}{\tau_{effective}} = \frac{1}{\tau_{bulk}} + D_a\alpha_1^2 \tag{4.41}$$

This latter period of the decay has a fixed time constant, in contrast with the initial decay period when the high initial surface carrier density decays rapidly and the time constant is time-dependent. This explains the shape of the graphs above, for which the effective lifetimes are $376\mu s$ and $287\mu s$ for low and high S respectively. This principle of an effective carrier lifetime at the start of the decay and for $t >> T$ is used in Section 5.1 to validate the carrier distribution model. Although neither the initial or final decay constants are unique functions of S and τ_{bulk}, both decay constants have a different dependence on these parameters which are used graphically to solve for these parameters in Section 5.2.1.

4.3.2 Separation of bulk and surface effects: microwave reflectance

The model in the previous section detailed the effective lifetime observed via the transmission of an excited sample at $10\mu m$. The effective lifetime combines surface and bulk effects which are not readily separated at this wavelength. One method of separating these effects is through surface treatment to induce high and low surface recombination at either surface. By solving the differential equations with respective boundary conditions for each condition, experimental measurements of the $10\mu m$ sample transmission can be used to fit the S and τ_{bulk} parameters in this model. This method is both destructive and time-consuming. A more suitable method is to use a longer (microwave) wavelength and monitor the microwave reflectance which depends on the *distributed* carrier density throughout the sample. At longer wavelength there is a slower phase variation with displacement. The total power reflected by the sample depends on the combined reflectance from the front and back surfaces, and the relative phase of these components. The slower phase variation with displacement means that interference effects are resolved. Monitoring the reflectance therefore gives information on the spatial evolution of the profile over time. The experiment used to achieve this is detailed in Chapter 5; at this stage only the model predicting the microwave reflectance is given.

The microwave reflectance model uses the spatial and temporal carrier distribution following square pulse excitation with one-dimensional diffusion that was developed in Section 4.3.1, to determine the temporal dependence of the microwave reflectance resulting from carrier decay.

The refractive index is defined as the square root of the dielectric constant. The dielectric constant has a significant imaginary part at moderate excess carrier densities, giving an imaginary part in the refractive index which determines the absorption. This microwave absorption is hereafter termed attenuation to distinguish it from the modulator's absorption in the $10\mu m$ region. Free carrier absorption increases the imaginary part of the dielectric constant and its effect in the infrared was discussed in Chapter 2 as being minimal at $10\mu m$ at the carrier densities involved in this work. At microwave wavelengths the λ^2 dependence of free carrier absorption gives much higher attenuation. Optical excitation is used to modulate the carrier density, the spatial distribution of which is temporally monitored through concurrent measurement of the microwave reflectance using a microwave probe beam. Information on the spatial distribution of the resulting electron-hole plasma is then used to validate the one-dimensional carrier diffusion model.

The excess carrier densities involved in the excitation of the modulator cause a shift in the plasma frequency. This is the optical frequency below which the refractive index becomes imaginary. Well above the plasma frequency (short wavelength) the semiconductor is transparent and below the plasma frequency the semiconductor is highly reflecting. Optical excitation of the germanium increases the carrier density and moves the plasma frequency to shorter wavelength where the reflectance subsequently increases. At a frequency just above the plasma frequency the plasma 'dip' occurs. At the plasma dip the imaginary part of the refractive index makes the germanium strongly attenuating, and the reflectance drops below that of unexcited germanium. As the carrier density is increased, the plasma frequency increases and the attenuation at the plasma dip intensifies. Depending on the location of the plasma frequency with respect to the microwave probe frequency, the reflectance will change from its unexcited-state value as the carrier density in a sample is increased by optical excitation.

The dielectric constant $\epsilon(\omega)$ is given [101] by the sum of the susceptibility contributions due to lattice vibrations, $\chi_{pm}(\omega)$, free carriers, $\chi_{fc}(\omega)$, and bound valence electrons $\chi_{ve}(\omega)$:

$$\epsilon(\omega) = 1 + \chi_{ve}(\omega) + \chi_{fc}(\omega) + \chi_{pm}(\omega) \tag{4.42}$$

In the infrared the contribution of valence electrons is approximately real and frequency-independent, hence:

$$1 + \chi_{ve} = \epsilon_{\infty} \tag{4.43}$$

$$\epsilon(\omega) = \epsilon_{\infty} + \chi_{fc}(\omega) + \chi_{pm}(\omega) \tag{4.44}$$

In Equation 4.44 the first and last terms are indistinguishable during optical or microwave determination of the dielectric constant, which is that quoted for unexcited material in Palik [97] (16.0 at $10.0\mu m$), for example. Equation 4.44 can therefore be written as:

$$\epsilon(\omega) = \epsilon_{Palik} + \chi_{fc}(\omega) \tag{4.45}$$

When free carriers are introduced, then, for holes,

$$\chi_{fc}(\omega) = -\frac{{\omega_p}^2}{\omega^2 + {\omega_\tau}^2} + \frac{j{\omega_p}^2\omega_\tau}{\omega(\omega^2 + {\omega_\tau}^2)} \tag{4.46}$$

where the plasma frequency and scattering frequency are given respectively by:

$$\omega_p = \sqrt{\frac{nq^2}{\epsilon m^*}} \tag{4.47}$$

$$\omega_\tau = \frac{q}{m^* \mu} \tag{4.48}$$

μ is the carrier mobility, assumed constant over the excess carrier density range encountered, following mobility arguments in Chapter 3, and m^* is the effective mass. A similar expression exists for electrons, giving the refractive index as a function of microwave probe frequency ω as:

$$\eta(\omega) = \sqrt{\epsilon_{Palik} - \frac{{\omega_{pp}}^2}{\omega^2 + {\omega_{\tau p}}^2} + j\frac{{\omega_{pp}}^2 \omega_{\tau p}}{\omega(\omega^2 + {\omega_{\tau p}}^2)} - \frac{{\omega_{pe}}^2}{\omega^2 + {\omega_{\tau e}}^2} + j\frac{{\omega_{pe}}^2 \omega_{\tau e}}{\omega(\omega^2 + {\omega_{\tau e}}^2)}} \tag{4.49}$$

where subscripts p and e refer to holes and electrons respectively. To predict the sample reflectance it is divided into a number of layers of equal thickness perpendicular to the microwave probe beam. The layer thickness is sufficiently thin for the carrier density in each layer to be treated as a constant. The average refractive index in each of these layers is computed as a function of time using Equation 4.49 and the average carrier density determined by integration of Equation 4.35 over the appropriate range. The layers are then treated as layers of a multilayer mirror, each with a time-dependent refractive index, and the total reflectance as a function of time is determined using the same technique as for a multilayer dielectric mirror [101] except with a complex layer refractive index.

The technique involves separation of the sample into n layers of equal thickness. Each layer is represented by a 2 × 2 characteristic matrix which relates the electric field in the x and y planes to an arbitrary z plane. The matrix configuration used solves the wave equation subject to the boundary conditions for each layer. The matrix for an entire stack of such layers is given by the product of all the characteristic matrices in the stack. Elements are then extracted from the stack matrix and used to determine the transmission or reflectivity of the entire stack. The characteristic equation for layer r of thickness h_r is given by M_r:

$$M_r = \begin{bmatrix} cos\beta_r & -\frac{j}{p_r} sin\beta_r \\ -jp_r sin\beta_r & cos\beta_r \end{bmatrix} \tag{4.50}$$

$$\beta_r = \frac{2\pi}{\lambda_0} \eta_r h_r cos\theta_r \tag{4.51}$$

$$p_r = \eta_r cos\theta_r \tag{4.52}$$

where λ_0 is free-space microwave wavelength, η is the refractive index, h is the layer thickness and θ is the incidence angle of the layer. The model used here requires normal incidence alone, thus $\theta = 0$. Multiplication of the individual layer matrices gives the stack matrix as:

$$M = \prod_r M_r = \begin{bmatrix} m_{11} & m_{12} \\ m_{21} & m_{22} \end{bmatrix} \tag{4.53}$$

The power reflection coefficient is then given by:

$$R = |r|^2 = \left| \frac{(m_{11} + m_{12}p_{back})p_{front} - (m_{21} + m_{22}p_{back})}{(m_{11} + m_{12}p_{back})p_{front} + (m_{21} + m_{22}p_{back})} \right|^2 \tag{4.54}$$

where front and back refer to the above parameters for incident and exit medium, in this case, air. The spectral dependence of the power reflectance resulting from a range of uniform excess carrier densities in a $5mm$ germanium sample is shown in Figure 4.11.

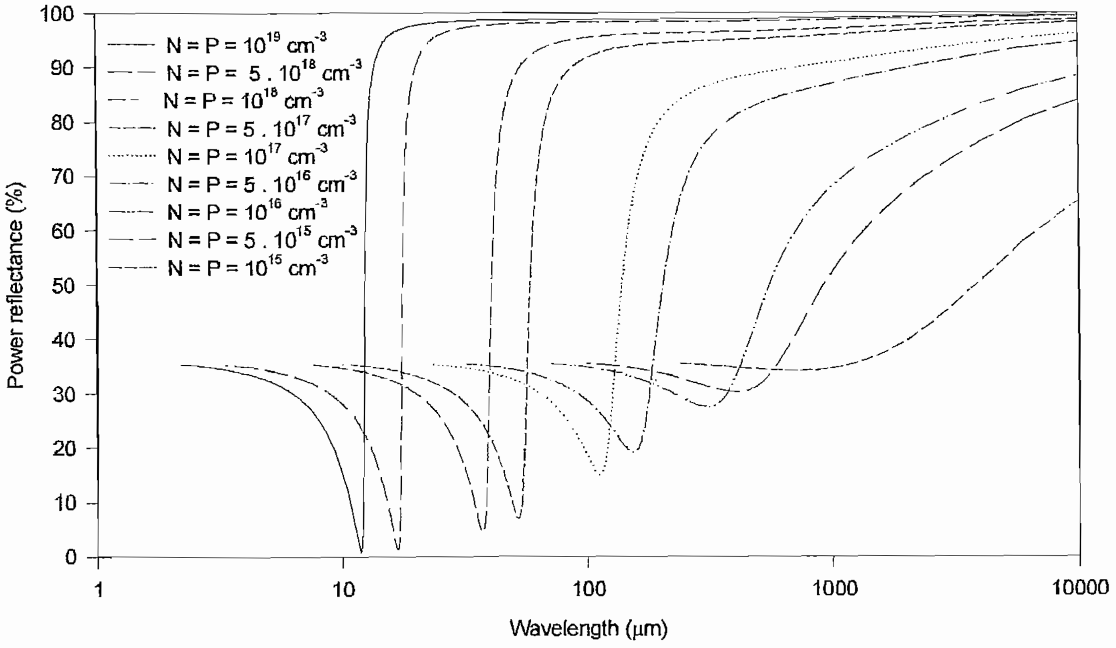

Figure 4.11: Predicted microwave reflection coefficient in intrinsic germanium vs wavelength for a range of uniform excess carrier densities in s semi-infinite sample

Figure 4.11 shows the reflectance vs wavelength for a uniform excess carrier density in a semi-infinite germanium sample. The average reflectance at the short wavelength limit asymptotes to 36.8%, where the sample is transmitting, and at the long wavelength limit the 'metallic' reflectivity tends toward unity. Between these limits the reflectance drops below the short wavelength asymptote. The minimum occurs close to the plasma frequency, at a free space wavelength $2\pi c/\omega_p$ (Equation 4.47). At the (resonant) plasma frequency the amplitude of electron oscillations about their mean position in the plasma is large. Much work is done through damping as the electron traverses the electric field and hence the absorption is high. In the limit $\omega >> \omega_p$ the electron-hole plasma cannot keep up with the oscillating incident field. The amplitude of oscillations and hence absorption due to damping is low and the germanium transmission is high. In the limit $\omega << \omega_p$ the transmitted wave becomes evanescent and the reflectivity increases. The free space wavelength corresponding to the plasma dip is shown as a function of excess carrier density in Figure 4.12.

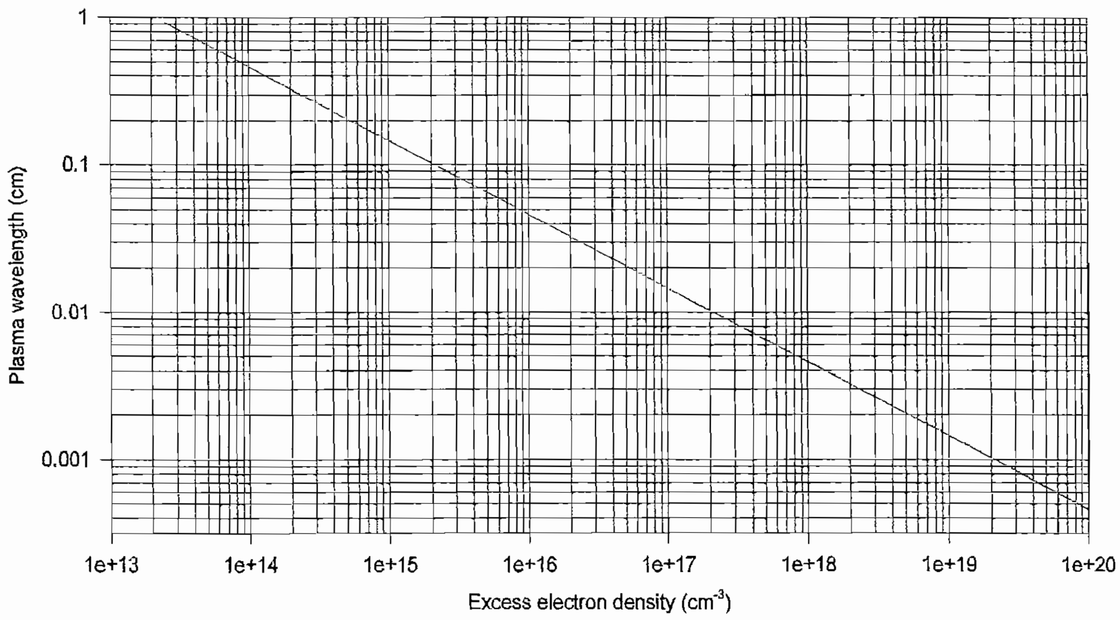

Figure 4.12: Free space wavelength corresponding to the plasma dip as a function of uniform excess doping density

Figure 4.12 shows the high carrier density required to shift the plasma frequency to the $10\mu m$ region, justifying the statement in the introduction that modulation in the infrared using plasma switching in germanium in a low power device would restrict operation to low repetition rates. The total carrier density in germanium at which the plasma frequency occurs at $10GHz$ ($3cm$), where microwave probe equipment is readily available, is $2.4 \times 10^{12} cm^{-3}$, an order of magnitude below the intrinsic carrier density at $300°K$. Higher carrier densities reduce the plasma wavelength, so the plasma wavelength will not pass through this probe wavelength when germanium is optically excited. Additionally, the plasma dip occurs at slightly shorter wavelength than the plasma wavelength. From this aspect the reflectance of optically excited germanium, monitored by a $3cm$ probe wavelength, should therefore only increase with increasing carrier density. However, Figure 4.11 was plotted for a semi-infinite sample. In a sample of finite thickness, interference fringes due to reflections from the back germanium-air interface are important when low absorption exists in the germanium, and depending on the sample thickness these decrease or increase the reflectivity from its unexcited-state value.

Figure 4.13 shows the reflectivity of a $5mm$ sample with a uniform excess carrier density of $10^{17} cm^{-3}$, showing the envelope of the rapidly spectrally-varying interference fringe pattern. At lower excess carrier densities the plasma frequency and interference fringe envelope move toward longer wavelength. Although the effect of the plasma frequency was described above as unimportant at the $3cm$ probe wavelength, the interference fringes are significant at $3cm$ wavelength. The interference fringes are now discussed, being of crucial importance at $3cm$ wavelength in germanium where they produce a very similar change in reflectivity to that previously described as being due to the plasma dip. During this discussion the reflectivity vs wavelength for a $5mm$ germanium sample is given for an excess carrier density of $10^{17} cm^{-3}$ in Figure 4.13. This figure is subdivided into regions A to E. Toward shorter wavelength the reflectivity limits of the densely-packed fringe envelope are represented by the split lines. Later, the effects of changing the uniform excess carrier density and the sample thickness are discussed. These assist understanding the microwave reflectivity results and the subsequent extraction of carrier parameters in Section 5.4.

Region A

In the short wavelength region of Figure 4.13 the sample has a low attenuation. This region is well above the plasma frequency, and so the absorption is insignificant. Reflections from the back germanium-air interface cause fringes in the net reflectance. The fringe spacing depends on the sample phase thickness. For the carrier density plotted, these are only resolved experimentally if extremely narrow spectral bandwidths are used.

Region B

Toward slightly longer wavelength the attenuation in the sample due to the finite imaginary part of the refractive index reduces the back-reflection intensity from the back

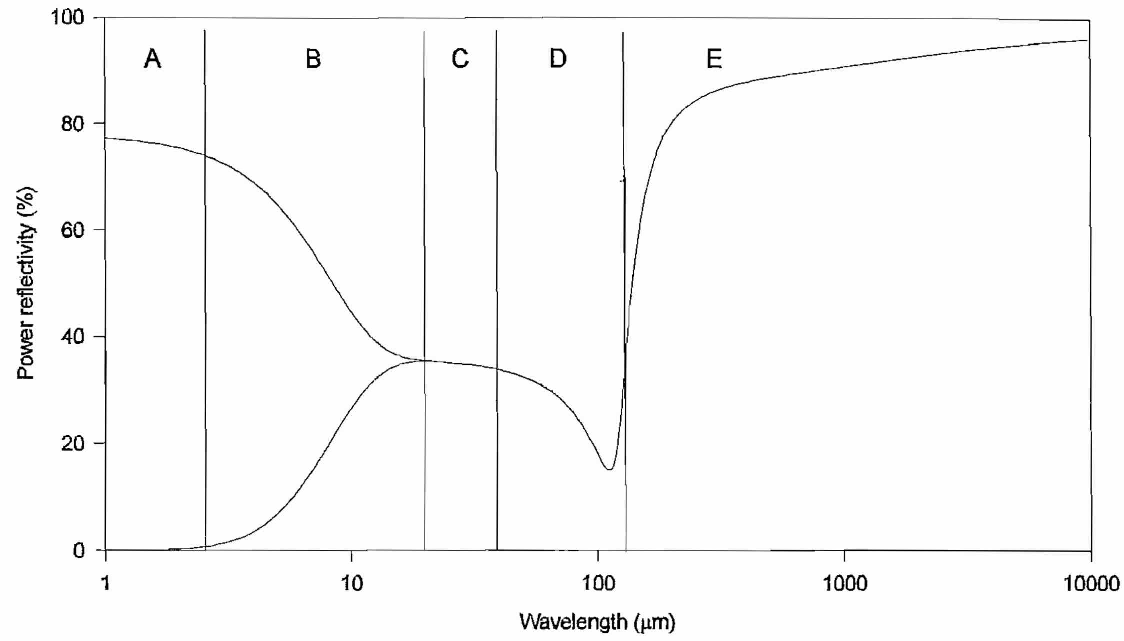

Figure 4.13: Microwave reflectivity vs wavelength for a $5mm$ germanium sample with a uniform excess carrier density of $10^{17}cm^{-3}$

germanium-air interface. The fringe amplitude (originating in region A) therefore reduces. At the long wavelength limit of region B the fringe amplitude asymptotes toward zero as the reflectivity is determined by the (complex) refractive index, and the attenuation in this $5mm$ sample is sufficiently high that negligible reflection occurs from the back germanium-air interface.

Region C

Within region C the reflectivity shows no fringes as the intensity of back-reflection from the back germanium-air interface is negligible. The reflectivity is practically constant with wavelength as the effect of the (broad) plasma dip causes little increase in attenuation within this region. Since the reflectivity from the back surface is negligible, the power reflectivity [101] R (Equation 4.55) is given by that of a single interface with the germanium having a complex refractive index $n_c = n_{ge} - ik$ as:

$$R = \frac{n^2 \cdot \left(1 + (\frac{k}{n})^2\right) + 1 - 2n}{n^2 \cdot \left(1 + (\frac{k}{n})^2\right) + 1 + 2n} \tag{4.55}$$

For example at $35\mu m$ an excess carrier density of $10^{17}cm^{-3}$ gives a refractive index of

$3.834+0.011i$. The absorption coefficient ($4\pi k/\lambda$) here is $39.49 cm^{-1}$. The imaginary part is sufficiently high that the back reflection from a $5mm$ germanium sample is negligible, Equation 4.55 can therefore be used accurately, giving a reflectivity of 34.38%. This is also predicted by Equation 4.54 and seen at this carrier density in Figure 4.13.

Region D

Within this region the attenuation due to the plasma dip considerably reduces the reflectivity. The plasma dip occurs at slightly higher frequency than the plasma frequency. Toward the longer wavelength limit of this region the reflectivity increases more sharply. As the frequency moves away from resonance the amplitude of plasma oscillations reduces, hence the energy lost through damped oscillations falls, as does the plasma dip absorption. The reflectivity subsequently rises.

Region E

The reflectivity increases steadily within the short wavelength section of this region. At these sub-plasma-resonance frequencies the absorption reduces and the transmitted wave becomes evanescent and the plasma cannot absorb energy from the slowly-oscillating field; the reflectivity therefore increases.

The above discussion was for a moderate excess carrier density with the plasma wavelength close to $100\mu m$. As the excess carrier density is reduced the plasma wavelength moves toward longer wavelengths. This is shown in Figure 4.14.

Figure 4.14 shows that in addition to the movement of the plasma wavelength toward longer wavelengths and changes to the plasma dip, fringes extend toward longer wavelengths as the excess carrier density is reduced. At lower excess carrier densities the attenuation due to free carrier absorption only becomes significant at longer wavelengths. In the case of intrinsic germanium with zero excess carrier density, the reflectivity fringes in a $5mm$ sample extend to just beyond the $3cm$ probe wavelength. Thus when monitoring the microwave reflectivity of an optically-excited sample of $\sim 5mm$ thickness, the sample reflectivity is dependent on the excitation level, since this determines the contribution from the reflection by the back germanium-air interface. The unexcited-state (intrinsic) reflectivity is dependent on sample thickness. As the excess carrier density is increased the reflectivity contribution from the back surface reduces, and, depending on the relative phase of this contribution (which depends on sample thickness and refractive index through the excess carrier density), the reflectivity will increase or decrease from its intrinsic value. The reflectivity fringes at the experiment's $3cm$ probe wavelength are now considered as a function of sample thickness and uniform excess carrier density. This is shown (from Equation 4.54) in Figure 4.15.

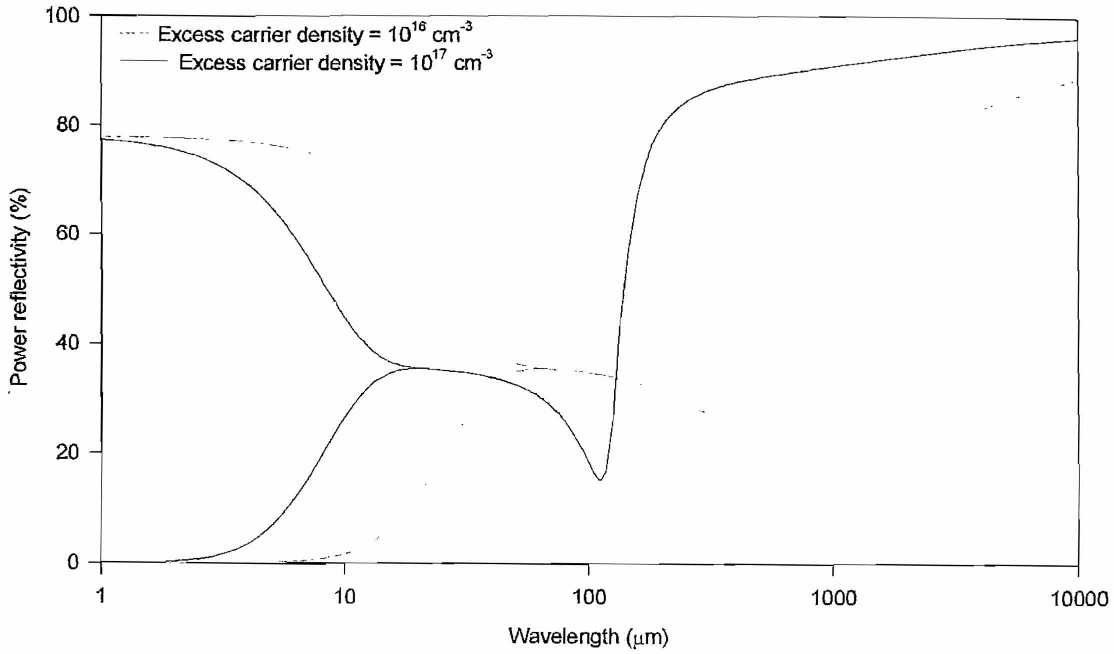

Figure 4.14: Reflectivity vs wavelength for two levels of excess carrier density showing onset of fringe envelope

Figure 4.15 for intrinsic germanium shows that increasing the sample thickness reduces the amplitude of the reflectivity fringes since the back surface contribution to reflectivity reduces. At sufficient thickness ($>\sim 30mm$) the reflectivity is determined only by the front surface. For intrinsic germanium the refractive index of $n_c = 4.022 + 0.498i$ at $\lambda_0 = 3cm$ gives a front surface reflectivity of 36.83%. For sample thicknesses less than $\sim 10mm$, where significant fringes exist for intrinsic material in Figure 4.15, a small increase in excess carrier density reduces the fringe amplitude whilst the mean reflectivity (that for large sample thickness) of the fringe increases little. For example this occurs with an excess carrier density of $2.4 \times 10^{13} cm^{-3}$. For sample thicknesses whose intrinsic reflectivity is greater than that for large thickness, a small increase in excess carrier density reduces the reflectivity, after which the reflectivity increases. This initial decrease and then increase with excess carrier density, characteristic of sample thicknesses in the $5 - 6mm$ region in particular, is used in experiments in Chapter 5 to extract the bulk carrier lifetime and surface recombination velocity parameters from microwave reflectivity measurements.

These experiments monitor the reflectivity at $3cm$ wavelength of an optically excited sample. This gives information on the progress of the excited carrier plasma in the ger-

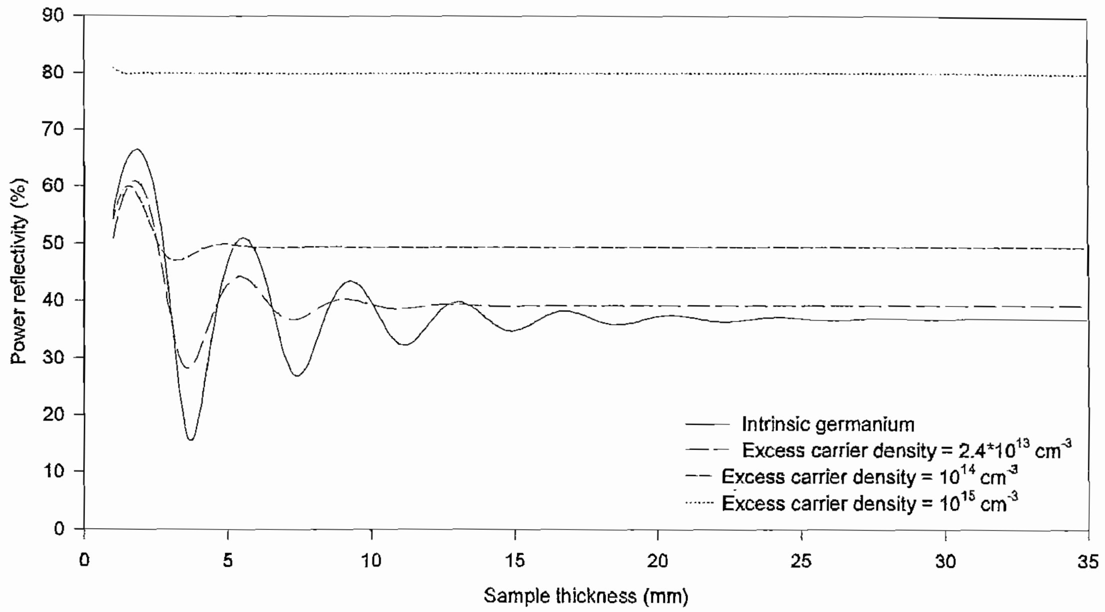

Figure 4.15: Reflectivity at $3cm$ wavelength in intrinsic germanium as a function of sample thickness for various uniform excess carrier densities

manium that is predicted by the diffusion model in the previous section. Thus the two models are used in combination to validate the experiment and iteratively fit the surface recombination velocity and bulk carrier lifetime parameters in the model. The initially high reflectivity of an excited sample reduces as carriers in the 'metallic' germanium decay. Once the sample's bulk absorption is sufficiently low that the contribution to reflectivity from the back surface becomes significant, the phase of this reflected component serves initially to reduce the reflectivity from that of the unexcited sample. The reflectivity then increases to that of unexcited germanium as the attenuation of this back reflection falls toward zero. For sample thicknesses not covered by the $5-6mm$ thickness requirement, the reflectivity only increases with increasing excess carrier density. The effect of the plasma dip, which produces an effect almost identical to that described above, for the same $5-6mm$ sample thickness range is therefore unimportant in the measurements at $3cm$ wavelengths, although its understanding is essential in distinguishing the two effects.

Measurements of the microwave reflectivity at $3cm$ wavelength are fitted in Section 5.4 to simulations of the microwave reflectivity during carrier decay in an excited sample. A simulation of the reflectivity for a range of S and τ_{bulk} parameters in an excited intrinsic germanium sample is given during carrier decay in Figure 4.16.

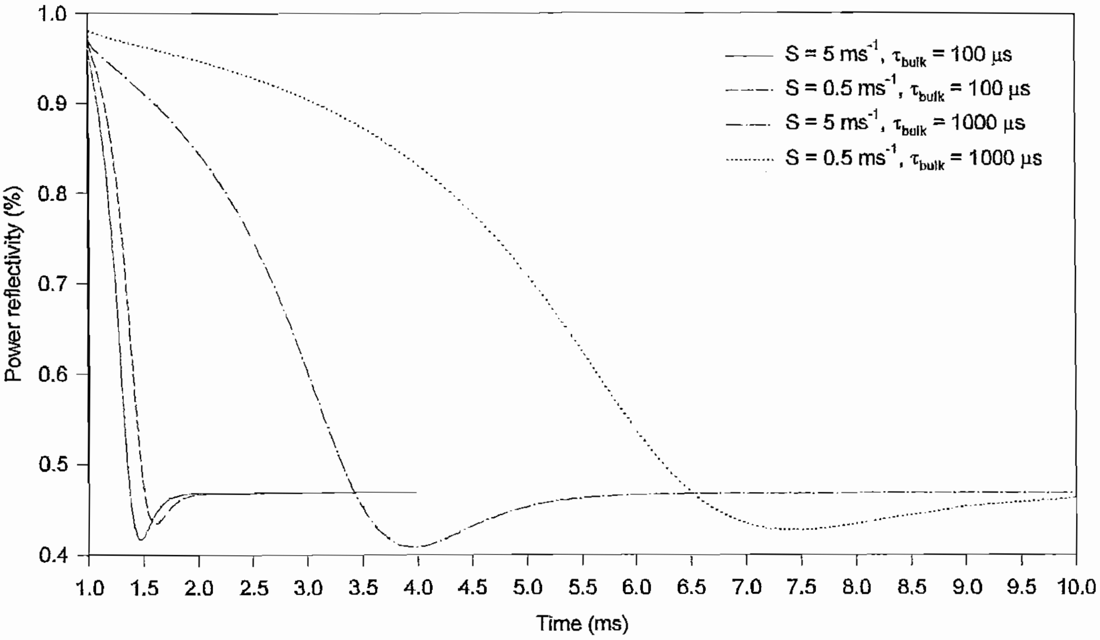

Figure 4.16: Microwave reflectance at $10.0GHz$ during carrier decay in $5mm$ germanium sample following $10W\ cm^{-2}$ absorbed optical power from $1ms$ pulse at $980nm$

Figure 4.16 shows the reflectivity at $10.0GHz$ ($3cm$ wavelength) for this $5mm$ germanium sample. The reflectivity dip should not be confused with the plasma dip detailed earlier in this section and seen in Figure 4.11, which occurs at shorter microwave probe wavelengths, but which here is due to interference fringes. The superficial similarity between the plasma dip and that observed here should be noted however. The reflectivity in the unexcited state (at large time when all carriers have decayed) is 46.8%, following Figure 4.15. The temporal position of the 'dip' defines a characteristic sample absorption, which is characterised by a carrier concentration and distribution. This signature enables use of such simulations in Chapter 5 in the validation of the carrier decay model by separating the surface and bulk effects.

The short-wavelength asymptote of the reflectivity is now considered for completeness. In Figure 4.14 the average fringe reflectivity appears to be that of the region between the long wavelength limit of the fringes and the plasma dip. This is not the case. In the limit of λ_0 tends toward zero, the refractive index of unexcited germanium (Equation 4.49) tends toward $\sqrt{\epsilon_{Palik}} = 4.0$. This is expected if dispersion is ignored. The refractive index of unexcited intrinsic germanium is real and equal to 4.0

at $\lambda_0 = 10\mu m$, as predicted by Equation 4.49. Since the loss is negligible at $10\mu m$, the average power reflectivity predicted by Equation 4.54 should be the same as the Fresnel reflectivity accounting for multiple reflections, given by:

$$R = r + \frac{r(1-r)^2 e^{-\alpha d}}{1 - r^2 e^{-2\alpha d}} \tag{4.56}$$

Equation 4.56 gives the *average* reflectivity over a fringe as it ignores the phase term in the solution to the wave equations. $r = 0.36$ per surface for $n = 4.0$. Hence if the absorption is negligible, $\alpha d = 0$ and the power reflectivity is:

$$R = r + \frac{r(1-r)^2}{1 - r^2} = 52.9\% \tag{4.57}$$

The average reflectivity predicted by Equation 4.57 is that averaged over the fringe in this spectral region. Figure 4.17 shows the fringes from a $5mm$ sample resulting from a real refractive index of 4.0, over a reduced spectral range close to $10\mu m$.

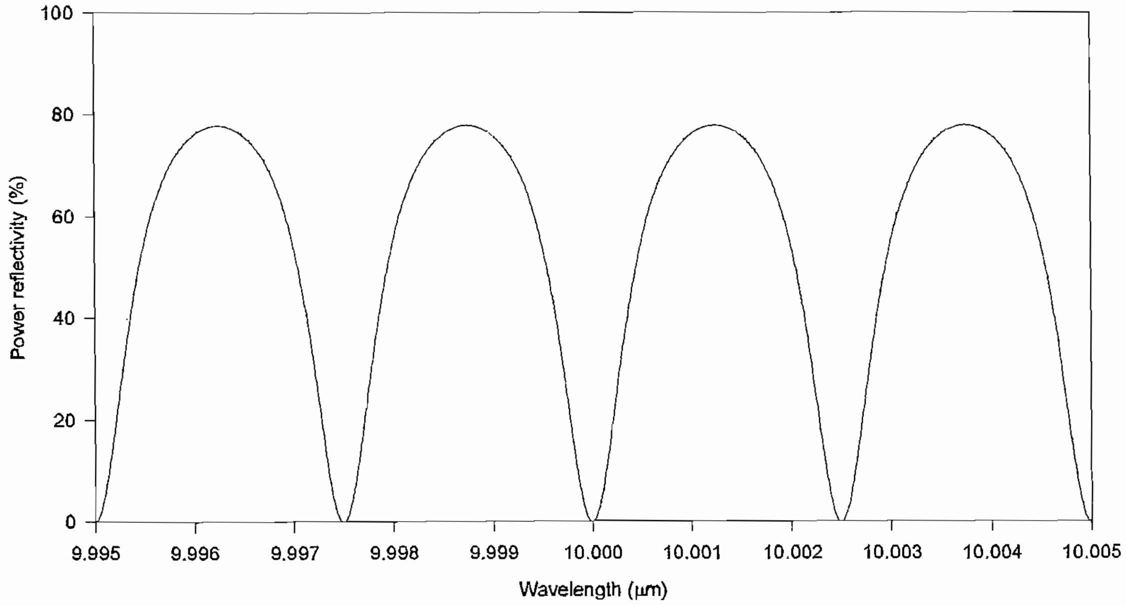

Figure 4.17: Resolved fringe pattern close to $10\mu m$ in $5mm$ germanium sample

The fringe pattern in Figure 4.17 shows reflectivity minima where the sample thickness is an even multiple of $\lambda_0/4n$. The average reflectivity of these fringes is 52.9%, as expected from Equation 4.57. In measurements where the fringe separation is not resolved, this would be the measured reflectivity. Equation 4.54 therefore agrees with the Fresnel reflectivity from Equation 4.57 in the case of zero loss. Toward the shorter wavelength (lower loss) region of Figure 4.11 the fringes in this $5mm$ sample were omitted for clarity. In the limit of zero loss (low excess carrier density) and a real refractive index of 4.0, these are the fringes that would be observed.

4.4 Two-dimensional (optical stripe excitation) transient diffusion model

Having modelled the transient carrier density in the x direction for an infinite lateral source, finite-source optical excitation is now considered. One application of the modulator requires an absorbing pattern to be generated over the modulator's aperture. Lateral carrier diffusion was not considered by the previous models since uniform excitation of the aperture was assumed. However, the use of a laterally-finite optical source to generate the carriers means lateral diffusion is important in limiting the definition of such an absorbing pattern. These models are also validated in the experimental Chapter 5, by measuring lateral carrier diffusion profiles following continuous optical excitation. This section is therefore divided into two parts. Firstly the time-dependent and steady-state models for spatially gaussian- and square-function stripes, infinite in one direction, are presented, then the models are presented for two-dimensionally finite excitation functions, for the gaussian function and for a box-shaped function. These functions are chosen since they can be produced practically to verify these models. A gaussian excitation function is produced by a diode bar laser (gaussian stripe illumination) or as a two-dimensionally finite pattern by the emission from a fibre-coupled diode laser. Spatially-square-edged optical power distributions are less easy to produce practically, but are important in predicting the definition in the absorption arising from such an excitation. The purpose of this is to replicate the effect of an absorbing edge being scanned across the aperture, which is currently achieved in the application by an Archimedean-spiral mechanical chopper blade. Extension of the models to other excitation patterns is relatively straightforward. These models are also important in their identification of another 'apparent' lifetime, observed when the transmission through the centre of the absorbing region is monitored. In addition to the translational carrier diffusion and surface recombination considered by the one-dimensional diffusion equations, lateral carrier diffusion acts to reduce the apparent lifetime.

4.4.1 Excitation using a gaussian stripe function

This section solves the diffusion continuity equation for optical excitation of carriers by a line of excitation illumination which is gaussian in the y direction, and infinite in the z direction, as illustrated by Figure 4.18.

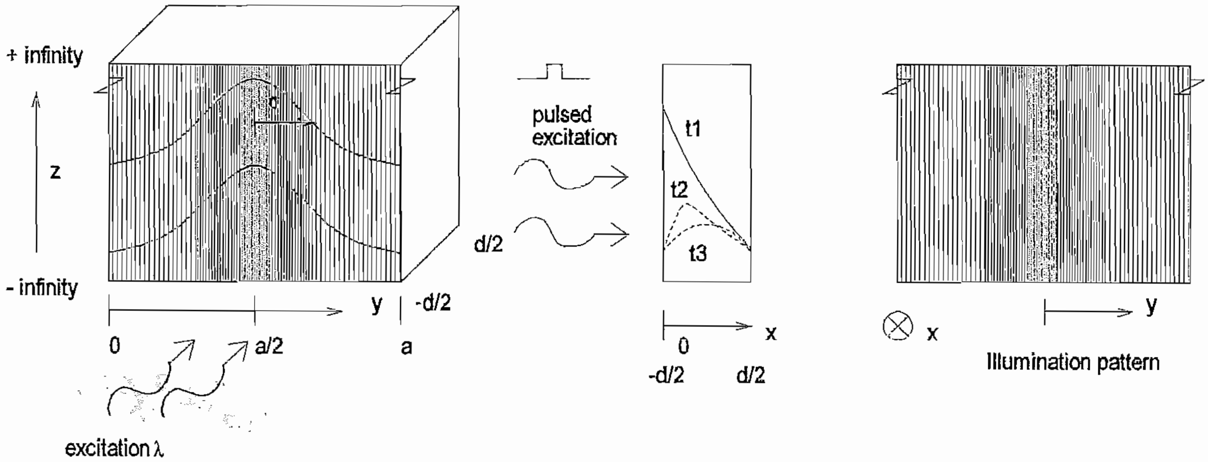

Figure 4.18: Gaussian line-function excitation geometry

Under the condition of zero electric field, the two-dimensional continuity equation for the x and y directions is given by Equation 4.58. The generation term is again used as an initial condition. The steady-state response is determined by integration of the impulse response over time from $t = 0$ to $t = \infty$, and the temporal response is obtained by convolution of the impulse response.

$$\frac{\partial n(x,y,t)}{\partial t} = D_a \frac{\partial^2 n(x,y,t)}{\partial x^2} + D_a \frac{\partial^2 n(x,y,t)}{\partial y^2} - \frac{n(x,y,t)}{\tau_{bulk}} \tag{4.58}$$

If the initial carrier distribution is given by Equation 4.59 where σ is the (y) displacement from the excitation peak at which the excitation power is $1/e^2$ of that at the peak, N_0 is the volume carrier density per unit length in the y direction is now given by Equation 4.60, and the boundary conditions are given by Equations 4.61, Equation 4.62 and 4.63.

$$n(x,y,0) = n_0 e^{-\alpha_{ill}\left(x+\frac{d}{2}\right)} \cdot e^{-\frac{1}{2}\left(\frac{y-\frac{a}{2}}{\sigma}\right)^2} \tag{4.59}$$

$$N_0 = \frac{2\alpha_{ill} P_{Excabs} \lambda_{exc} T}{hc\sigma\sqrt{2\pi}} \tag{4.60}$$

N_0 represents the initial area carrier density cm^{-2} , per cm of length in the z-plane at the surface.

$$D_a \frac{\partial n(x,y,t)}{dx}\bigg|_{x=-\frac{d}{2}} = S \cdot n(x,y,t)|_{x=-\frac{d}{2}} \tag{4.61}$$

$$D_a \frac{\partial n(x,y,t)}{dx}\bigg|_{x=\frac{d}{2}} = -S \cdot n(x,y,t)|_{x=\frac{d}{2}} \tag{4.62}$$

$$n(x,0,t) = n(x,a,t) = 0 \tag{4.63}$$

The impulse response is found through separation of the variables technique. Convolution of the impulse response with a square pulse of period T gives the response to pulsed excitation during the decay as:

$$\begin{aligned} n_p(x,y,t) \ &= \tfrac{1}{T}\textstyle\sum_{m,n}\Bigg[\frac{A_{m,n}\cos(\alpha_m x)\sin\left(\frac{n\pi y}{a}\right)}{\frac{1}{\tau_{bulk}}+D_a\left[\left(\frac{n\pi}{a}\right)^2+\alpha_m^2\right]} \cdot e^{-\left(\frac{1}{\tau_{bulk}}+D_a\left[\left(\frac{n\pi}{a}\right)^2+\alpha_m^2\right]\right)t} \cdot \left[e^{\left(\frac{1}{\tau_{bulk}}+D_a\left[\left(\frac{n\pi}{a}\right)^2+\alpha_m^2\right]\right)T} - 1\right] \\ &\quad + \frac{B_{m,n}\sin(\beta_m x)\sin\left(\frac{n\pi y}{a}\right)}{\frac{1}{\tau_{bulk}}+D_a\left[\left(\frac{n\pi}{a}\right)^2+\beta_m^2\right]} \cdot e^{-\left(\frac{1}{\tau_{bulk}}+D_a\left[\left(\frac{n\pi}{a}\right)^2+\beta_m^2\right]\right)t} \cdot \left[e^{\left(\frac{1}{\tau_{bulk}}+D_a\left[\left(\frac{n\pi}{a}\right)^2+\beta_m^2\right]\right)T} - 1\right]\Bigg] \end{aligned} \tag{4.64}$$

where the coefficients $A_{m,n}$ and $B_{m,n}$ are given respectively by:

$$\begin{aligned} A_{m,n} = \quad & \frac{8Ne^{-\frac{\alpha_{ill}d}{2}}}{ad(\alpha_m^2+\alpha_{ill}^2)}\left[\alpha_m sin\left[\frac{\alpha_m d}{2}\right]cosh\left[\frac{\alpha_{ill}d}{2}\right] + \alpha_{ill}cos\left[\frac{\alpha_m d}{2}\right]sinh\left[\frac{\alpha_{ill}d}{2}\right]\right] \cdot \\ & \int_0^a e^{-\frac{1}{2}\left[\frac{y-\frac{a}{2}}{\sigma}\right]^2} sin\left[\frac{n\pi y}{a}\right]dy \end{aligned} \tag{4.65}$$

$$\begin{aligned} B_{m,n} = \quad & \frac{8Ne^{-\frac{\alpha_{ill}d}{2}}}{ad(\beta_m^2+\alpha_{ill}^2)}\left[\beta_m cos\left[\frac{\beta_m d}{2}\right]sinh\left[\frac{\alpha_{ill}d}{2}\right] - \alpha_{ill}sin\left[\frac{\beta_m d}{2}\right]cosh\left[\frac{\alpha_{ill}d}{2}\right]\right] \cdot \\ & \int_0^a e^{-\frac{1}{2}\left[\frac{y-\frac{a}{2}}{\sigma}\right]^2} sin\left[\frac{n\pi y}{a}\right]dy \end{aligned} \tag{4.66}$$

and the coefficients α_m and β_m are given by Equations 4.67, 4.68 respectively:

$$cot\left(\frac{\alpha_m d}{2}\right) = \frac{D_a\alpha_m}{S} \tag{4.67}$$

$$tan\left(\frac{\beta_m d}{2}\right) = -\frac{D_a\beta_m}{S} \tag{4.68}$$

Typical carrier profiles as a function of time, resulting from this excitation function are given for the x and y directions in Figures 4.19, and 4.20. The parameters used in the model are $\tau_{bulk} = 1ms$, $\sigma = 0.5mm$, $S = 1ms^{-1}$, $T = 1ms$ and $d = 5mm$.

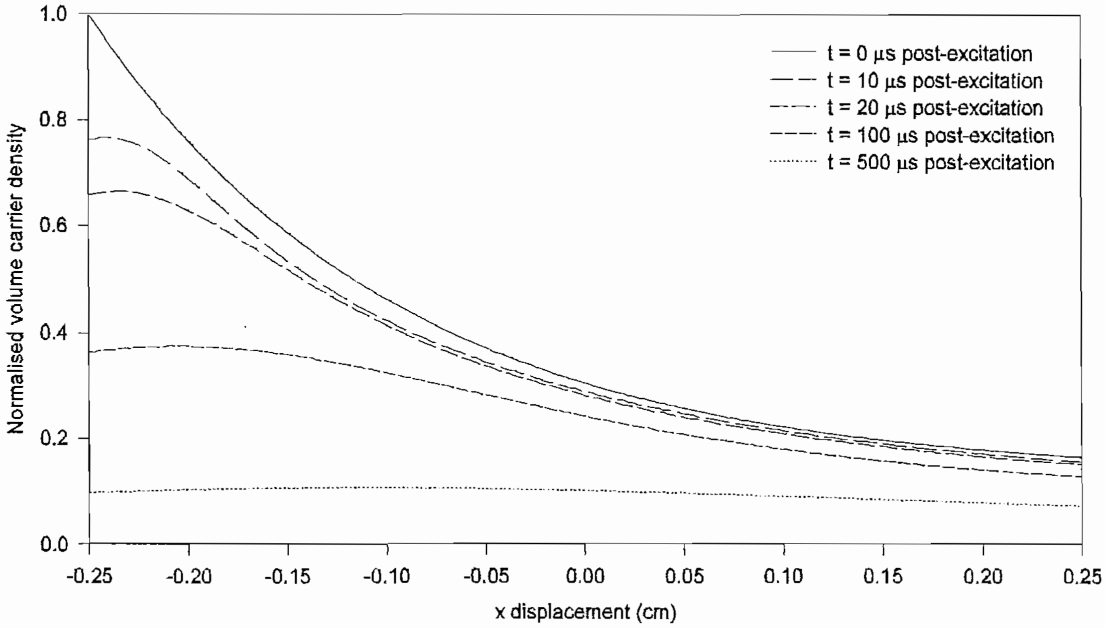

Figure 4.19: Normalised carrier distribution profiles in the x-plane resulting from lateral and axial diffusion

The solution for the steady-state response to the gaussian illumination function is given by integration of the impulse response over $t = 0$ to $t = \infty$, giving:

$$n_{pss}(x,y) = \sum_{m,n}\left[\frac{A_{m,n}cos(\alpha_m x)sin(\frac{n\pi y}{a})}{\frac{1}{\tau} + D_a(\frac{n\pi}{a})^2 + \alpha_m^2} + \frac{B_{m,n}sin(\beta_m x)sin(\frac{n\pi y}{a})}{\frac{1}{\tau} + D_a(\frac{n\pi}{a})^2 + \beta_m^2}\right] \tag{4.69}$$

A graph of this for the above simulation, integrated over x to give the area carrier density and showing the excitation function is shown for the y plane in Figure 4.21.

Figure 4.21 shows the importance of surface recombination velocity through its alteration of the shape of the diffused profile; a gaussian excitation function does not give

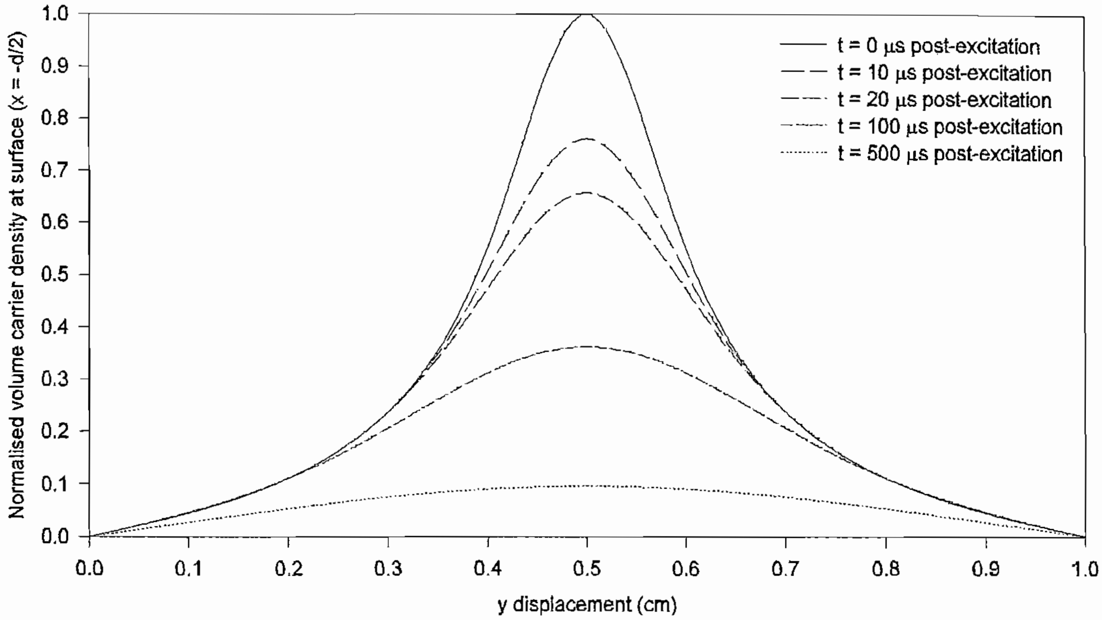

Figure 4.20: Normalised carrier distribution profiles in the y-plane resulting from lateral and axial diffusion

a simple function for the diffused profile. It is therefore important to graphically compare measurements of diffused profiles in the experiments in Section 5.3.2 as opposed to characterising them by say a $1/e^2$ width.

4.4.2 Excitation using a uniform line excitation function

The solutions to a uniform line function illumination source are now given. The steady state solution to this situation determines the extent of lateral carrier diffusion and hence the resolution of an absorbing stripe generated on the modulator aperture. The technique used to determine these solutions is through separation of the variables twice, and then inserting the boundary conditions. The source function is given by the initial conditions as:

$$n(x,y,0) = N_0 e^{-\alpha_{iu}\left(x+\frac{d}{2}\right)} \tag{4.70}$$

for $\frac{a}{2} - \delta \leq y \leq \frac{a}{2} + \delta$ or $n(x,y,0) = 0$ otherwise, where N_0 is the surface initial area carrier density in cm^{-2} per cm of length in the z-plane.

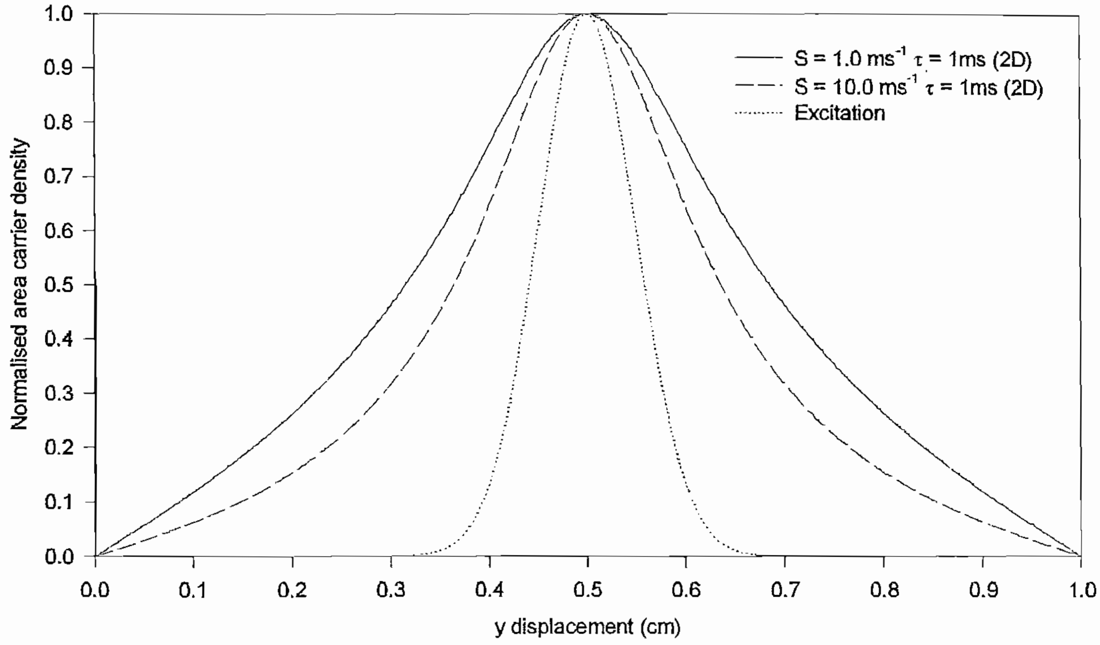

Figure 4.21: Lateral diffusion profile resulting from gaussian line excitation

$$N_0 = \frac{T P_{Excabs} \lambda_{exc} \alpha_{ill}}{2hc\delta} \tag{4.71}$$

The form of the impulse response and pulse response is the same as that for the gaussian line; the α_m and β_m coefficients remain the same, but the coefficients $A_{m,n}$ and $B_{m,n}$ become:

$$A_{m,n} = \frac{16Ne^{-\frac{\alpha_{ill}d}{2}} sin(\frac{\delta n\pi}{a}) sin(\frac{n\pi}{2})}{dn\pi(\alpha_m^2 + \alpha_{ill}^2)} \left[\alpha_m sin\left(\frac{\alpha_m d}{2}\right) cosh\left(\frac{\alpha_{ill}d}{2}\right) + \alpha_{ill} cos\left(\frac{\alpha_m d}{2}\right) sinh\left(\frac{\alpha_{ill}d}{2}\right)\right] \tag{4.72}$$

$$B_{m,n} = \frac{16Ne^{-\frac{\alpha_{ill}d}{2}} sin(\frac{\delta n\pi}{a}) sin(\frac{n\pi}{2})}{dn\pi(\beta_m^2 + \alpha_{ill}^2)} \left[\beta_m cos\left(\frac{\beta_m d}{2}\right) sinh\left(\frac{\alpha_{ill}d}{2}\right) - \alpha_{ill} sin\left(\frac{\beta_m d}{2}\right) cosh\left(\frac{\alpha_{ill}d}{2}\right)\right] \tag{4.73}$$

The solution to the steady state response for this source function is therefore given by Equations 4.69, 4.72, 4.73, 4.67 and 4.68. The excitation function is shown schematically in Figure 4.22.

A simulation of the steady state response for the line excitation is shown in Figure 4.23, showing also the excitation function.

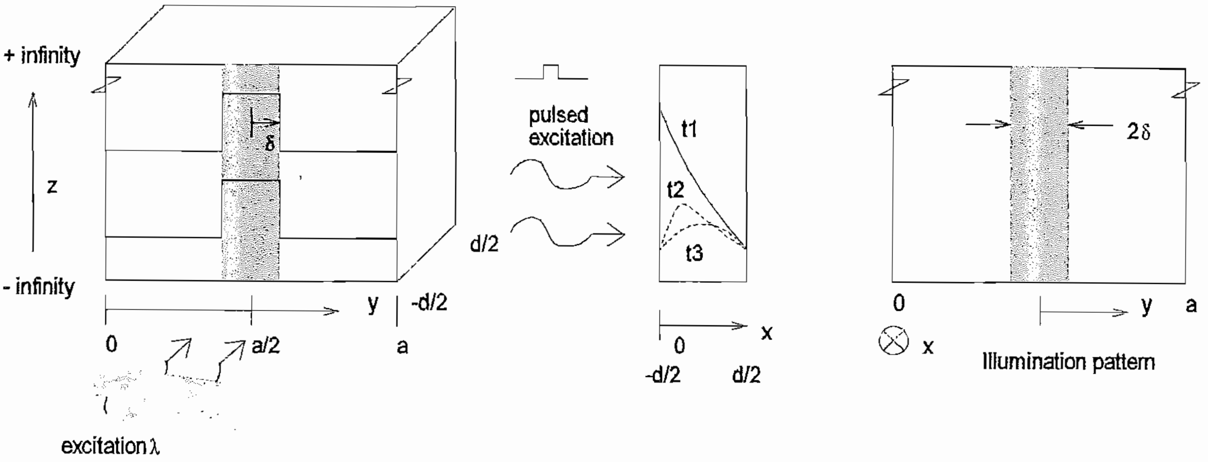

Figure 4.22: Square-line excitation function geometry

Figure 4.23 shows the extent of steady state lateral diffusion for two values of surface recombination velocity. The diffusion profile for low S outside the excited region shows an $e^{-y/L}$ dependence as expected from simple diffusion. At the edge of the excitation ($y = 0.6cm$) the $S = 1ms^{-1}$ curve shows an excess carrier density of $8.87 \times 10^{15} cm^{-2}$. At a distance one diffusion length from this ($0.081cm$) the carrier density has dropped to $3.18 \times 10^{15} cm^{-2}$, just less than $1/e$ of that at the edge of the excitation. The discrepancy is due to the finite S used in the model. The implication of this in generating such an absorbing line pattern is that the absorption inside the excited region will not be uniform, a small variation in carrier density being due to lateral diffusion. However, outside this region the area carrier density and hence induced absorption follows an $e^{-y/L}$ dependence. The definition of the absorbing edge is improved by using material with a shorter bulk carrier lifetime, or material with a higher surface recombination velocity (as demonstrated by Figure 4.21). Both of these techniques are at the expense of higher optical power for the same level of absorption.

In the presence of a surface recombination velocity which gives a comparable recombination rate to that in the bulk, carriers decay with a shorter diffusion length, and the lateral carrier distribution profile is no longer fitted by a simple exponential curve. This has implications in the fitting process used in Chapter 5.

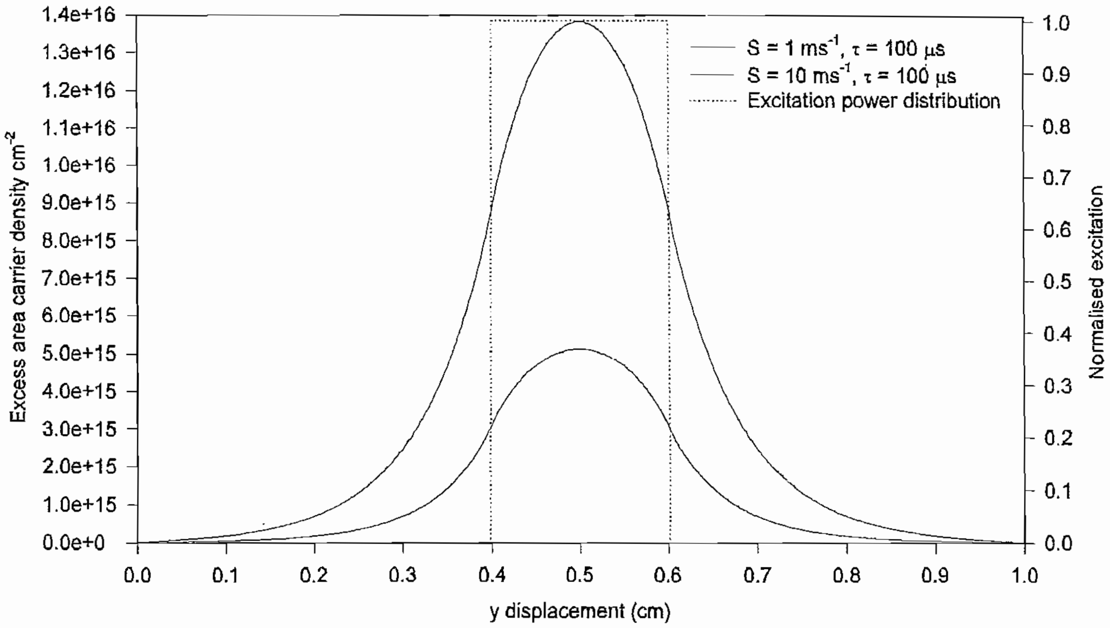

Figure 4.23: Line excitation function and resulting steady state diffusion profile

4.5 Three-dimensional (gaussian pulse) transient diffusion model

This section presents the solution to the three-dimensional diffusion equation. This models diffusion resulting from an excitation profile that is restricted in two directions, and is generated by a gaussian circular beam or a square-shaped beam. Extension to other excitation beam shapes is simple. For zero electric field the continuity equation in three dimensions becomes:

$$\frac{\partial n(x,y,z,t)}{\partial t} = D_a\frac{\partial^2 n(x,y,z,t)}{\partial x^2} + D_a\frac{\partial^2 n(x,y,z,t)}{\partial y^2} + D_a\frac{\partial^2 n(x,y,z,t)}{\partial z^2} - \frac{n(x,y,z,t)}{\tau_{bulk}} \tag{4.74}$$

The boundary conditions in this case are given by Equations 4.61 and 4.61 but for three dimensions, and:

$$n(x,0,z,t) = n(x,a,z,t) = n(x,y,0,t) = n(x,y,b,t) = 0 \tag{4.75}$$

This assumes carrier recombination at only the front and back surfaces, and that no carriers reach the upper and lower sample sides. This assumption requires that the optical excitation width and carrier diffusion length are much shorter than sample lateral dimensions.

4.5.1 Three dimensional diffusion: gaussian excitation

In this case the excitation is a two-dimensional gaussian function as shown in Figure 4.24. The initial gaussian carrier distribution is given by:

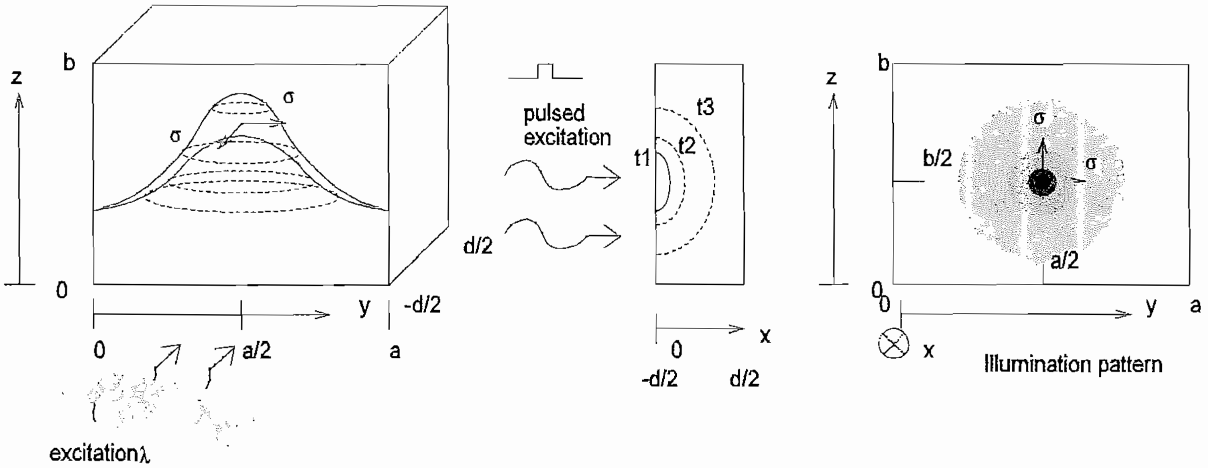

Figure 4.24: Schematic of the three-dimensional time-dependent diffusion model for two-dimensional gaussian illumination

$$n(x,y,0) = n_0 e^{-\alpha_{ill}\left(x+\frac{d}{2}\right)} \cdot e^{-\frac{1}{2}\left(\frac{y-\frac{a}{2}}{\sigma}\right)^2} \cdot e^{-\frac{1}{2}\left(\frac{z-\frac{b}{2}}{\sigma}\right)^2} \qquad (4.76)$$

where N_0 is the surface carrier density cm^{-3} and σ is the $1/e^2$ width of the gaussian power excitation profile. The impulse response is given by Equation 4.77.

$$\begin{aligned} n_i(x,y,z,t) = & \sum_{m,n,c} \Bigg[A_{m,n,c} cos(\alpha_m x) sin\left(\frac{n\pi y}{a}\right) \cdot sin\left(\frac{c\pi z}{b}\right) \cdot e^{-\left(\frac{1}{\tau_{bulk}}+D_a\left[\alpha_m^2+(\frac{n\pi}{a})^2+(\frac{c\pi}{b})^2\right]\right)t} + \\ & B_{m,n,c} sin(\beta_m x) sin\left(\frac{n\pi y}{a}\right) \cdot sin\left(\frac{c\pi z}{b}\right) \cdot e^{-\left(\frac{1}{\tau_{bulk}}+D_a\left[\beta_m^2+(\frac{n\pi}{a})^2+(\frac{c\pi}{b})^2\right]\right)t} \Bigg] \qquad (4.77) \end{aligned}$$

The α_m and β_m coefficients, common to both source functions, are given by Equations 4.67 and 4.68 and the $A_{m,n,c}$ and $B_{m,n,c}$ coefficients for the gaussian source are given by:

$$A_{m,n,c} = \frac{16Ne^{-\frac{\alpha_{ill}d}{2}} sin(\frac{\delta n\pi}{a}) sin(\frac{n\pi}{2})}{abd(\alpha_m^2 + \alpha_{ill}^2)} \left[\alpha_m sin\left[\frac{\alpha_m d}{2}\right] cosh\left[\frac{\alpha_{ill}d}{2}\right] + \alpha_{ill} cos\left[\frac{\alpha_m d}{2}\right] sinh\left[\frac{\alpha_{ill}d}{2}\right]\right] \cdot \int_0^a \int_0^b e^{-\frac{1}{2}\left(\frac{y-\frac{a}{2}}{\sigma}\right)^2} \cdot e^{-\frac{1}{2}\left(\frac{z-\frac{b}{2}}{\sigma}\right)^2} sin\left[\frac{n\pi y}{a}\right] \cdot sin\left[\frac{c\pi z}{b}\right] dydz \tag{4.78}$$

$$B_{m,n,c} = \frac{16Ne^{-\frac{\alpha_{ill}d}{2}} sin(\frac{\delta n\pi}{a}) sin(\frac{n\pi}{2})}{abd(\beta_m^2 + \alpha_{ill}^2)} \left[\beta_m cos\left[\frac{\beta_m d}{2}\right] sinh\left[\frac{\alpha_{ill}d}{2}\right] - \alpha_{ill} sin\left[\frac{\beta_m d}{2}\right] cosh\left[\frac{\alpha_{ill}d}{2}\right]\right] \cdot \int_0^a \int_0^b e^{-\frac{1}{2}\left(\frac{y-\frac{a}{2}}{\sigma}\right)^2} \cdot e^{-\frac{1}{2}\left(\frac{z-\frac{b}{2}}{\sigma}\right)^2} sin\left[\frac{n\pi y}{a}\right] \cdot sin\left[\frac{c\pi z}{b}\right] dydz \tag{4.79}$$

Integration of the impulse response in Equation 4.77 gives the steady state response as:

$$n_{ss}(x,y,z) = \sum_{m,n,c} \left[\frac{A_{m,n,c} cos(\alpha_m x)}{\frac{1}{\tau} + D_a(\alpha_m^2 + \frac{n\pi}{a})^2 + \frac{c\pi}{b})^2} + \frac{B_{m,n,c} sin(\beta_m x)}{\frac{1}{\tau} + D_a(\beta_m^2 + \frac{n\pi}{a})^2 + \frac{c\pi}{b})^2}\right] \left[sin(\frac{n\pi y}{a}) sin(\frac{c\pi z}{b})\right] \tag{4.80}$$

The temporal response is shown for two S values in Figures 4.25 and 4.26 for $\tau_{bulk} = 1ms$, $\sigma = 0.5mm$ $P = 0.5W\ cm^{-2}$, $T = 1ms$ in the x direction. Figure 4.27 gives the steady state response for the y direction for these two S values, showing the effects of lateral carrier diffusion. As with the two-dimensional diffusion case, the effect of the increased surface recombination velocity is to give a greater carrier density gradient at the surface of the sample for time $> T$, and to significantly reduce the extent of lateral carrier diffusion.

The effect of these models is seen in Section 4.6 which compares the situations of two and three-dimensional diffusion.

4.5.2 Three dimensional lateral diffusion: box-function excitation

This section gives the model for diffusion in three dimensions, and is a development of the gaussian excitation case. The excitation is assumed as in Figure 4.28.

The initial conditions resulting from the box function excitation are assumed:

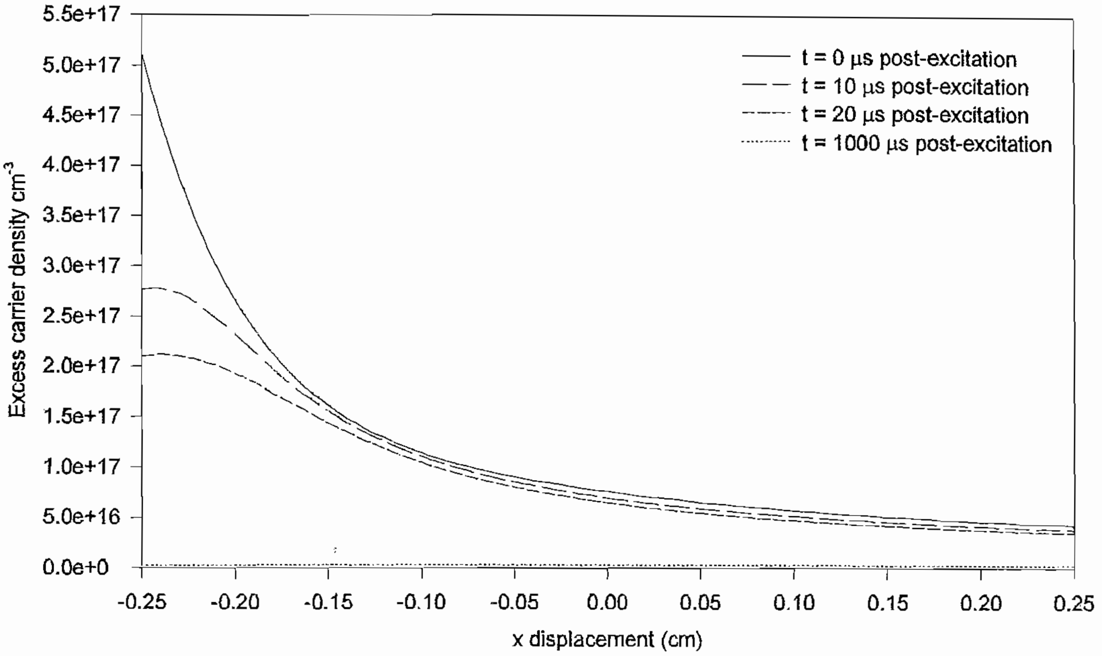

Figure 4.25: Carrier distribution vs x for three-dimensional diffusion from gaussian source; $S = 1ms^{-1}$, $\tau = 1ms$, $\sigma = 0.5mm$, $T = 1ms$ and $P = 0.5W\ cm^{-2}$

$$n(x,y,z,0) = N_0 e^{-\alpha_{ill}\left(x+\frac{x}{2}\right)} \tag{4.81}$$

for $\frac{a}{2} - \delta \leq y \leq \frac{a}{2} + \delta$, and $\frac{b}{2} - \gamma \leq y \leq \frac{b}{2} + \gamma$, and N_0 is given by:

$$N_0 = \frac{\alpha_{ill} P_{Excabs} \lambda_{exc} T}{4\gamma\delta} \tag{4.82}$$

where γ and δ are given by Figure 4.28. The impulse response is the same as in Equation 4.77, with the α_m, β_m coefficients as in Equations 4.67 and 4.68, but the coefficients $A_{m,n,c}$ and $B_{m,n,c}$ must be modified to:

$$\begin{aligned} A_{m,n,c} = \quad & \frac{64 N e^{-\frac{\alpha_{ill} d}{2}}}{dnc\pi^2(\alpha_m^2 + \alpha_{ill}^2)} \cdot \left[sin\left(\frac{n\pi}{2}\right) sin\left(\frac{\delta n\pi}{a}\right) sin\left(\frac{c\pi}{2}\right) sin\left(\frac{\gamma c\pi}{b}\right) \right] \cdot \\ & \left[\alpha_m sin\left(\frac{\alpha_m d}{2}\right) cosh\left(\frac{\alpha_{ill} d}{2}\right) + \alpha_{ill} cos\left(\frac{\alpha_m d}{2}\right) sinh\left(\frac{\alpha_{ill} d}{2}\right) \right] \end{aligned} \tag{4.83}$$

$$\begin{aligned} B_{m,n,c} = \quad & \frac{64 N e^{-\frac{\alpha_{ill} d}{2}}}{dnc\pi^2(\beta_m^2 + \alpha_{ill}^2)} \cdot \left[sin\left(\frac{n\pi}{2}\right) sin\left(\frac{\delta n\pi}{a}\right) sin\left(\frac{c\pi}{2}\right) sin\left(\frac{\gamma c\pi}{b}\right) \right] \cdot \\ & \left[\beta_m cos\left(\frac{\beta_m d}{2}\right) sinh\left(\frac{\alpha_{ill} d}{2}\right) - \alpha_{ill} sin\left(\frac{\beta_m d}{2}\right) cosh\left(\frac{\alpha_{ill} d}{2}\right) \right] \end{aligned} \tag{4.84}$$

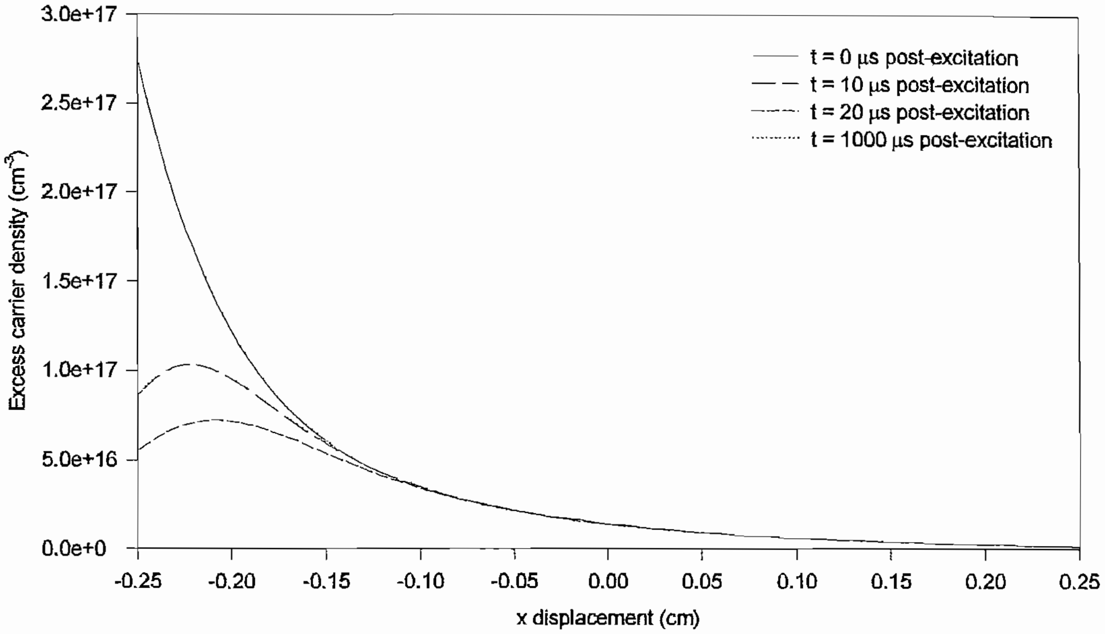

Figure 4.26: Carrier distribution vs x for three-dimensional diffusion from gaussian source; $S = 10ms^{-1}$, $\tau = 1ms$, $\sigma = 0.5mm$, $T = 1ms$ and $P = 0.5W\ cm^{-2}$

This model was considered for completeness to determine the effect of generating such an absorbing pattern on the aperture. Its application is in generating square or rectangular absorbing patterns that modulate specific regions of detector pixels. Practically, this pattern is difficult to generate and is not validated experimentally in this work.

4.6 Carrier diffusion models and their effect on the modulator

This section has considered carrier diffusion models in one, two and three dimensions which predict the modulator's absorption in the steady-state and dynamic cases. To optimise the level of absorption in the steady state, as high a value of bulk carrier lifetime and as low a value of surface recombination velocity as possible are required. S is reduced by etching, whilst the bulk carrier lifetime is fixed after crystal growth. Experiments have therefore concentrated on using the highest purity germanium available, HPGe, and the emphasis has been to reduce S to take advantage of the long bulk carrier

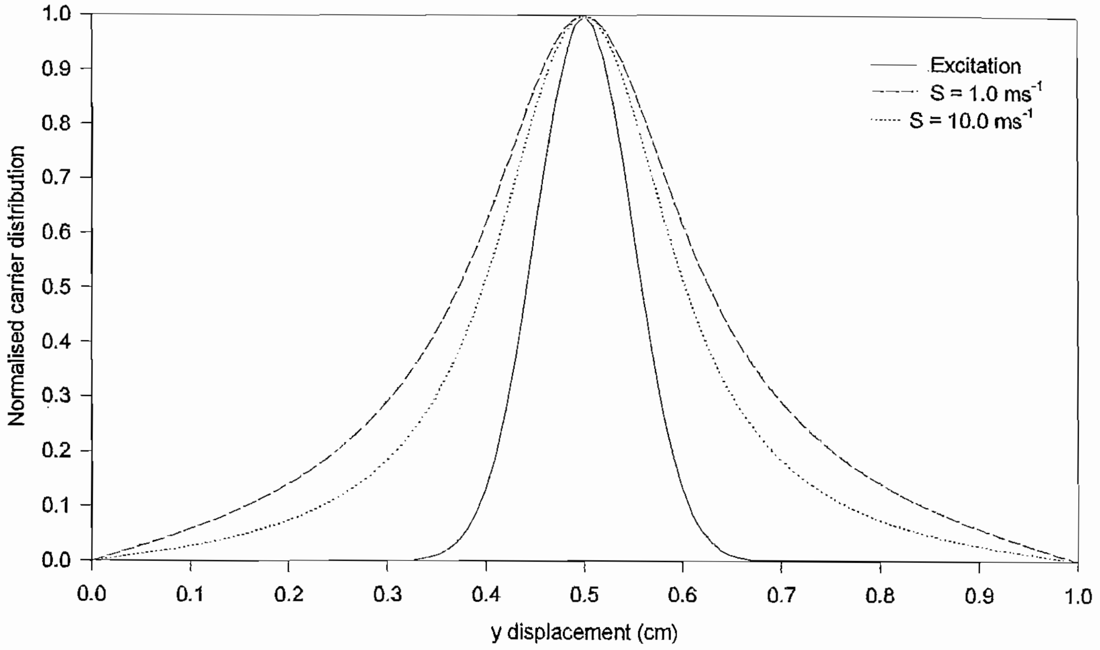

Figure 4.27: Steady state lateral carrier distribution for three-dimensional diffusion from a gaussian source for two S values

lifetime. Typical HPGe values of τ_{bulk} in the order of $1ms$ provide an upper limit to the modulator's efficiency.

Chapter 3 assumed the bulk carrier lifetime and diffusion coefficient were constants, providing the excess carrier density did not exceed $\sim 10^{17}cm^{-3}$ and $\sim 10^{19}cm^{-3}$ for the respective parameters in the presence of a $1ms$ bulk carrier lifetime. These assumptions are validated using the steady state carrier distribution model for a semi-infinite sample in Section 4.2.1. Figures 4.29 and 4.30 show the power density and surface carrier density (cm^{-3}) respectively as a function of S and τ_{bulk}, required to give 5% 'off' state transmission. Following Figure 4.3, the surface carrier density (at $x = 0$) is within 0.1% of the maximum carrier density encountered during the steady 'off' state over a practical range of S from 0 to $10ms^{-1}$.

Based on the assumptions of constant D_a and τ_{bulk}, Figure 4.30 shows the maximum carrier density for reasonable values of S and τ_{bulk} is $7 \times 10^{16}cm^{-3}$. The apparent independence of the plotted carrier density on S occurs because these S values only affect the shape of the steady-state carrier distribution profile within $\sim 1\mu m$ of the surface. The surface carrier density is within 0.1% of the peak carrier density for these values, producing the apparent independence. This was shown by Figures 4.2 and 4.3.

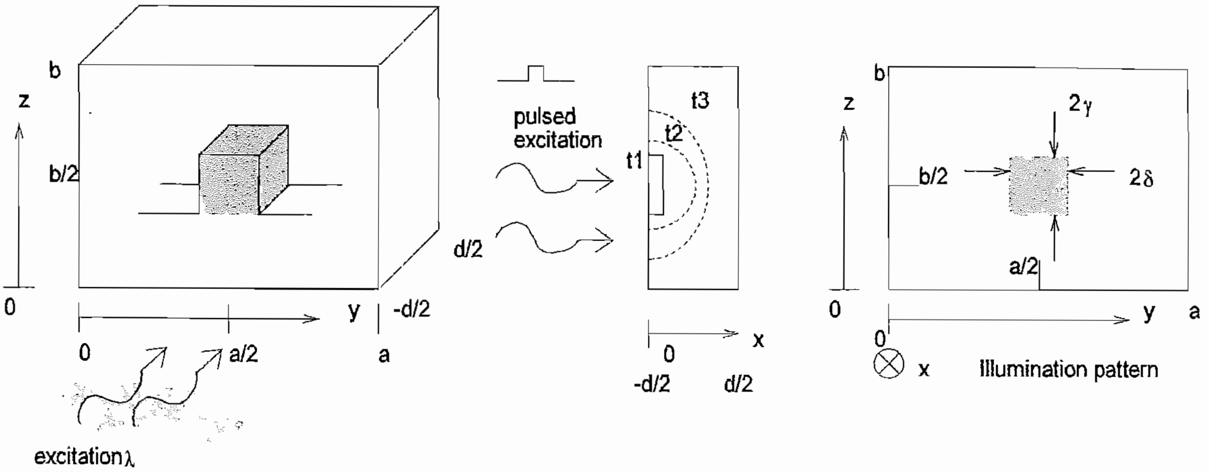

Figure 4.28: Diagram of three-dimensional time-dependent diffusion model for two-dimensional box-profile illumination

Using the Auger recombination coefficient of $\gamma_3 = 10^{-32}cm^6s^{-1}$ gives a minimum Auger lifetime of $20.4ms$. This has insignificant effect in the presence of the assumed $1ms$ SRH bulk lifetime. In any case, this carrier density only occurs for 5% transmission with a bulk carrier lifetime of $100\mu s$ (Figure 4.30), where this Auger lifetime is even less significant. Since the carrier density in the off state (5%) is lower than that which causes a change in diffusion coefficient or the lifetime due to the Auger process, the use of constant values for these parameters in this work is justified.

Initially this section predicted that a value of $S = 3ms^{-1}$ was required in the presence of $\tau_{bulk} = 1ms$ to optimise the induced absorption. The effects of these parameters in the modelled situations and on the modulator are now summarised.

During steady-state excitation of a finite sample, carriers recombine at both front and back surfaces due to the finite S on real surfaces. Although S is reduced in practice by etching, its effect at the back surface is minimised by increasing sample thickness until the carrier density there becomes negligible. Simple theory suggests this is achieved by making the sample a few diffusion lengths thick. The steady state model has quantified this dependence, in Figures 4.7 and 4.7, showing that for typical germanium parameters a sample thickness of $5mm$ is adequate to achieve this. An unreasonable sample thickness

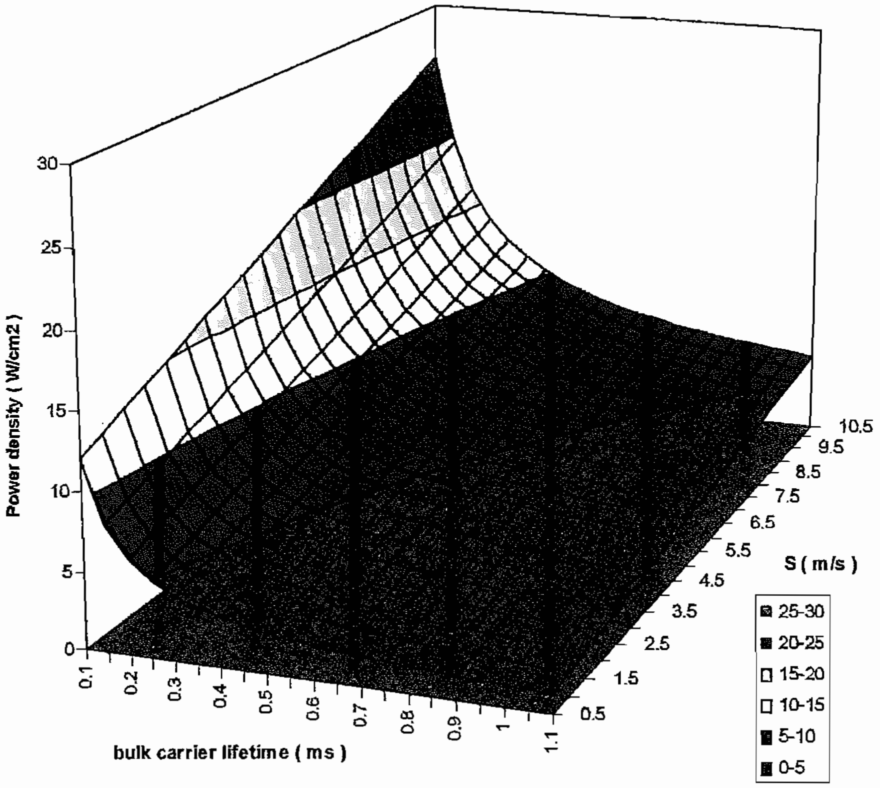

Figure 4.29: Power density $W\ cm^{-2}$ required to give 5% 'off' state transmission as a function of S and τ_{bulk}

is required to significantly further-reduce the effect of back-surface S.

The effect of non-uniform excitation was shown by the two- and three-dimensional models in Sections 4.4 and 4.5. During non-uniform steady-state illumination, lateral diffusion reduces the definition of the absorption resulting from such an illumination profile. The effect was shown to laterally 'spread-out' the absorbing region. The extent of lateral diffusion increases with bulk carrier lifetime and reducing S, altering the profile's shape, although in the presence of a high S and low τ_{bulk} the diffused profile is much closer to that of the excitation profile due to reduced lateral diffusion. Consequently, measurements of the diffused profiles are not fitted by simple functions and their characterisation by, for example a $1/e^2$ width is meaningless. In the presence of a low surface recombination velocity the carrier distribution resulting from a square excitation function is reduced by a factor of $1/e$ at a distance L_d from the edge of the excitation. In the presence of moderate S ($> 5ms^{-1}$) the absorption profile has larger spatial derivatives at its edges, but no longer decreases exponentially with lateral displacement. The implication of this on experiments in Chapter 5, requires exact comparisons of the modelled and measured profiles to enable the fitting of carrier parameters. The effect of even moderate S was shown to further alter the lateral shape of the resulting absorbing

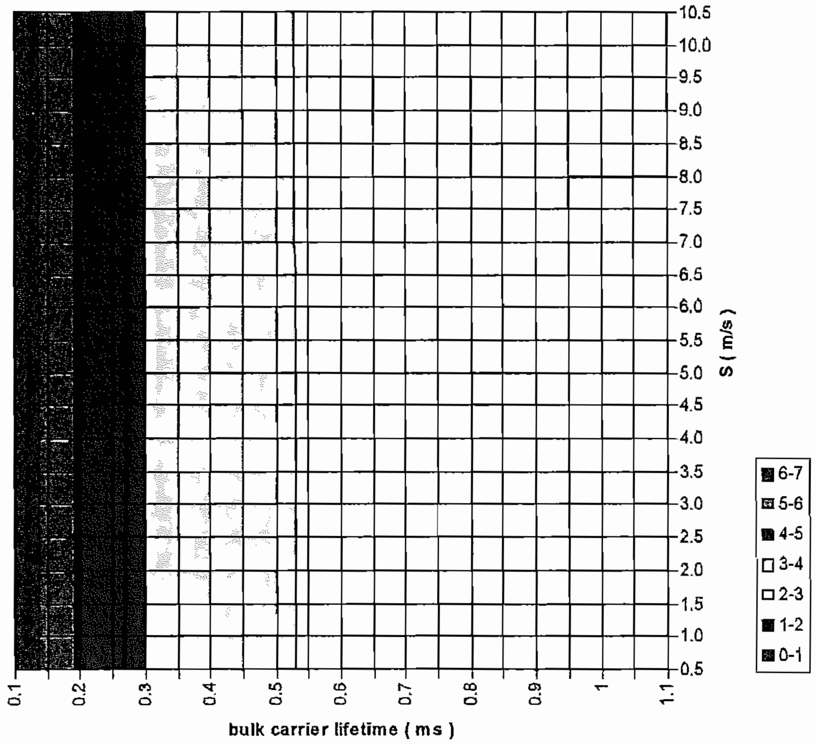

Figure 4.30: Maximum carrier density ($\times 10^{16} cm^{-3}$) required for 5% 'off' state transmission as a function of S and τ_{bulk}

profile, showing that despite the preference for long bulk carrier lifetime to increase the absorption, the definition of such an absorbing profile could be improved by the presence of finite S. The effect of lateral diffusion in two and three dimensions is illustrated in Figure 4.31 for the same material parameters and a gaussian excitation function.

Figure 4.31 shows the significantly-reduced extent of lateral diffusion in the two-dimensional case compared to that in three dimensions. This effect is important, even in the absence of surface recombination. Carriers diffusing in three dimensions generate a sharper-definition absorbing profile than that resulting from two-dimensional diffusion, such as that generated by a line excitation function. In the presence of a very high surface recombination velocity the difference between these profiles is greatly reduced.

The modelled temporal-decay of carriers is important in determining the modulator's switching speed. During uniform excitation, the rate of switching-off the transmission is controlled by the carrier generation rate, and is determined primarily by the excitation power density. Following termination of the excitation the modulator's maximum switching rate is however controlled by the much slower process of one-dimensional carrier diffusion and decay. Initially carrier decay is fast since surface recombination affects the high front-surface carrier density. The carrier distribution subsequently achieves a

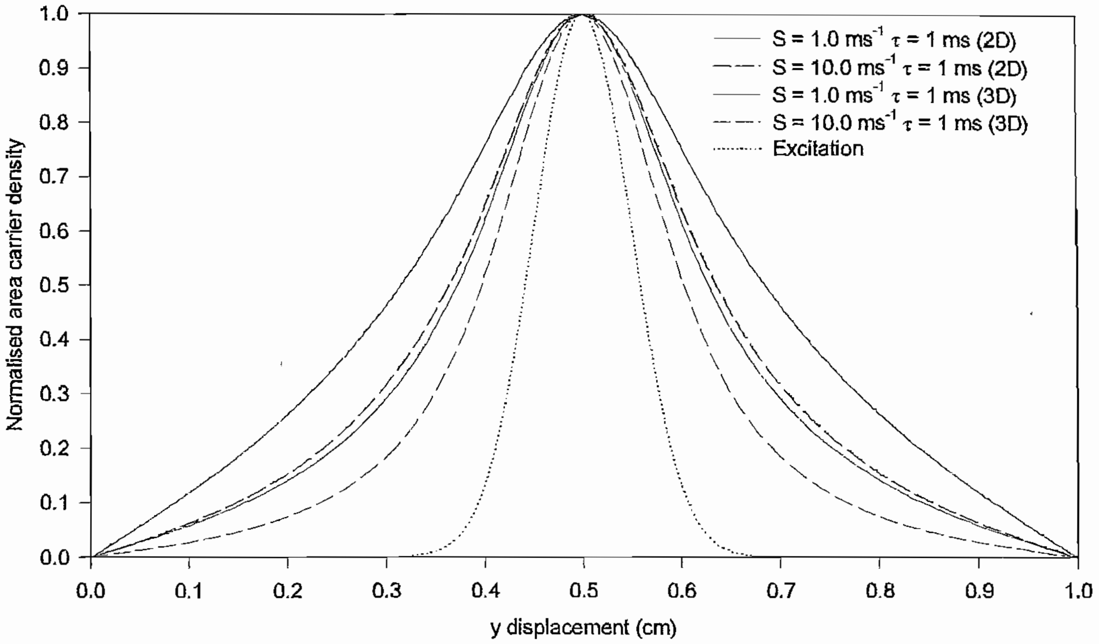

Figure 4.31: Carrier decay vs lateral displacement at the centre of two and three dimensional absorbing profiles

stable shape, and the carriers decay with a time constant that depends on both bulk and surface recombination. Generally speaking, the initial carrier decay rate is increased by using a high surface recombination velocity, although reduction of the bulk carrier lifetime is necessary to increase the rate at which most of the absorption is switched. However, the two effects are to a certain extent important during all stages of decay. The difference in decay constants over these periods was shown by the difference in gradients in Figure 4.10. The differences in these decay constants are used to fit S and τ_{bulk} to experimental data in Chapter 5 to validate this model. This temporal one-dimensional diffusion equation is also used in Chapter 5 to extract these material parameters from measurements of the microwave reflectivity following uniform optical excitation. Unlike measurements of the transmission in the infrared, this technique has the additional benefit of enabling the separation of bulk and surface effects. These models together enable experimental verification of the assumptions that S and τ_{bulk} were independent of the levels of excess carrier densities encountered in the modulator, in Chapter 5.

An additional effect of diffusion in two- and three dimensions is to give different effective lifetimes during carrier decay. For the same parameters, the absorption seen looking along a line through the peak of the excited region shows a higher decay constant for the three-dimensional diffusion than that for two-dimensional diffusion, as shown in Figure 4.32.

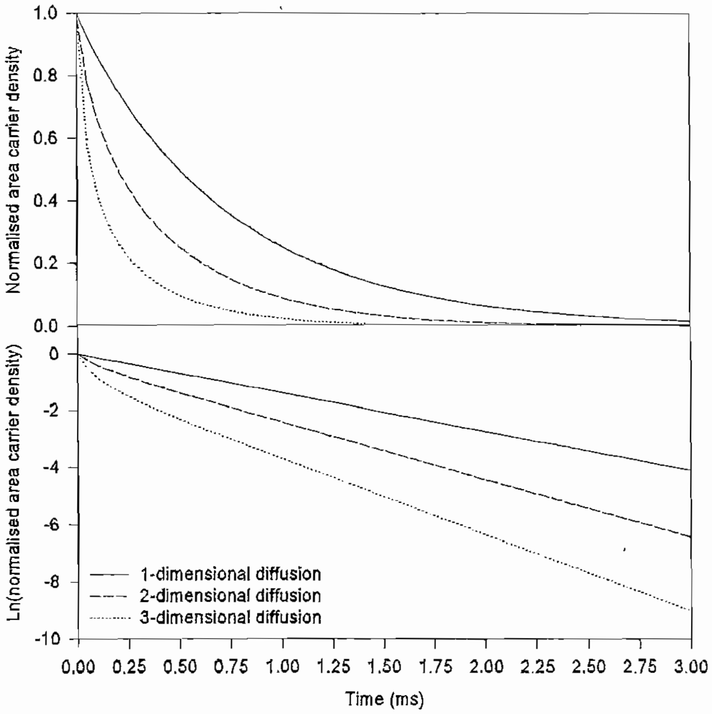

Figure 4.32: Temporal decay of the area carrier density, modelled for one-, two- and three-dimensional diffusion for the same parameters; $S = 1ms^{-1}$, $\tau_{bulk} = 1ms$, $T = 1ms$ and $d = 5mm$

Figure 4.32 shows the normalised area carrier density (proportional to the induced absorption coefficient) decaying as a function of time in the three cases. Faster decay is observed with increasing number of directions in which the carriers diffuse. The decay constant for the distribution is given by the gradient of the lower graph in Figure 4.32. The use of a low surface recombination velocity in the simulation ensures minimal change in shape of the carrier distribution at the surface, so the decay constant for the one-dimensional case is practically constant over time. For the two-dimensional case the shape of the carrier distribution changes significantly over the first $0.25ms$ after the excitation is extinguished, although a constant shape of carrier distribution is maintained thereafter. For the three-dimensional case the decay constant is markedly different during the initial $0.25ms$ after the excitation terminates, compared to that at longer time values. The decay constant for large time is still affected by the ability of the carriers to decay in three dimensions, as seen by its higher values. Effective carrier lifetimes of $736\mu s$, $501\mu s$ and $127\mu s$ are found in Figure 4.32 for the one-, two- and three-dimensional cases respectively. This greatly affects the modulator's switching speed, since all calculations were made for $1ms$ bulk carrier lifetime material and a low $(1ms^{-1})$ surface recombination velocity. The effective carrier lifetime in these cases is therefore not a simple function of the S and τ_{bulk} parameters.

The effect of the different decay constants was observed practically during the experiments, giving misleading results which were initially interpreted as evidence of a high surface recombination velocity. When optical excitation was incident solely within an aperture on the germanium surface, higher initial and large-time decay constants were observed than when the germanium was excited uniformly. This shows the importance of using the correct illumination function when predicting the modulator's switching speed, and that faster switching in long bulk carrier lifetime material can be achieved in a practical device by using such an illumination source that is restricted in lateral extent. Determination of the actual decay constant requires modelling with the exact parameters.

Chapter 5

Diagnostic techniques and analysis of results

Having developed various models in the previous chapter to predict the spatial and temporal dependence of the carrier density and hence induced absorption coefficient, experimental validation is required to verify the assumptions in these models and to ensure the physical situations is correctly modelled. This chapter presents the experimental techniques used to determine the performance of germanium test samples, which are also used in Chapter 6 in optimising the induced absorption. The temporal dependence of the absorption and microwave reflectivity following uniform excitation from a pulsed laser source, and spatial dependence of absorption following continuous excitation from a characterised spatial illumination function are measured in separate experiments to validate these models. The microwave experiment enables the extraction of carrier parameters for a given sample, and the validity of assumptions over these parameters is demonstrated by their use in the other models which backup other experimental results. Additionally the depth of modulation in the 8 to 14μm region is determined when the samples are excited by pulsed optical excitation to determine the effectiveness of etchants at reducing the fraction of carriers recombining at the surfaces.

5.1 Absorption diagnostics

IR Depth of modulation instrument design

The level of induced absorption in a continually excited sample can easily be measured by FTIR spectroscopy. However, FTIR is notoriously poor at accurately measuring the transmission of strongly absorbing samples, especially when the sample surface is highly reflecting. Optically excited germanium falls into this category, and spectrometer radiation reflected by the sample back into the FTIR interferometer results in double-modulation of the incident wavelengths. This introduces slowly-varying wavelength-dependent changes in the measured transmission which are not easily accounted for, requiring precise sample alignment to ensure reproducibility. Additionally, the presence of a few mm thick germanium sample in the sample compartment of an FTIR that is aligned for an air path, de-focuses the IR beam due to the reduced optical path length, making accurate absolute transmission measurements difficult. Back-reflections are reduced by tilting the sample in the sample compartment but this changes the optical path length in the sample and steers the beam off the detector, further complicating analysis of the results.

In experiments to optimise the induced absorption, germanium surfaces were etched to reduce the surface recombination velocity. The chemical and reactive ion etching processes necessitated use of laboratories remote from the fixed FTIR instrument. Following etching the induced absorption had to be determined after different amounts of surface material were removed, in order to determine changes in the surface recombination velocity. This repetitive process required the construction of a portable instrument to measure the induced absorption against a known level, and which would not be as susceptible to the limitations of FTIR spectroscopy. The construction of this induced-absorption instrument is now described.

Determination of the induced absorption in a sample requires measurement of the infrared transmission in the unexcited and optically-excited states. To achieve this the infrared transmission is measured first by modulation of the source with a mechanical chopper, and secondly by pulsed optical excitation of the $880nm$ LED excitation during continuous source illumination. The infrared source is a hot resistor emitting in the 8 to $14\mu m$ region. Part of the image of this large resistor is crudely focussed onto a pyroelectric detector by a KBr lens after passing through the germanium sample which is situated immediately behind an aperture. A bandpass filter restricts the range of wavelengths incident on the detector, so the average depth of modulation in a given spectral band is measured. The operation of the instrument is illustrated schematically by Figure 5.1.

The system in Figure 5.1 operates in one of two modes. In 'calibration' mode the mean germanium transmission is determined. This is necessary due to variations in surface quality after etching samples. Initially the germanium is removed from the instrument and the reference transmission signal is measured. The mechanical chopper

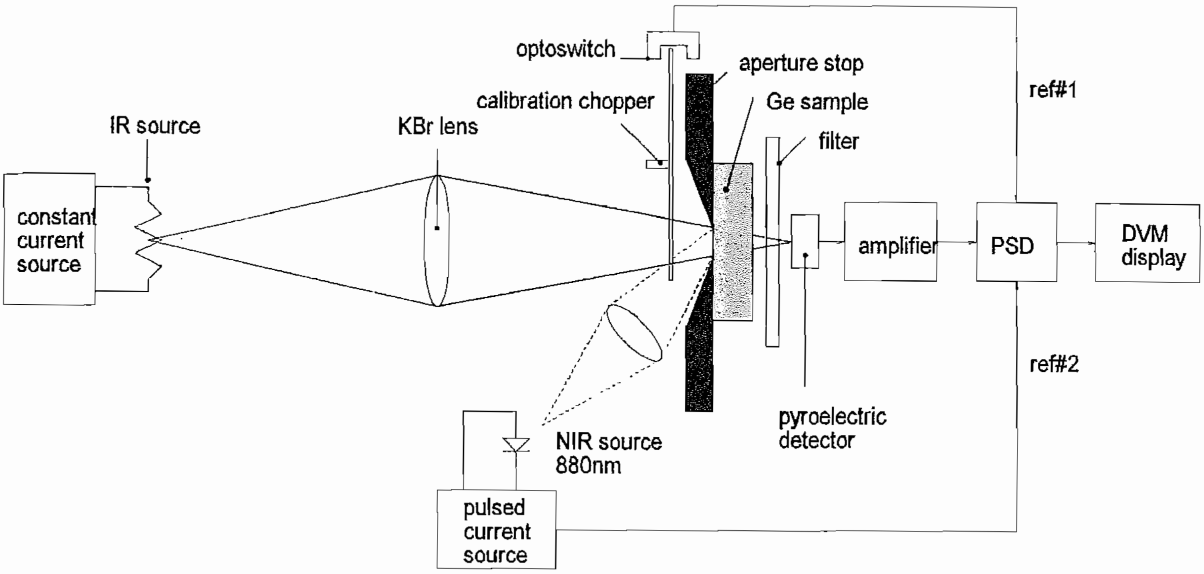

Figure 5.1: Operational diagram of the induced-absorption instrument

interrupts the beam at $35Hz$ and the detector's amplified signal passes through the phase sensitive detector (PSD) where an optoswitch, aligned for 0° phase shift, provides the reference signal. The digital voltmeter (DVM) reading is recorded, giving the 100% transmission signal. Next the germanium is placed in the instrument and the same process gives the germanium transmission signal. The optical filter passband of 6.63 to $15.5\mu m$ gives the measured signal in this region as the spectral average of the product of the emission from the $450°K$ black body hot source, and the transmission of the filter, KBr lens and germanium. In 'operation' mode the mechanical chopper is stopped and the pulsed current source to the LED's is operated. The reference signal to the PSD with 0° phase shift is provided by the pulsed current source. The depth of modulation is measured while the sample is excited by a pulsed fixed peak power density $880nm$ LED signal, and the PSD output voltage is again measured. The instrument therefore measures the average excited-state transmission across the filter bandwidth. This is representative of the real situation in a pyroelectric thermal imaging camera where the average emission from a blackbody image is monitored. Having determined signals proportional to the germanium transmission in the unexcited and excited states, a figure of merit (FOM) which is proportional to the induced absorption as a spectral average over the 6.6 to $15.5\mu m$ region is determined using Equation 5.1. To account for instrument drift over time, a reference sample that is never etched is used as a benchmark to give a depth of modulation which is compared against the depth of modulation attained by the etched sample. Intermittently the instrument calibration is verified by placing the reference sample in the instrument. A FOM for the induced absorption and a *'relative FOM'* compared to the reference sample is thus determined from the instrument readings. These are given by:

$$FOM = ln\left(\frac{Average\,transmission\;signal\;unexcited}{Average\,transmission\;signal\;excited}\right) \tag{5.1}$$

$$Relative\,FOM = \frac{FOM\;for\;sample}{FOM\;for\;reference\,sample} \tag{5.2}$$

The instrument is shown schematically in Figure 5.2.

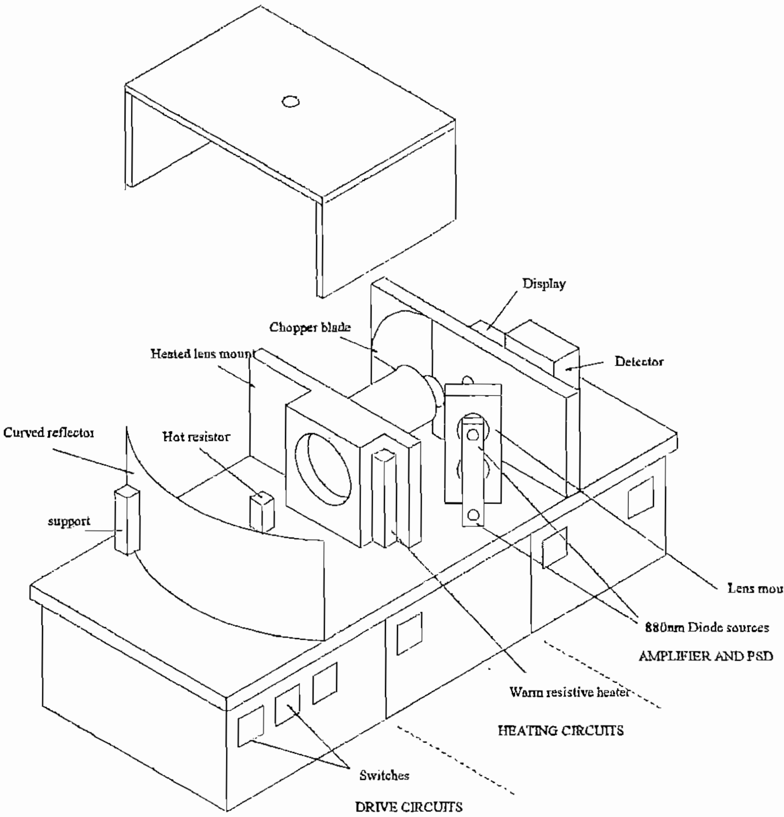

Figure 5.2: Schematic diagram of induced absorption instrument

The signal to noise ratio from this system is now calculated to predict the minimum detectable change in sample induced-absorption. Integration of the black body curve over the filter passband of 6.6 to $15.5\mu m$ gives the emitted power from the $200^{o}C$ resistor source as $149mW\ cm^{-2}$. Allowing for the collection efficiency of the optics and optical component transmission, the power intercepted by the detector is $17.1\mu W$. The detector's responsivity was $100V/W$. In calibration mode the depth of modulation is

100% and a signal of $1.71mV_{pp}$ is given at the detector output prior to amplification. Assuming the system's noise to be detector-limited, the total noise within the PSD's $1Hz$ bandwidth at this chopping frequency is $14nV$, giving a signal to noise ratio of 1.22×10^5.

The minimum detectable change in sample transmission therefore gives rise to a $14nV$ signal in the $1Hz$ bandwidth. This enables measurement of an absolute change in transmission of $0.8 \times 10^{-3}\%$. The depth of induced-modulation as a function of excitation power density is now used to demonstrate the adequacy of this. The depth of modulation for a high bulk purity etched sample without AR coatings with $10W\ cm^{-2}$ of excitation at $980nm$ has been found to change the transmission from 47% to 5% at $10\mu m$. This gives an induced-absorption transfer function of 0.224 per W per cm^2 at $10\mu m$. Allowing for optical collection efficiency, component transmission and the wavelength-shift of the excitation, the LED's are predicted to give an absolute change in transmission of 1.2%. With this absorption the signal to noise ratio is $1.2\%/0.8 \times 10^{-3}\% = 1500 : 1$. Although the germanium transmission in the excited state is not uniform over wavelength over the measured 6.6 to $15.5\mu m$ band, the signal to noise ratio is still very high. Hence at this level of absorption in high purity germanium there is no difficulty in accurately determining changes in absorption. Much of the etching work to determine changes in surface recombination velocity on germanium samples took place initially with low bulk purity samples in which lower changes in transmission were induced. In these experiments the much lower signal-to-noise ratio was still seen to give accurate results with little noise. Typical results for the FOM values obtained are given in the next section.

5.1.1 Experimental results using absorption diagnostics

The experimental results of etching samples to reduce their surface recombination velocity are given here, and the background theory is outlined in Chapter 6. In summary, etching is used to reduce the surface recombination velocity through removal of the mechanically-damaged surface which occurs during polishing, and through the termination of the surface with a uniform oxide, which bends the energy bands upward as described in Section 3.2.2. This results in a pronounced increase in the excited steady-state carrier density since optically-excited carriers are generated so close to the front sample surface. The change in transmission induced by pulsed excitation of the sample at $35Hz$ is sufficiently fast to give a PSD signal which is proportional to the depth of modulation in the steady state as a spectral average over the filter passband.

The instrument was used to determine the depth of modulation of mechanically-polished samples, and their induced absorption was calculated by the FOM. It was essential to etch samples for them to show any optically-induced absorption whatsoever. The experiment uses a wide range of chemical, electrolytic and reactive ion etch techniques with samples of different purity to determine the FOM achieved after progressive etching. The etch rate and hence depth of material removed during each etch period was determined by masking a test sample. Repetitive etching of a sample for fixed short periods removed layers of polish-damaged germanium, reducing the surface recombination velocity. Determination of the FOM using the instrument showed the improvement after each etch period. Mechanical polishing physically disturbs the surface to a depth ten times the particle size used in the final stage of polishing [102], giving a predicted damage depth of up to $3\mu m$. Fractions of this damaged layer were removed during each etch period to see the effect of progressively reducing the surface recombination velocity.

The FOM, or depth of modulation attained, was expected to steadily increase with removal of the damaged-layer until it was completely removed and the surface recombination velocity reached a minimum for that particular etch. At this point the depth of modulation attained would be limited by the recombination of carriers in the bulk, further material removal causing the depth of modulation to plateau. If two surface effects occurred during etching, such as the removal of the damaged layer and its subsequent termination, two depth-of-modulation plateaux might be observed. The surface-termination plateau may occur after removal of a thin layer of surface material, and the damaged material plateau may occur after a thicker layer of $\sim 3\mu m$. Three typical graphs showing the relative FOM from Equation 5.2 vs depth of material removed are shown for different etchants (detailed in Appendix B) in Figure 5.3

Figure 5.3 clearly shows the presence of only one plateau on each trace. This occurs well-before removal of the $3\mu m$ polish-damaged layer, and was typical for wide range of etchants used, indicating that one process dominates in determining the maximum depth of modulation attained. Since this plateau occurs before the damaged layer is completely removed, it is the surface termination that is more important in giving a low surface recombination velocity than the quality of the surface, after a thin layer of material has been removed. The absence of a second plateau after $3\mu m$ indicates the relative unimportance of the surface damage after its termination. Complete results for both wet and dry etch techniques are presented in Chapter 6, in optimising the induced absorption.

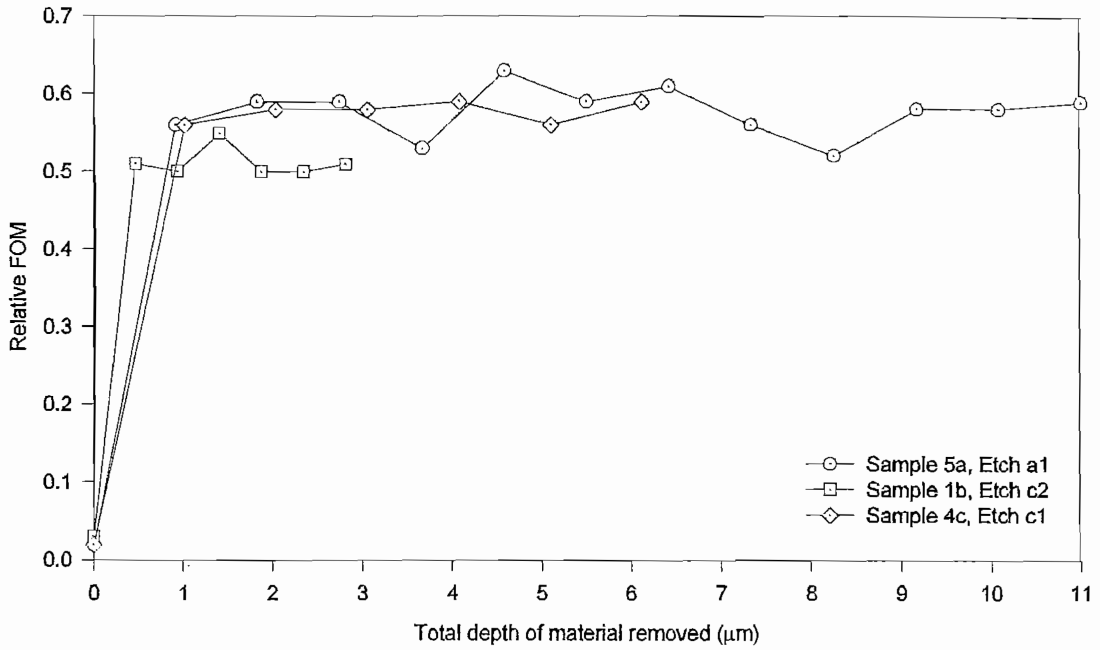

Figure 5.3: Relative *FOM* for two samples vs total depth of material removed

5.2 Temporal diagnostics: CO_2 laser probe

This section reports an experiment to determine the temporal change in sample transmission in the 8 to $14\mu m$ region when absorption is induced by a spatially-uniform optical pulse. This is used to validate the temporal response model for one-dimensional diffusion in Section 4.3.1. This required an infrared beam to probe the excited region during carrier excitation and decay. Determination of the induced absorption at a spot wavelength is preferable to that over a wider spectral region (such as from a filtered black body beam) since it provides validation of the model at a wavelength at which the hole absorption cross section is known. This is quoted in the literature for $10.6\mu m$, a common CO_2 laser wavelength, and is also used here. The use of a laser beam probe has the advantage of probing a small cross sectional area, although its coherence results in interference between reflections from the germanium-air interfaces. The strongly temperature-dependent refractive index of germanium in the presence of temperature changes significantly alters the transmitted intensity, complicating analysis of transmission measurements. Tilting the sample reduces the effect of multiple internal reflections but measures the transmission off normal incidence. However, if transmission measurements are made at normal incidence over a short time, prior to which the sample has attained a steady temperature from the optical excitation, then subsequent temperature changes are very small and have negligible effect on the transmission.

The temporal transmission of various samples was measured during pulsed optical excitation from a fixed peak power density ($10W\ cm^{-2}$) $1ms$ pulse at $980nm$ using a CO_2 laser probe beam and Thermo-Electric (TE) cooled Mercury Cadmium Telluride (MCT) detector. The MCT detector was used primarily due to its fast temporal response. Although a pyroelectric detector may be configured for fast response at the expense of responsivity, a much higher power at $10.6\mu m$ probe wavelength is required to give a high signal-to-noise ratio. The experimental setup is shown in Figure 5.4.

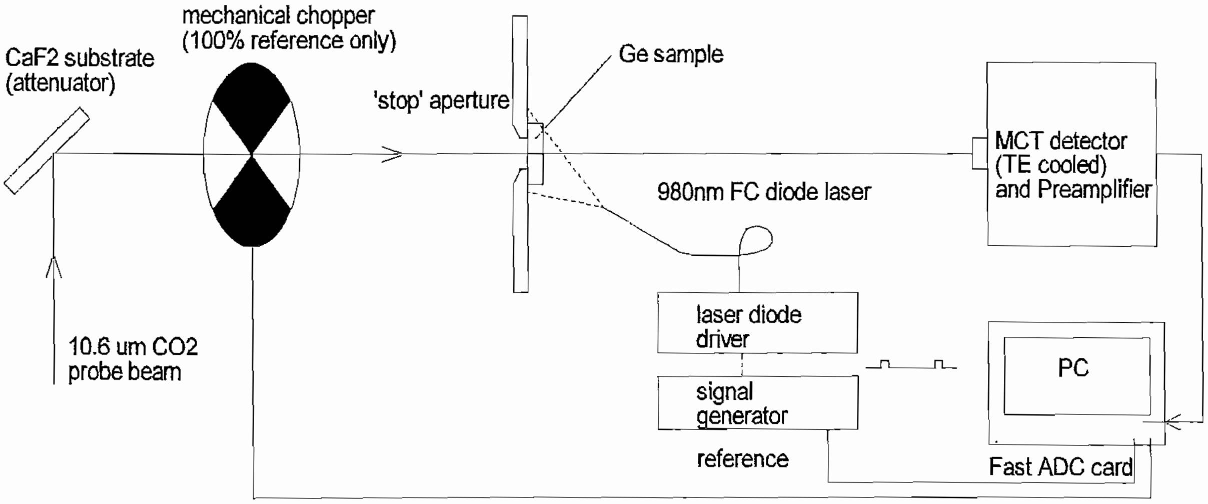

Figure 5.4: Experimental setup to determine temporal change in transmission

The depth of modulation in Figure 5.4 is calibrated using the mechanical chopper with the germanium in place. In the absence of the $980nm$ optical excitation, this gives the 100% depth of modulation signal . Subsequent transmission measurements with the chopper halted and the germanium optically excited are then scaled to this 100% signal to give the % transmission. It is essential that the optical excitation uniformly excites a region several diffusion lengths around the area sampled by the CO_2 probe beam. Excitation of only the probed aperture gives rise to lateral diffusion during carrier decay, which is not modelled by the one-dimensional diffusion equations in Section 4.3.1. Lateral diffusion occurs (Section 4.5) during apertured excitation in the presence of a significant lateral excitation power density gradient. Lateral diffusion is modelled by the latter equations in Chapter 4, although accounting for this unnecessarily complicates simulations which already require considerable computation time.

5.2.1 Experimental results using CO_2 laser probe

Three etched samples of different bulk purity and surface properties were used in the temporal transmission experiments described here, in the spatial carrier distribution experiments, and the microwave experiments described in the next two sections to provide continuity between results. The sample properties were tested in the centre of each face to avoid effects associated with enhanced carrier recombination at the sample edges. The transmission was monitored as a function of time using the setup in Figure 5.4, and is given in Figure 5.5. The carrier decay constant $(1/\tau_{effective})$ was then determined using Equations 5.3 and 5.4. Ignoring multiple reflections, the transmission is related to the absorption to a good approximation by Equation 5.3:

$$T(t) = T_0 e^{-\alpha(t)} \tag{5.3}$$

$$\alpha(t) \propto N_{area} e^{-\frac{t}{\tau_{effective}}} \tag{5.4}$$

Where N_{area} is the area carrier density and the constant of proportionality is the hole absorption cross section at $10.6\mu m$. As shown in Figure 4.10, Section 4.3.1, the carrier decay constant is given by the gradient of the $ln(\alpha(t))$ curve, which in the presence of a high surface recombination velocity is initially steep, reducing with time to a constant gradient once the carrier distribution reaches a stable shape. The transmission normalised to the unexcited state transmission, and accompanying $ln(\alpha(t))$ vs time graphs are shown in Figures 5.5 and 5.6 respectively.

The important region of Figure 5.6 is the decay period, for time $> 1.0ms$. This shows the predicted slightly faster initial decay constant and its subsequent reduction to a constant value. The gradients during these two stages of carrier decay are similar to that predicted for low surface recombination velocities in Figure 4.10. A smaller difference in gradients indicates a lower surface contribution to the total carrier recombination rate. The initial and later, constant, effective lifetimes are calculated from the decay constants using Equations 5.3 and 5.4 by measuring the gradients of the above graphs and are shown in Table 5.1.

Since the final $\tau_{effective}$ reduces with reducing bulk carrier lifetime and increasing

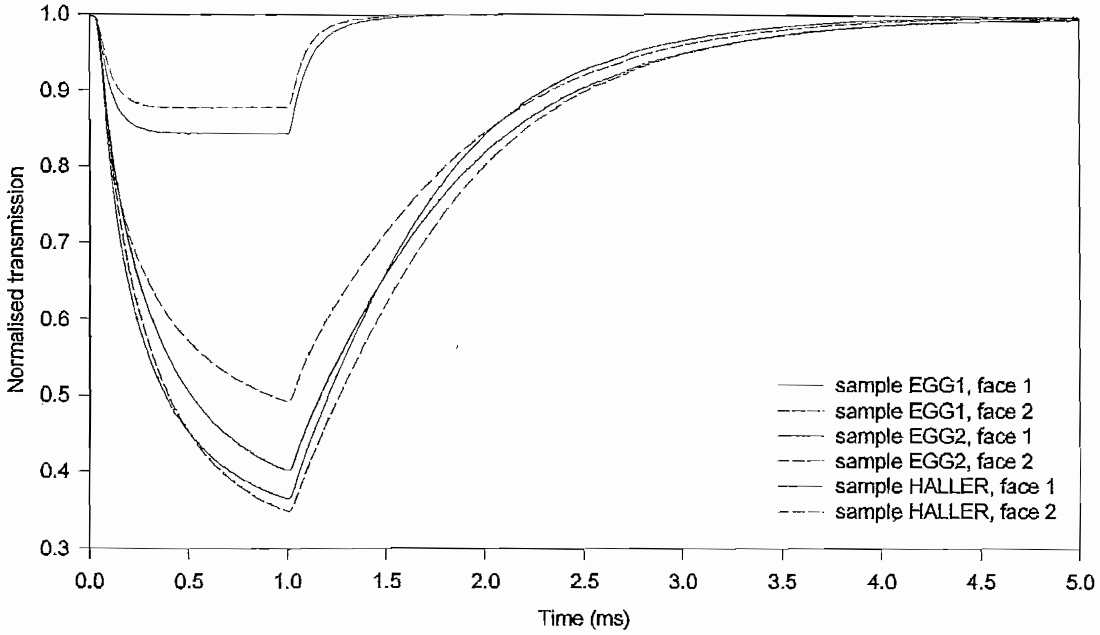

Figure 5.5: Transmission of samples at $10.6\mu m$ following optical excitation by a $1.0ms$ pulse of $5W\ cm^{-2}$ at $980nm$

surface recombination velocity, longer effective lifetimes are expected in samples which attain a higher depth of modulation, and this is seen in Figure 5.6. Since this experiment measures transmission, the effects of surface and bulk recombination are combined in both the above effective lifetimes. The separation of bulk and surface effects requires an alternative technique to eliminate one of the effects. This is achieved practically when one effect dominates, so if surface recombination were negligible, the bulk lifetimes would be given by the final $\tau_{effective}$ above, and this would equal the initial $\tau_{effective}$. In the Haller sample it is likely that the bulk carrier lifetime is low, so the effective lifetime is dominated by bulk recombination. In the two EGG samples the bulk lifetime is much longer, so both surface and bulk effects determine the effective lifetime. Separation of the bulk and surface recombination effects is achieved by the techniques in the two following sections, which subsequently validate the carrier distribution model.

Although neither the initial or final decay constants are unique functions of S and τ_{bulk}, these decay constants were plotted and the two unknown parameters, S and τ_{bulk}, were solved-for graphically. The time-dependent one-dimensional diffusion model was used to simulate the initial and final effective carrier lifetimes as a function of the S and τ_{bulk} parameters, for the two effective lifetimes independently. The best fit param-

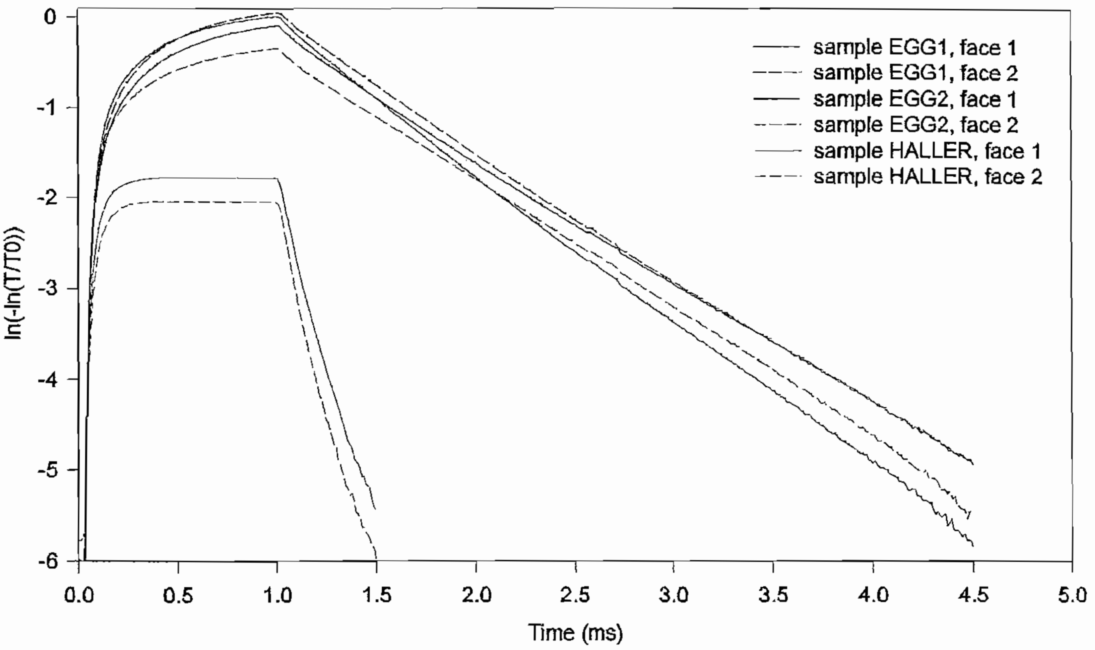

Figure 5.6: Variation in decay constant with time for graphs in Figure 5.5

eters occurred at the intersecting point of the two effective lifetime dependencies. The dependence of the two lifetimes on S and τ_{bulk} is shown graphically for Sample 2 face 2 in Figures 5.7 and 5.8. The decay constant (s^{-1}) (reciprocal effective carrier lifetime in Table 5.1) is plotted in the two figures.

Figure 5.7 gives the predicted initial decay constant (s^{-1}) for sample EGG2, showing detail for the extraction of the face 1 initial decay constant of $2390s^{-1}$. The S and τ_{bulk} parameters corresponding to this decay constant occur along the light blue line (fourth bar up). The yellow (top left) and dark blue (bottom right) portions of the graph mask further similar curves and are filled-in to highlight the important inner region. Figure 5.8 shows the dependence of the final decay constant for this sample thickness, giving detail for extraction of the EGG2 face 1 final decay constant of $1550s^{-1}$. The light blue line (fourth bar up) corresponds to this value. When overlaid, the marked intersecting point of these two light blue lines gives the fit parameters which are shown in Table 5.2.

For the thinner Haller sample the two modelled decay constants showed near-parallel r-shapes in the above figures as opposed to the intersecting lines seen in the figures. For this sample the intersection occurred over a wide range of S and τ_{bulk} parameters, showing that the technique is not accurate for thin samples with high rates of surface and bulk recombination. The similar results for the bulk carrier lifetime for each sample

sample	surface	initial $\tau_{effective}$ μs	final $\tau_{effective}$ μs
EGG1	1	468	782
EGG1	2	495	749
EGG2	1	480	669
EGG2	2	453	735
Haller	1	91	196
Haller	2	79	186

Table 5.1: Initial and final decay constants for carrier decay in three samples for both surfaces

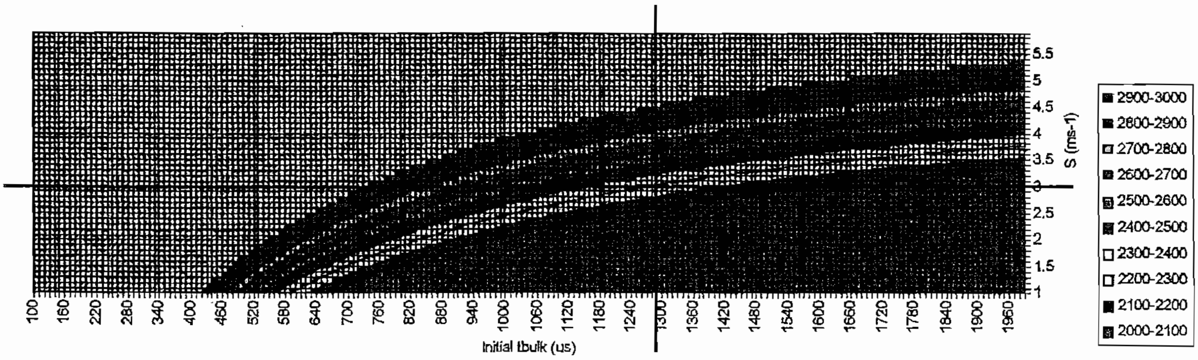

Figure 5.7: Decay constant dependence on S and τ_{bulk} for initial $\tau_{effective}$ showing best-fit point of intersection

in Table 5.2 show the accuracy of this technique for these particular values of S and τ_{bulk}. The S parameter was not expected to be identical for all samples, despite use of the same etchant, based on its known variability following wet chemical etching (Section 6.1.3). The S and τ_{bulk} results from this experiment are compared with those extracted from other experiments in Section 5.5.

5.3 Lateral diffusion diagnostics: blackbody probe

The models developed in Section 4.3 predicted the carrier distribution following optical excitation by a gaussian line of carriers, or by a circular gaussian illumination function. The present section gives the experimental results for the absorption profiles result-

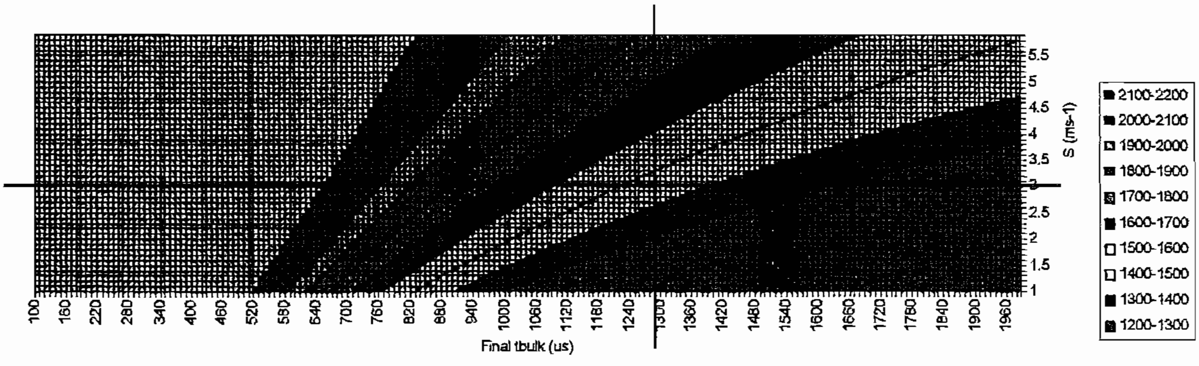

Figure 5.8: Decay constant dependence on S and τ_{bulk} for final $\tau_{effective}$ showing best-fit point of intersection

sample	**surface**	**fitted τ_{bulk} μs**	**fitted S ms^{-1}**
EGG1	1	1390	2.8
EGG1	2	1280	2.5
EGG2	1	1140	3.0
EGG2	2	1290	3.0
Haller	1	no fit	no fit
Haller	2	850	9.5

Table 5.2: Parameters extracted from the initial and final lifetimes during temporal carrier decay

ing from three-dimensional carrier diffusion during continuous generation by a circular gaussian-like source from an optic fibre. These are compared to the modelled situation using the carrier parameters extracted from the temporal carrier-decay measurements, given in Table 5.2.

The sample is optically excited by a collimated optic fibre source at $980nm$. The resulting lateral carrier distribution is measured via the transmission of a filtered focussed black body beam probe, which is scanned across the sample to determine the transmission as a function of position through the peak of the excitation's power profile. The filtered black body beam has a much wider spectral and physical width than a CO_2 laser probe. However a CO_2 laser is unsuitable in this experiment which takes up to an hour to scan a $15mm$ width sample. Over this period, temperature and hence refractive index variations, especially in the excited-surface region, cause interference fringes that are not easily accounted for. More importantly, inevitable variations in sample thickness across the scanned region cause interference fringes which complicate transmission measurements. This is avoided by using antireflection coatings or a wedged sample, but the required wedge angle is destructive to the sample, and the application of AR coatings is time-consuming. Therefore a blackbody probe beam is more appropriate in this experiment, and the effects of its physical width and finite optical bandwidth are accounted for. The experimental setup is shown in Figure 5.9.

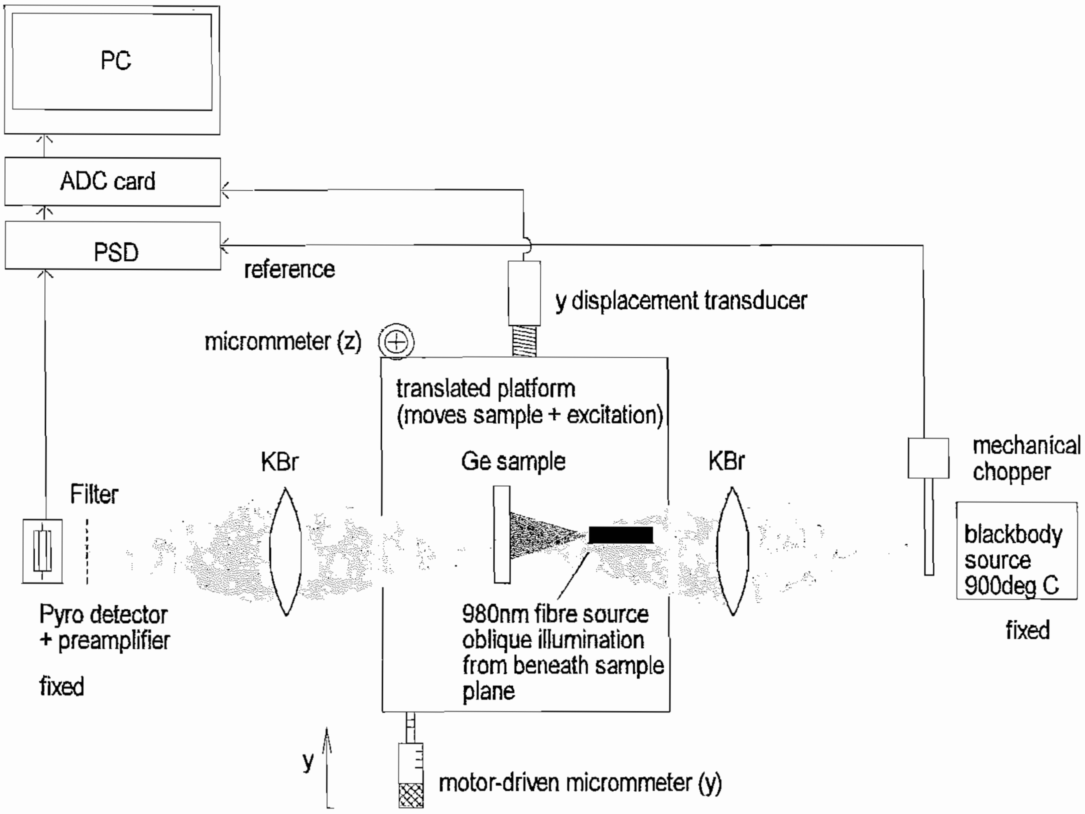

Figure 5.9: Experimental setup to determine extent of lateral diffusion

In Figure 5.9 the continually-excited sample is scanned in the y direction across the fixed chopped black body probe beam and the transmission $T_{excited}(y)$ is determined by the pyroelectric detector and PSD. The transmission measurement is repeated with the excitation source extinguished, giving a reference transmission $T_{unexcited}(y)$.

The 3D carrier diffusion model in Section 4.5.1 predicts the carrier distribution during steady state optical excitation by a known source function as a function of lateral position y and axial position x, along a line $z = b/2$ through the excitation peak. Integration of the volume carrier density $n(x, y)$ over x gives the area carrier density, $n_{area}(y)$, enabling calculation of the transmission at wavelength λ using Equation 5.5 and the experimentally-determined absorption cross section as a function of wavelength $\alpha(\lambda)$.

$$T(y,\lambda) = \frac{(1-R)^2 \cdot e^{-\alpha(\lambda)\cdot n_{area}(y)}}{1 - R^2 e^{-2\cdot\alpha(\lambda)\cdot n_{area}(y)}} \tag{5.5}$$

5.3.1 Effects of the blackbody beam on the experiment

In addition to the spectral dependence of the absorption of excited germanium, the spectral emission of the 900°C blackbody power, $BB(\lambda)$, and the spectral transmission functions of the optical components in the experiment's beam-path determine the power spectral density incident on the detector. In the optical setup in Figure 5.9 the bandpass filter has extreme cutoff limits of $6.63\mu m$ (λ_1) and $15.5\mu m$ (λ_2), over which both the KBr lenses and unexcited germanium have constant spectral transmittance. However, the filter transmission function, $Filter(\lambda)$, has passband ripples which must be accounted for in determining the detector's response. The pyroelectric detector, with constant spectral sensitivity, gives a response ($Signal$) proportional to the incident power, averaged over wavelength. This is given by:

$$Signal_{Excited}(y) = \frac{P}{\lambda_2 - \lambda_1} \int_{\lambda_2}^{\lambda_1} BB(\lambda) \cdot T(y,\lambda) \cdot Filter(\lambda) d\lambda \tag{5.6}$$

P is a constant scaling factor given by the absolute values of blackbody power, lens transmission and detector sensitivity. The signal in the unexcited state is given by Equations 5.6 and 5.5 with $n_{area}(y)$ set to zero. The transmission spectrum $Filter(\lambda)$ was determined using a spectrophotometer.

The blackbody beam has a finite spatial width described by $BB(y)$, its spatial power profile at the spot sampling the transmission on the germanium surface. When a sharp absorbing edge is scanned across the blackbody beam, the transmission profile measured by the experiment is smeared-out in the y direction. This must be accounted for to accurately predict the lateral y width of the absorbing region in the germanium. Equation 5.6 predicted the detector signal at a *point* y on the sample. The blackbody power measured at the detector is given (Equation 5.7) by a convolution-like function, which is the integral of the product of the blackbody's spatial power profile and the Signal function (Equation 5.6) as the blackbody is scanned across the absorbing region in the y direction.

$$P_{Excited}(y) = \int_{-\infty}^{\infty} Signal_{Excited}(\chi) \cdot BB(y-\chi) d\chi \tag{5.7}$$

The exponential dependence of transmission on area carrier density alters the shape of the area carrier density profile, producing a transmission ratio profile which is broadened more at its widest point than at its narrowest. The blackbody's spatial power profile $BB(y)$ was determined by measuring the visible spatial emission profile of the $900°C$ source using a CCD array camera, and assuming it to be the same as the spatial IR profile. The measured profile was found empirically to fit the product of a Gaussian and Lorentzian function, given by $BB(y)$ with $\sigma_1 = 0.81mm$. The blackbody and laser excitation power distribution profiles are shown in Figure 5.10.

$$BB(y) = \left[e^{-\frac{1}{2}\left(\frac{y}{\sigma_1}\right)^2} \cdot \frac{\sigma_1^2}{y^2 + \sigma_1^2}\right] \tag{5.8}$$

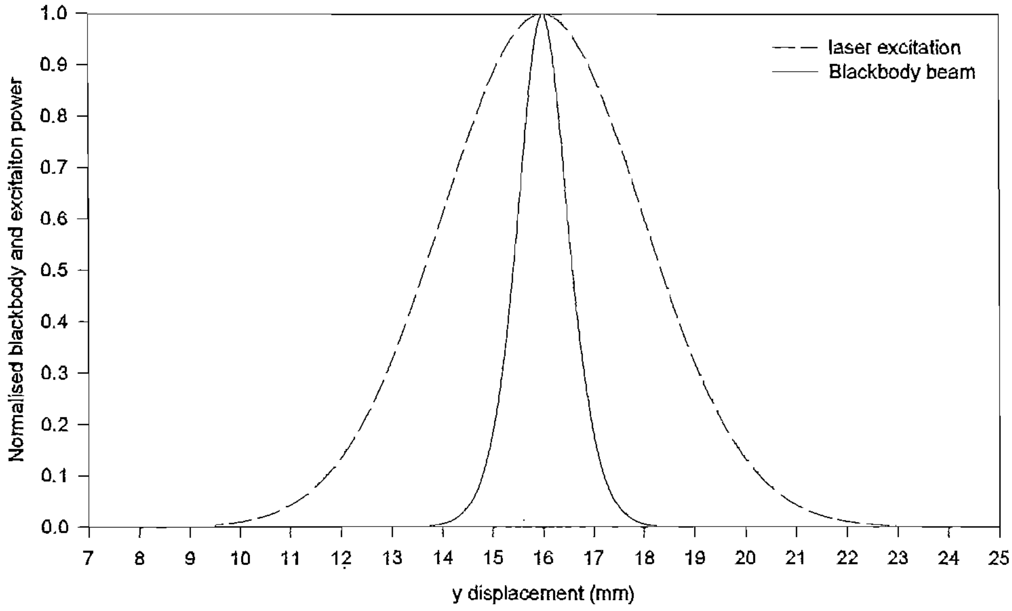

Figure 5.10: Measured spatial power profiles of the blackbody and laser excitation

Verification of the blackbody profile was achieved by scanning a metal strip of known thickness across the blackbody beam and comparing the profile predicted by Equation 5.7. The measured and fitted transmission profiles for a spatially square absorbing function are shown in Figure 5.11, in this case for a strip of razor blade of width $1.94mm$.

The agreement of the fit in Figure 5.11, in addition to that for several other widths of absorbing razor blade strips gave confidence that lateral smearing of the measured transmission profile was accurately accounted for by this value of σ_1 in the convolution process.

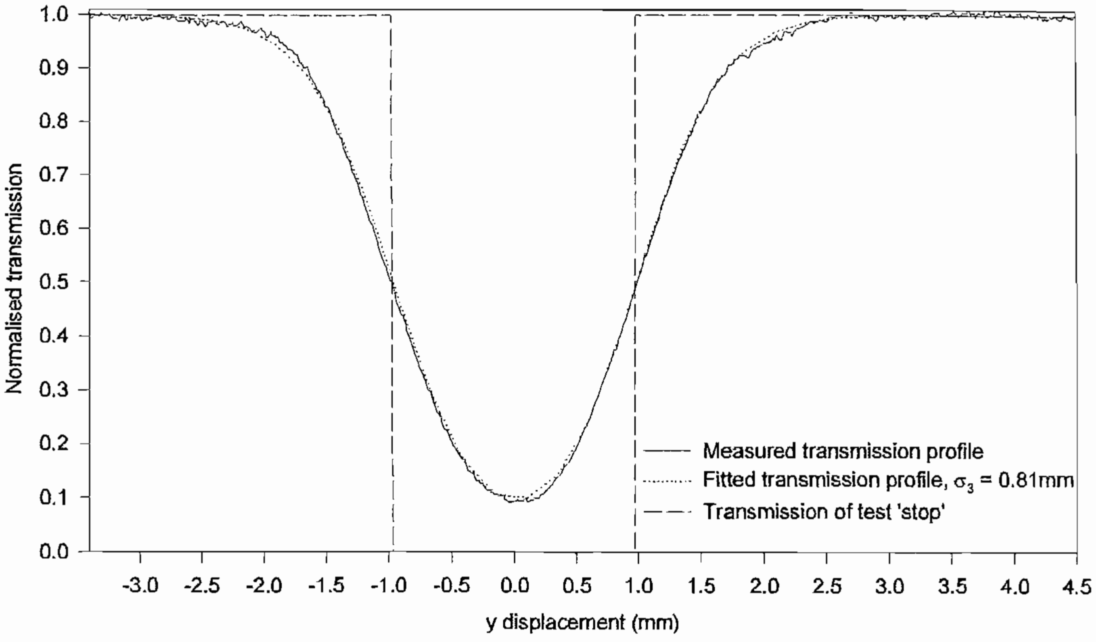

Figure 5.11: Measured and predicted absorption profiles resulting from scanning a razor blade across the blackbody beam

5.3.2 Experimental results: lateral diffusion

This experiment measures the lateral transmission profiles during constant excitation by a near-circular power distribution function from a laser beam using the setup in Figure 5.9. The normalised transmission as a function of lateral position y is calculated as the ratio of the transmission in the excited to unexcited states. The measured transmission is an average over the filter bandwidth, thus the transmission at $10\mu m$ is lower than shown by these graphs. The normalised transmission profiles are given in Figures 5.13 to 5.18 for both faces of the same three samples used in the temporal measurements. These figures also show the predicted transmission profiles using the convolution technique in Equation 5.7, which uses the lateral three-dimensional diffusion model to predict $n_{area}(y)$. Profiles are shown for the extracted carrier parameters in Table 5.2, and for $S = 3ms^{-1}$ and low values of τ_{bulk}. The power distribution of the excitation laser beam distribution is slightly elliptical due to non-normal incidence on the germanium and to a good approximation is treated as circular. This was measured along a line y through the peak of the emission profile using a linear silicon CCD array camera, and is shown in Figure 5.12.

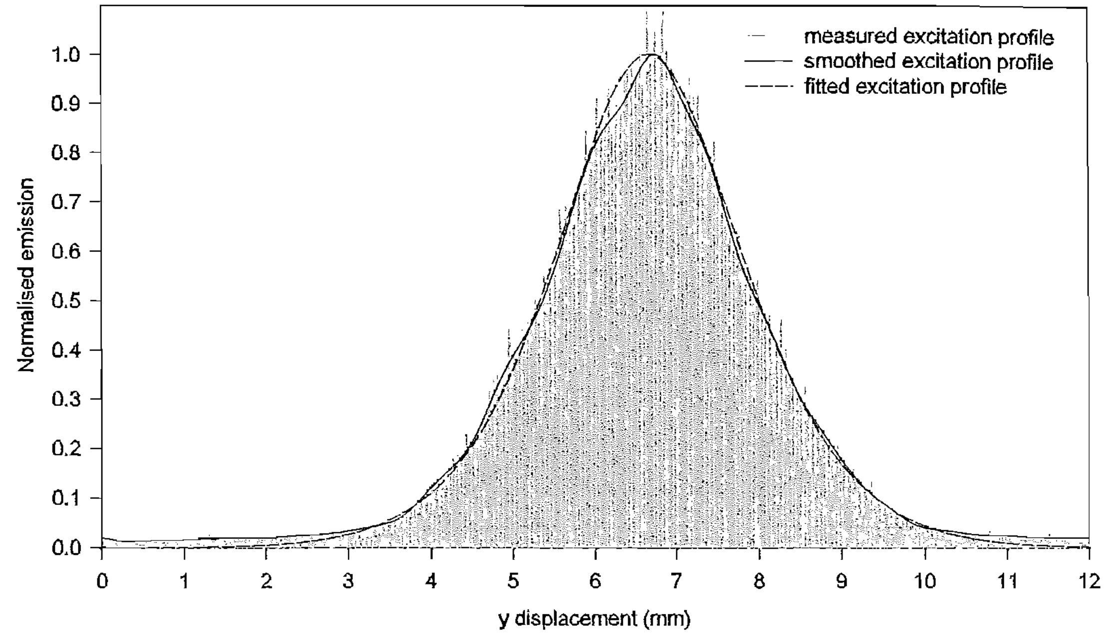

Figure 5.12: Scan through the peak of the 980nm excitation profile, and the fitted profile

The measured power excitation profile in Figure 5.12 is a rapidly spatially-varying multimode function. This was Fourier-transformed and the high frequency harmonics were removed to determine an average power distribution profile, shown by the 'smoothed' excitation profile. Various functions were fitted to this smoothed profile to obtain the best fit function and its parameters. The smoothed function was well-fitted by the product of a Gaussian and a Lorentzian power distribution function (Equation 5.8) shown in the figure, with $\sigma_1 = 1.84mm$ and centred in the middle of the sample, $y = a/2$.

The steady-state solution to the three-dimensional diffusion equation in Section 4.5.1, with this particular source function was used to determine the area carrier density $n_{area}(y)$ through the centre of the excitation, $z = b/2$, enabling calculation of the transmission ratio profiles in Figures 5.13 to 5.18.

Figures 5.13 to 5.18 show lateral carrier diffusion altering the measured absorption profile from the power profile incident on the sample surface. Due to the non-abrupt excitation profile, determination of the carrier diffusion length is not given by a simple function by looking at Figures 5.13 to 5.17. As expected, lateral diffusion is more pronounced in the case of the longer bulk carrier lifetime EGG1 and EGG2 samples. However, the extent of lateral diffusion measured by the experiment is much less than that predicted using the bulk carrier lifetime and surface recombination velocity pa-

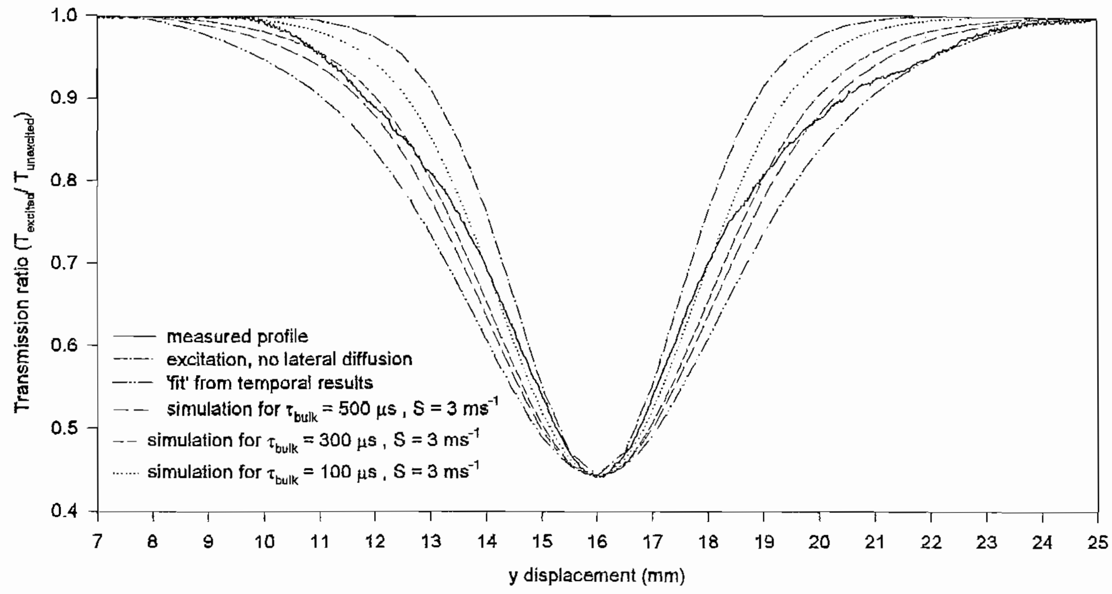

Figure 5.13: Laterally convolved excitation function, measured and predicted induced absorption profiles for sample EGG1 face 1

rameters extracted from the temporal measurements. The fact that the shapes of the functions are dissimilar is suggestive of incorrect parameters, but no combination of S and τ_{bulk} parameters were found to satisfactorily fit the measured data. The shape of the profile is incorrect for simulations with low bulk carrier lifetime.

The above experiments were repeated many times to verify the discrepancy between modelling and the experiment. The sources of experimental or modelling error were rigorously checked, but none could account for the level of discrepancy observed. With hindsight from the microwave modelling (Section 5.4) and its experimental results, confidence existed that the 'fit' bulk carrier lifetime and surface recombination velocity parameters used in the present simulations were reasonable. The areas investigated for errors are now summarised.

Calibration errors: Linear displacement transducer on translated platform: micrommeter reading on travelling-tables ensured the automated transducer gave accurate readings. Silicon CCD beamscanner used to measure the excitation diode laser profile: beam width measurement verified by measuring an aperture of known width. Laser excitation power variation: Power meter used to ensure negligible drop in laser power over two-hour period of experiment.

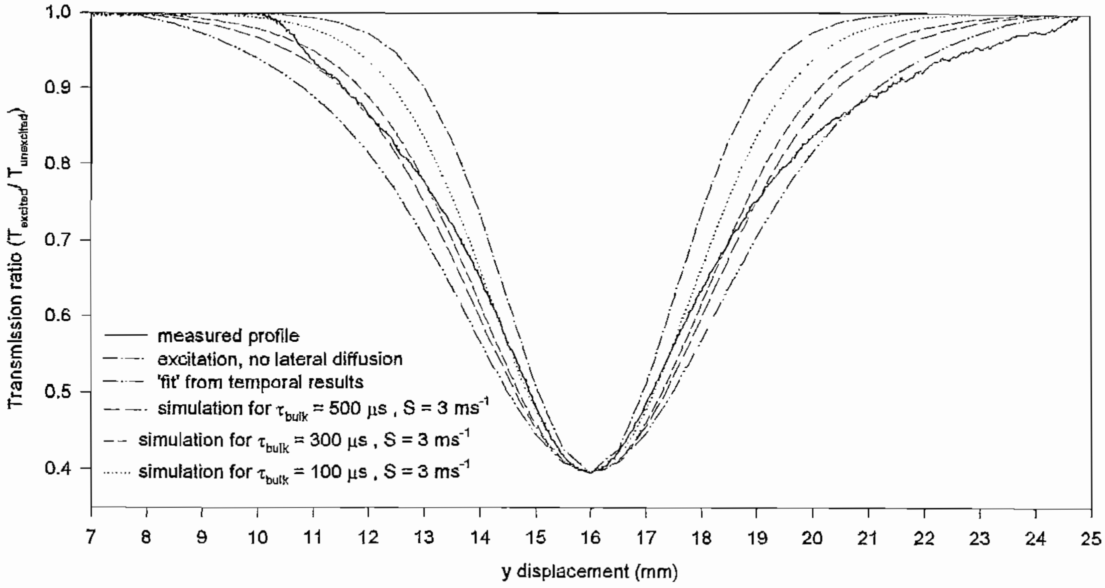

Figure 5.14: Laterally convolved excitation function, measured and predicted induced absorption profiles for sample EGG1 face 2

Experimental errors: The same region was measured on all samples to ensure any (unlikely) sample inhomogeneities were unimportant. Optical errors: germanium in the optical path instead of air, causing a beam-steering effect. This was verified by accurately measuring the width of thin metal strips on the germanium surface using the blackbody probe technique, simulating the absorption resulting from optical excitation of the germanium. This gave confidence that the blackbody beamwidth was accurately known. Time-dependent effect: room temperature-drift effects were verified by making transmission measurements at a fixed point on a continually-excited sample and showed negligible change over time. Divergence of laser beam affecting measurement of its profile width: divergence was measured as insignificant.

Modelling errors: Model parameters were verified, and the simulated extent of lateral diffusion was reasonable in the absence of very high S.

Real effects: Thermal lensing of the germanium: heating of the sample by the excitation causing a change in refractive index. Temperature gradients are very low due germanium's high thermal conductivity. There was no difference in the measured transmission when free-standing, and when a nitrogen jet cooled the sample surface during excitation.

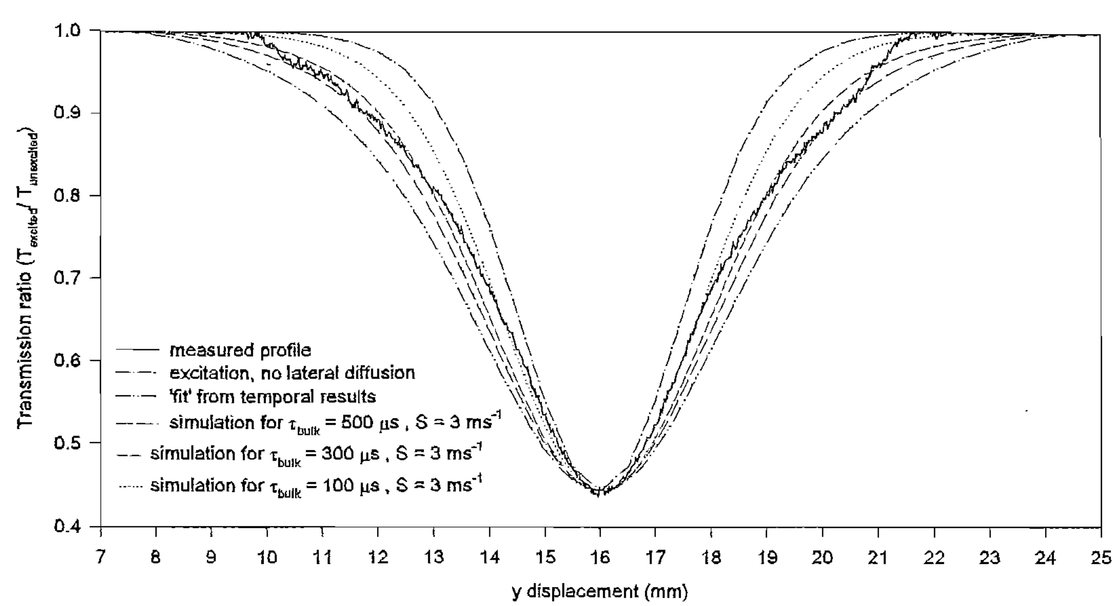

Figure 5.15: Laterally convolved excitation function, measured and predicted induced absorption profiles for sample EGG2 face 1

Is the surface recombination velocity excitation-intensity dependent? Measurements of the absorption profiles with half the excitation power as in above figure gave normalised absorption profiles which, when scaled, overlaid those in the above figures, showing that unless a saturation effect occurred, S and τ_{bulk} were not strongly linked to the excitation intensity. This gave confidence that carrier dynamics occur in a linear regime and that any effect of lifetime-dependence on carrier density is insignificant.

The parameters which gave a reasonable fit are shown in Table 5.3, although these are only rough parameters that do not accurately model the measured profiles. They are given to highlight the discrepancy between results from the temporal and, later, microwave reflectance techniques. A surface recombination velocity of $3ms^{-1}$ and $10ms^{-1}$ for the EGG and Haller samples respectively is used in the table. These values were close to those given by the two other techniques. $S =\sim 3ms^{-1}$ is reasonable after etching, based on the literature.

The large discrepancy between the model parameters that gave a reasonable fit in Table 5.3 and those extracted from experiments using the temporal and (later) microwave reflectance techniques shows that a significant and real effect, unaccounted for by the model, occurred with the lateral diffusion experiments. It is concluded that this is due

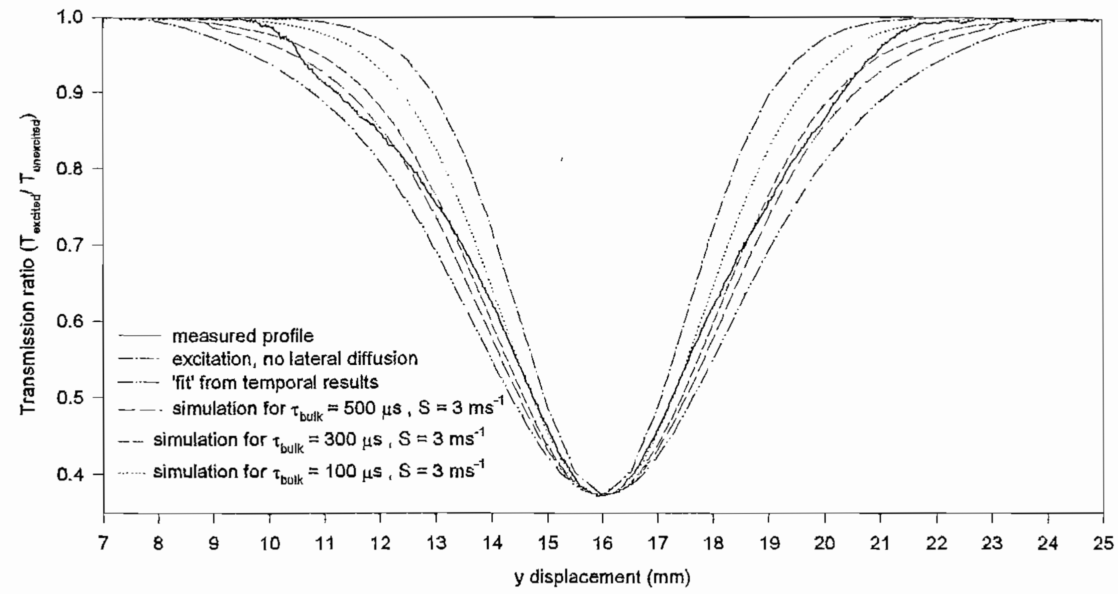

Figure 5.16: Laterally convolved excitation function, measured and predicted induced absorption profiles for sample EGG2 face 2

to a reduction in carrier mobility close to the surface due to enhanced surface scattering. The energy band diagram is bent upward at the excited germanium surface by the adsorbed species and oxide layer left by the etching process, as described in Section 3.2.2. The reduction in surface recombination velocity is due to the upward-bending of the energy bands. This increases the physical separation between conduction band electrons and energy levels of fast surface states which act as recombination centres, reducing the probability of electron transitions via these centres at the surface, as shown by Figure 3.4. However the upward bending of the energy bands creates a potential well

sample	**surface**	**fitted** τ_{bulk} μs	**fitted** S ms^{-1}
EGG1	1	100	3
EGG1	2	100	3
EGG2	1	100	3
EGG2	2	100	3
Haller	1	< 25	10
Haller	2	< 25	10

Table 5.3: Lateral diffusion profile model parameters

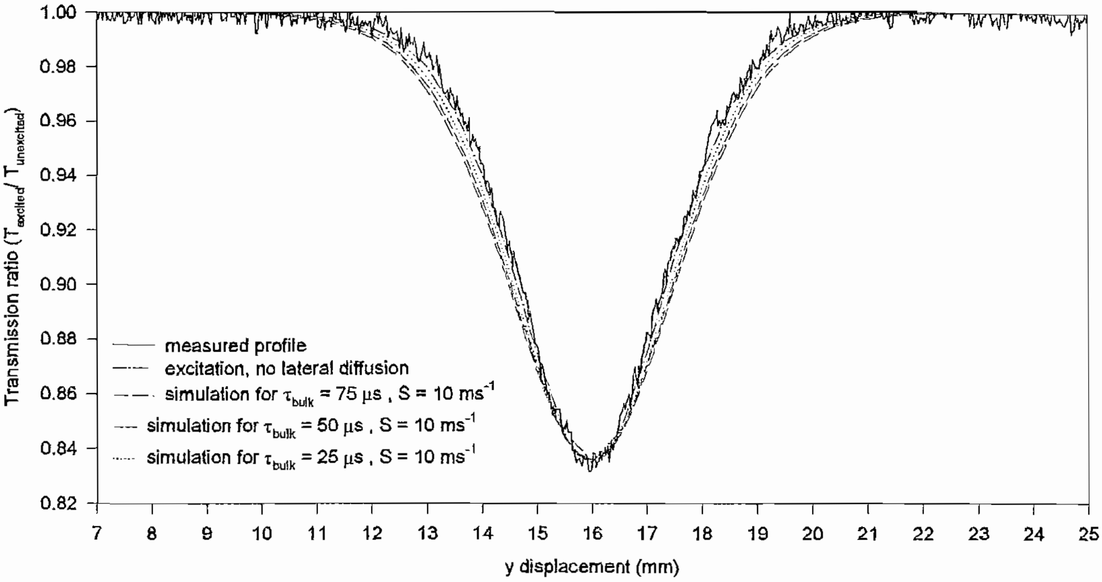

Figure 5.17: Laterally convolved excitation function, measured and predicted induced absorption profiles for sample HALLER face 1

at the surface which confines holes. Carriers generated near the surface by the optical excitation move laterally and axially into the germanium. Carriers moving axially are affected by both diffusion and drift due to the electric field resulting from the band bending in this direction. Under moderate excitation levels (only within the excited region) the hole states in the potential well are easily filled by the excitation, and axial diffusion due to the concentration gradient of the excess holes takes place. At the same time the electrons move axially by both drift (from the band-bending electric field) and diffusion (from the axially-decaying optically-excited carrier distribution). The net effect is to enhance the rate at which both electrons and holes move axially into the sample, reducing the recombination rate at the surface as the carrier plasma preferentially moves away from the excited surface. The effect of this enhancement of the axial rate of plasma movement is accounted for by the surface recombination velocity in its reduction in the recombination current flowing to the surface. This is modelled by theory as simply a diffusion process but is achieved practically (following etching in any case) by both a diffusion and a drift process through bending of the energy bands. The carriers that move laterally are now considered. Carriers generated by the optical excitation have a lateral concentration gradient, the effect of which is modelled by the three-dimensional diffusion

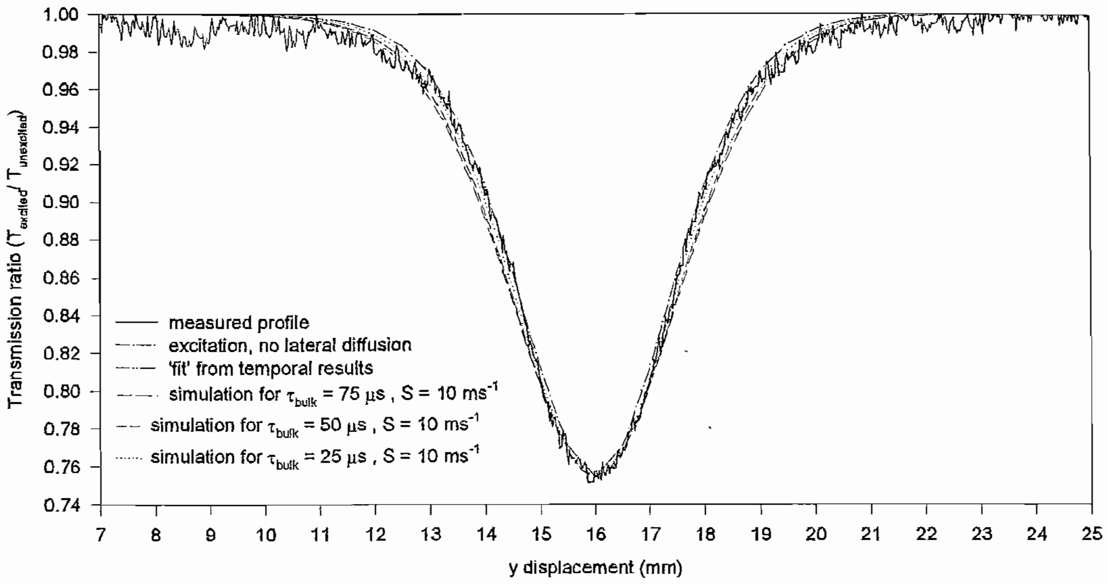

Figure 5.18: Laterally convolved excitation function, measured and predicted induced absorption profiles for sample HALLER face 2

model. However, this assumed a constant homogeneous diffusion coefficient. Optically generated carriers have a high concentration within an absorption depth ($\sim 0.5\mu m$) of the surface. If the energy bands are bent over this region, holes diffusing laterally outside the excited region, experience a macroscopic force toward the surface potential well. The absence of carrier generation outside the excited region means the well is not filled and so axial diffusion is reduced. If a carrier's mean free path is similar to the width of the potential well, enhanced surface scattering is effective at reducing the carrier mobility in the potential well [103]. Since this is more important to the laterally-diffusing carriers, this process leads to an inhomogeneous diffusion coefficient, which is higher in the axial direction than the lateral. A homogeneous diffusion coefficient is assumed by the models in Chapter 4. The condition for reduced lateral diffusion is now evaluated to show its importance in the experiments.

If the surface energy band diagram in Figure 5.19 is assumed, where the surface charge density in the ambient is equal to that in the potential well, n_s and n_0 are the volume carrier concentration at the surface of the germanium and in the bulk respectively, qV_s is the energy difference of the band bending at the surface.

This discussion initially determines the mean free carrier path length for electrons and

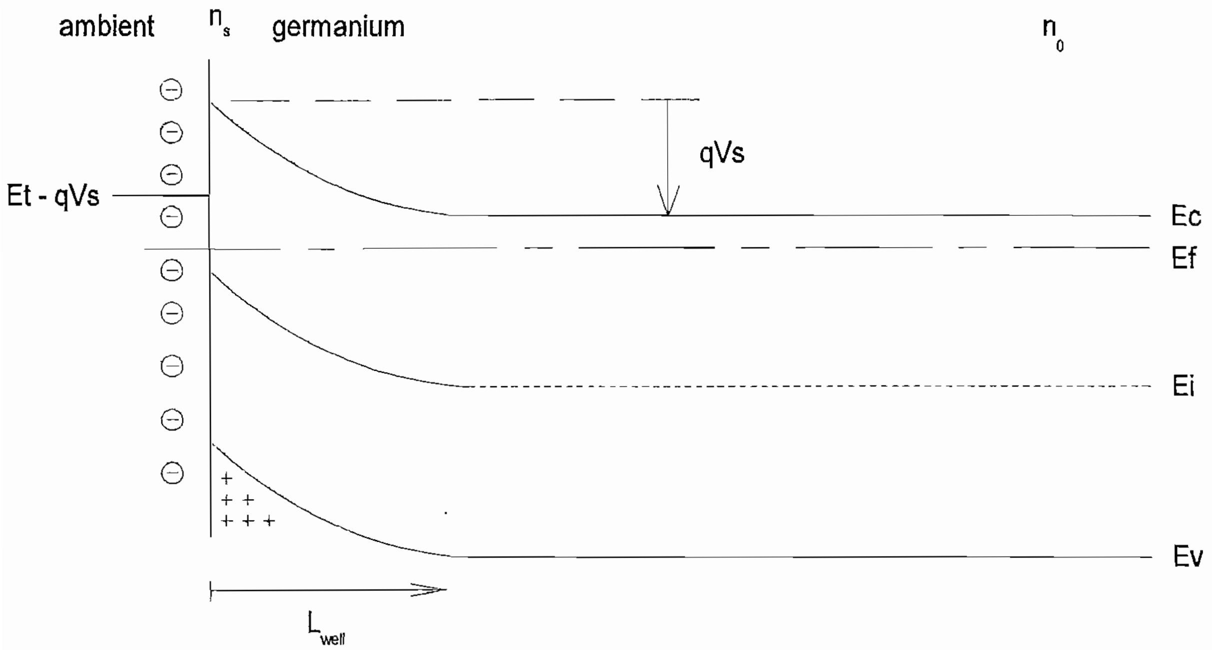

Figure 5.19: Energy band diagram of n-type germanium at the excited surface

holes. This is shown to be small in comparison the length L_{well} over which the potential well exists from the surface, showing that surface scattering is important. The reduction in carrier mobility in the potential well is then quantified from theory [103]. Finally, the mobility reduction is shown to be significant in the presence of optical excitation levels used in the modulator.

The carrier's average thermal velocity is given by equating the carrier kinetic energy $(1/2m\overline{v}^2)$ with the thermal energy $(3kT/2)$. Use of the carrier mobility Equation 5.9 gives the time between collisions, enabling calculation of the mean distance between collisions.

$$\mu_{e,h} = q\frac{\tau_{scatter}}{m^{\star}_{e,h}} \tag{5.9}$$

If the room-temperature bulk mobility of 3900 and $1900cm^2/Vs$ is used for electrons and holes respectively, the maximum mean distances between collisions are $89.6nm$ and $66.7nm$ for electrons and holes respectively. Solution of Poisson's equation at the surface [30] gives the depth of the surface potential well as:

$$L_{well} = \sqrt{\frac{2kT\epsilon_0\epsilon_L}{q^2 n_0}} \tag{5.10}$$

where ϵ_0 is the permittivity of free space and ϵ_L is the relative permittivity of germanium, 16.0. A well width of $L_{well} = 1.38\mu m$ is calculated for intrinsic germanium; much longer than the inter-collision scattering distance. Therefore in intrinsic germanium the surface mobility is affected by enhanced surface scattering. The degree to which this is affected is given theoretically by Schrieffer [103], and depends on the level of surface energy band bending (qV_s). Experiments varying the contact potential (qV_s) on germanium [104] surfaces by using various gaseous ambients showed this could be changed by $18kT/q$ by bubbling oxygen through water and passing it over the sample. Using this level of band bending as an extreme case that may be achieved by a low surface recombination velocity etch, the predicted [103] ratio of surface (μ_{surf}) to bulk mobility is 0.28, and this ratio increases toward unity with increasing carrier density. The lateral diffusion length in this direction therefore decreases by a factor $\sqrt{\mu_{surf}} = 0.53$ compared to that in the bulk. The surface adsorbed charge density (n_{ads}, cm^{-2}) required to support this surface potential is now calculated from the solution to Poisson's equation:

$$n_{ads} = \sqrt{\frac{2\epsilon_0\epsilon_L n_0 V_s}{q}} \tag{5.11}$$

For intrinsic germanium this gives a surface charge density of $1.4 \times 10^{10} cm^{-2}$, which is reasonable since germanium has a surface atomic density of $3 \times 10^{14} cm^{-2}$. This corresponds to an adsorbed atom in every 21000, each giving rise to one unit of charge.

The above calculations considered intrinsic germanium. However the experimental situation involves much higher carrier densities in optically excited germanium. In optically excited germanium the Fermi level splits into two quasi Fermi levels: one for electrons and one for holes. These move toward the conduction and valence bands respectively under increased optical excitation, and are situated within kT/q of the respective bands at the point of degeneracy. Degeneracy begins at a carrier density of $\sim 10^{19} cm^{-3}$. As the optical excitation is increased the band bending at the surface reduces. The Fermi levels of the surface ambient and bulk material no longer align as the slow surface states giving rise to the surface charge density (with lifetimes in the order of hours or more) are no longer in equilibrium with the bulk germanium, so the conduction and valence bands flatten. This is predicted by Equation 5.11, which shows that an increase in bulk carrier density (n_0) causes a reduction in surface potential difference to maintain a constant surface charge density. At a uniform bulk carrier density corresponding to the onset of degeneracy ($n_0 = 10^{19} cm^{-3}$) the surface charge density required to maintain the $18kT/q$ surface potential is $9.07 \times 10^{12} cm^{-2}$. This corresponds to a 3% covering of the surface germanium atoms with unit charges. At this bulk carrier density the well depth L_{well} reduces to $2.14nm$, which is less than the mean distance between collisions, assuming Maxwell-Boltzmann statistics still apply a the onset of degeneracy. Hence a reduced mobility due to surface carrier scattering does not occur at very high bulk carrier densities. For the well depth to be equal to the mean free path for carriers, $89.6nm$ for electrons, the maximum bulk carrier density (Equation 5.10) is $5.7 \times 10^{15} cm^{-3}$. The assumption made here is that of a uniform bulk carrier density. In practice the axial steady state carrier distribution following continuous excitation has been shown (Chapter 4) to be exponentially decaying with displacement from the surface. Since the bulk carrier density several tens of microns from the surface is much lower than that at the surface, the maximum surface free carrier density in the germanium at which the reduced mobility due to enhanced surface scattering occurs should be up to an order of magnitude above this. Additionally, the region where the carriers diffuse laterally is outside the optically-excited region. Here much lower bulk carrier densities exist, so the lateral mobility still remains low, and this is the region where the reduced diffusion appears to be taking place.

It is therefore concluded that in the presence of a low surface recombination velocity that is achieved through surface energy-band bending, such as etching, the lateral diffusion coefficient is reduced. This is due to a reduction in surface mobility arising from enhanced carrier scattering over distances shorter than the width of the potential well. In the presence of optical excitation the enhanced carrier density reduces the width of the surface potential well compared to a carrier's mean free path, and the mobility due to surface scattering is only slightly reduced from its bulk value. Outside the excited region the surface potential well is much deeper, and therefore on average more holes collide with the surface and the mobility is more strongly reduced. The net effect of this is to give an inhomogeneous diffusion coefficient which is highest axially within the excited region, and lowest in a lateral direction outside the excited region. The effect of this on a carrier distribution resulting from gaussian optical excitation is to narrow the lateral profile in a region of intense optical excitation, and to reduce the extent of lateral diffusion outside the excited regions. This explains the measured diffusion profiles in Figures 5.13 to 5.18 which are narrower than predicted (for homogeneous diffusion) within the intensely-excited region although are more-readily fitted by low bulk carrier lifetime at the base of the measured functions where lower level excitation exists. The reduction in diffusion coefficient has the same effect on lateral diffusion as a reduction in the lifetime. The lifetime in the lateral direction however does not change due to this effect, which only alters the extent of lateral diffusion, and carriers still recombine with the surface lifetime.

Evidence for a reduced surface mobility has been observed through measurements of the Hall mobility in thin samples [105] [106]. The Hall voltage and resistivity of a cleaned n-type germanium sample placed in a vacuum was measured as oxygen was admitted to the system. The initial high conductivity due to the p-type surface was reduced as the increase in oxygen adsorption reduced the surface potential. Eventually the surface energy bands became flat. The calculated Hall mobility increased throughout the experiment, reaching the bulk value for the flat-band condition. The results are in qualitative agreement with Schrieffer's predictions [103]. More recent experimental evidence analysing the limitations of MOS structures [107] also supports the theory of a reduced surface mobility. In this case the channel mobility is varied by the applied gate bias. No literature covering the lateral diffusion coefficient following optical excitation such as that in the present experiments could be found. One reference [108] details an elaborate technique using pulsed optical excitation to generate a series of parallel lines of carriers on a silicon surface, and probing the temporal decay of the diffusing carrier profile parallel to the lines of carriers using a HeNe laser directed through the edge of the bulk sample. However, the primary purpose of that experiment was to measure the diffusion coefficient as a function of injected carrier density, and therefore the sample was probed in its centre to avoid the surface effects of interest here. The diffusion coefficient was calculated from the temporal carrier decay as a function of position on the carrier grid. In principle, such a technique of probing the axial extent of carrier diffusion but using a continuous excitation source could be used in future work in combination with the present results to provide further confirmation of the observations.

The effect of reduced lateral diffusion on the modulator is to increase the definition of a sharp-edge absorbing profile generated on the germanium surface, compared to that predicted by the models in Chapter 4. To fully model these effects would initially require the use of inhomogeneous diffusion coefficients in the three-dimensional diffusion models in Chapter 4. A more complete model would account for the electric field due to the band bending although an analytic solution to this problem is unlikely to exist. However, for uniform excitation of the germanium surface, even in the presence of strong band bending, surface recombination is likely to be adequately accounted for by its usual definition as simply a diffusion process. The effect of the drift component to the recombination current from the band bending is accounted for by a slightly lower surface recombination velocity.

5.4 Carrier decay diagnostics: Microwave reflectance

This section describes the microwave reflectance experiments used to validate the temporal one-dimensional carrier diffusion model in Section 4.2.1 and its extension to the microwave reflectance model in Section 4.2.2. The microwave reflectance of an excited sample is determined by the contribution from the front and back surfaces to the reflectance, which are functions of the excess carrier density and distribution. In this section the microwave reflectance of samples at $10GHz$ ($\lambda = 3cm$) is measured following uniform excitation by $980nm$ with a $5ms$ pulse of peak power density $10W\ cm^{-2}$. The experimental setup is shown in Figure 5.20.

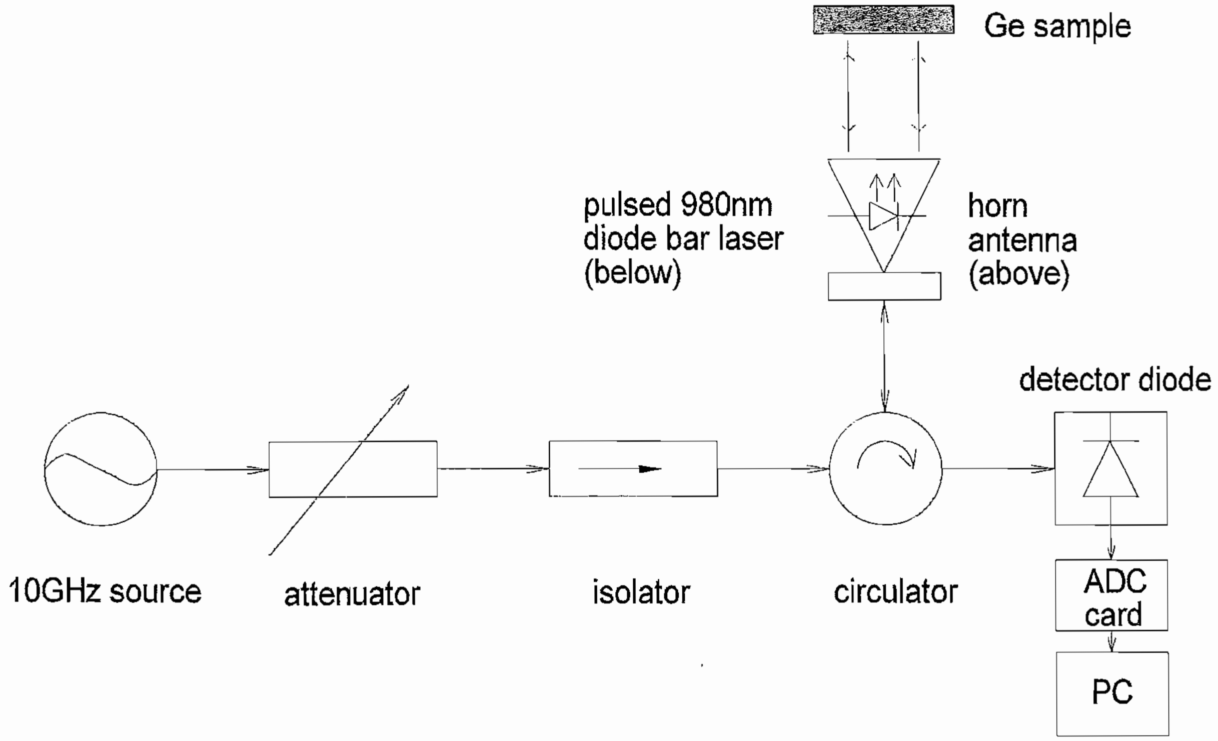

Figure 5.20: Experimental setup used to determine microwave reflectance

In Figure 5.20 the microwave source signal passes through the directional coupler to the horn antenna where it is reflected by the germanium. The power returning to the circulator is directed to the next port, where the microwave detector diode gives a voltage proportional to the reflected power. The ADC card is used to reduce the noise in the reflectance signal through a co-add into memory function, averaging each correlated time step for 400 reflectance traces. To avoid reflections from the detector being coupled to the source via the circulator's third port, an additional isolator was added between the circulator input port and the source. It is important that the power density on the sample is uniform, as modelled in Section 4.2.1 to avoid reflectance anomalies due to lateral carrier diffusion. Uniform excitation is achieved using a laser diode bar source which is placed sufficiently far ($5cm$) from the sample that the combined power from its separate emitters have overlapped. Microwave reflections from the metal diode bar mount are eliminated by its situation under the horn antenna. To avoid additional reflectance and possible interference effects the sample was supported by thin monofilament line. Reflections from nearby surfaces were reduced by covering them with a carbon-loaded microwave-absorbing foam. The measured reflectance profiles during carrier decay are shown in Figure 5.21.

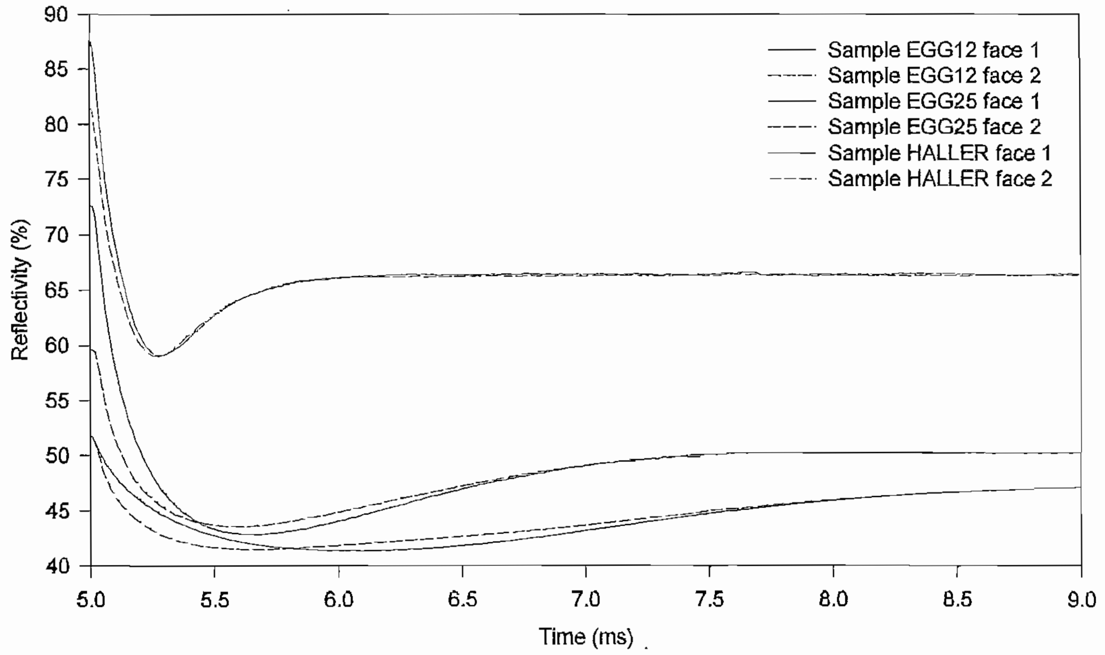

Figure 5.21: Microwave reflectance vs time for three samples during carrier decay

Following Figure 4.15, sample thicknesses of close to $6mm$ or close to $2mm$ were used to ensure the reflectivity always decreased initially before increasing with further excess carrier density. The generation of this characteristic 'dip' is necessary in extracting S and τ_{bulk} from the fitted model.

5.4.1 Microwave reflectance experimental results

Following the discussion in Section 4.3.2, the monitored microwave reflectance at $3cm$ wavelength depends on the interference fringes via the excess carrier density, and no absorption due to the plasma dip is observed. Section 4.3.2 assumed the use of a uniform axial excess carrier distribution, although following optical excitation the axial distribution during carrier decay was shown in Section 4.1 to be non-uniform with displacement x. The total reflectance is not simply determined by the average volume carrier density since the reflectance is a nonlinear function of the excess carrier density. The microwave reflectance model determines the effect of this distribution on the temporal changes in reflectance during carrier decay. The microwave reflectance depends on the carrier distribution (with x), which depends on the carrier diffusion parameters and the bulk carrier lifetime, and is therefore used to provide further information with which to back-up the one-dimensional diffusion equation models.

The measured microwave reflectance as a function of time, and the fits to these profiles using the microwave reflectance model during carrier decay are shown in Figures 5.22 to 5.27 for both faces of the same three samples as before. Fitting these profiles required a relative reflectivity scale. This required two absolute reflectivity measurements, against which all other reflectivity measurements for a particular sample were scaled. Unlike the transmission experiments where calibration of a 100% transmission signal is simple, here the motion of any moving part that reflects the much broader microwave beam complicates the measured reflectivity. Therefore it is not possible for example to use a rotating chopper blade to generate a 100% depth of modulation reference signal from a metallic reflector with the sample's cross sectional area. The model requires accurate measurement of the incident excitation power density on the sample, although this is difficult due to large sample dimensions. However, prediction of the minimum-reflectivity 'dip', and the unexcited-state reflectivity is possible using the sample thickness and free electron and hole densities. The former calculation is based on calculation of a graph similar to Figure 4.15 for the sample-specific parameters. The sample resistivity (all were intrinsic) was measured to calculate the unexcited state free carrier density. Having predicted the unexcited state reflectivity, occurring a long time after the excitation terminates, and the minimum reflectivity for a specific sample, an absolute value for the reflectance at any time for a given sample was determined by scaling the measured reflectivity to these two known points on the reflectivity vs time trace. This resulted in good agreement with the measured power density on the sample, and was verified using the power density as a variable parameter in the model. The S and τ_{bulk} parameters in the model were then iterated, giving the best fits seen in Figures 5.22 to 5.27.

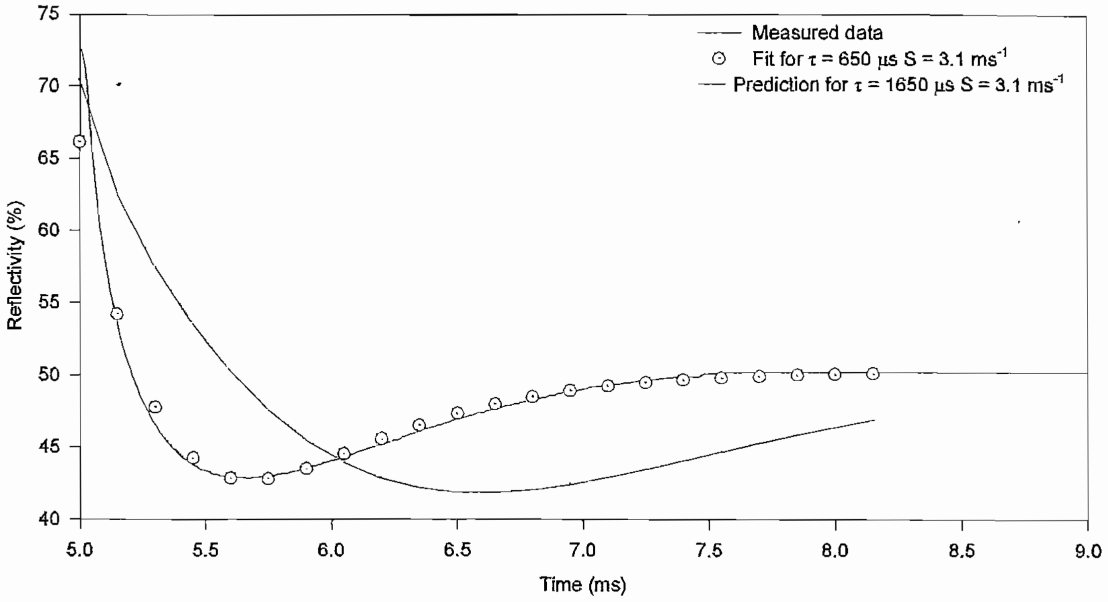

Figure 5.22: Measured and fitted microwave reflectance profiles for sample EGG1 face 1 during carrier decay

Figures 5.22 to 5.27 show the measured reflectivity, the best fit reflectivity, and the effect of variation of the S and τ_{bulk} parameters individually. These are used in the discussion on the fit. The fits were obtained by simulating the reflectivity vs time following optical excitation using the combined one-dimensional diffusion model and microwave reflectivity model in Section 4.2.2. The excessive duration of the simulations required the writing of a dedicated compiled PowerBasic program. The mean sum of the squares difference in % reflectivity was computed for each simulation over n (20) time intervals during the complete decay period. This is given by Equation 5.12 and the fit for sample EGG2 face 1 is shown in Figure 5.28.

$$SSE = \frac{1}{n}\sum_{n}(R_{n\,measured} - R_{n\,sampled})^2 \tag{5.12}$$

To demonstrate the accuracy required by the fit in Figure 5.28, an absolute error of 1% on all points would result in unity sum-of-squares difference. On the restricted scale plotted in Figure 5.28, similar families of curves exist outside the banded region, although these were omitted for clarity. The best fit given in Table 5.4 is located at the

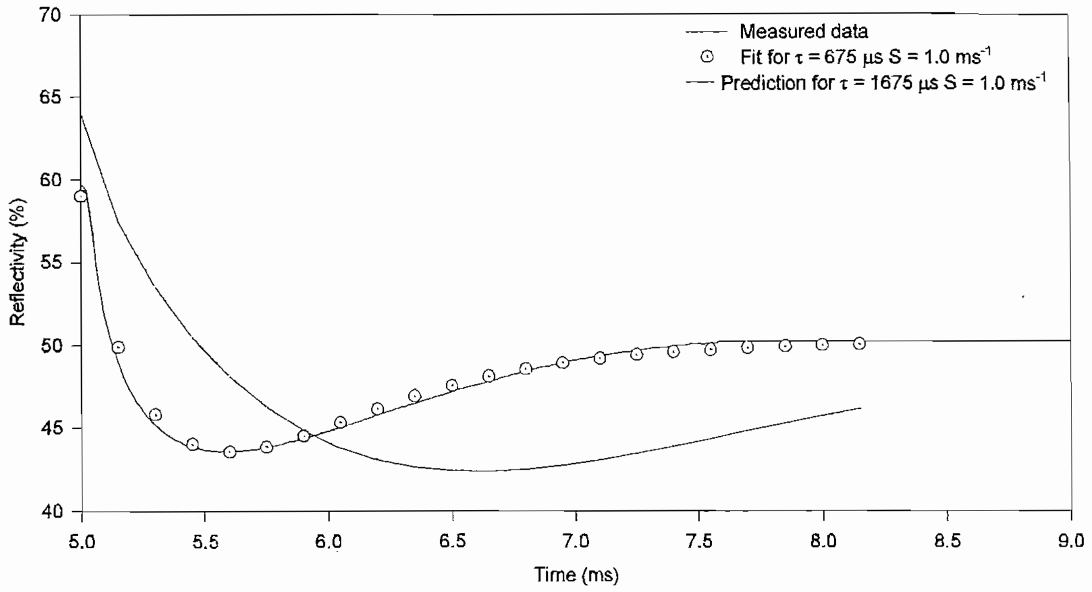

Figure 5.23: Measured and fitted microwave reflectance profiles for sample EGG1 face 2 during carrier decay

marked point within the red $(0-0.2)$ contour. To illustrate the error implied by the $0.2-0.4$ contour in this figure, Figure 5.24 also shows the simulation for $\tau_{bulk} = 2500\mu s$ and $S = 2.0$, which is clearly a poorer fit. Figures 5.22, 5.23 and 5.25 are plotted for the fit $\tau_{bulk} + 1ms$, and Figures 5.26 and 5.27 are plotted for $\tau_{bulk} + 50\mu s$ to demonstrate that the *apparent* fits implied by the long $0.2-0.4$ contour in graphs such as Figure 5.28 are in effect superficial. Typically the plot in Figure 5.28 for the above figures gave similar-shaped contours. The accuracy with which the parameters are determined is seen graphically as roughly $\tau_{bulk} = 2ms\pm \sim 0.1ms$ and $S = 2ms^{-1} \pm 0.05ms^{-1}$.

sample	**surface**	**fitted** τ_{bulk} μs	**fitted** S ms^{-1}
EGG1	1	650	3.1
EGG1	2	675	1.0
EGG2	1	2080	1.5
EGG2	2	1930	1.5
Haller	1	120	2.0
Haller	2	130	1.0

Table 5.4: Extracted S and τ_{bulk} parameters from microwave reflectivity experiments

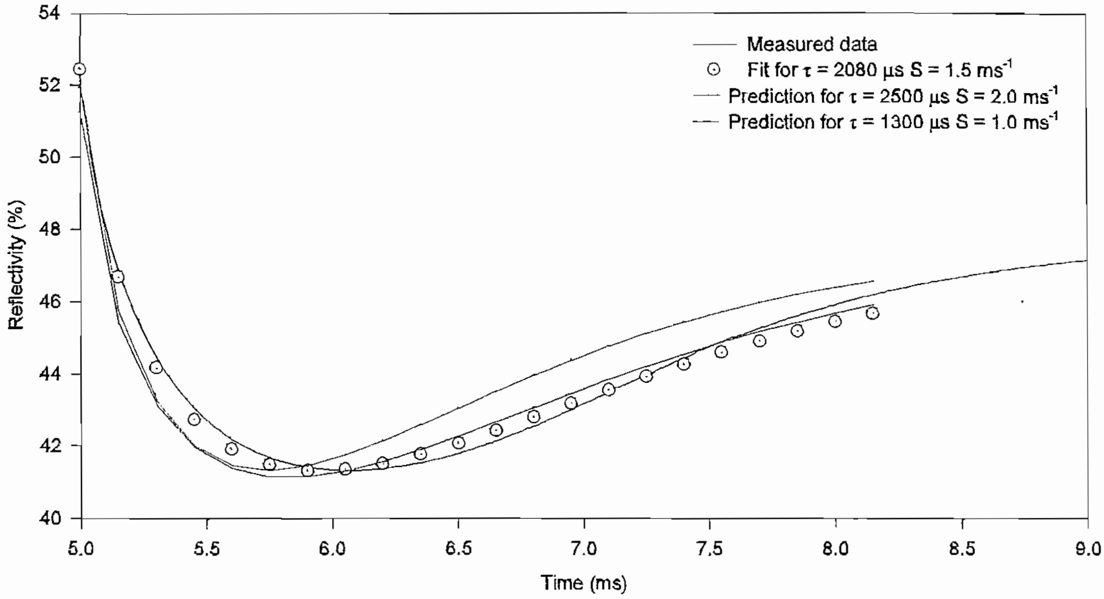

Figure 5.24: Measured and fitted microwave reflectance profiles for sample EGG2 face 1 during carrier decay

5.5 Comparison of results from diagnostic experiments

The S and τ_{bulk} parameters extracted from the temporal decay, lateral diffusion and microwave reflectivity experiments in this chapter are now compared. Tables 5.2, 5.3 and 5.4 are summarised in Table 5.5. Table 5.5 shows consistency between the bulk carrier lifetime results from a given experiment for the two sample faces for any given method. The surface recombination velocity values for both sample faces are not expected to be equal due to the known variation in S after wet chemical etching. Comparison of extracted parameters between the experiments is only valid for the 'temporal' and 'microwave' results, due to the presence of a reduced lateral diffusion coefficient in the 'lateral' results. The results that can be compared are marked $\bullet$ and $\star$ respectively.

The lateral diffusion results from these experiments have highlighted an important reduction in lateral diffusion length due to enhanced scattering of carriers at the surface, which in the above experiments was approximately half its bulk value. Such results were not found in the older literature, despite the use of similar techniques [109]. In the cited work the lateral diffusion length was determined in etched germanium using a white light

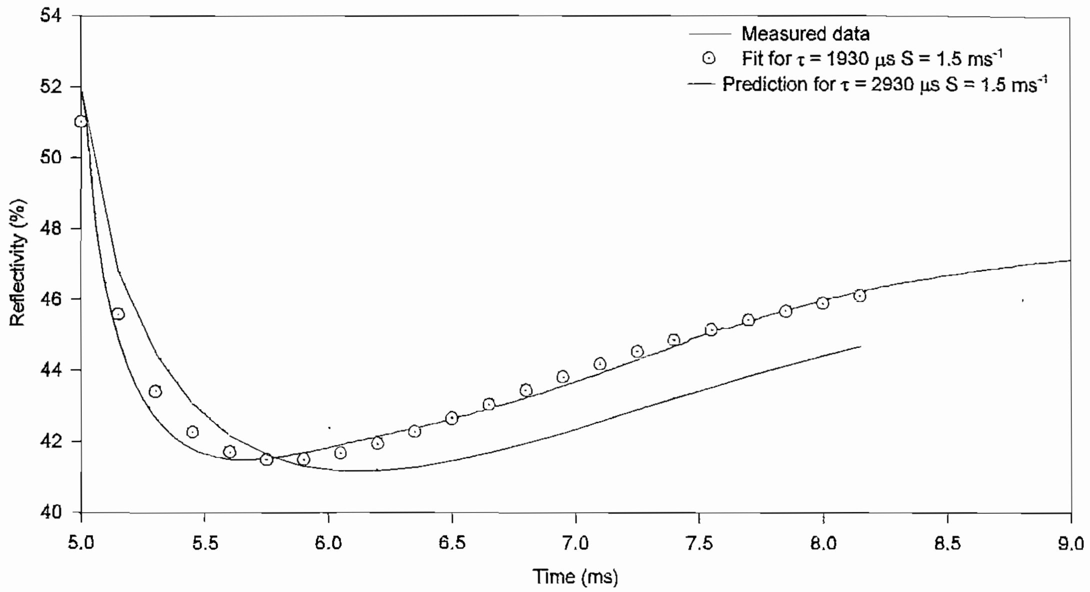

Figure 5.25: Measured and fitted microwave reflectance profiles for sample EGG2 face 2 during carrier decay

spot excitation by measuring the change in surface conductivity, but assumed negligible surface recombination velocity. The true lifetimes of samples in the cited experiment are likely to have been higher than were measured due to the reduced surface mobility. Experiments were also performed in the past [110] which measured the carrier diffusion length by measuring changes in infrared transmission following electrical carrier-injection into a germanium bar. Surface carrier recombination was accounted for but the injection of carriers into the bulk material made them less susceptible to surface recombination.

Despite the good fits shown for the microwave reflectivity experiments, for the EGG1 sample the τ_{bulk} results (•) are approximately half those of the 'temporal' experiments, and those for the EGG2 sample are approximately twice those for the 'temporal' experiments. The poor quality of the Haller sample fit in the 'temporal' experiments does not permit its comparison. The basis of the model for the 'temporal' and the 'microwave' experimental validation is the same one-dimensional diffusion equation, therefore similar S and τ_{bulk} results are expected. Indeed, the good fits to the data obtained from both these experiments indicate an accurate model. It is therefore concluded that different effects have been measured by the two experiments.

The importance of a reduced lateral diffusion coefficient in the presence of non-

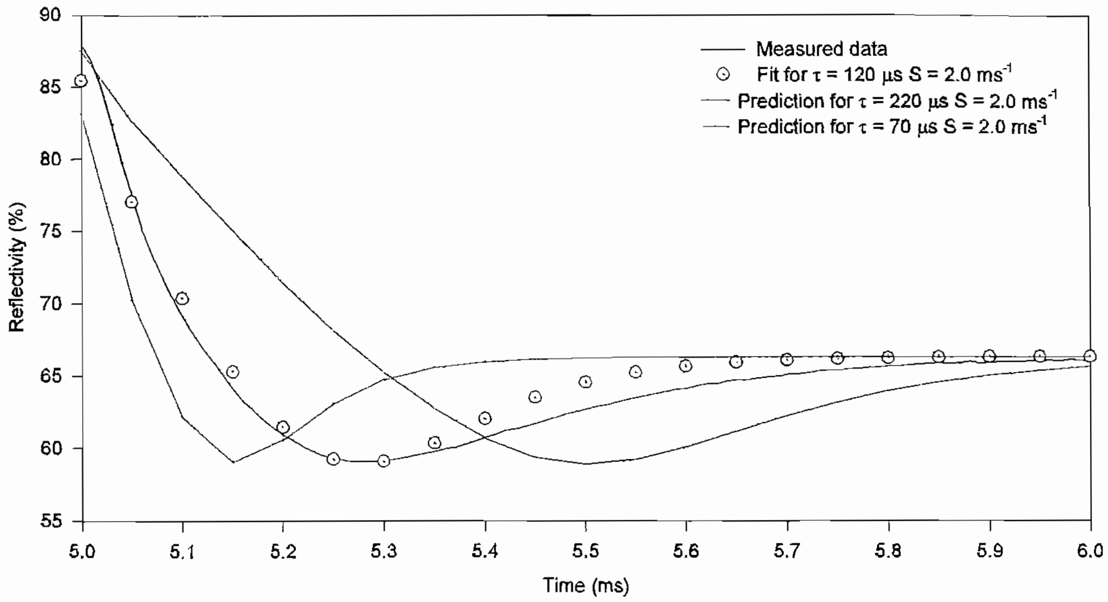

Figure 5.26: Measured and fitted microwave reflectance profiles for sample Haller face 1 during carrier decay

uniform excitation has been shown by the 'lateral' experiments. Although attempts were made to ensure uniform excitation occurred in the temporal and microwave experiments by exciting samples in both experiments with only the central region of a diode laser bar emission profile, it is known from later measurements (Section 7.3.2) of the power profile that this is not uniform along the bar's length. In the 'temporal' measurements only a small sample cross-sectional area ($\sim 2mm$ dia.) was probed, compared to the entire surface area ($\sim 1.5 \times 1.5cm$) of the sample in the microwave experiments. When the sampled area is less than a diffusion length, providing the excitation is on for longer than the bulk carrier lifetime, such excitation non-uniformity becomes unimportant in its effect on carrier decay since the non-equilibrium steady-state spatial carrier distribution is smoothed-out. When the entire sample area is monitored by the microwave measurements, such excitation non-uniformities are not smoothed-out over the entire sample area and different reflectivity contributions are given by different points on the sample surface, changing the net reflectivity measured. The 'temporal' measurements over a small sample area therefore more accurately monitor the modelled decay in the presence of non-uniform excitation. This may account for the discrepancy in the τ_{bulk} parameters measured by the two techniques. The reduced lateral diffusion

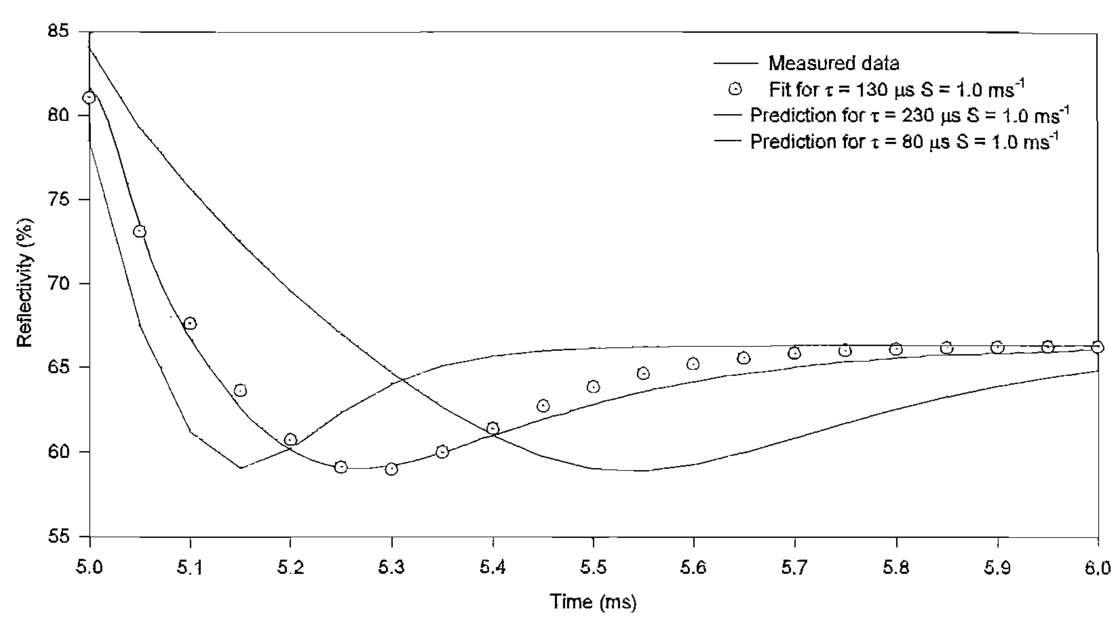

Figure 5.27: Measured and fitted microwave reflectance profiles for sample Haller face 2 during carrier decay

coefficient does not however reduce the lateral carrier lifetime, only the lateral diffusion length. Reduced lateral diffusion simply reduces the rate at which these move laterally, and carriers still recombine with the effective carrier lifetime. Recombination at the edges of a sample could be significant however, and this does increase the net carrier recombination rate. It is thought that this explains the discrepancy between τ_{bulk} results for the microwave and temporal results for the EGG1 sample.

The reason for the larger τ_{bulk} values from the EGG2 samples in the microwave results, compared to the temporal results is unknown. Possible factors are the increase in carrier lifetime with excitation predicted in Chapter 3, based on an argument over recombination centres, trapping, and more likely, thermal effects. No excitation-dependence of lifetime was observed in any other experiment, and although trapping provides a characteristic slow decay 'tail', only this experiment gave such long lifetimes showing that these processes are insignificant. Thermal effects are significant on a $2ms$ timescale in a sample that has not thermally equilibrated with the room temperature. In some cases the amplitude of the 'dip' was seen to reduce over the first 30 seconds after the excitation was switched-on. An increase in intrinsic carrier density due to heating during the excitation period, and its cooling during the off period before thermal equilibration

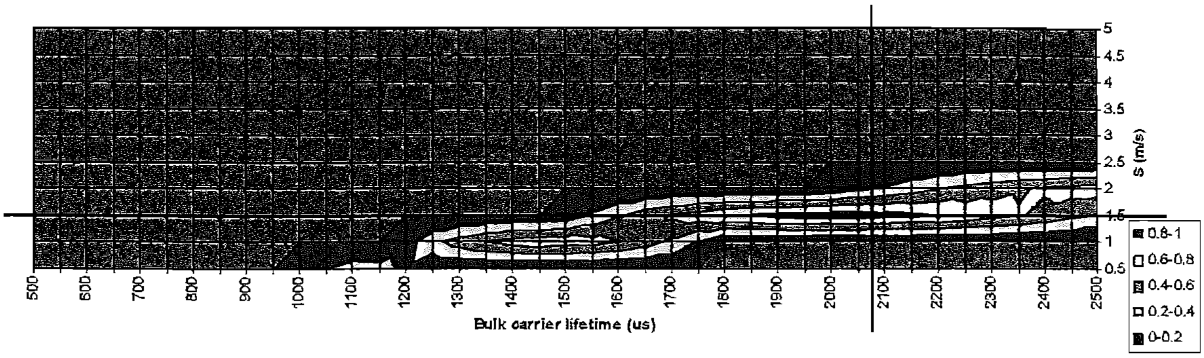

Figure 5.28: Microwave reflectance mean sum of squares difference vs S and τ_{bulk} for sample EGG2 face 1

sample	**surface**	**lateral** τ_{bulk} μs	**lateral** S ms^{-1}	**• temporal** τ_{bulk} μs	**⋆ temporal** S ms^{-1}	**• microwave** τ_{bulk} μs	**⋆ microwave** S ms^{-1}
EGG1	1	100	3	1390	2.8	650	3.1
EGG1	2	100	3	1280	2.5	675	1.0
EGG2	1	100	3	1140	3.0	2080	1.5
EGG2	2	100	3	1290	3.0	1930	1.5
Haller	1	< 25	10	no fit	no fit	120	2.0
Haller	2	< 25	10	850	9.5	130	1.0

Table 5.5: Comparison of parameters extracted from models of the three experiments

occurs, may explain the slow return to the unexcited state reflectance and subsequent long bulk lifetime extracted. The reflectance close to the 'dip' is strongly dependent on low excess carrier densities (Figure 4.15), and the intrinsic carrier density increases by $\sim 6\%$ over a $1°C$ temperature rise from $300°K$ [96]. Sample alignment should not be too critical with this technique since the high refractive index straightens microwave rays in the excited germanium. It is thought that this particular discrepancy is due to experimental error and not the modelling process.

Since the 'microwave' values obtained for τ_{bulk} are likely to have been affected by thermal effects, the extracted values for S will also be affected, and so accurate agreement with the temporal results is not expected. However, the S values are in the region of a few ms^{-1}, as with the temporal results, providing confirmation of their order.

Due to the experimental limitations of the three techniques used to measure the S and τ_{bulk} parameters, the temporal technique has provided the most reliable results. The lateral diffusion results were subject to a inhomogeneous diffusion coefficient due to surface scattering, which produced different profiles from those predicted, and accurate values could not be extracted. The microwave results, although providing accurate fits to the data, are thought to have been affected by thermal effects, significant carrier recombination at the sample edges, and non-uniform excitation, although in the absence of these issues, are thought to provide an accurate method. The temporal results were obtained by probing a smaller section of the excited region and were therefore less subject to the effects of non-uniform excitation, and the nature of the experiment provided longer between turn-on and result collection, by which time thermal effects would have equilibrated. The temporal results are deemed more reliable for this reason. A future experiment would ideally perform both microwave and temporal experiments simultaneously to verify these conclusions, and if a shorter microwave wavelength were used, a smaller sample area could be probed and the technique becomes more sensitive to resolving the depth of the excited plasma. The temporal measurements are therefore used in subsequent references to these samples. In the absence of accurate results for the thin Haller sample from this technique, the microwave results are used for this sample.

The extracted values for S, close to $3ms^{-1}$, are similar to the requirements for an efficient modulator in the conclusions of Chapter 4. Etching therefore provides the sought low surface recombination velocity although its further reduction would enable a more efficient device. These values are of the same order as the ms^{-1} values quoted in the etching literature [30]. Based on the bulk carrier lifetime expected from the dislocation density in Chapter 3, Equation 3.10, bulk carrier lifetimes of from $250\mu s$ to $25ms$ are expected from this nuclear detector grade material in the EGG samples. The Haller sample is of unknown bulk purity. The two EGG samples were from the same supplier but different germanium boules, different values for τ_{bulk} are therefore expected. The extracted values of $\sim 1300\mu s$ are both within the dislocation specification's prediction of the lifetime, although no lifetime information was provided by the supplier, only that the electrically active impurity concentration was $< 10^{10}cm^{-3}$. In the absence of data on the energy levels and individual densities of impurities in the HPGe, it is not possible to calculate whether impurities or dislocations limit the bulk lifetime. Since no exponential 'tail' was observed on traces of the induced absorption following optical excitation, if the bulk lifetime is limited by dislocations, these certainly do not act as 'traps', and have the same effect on the lifetime as recombination centres from impurities. In any case, the measured lifetimes indicate that recombination is surface-limited in these samples as opposed to bulk-limited. Figure 7.3 for $S = 3ms^{-1}$ and $\tau_{bulk} = 1ms$ suggests that an increase of factor of 2 is available in the steady state induced absorption coefficient by further reduction of S. However, practically, such a low value is unlikely to be stable over long periods of time. The optimisation of this through etching, and other areas of modulator performance is considered in Chapter 6.

Chapter 6

Optimisation of modulator performance

Optimising the induced absorption is necessary to reduce the excitation power density required for reasonable absorption, enabling use of the modulator in even lower power applications at reduced cost. The efficiency is optimised through four areas: i) maximising the effective carrier lifetime, ii) increasing the 'on' state transmission to essentially 100%, iii) increasing the fraction of absorbed excitation power, and iv) increasing the excitation wavelength. The first of these is at the expense of the modulator's switching speed, whereas the others are not. Ignoring multiple reflections, the modulator's 'off' state transmission is given by Equation 6.1, where A is given by the product of the carrier absorption cross section σ_h and the steady state carrier density in Equation 3.39 (Chapter 3). The unexcited state transmission is denoted T_0.

$$T = T_0 e^{-A} \tag{6.1}$$

The absorption cross section is a fixed material property. However, increasing the effective carrier lifetime, the absorbed power density, or the excitation wavelength all increase the modulator's efficiency. Increasing the unexcited state transmission T_0 to essentially unity increases the power on the detector in the application, improving the system signal to noise ratio. These are the subjects of the next four subsections.

6.1 Etching germanium: experimental

As seen in Chapters 3 and 4, the surface recombination velocity in a practical modulator must be reduced to $\sim 3ms^{-1}$. This is achieved by etching. After a germanium sample has been cut from the boule, commercial mechanical polishing techniques use progressively finer silicon carbide abrasive discs, finishing with polishing using alumina- or diamond-particle suspensions on a napped-glass cloth. Commercial polishing typically terminates with a $0.3\mu m$ or $0.05\mu m$ particle-size paste, leaving sub surface damage as deep as $3.0\mu m$. On unetched polished surfaces the surface recombination velocity is in the order of a few hundred ms^{-1}, the exact value depending on the final surface treatment. Etching is reported to reduce this to $2cms^{-1}$ [111] with one particular etchant, although maintaining such a low value is dependent on the post-etch environment. As an extreme value, on sandblasted germanium surfaces S is in the order of $100ms^{-1}$ [30].

In combination with surface damage, the surface bond-termination is important [111] [112] in obtaining and maintaining a low surface recombination velocity. This depends on the particular etch used to remove the damaged layer, and the sample's environment after etching. Whilst etching offers the possibility of reducing the surface recombination velocity, it is not without complication. The most suitable etchant depends on the sample's surface orientation, since many etchants have preferential etch planes which open-up microscopic polishing scratches into etch pits. Preferential etching characteristics were commonly used in the past to determine the surface orientation [102] [113].

The effects of electrolytic etching, reactive ion etching and wet chemical etching were investigated using the instrument detailed in Section 5. Etching increases the effective carrier lifetime and hence the modulator's efficiency. The instrument gives a relative figure of merit, which determines the effectiveness of each etchant. The relative FOM is higher for samples giving a higher depth of modulation, indicating a lower surface recombination velocity. The relative FOM is also affected by the sample's bulk purity. The highest value a sample may attain in the presence of zero surface recombination velocity is limited by the bulk carrier lifetime, higher bulk carrier lifetimes giving a higher attainable relative FOM. With the optical quality material used with the electrolytic etchants, a relative FOM of about 0.5 is good. With the higher bulk purity material used with the reactive ion etching and wet chemical etching a relative FOM of about 4 is good, in which case the surface recombination rate has been significantly reduced. The variation in FOM with depth of modulation attained in an actual modulator is linear.

6.1.1 Electrolytic etching

Electrolytic etching or polishing involves passing a current through a sample in an electrolyte. Anodic contact to germanium converts surface material into soluble products which are transported through the electrolyte to the submerged cathode. In most cases [102] the removal of a germanium atom requires four units of charge to remove the tetravalent atom. Electrolytic etching offers a greater degree of control than wet chemical etching (which typically has high etch rates) through its more immediate activation and termination [114]. Usually the electrolyte is chosen to give negligible etch rate in the absence of an external current, which therefore controls the rate of material removal, and the induction times observed during wet chemical etching do not occur. As with chemical etching, electrolytic etching can leave a clean surface via the formation of soluble reaction products, and therefore no residue is left on the surface. The reaction rate is determined by the hole density [102], which is increased via the etch current or optically exciting the surface. These factors can be used to define surface etch regions or to homogenise the surface etch in the presence of impurities or surface roughness.

The presence of surface roughness concentrates etching at sharp points on the surface, tending to planarise the surface. However the presence of cracks at the surface also concentrates the etching where the resistance to the sample-contact electrode is lower, tending to deepen cracks. Imperfections and dopants that perturb the local hole density also lead to variations in surface etch rate. Flooding the surface region with optically-generated holes is one means of reducing these parasitic effects and achieving a more-planar etched surface. The electrolytes and their concentrations used to etch germanium are not critical [102]. Strong alkalis are commonly used, such as KOH or NaOH into which the (germanate) reaction products readily dissolve, as are acidic electrolytes, in which germanium salts are formed [102].

Following literature [115] [116] [114] reporting low surface recombination velocities achieved using electrolytic etchants, the effects of several were investigated in this work. These were used without the more complicated optical carrier generation processes. The etchants used (Appendix B) were an oxalic acid-water solution (E1), an HF - acetic acid mixture (E2), KOH (E3), and a suspension of SbOCl in water (E4). Samples placed in the electrolyte were held in a purpose-built PCTFE etch cell and the current density increased to values reported in the literature. In the cell, compressive anodic contact was made to the back of a 25mm diameter, 2mm thick sample by a thin platinum plate. A 1cm square aperture masking the germanium face defined the etched region and enabled determination of the current density. The cathode was a platinum wafer situated 2cm away. A constant voltage was applied to the electrodes and the current was monitored. To verify the current density required for etching, the current-voltage curve was plotted. The literature reports that electropolishing takes place in the region where there is near-zero slope on the current-voltage curve. The idealised $I - V$ curve for electrochemical etching is shown [114] in Figure 6.1.

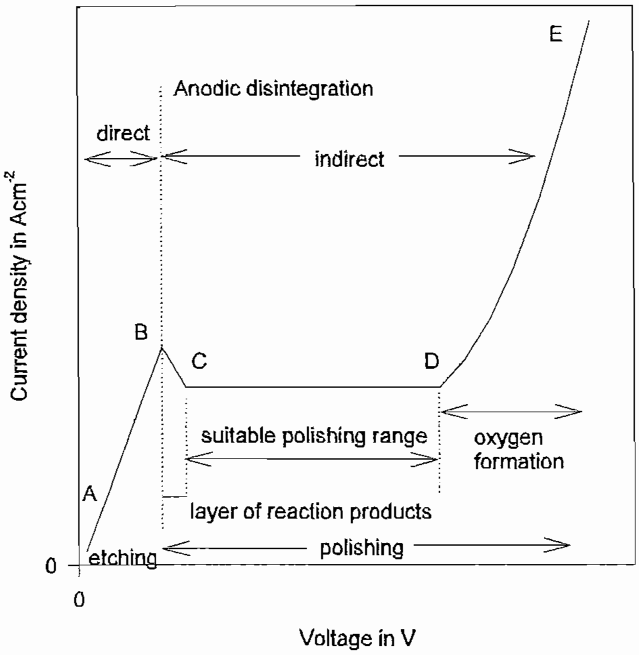

Figure 6.1: Idealised current-voltage curve for electrochemical etching

Along AB in Figure 6.1 the anode (germanium) goes straight into solution and electrolytic etching occurs. Along BC it is thought that a thin layer of reaction products causes passivity. Polishing occurs along CD due to diffusion and electrochemical processes. Along DE oxygen evolution commences. Close to D the bubbles adhere for long periods of time, resulting in pitting of the surface. An increase in voltage causes an increase in oxygen evolution rate and a reduction in bubble adherence time until the bubbles do not adhere at all. Only between C and D are the detrimental effects of pitting and layer formation avoided. The current density required to polish in this region was therefore determined graphically for each etch. From Faraday's law it is estimated that a convenient etch rate of $0.5 \mu m\ min^{-1}$ is achieved using a current density of $2.94 mA\ cm^{-2}$. A typical experimental result, shown for the KOH electrolyte, for an increase and subsequent decrease in voltage is given in Figure 6.2.

In Figure 6.2, increasing voltage gives a rapid initial increase in current, followed by a slower increase. The sudden current drop at a voltage of about $2.3V$ was coincident with the appearance of bubbles, and was seen to be due to the bursting of a large trapped bubble on the anode. Further increase in voltage appears to follow the original

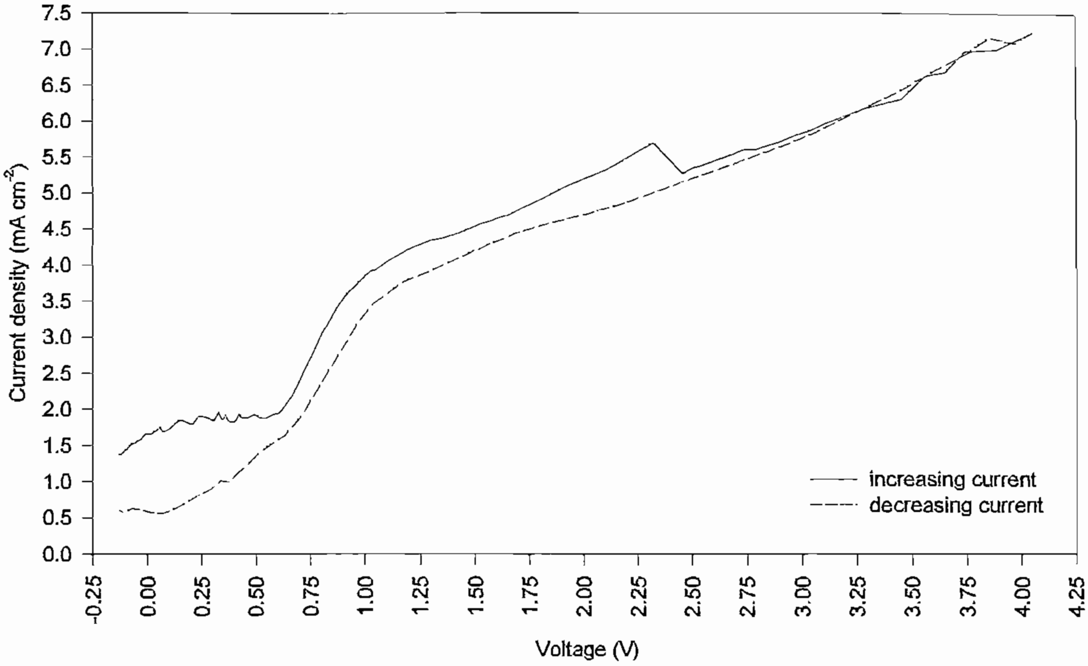

Figure 6.2: Current density vs applied voltage for germanium in KOH etchant

slope of the current increase. On decreasing the voltage, a smoother, lower current curve is followed, although the slopes of the curves are similar at a given voltage, so the electrolyte composition is not significantly changing as its resistance remains constant. The change in surface quality over the etch duration may explain the displacement of the reducing current curve from the increasing current curve. The current at zero potential is due to the battery effect of the platinum-Ge-KOH cell. This changes between the voltage increase and decrease, suggesting a change in surface properties of the more reactive germanium. On this graph it is difficult to distinguish the idealised region CD in Figure 6.1 for polishing. Much higher voltages beyond those plotted and using another sample resulted in faster bubble evolution in the 4 to $70V$ region where the slope of the curve remained constant. At $70V$ the current rapidly changed with time at a fixed voltage, and this is clearly in the region DE in Figure 6.1. It was therefore difficult to determine the ideal operating region CD. However, this occurs at a voltage higher than that causing film formation and below the onset of significant bubble evolution, and the film-formation peak B was never observed. It was concluded that the film formation region was insignificant for this particular etch, and the reaction products were capable of diffusing away from the surface at a sufficient rate. It was therefore decided that electropolishing should take place in the knee region of the graph, at a current density of $4mA\ cm^{-2}$, which was close to that predicted for a controllable etch rate by the calculation above.

The results of the electrolytic etching experiments were determined using the instrument detailed in Section 5.1, but due to the difficulty in replacing a sample in the etch rig, samples were etched for one period only. Despite using the same samples as with the other two etch techniques, the results varied for a given etch. Typically the FOM was in the order of 0.2, compared to 0.5 obtained using wet chemical etch techniques, although readings of 0.4 were obtained after longer etch periods. Obtaining even the low values left a pitted surface, which was worst in regions of better electrical contact. The surface recombination velocities obtained did not agree with the reported low values in the literature; $160cms^{-1}$ for etch E3 [116], $210cms^{-1}$ for etch E4 [116] in comparison to reported values for wet chemical etchants $1600cms^{-1}$ [116] for etch B1; for which the FOM obtained for the same samples was in the order of 0.5. The quality of the surface following the cited values was not given. However, the purpose of some of those electrochemical etchants was for the reduction of sample geometry and therefore did not necessarily require a planar surface.

Since pitting was more severe in regions close to the electrical contacts, pitting is caused by a high current, which was inhomogeneous across the etched region. This was due to the difficulty in obtaining good electrical contact to the sample's (unetched) back surface in a range of highly reactive etchants using one etch cell, which restricted the available materials to PCTFE and platinum. Although a different etch rig geometry, assisted by stirring or ultrasonic agitation may provide the desired result, the particular etch rig used did not provide the sought low surface recombination velocity accompanied by a planar surface.

6.1.2 Reactive Ion etching

Dry etching offers a high degree of control, which it was hoped might provide low surface recombination surfaces through the removal of damaged surface layers. Reactive ion etching (RIE) is one such dry etch technique, having a well-defined, orientation-independent etch rate. A higher degree of control is achieved since the etch requires no quench media, as do wet chemical etchants. This makes the etch easier to stop. The quench media used in wet chemical etching can also affect the germanium's surface termination. RIE uses a plasma of highly reactive ions which attack the surface germanium atoms, freeing them. One common etch gas is SF_6, which it was hoped might terminate the germanium with fluorine. It is thought that surface termination with fluorine [111] during wet chemical etching provides a low surface recombination velocity. RIE was used on samples of different bulk purity to determine its effectiveness at reducing the surface recombination velocity. Results showed that this particular etching mechanism did not produce the sought low surface recombination velocity, and instead produced a relatively high surface recombination velocity on samples which were known to offer lower values through wet chemical etching. Results from reactive ion etching, although generally poor, sometimes showed a reasonable depth of modulation, but this was not consistent, and not as high as values attained with the CP4 [117] wet chemical etchant.

RIE was attempted on a variety of samples at Heriot Watt University. Two etch gases commonly used with germanium were used on the samples: CHF_3 and SF_6, for a variety of etch periods. The etch rates are independent of surface orientation and were determined as $0.02\mu m\ min^{-1}$ in CHF_3 and $0.5\mu m\ min^{-1}$ in SF_6 by masking a region on a test sample. Only one sample face is etched at a time. Samples were placed in the etch chamber to etch one side, results were measured on both faces, the sample was then replaced in the etch chamber and another face etched. The etch history is shown for both faces for a typical sample in Figure 6.3. Circles represent a period in the chamber where a particular face is not etched, triangles represent etching of that face in CHF_3, squares represent etching in SF_6.

To give a basis for comparing the relative FOM in Figure 6.3, high purity material such as this sample attains a value of about 4 when etched with a successful wet chemical etch. In contrast, neither etch gas used with RIE left the surface with a FOM of greater than 0.35, suggesting this technique is of no use in the production of low surface recombination surfaces. All other results obtained were similar to this, and equally erratic. Nine samples were etched over a period of two days to ensure these results were decisive. In some cases the FOM decreased from the initial unetched values. Further etching increased the FOM to greater than the unetched value, and then it decreased again. It is thought that the bond termination left by the etch is not useful in leaving a low surface recombination velocity, although no experiments to determine this bond termination were performed. RIE has the merits of controllability and leaving flat surfaces, but does not leave the surface suitably terminated to give a low surface recombination velocity.

Whilst the RIE results showed that this etch process has no direct use as a final etching stage to produce a low surface recombination velocity, it is useful in producing a uniform, non-orientation-selective etch rate. It may have some use in etching through a thin damaged layer resulting from a polishing stage in order to leave a flat surface.

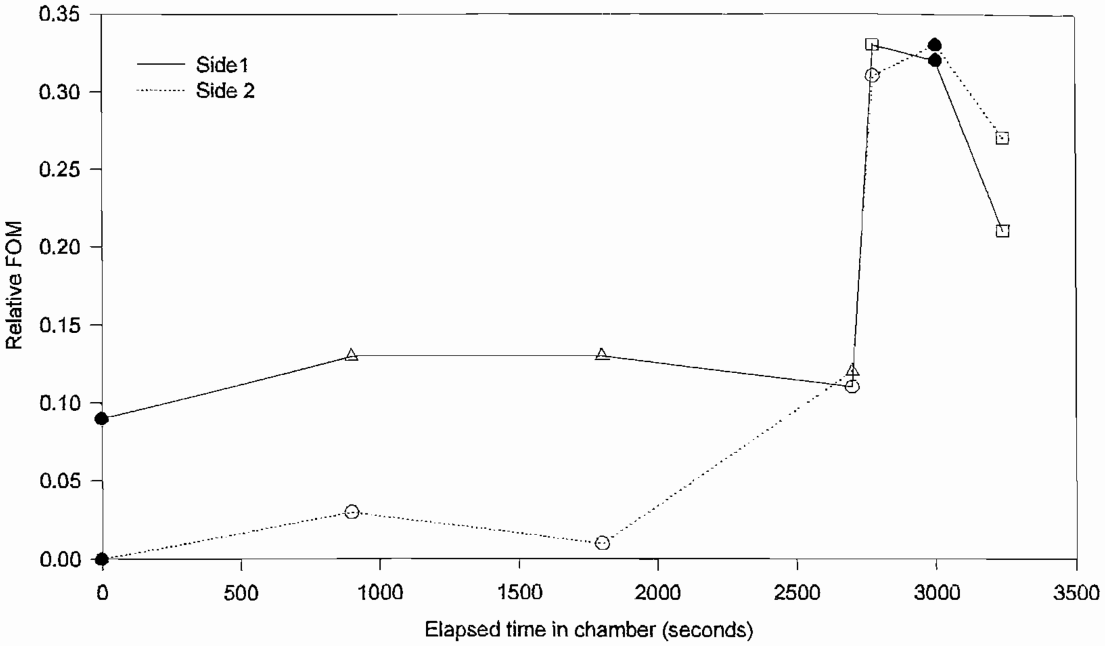

Figure 6.3: Reactive ion etching of sample ABC1: Relative *FOM* vs time in etch chamber

Care must be taken, however, to avoid RIE on samples with rough surfaces since the uniform etch rate tends to transfer patterns of damaged surface layers through to the material underneath. If used on the modulator, RIE would be followed by a very brief wet chemical etch to provide the correct surface termination without destroying surface figure.

6.1.3 Wet chemical etching

A wide range of wet chemical etchants [114] [118] [119] [120] [121] [122] [117] [123] were investigated for the removal of the polish-damaged surface layer and suitable termination of the surface. The wet chemical etchants were the most successful of the etch techniques used, and can be divided into film-forming etchants and non-film-forming etchants. Wet etching takes place by (1) transport of the reacting products to the reacting surface, (2) chemical reactions at the surface, and (3) transport of the reaction products away from the surface. Both film-forming and non-film-forming etchants produce an oxide or hydroxide layer in stage (2) but in stage (3) for the film-forming etchants the layer is not dissolved or diffused-away at a sufficient rate. This explains why varying the ratios of reagents of some etchants affects the tendence to form these films. The film-forming etchants left bluish films after etching, and produced an antireflection coating which was of little use due to difficulty in controlling its thickness. Non-film-forming etchants gave similarly low initial surface recombination velocities and more repeatable results.

Factors affecting the etch rate and performance of the wet etchants were reported to include the sample doping level, surface orientation, temperature, and reagent concentration. For example with the HF-H_20_2-H_20 group of etchants, changing the ratio of reagents alters both the tendency to form a passivating oxide layer and the etch rate. With respect to these, a good etchant has a high etch rate on the exposed surface, avoiding preferential etching and widening of surface scratches, a low temperature-dependence, and a low dependence on reagent concentration. In response to this, the performance of a large number of etchants was assessed on a variety of common surface orientations. Appendix B lists the etchants and their composition.

Despite the requirement for a non-preferential etch, a tradeoff exists between selecting an etchant effective at reducing the surface recombination velocity, and the amount of damage caused by preferential etching, since most wet chemical etchants in the literature have a preferred etch plane. Work on etching germanium started by determining the more effective etchants at minimising the surface recombination velocity, and then determined which etchants left minimal damage on particular surface orientations. Finally the minimum etch times were determined after which the surface recombination velocity had been reduced considerably, but the surface damage remained insignificant.

Samples were hand-polished prior to etching, which used progressively finer SiC paper, followed by polishing with alumina paste. The damaged layer thickness from this is up to $3\mu m$ deep. It is suggested [124] that carrier lifetime is affected up to the depth of the damaged layer. Etch times were therefore calculated to remove fractions of the $3\mu m$ layer. In the etching experiments outlined below, the effectiveness of particular etchants was analysed on samples of different purity. Initially samples were placed in the etchant for a fixed duration. The sample was then removed and its FOM evaluated. The sample was then replaced in the etch and the FOM re-evaluated. The amount of material that had to be removed by the etch was determined through the change in FOM.

Results of non-film forming etchants

The experimental procedure consisted of etching a sample for fixed periods until a maximum FOM plateau was reached. The etch container was stirred to stabilise the etch rate [124] in the event of diffusion issues. The sample was kept away from etchant vapours after etching, which can change the surface recombination velocity [125]. Rapid transfer of the sample to the water quench was essential to prevent the formation of a surface monoxide layer. Instrument readings were taken following a minimal delay after etching, to minimise the effects of the etched surface reacting with air. All samples used at this stage of the etching are of similar bulk purity and the same (111) surface orientation. Typical results are shown for etched samples in Figures 6.4 and 6.5.

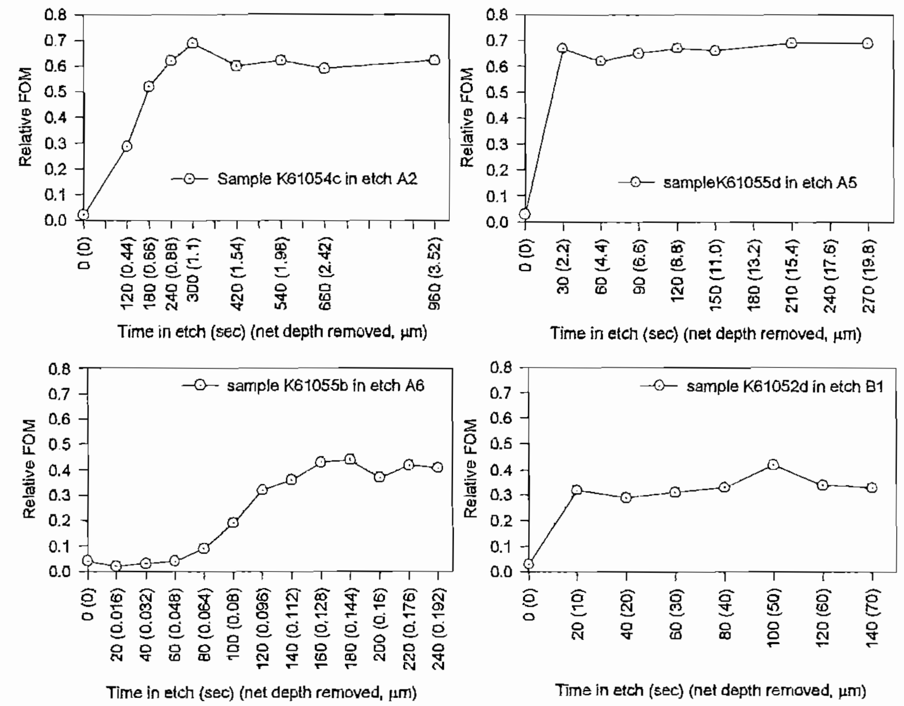

Figure 6.4: Typical graphs of *FOM* vs etch time obtained by etching samples of similar bulk carrier lifetime

Figures 6.4 and 6.5 show a sharp increase in *FOM* to approximately the maximum value ever attained, over the first period in the etchant. Thereafter the FOM fluctuates close to this initial value. For many etchants the fluctuation is more than the ±7% accuracy of the instrument, suggesting real changes in the surface recombination velocity after each etch. If the etch always leaves the surface with the same surface recombination velocity, these fluctuations may be due to different periods between the sample leaving the etchant, and measurement of the *FOM*. For some etchants [116] the surface recombination velocity is known to change over time when exposed to air. It is also possible that different times in the quench medium (de-ionised water) permit other bonds to form, which subsequently change the surface recombination velocity and give rise to the fluctuations. Figure 6.6 compares the maximum relative *FOM* values ever

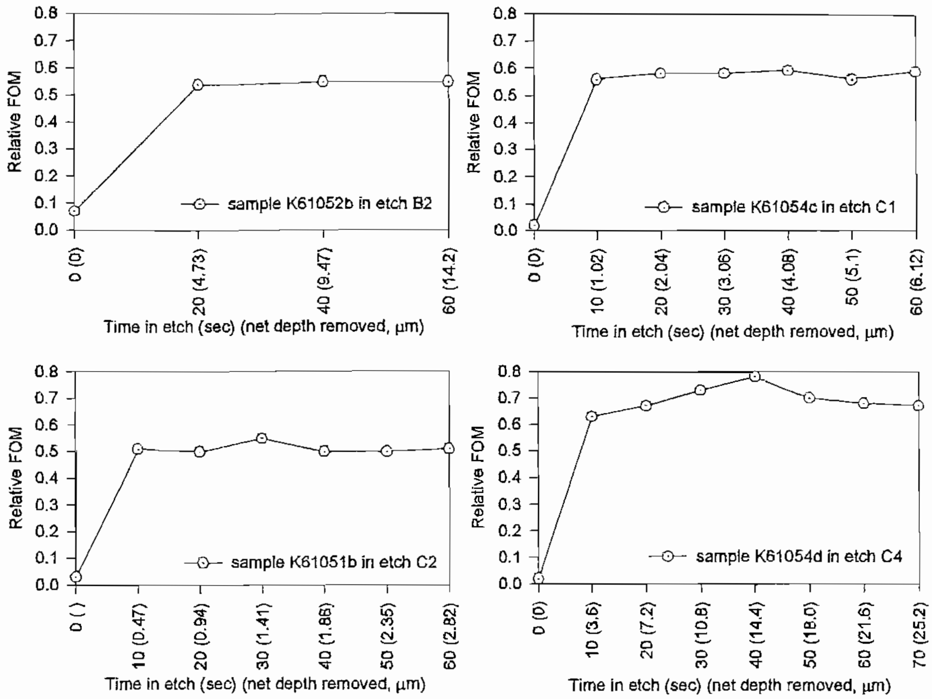

Figure 6.5: Typical graphs of *FOM* vs etch time obtained by etching samples of similar bulk carrier lifetime

attained by samples of similar levels of bulk purity in a particular etchant. Different symbols represent different samples in the etchants.

Small differences in the values attained by these samples are seen in Figure 6.6. This is partly due to small variations in bulk purity in the samples, but given the variation in results in Figures 6.4 and 6.5, the differences are mainly due to variations in surface quality. In these low bulk purity samples (optical grade germanium) the effects of both surface and bulk recombination are important in determining the *FOM*. To verify this, the variation in *FOM* obtained by two high purity samples in one etchant is shown in Figure 6.7.

In Figure 6.7 the maximum *FOM* values attained by the samples differ by a factor of nearly two. This is due to the higher bulk purity of sample 149B. However, the fractional variation in maximum *FOM* after an initial etch is similar for the two samples. This suggests that the surface recombination velocity after each etch period differs considerably. A larger fractional variation in *FOM* is seen in Figure 6.7 than in Figures 6.4 and 6.5 because in Figure 6.7, at low values of surface recombination velocity the *FOM* is more dependent on the surface recombination velocity than in the lower bulk purity samples. In lower bulk purity samples a change in surface recombination velocity after

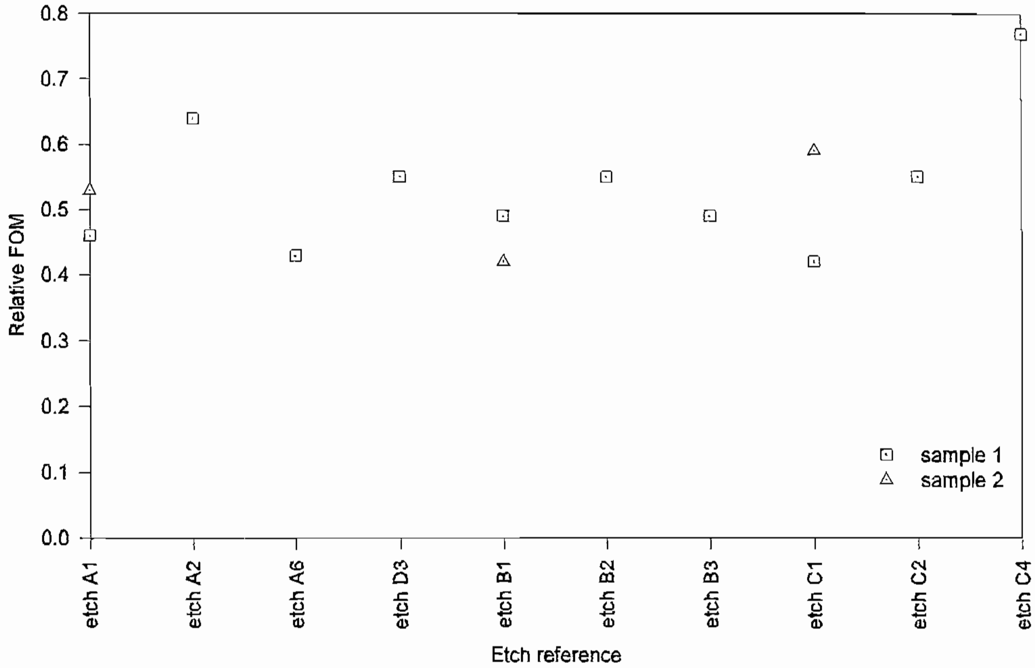

Figure 6.6: Summary of maximum FOM values ever attained in given etchants

a brief initial etch causes only a small change in net carrier recombination rate, which is dominated by the short bulk carrier lifetime. In the longer bulk carrier lifetime (high purity) samples the FOM is affected by lower values of surface recombination velocity that are achieved by the etch, and it is the fluctuations in the low value of the surface recombination velocity that cause the large observed variation in FOM. This was predicted by the steady state model for the dependence of the induced absorption on S and τ_{bulk} in Figure 4.4 (Chapter 4). This also confirms reports in the literature [102] that surface recombination velocity values obtained by wet chemical etching are not easily-repeatable.

To determine the best etchants at producing a repeatable (if possible) low surface recombination velocity, two high purity samples, which are more susceptible to the desired low surface recombination velocity, were subjected to a sequence of different etchants and their FOM evaluated after each etch. The duration of each etch stage was determined from previous work in order to permit maximisation of the FOM. The sequence of etchants was then randomised and the etch stages repeated to remove the possibility of correlated effects. Figure 6.8 shows the results.

Figure 6.8 shows results for the same two (100) orientation (re-polished) samples as in Figure 6.7. The two samples were etched simultaneously to ensure similar etch

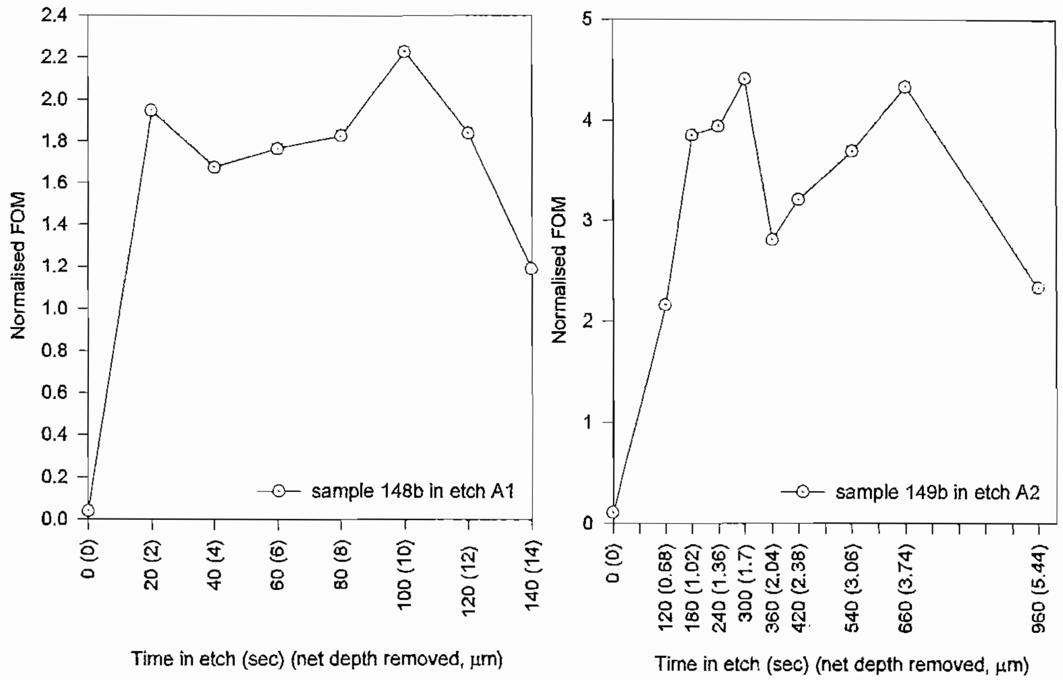

Figure 6.7: Normalised *FOM* vs time in etchant for two high purity samples

times and quench times. The samples show similar changes in *FOM* after each etch; when one result increases, the other also increases, showing that the surface properties of the two samples are similarly affected by even slight differences in etch time, quench time or times between the two processes. It is difficult to highlight the more repeatable etchants from the above graph. With additional consideration of the surface quality after etching, etchant A2 left a matt surface on (111) surfaces, etchants B1, C1 and C2, left a characteristic 'orange peel' surface, and etchant C4 left a lined pattern on (111) surfaces. Etchants A1 and B2 provided reasonable *FOM* values from the group, without the matt or orange-peel destruction of surface figure. For long etch durations, even commercially-polished surfaces were seen to have the minute scratches opened-up into lines of etch pits with etchants A1 and B2. Additionally, etchant B3 (not used in this experiment) also provided a high *FOM* with little destruction of surface figure. These three etchants were not found to produce films on the sample surfaces, and the etch pits on well-polished material were not significant until after high *FOM* values were achieved. These three etchants were therefore used as the preferred etchants in this work.

Despite the difficulty in gaining consistent values of surface recombination velocity by repeatedly etching the same sample, many results similar to those in the above exper-

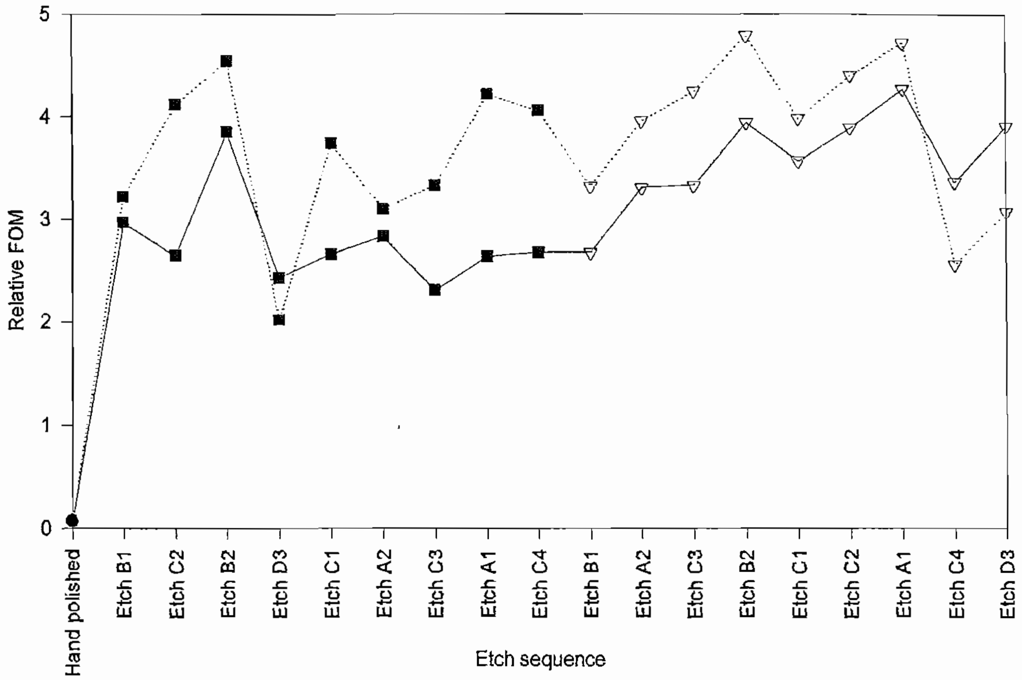

Figure 6.8: Relative FOM vs etch history for a series of non-film-forming etchants

iments showed that the surface recombination velocity is minimised in practice after only a brief etch which removed a layer much thinner than the polish-damaged layer. Much deeper etching did not result in the predicted second plateau region due to removal of the entire damaged layer. The minimisation in surface recombination velocity following removal of only a thin layer showed that the surface termination is more important than surface damage in determining the surface recombination velocity, after a thin layer of surface material had been removed. The post-etch surface termination reduces the effectiveness of subsurface damage at providing a high surface carrier recombination rate. This agrees with earlier work [112] which suggests that a high surface recombination velocity exists on mechanically-polished surfaces due to the lack of uniformity of oxide layer. Etching removes the damaged oxide layer and re-terminates the surface with a uniform oxide and a low surface recombination velocity. Prolonged etching is unnecessary, and most etchants were found to result in a pitted surface with characteristic etch pits on particular surface planes. Etch times were therefore restricted to four seconds, following which there appeared little to be gained in terms of reduced surface recombination velocity, and by which time the etch pits on the more common (100) germanium surfaces were still insignificant.

The observed changes in surface recombination velocity of an etched surface when exposed to air may be due to restructuring of the surface termination, or the diffusion of the gaseous ambient into the surface layer. The presence of different terminating species at the surface affects the surface recombination velocity as it alters the bending of the surface energy band structure, as detailed in Chapter 3. It is widely known that germanium does not form, as is the case of silicon, a stable passivating oxide layer. On germanium the initial oxide layer is patchy and later reacts with air over time to become more uniform. The *FOM* of one particular sample immediately after etching was found to drop by 25% over 25 minutes, thereafter remaining stable for a period in excess of two years in an invariant environment. The oxide layer is too thin for significant optical effects.

Surface orientation

In the attempt to produce even lower surface recombination velocity surfaces, surface orientation was also considered. The silicon (100) surface is known to have the lowest surface state density [91], and being of the same diamond lattice structure it was hoped that germanium would exhibit the same characteristic, with a minimum surface recombination velocity on this surface. Two cubes were cut with standard surface orientations from neighbouring regions of the same boule. This ensured equal bulk carrier lifetimes in the cubes, so any differences in effective carrier lifetime measurements were attributable to differences in surface recombination velocity. To include the common (100) and (111) surface orientations and to introduce a common cube face for direct comparison, one cube had (100), (011) and $(01\bar{1})$ surfaces, and the other had $(01\bar{1})$, $(\bar{2}11)$, and (111) surfaces. All surfaces were then polished commercially to a mirror finish.

Etching experiments had shown CP4 (B1 etch) to provide a low surface recombination velocity. A 10 second etch time was found to maximise the *FOM* from this etchant. In the experiments below, the cubes were etched for 10 seconds, washed, dried, and their infrared transmission was measured in the FTIR spectrophotometer in both the unexcited state, and when excited by $9.55W\ cm^{-2}$ of $980nm$ laser radiation, using a $2mm$ diameter circular aperture in the centre of each face. Equation 6.2 was then used to determine the induced absorption at $10\mu m$. The size of the cubes prevented their testing with the depth of modulation instrument outlined in Section 5.1.

$$A_{ind} = -ln\left(\frac{T_{excited}}{T_{unexcited}}\right) \tag{6.2}$$

The induced absorption is shown for all sample faces in Figures 6.10 and 6.11 for the (100) and (111) faced cubes respectively. The experiment was completed twice to show consistency. This is identified by the 'trial' number. The face orientation is shown in Figure 6.9, although in the experiment the faces are labelled S1 to S6 on both cubes. S1 and S3 are opposite, S2 and S4 are opposite, and S5 and S6 are opposite.

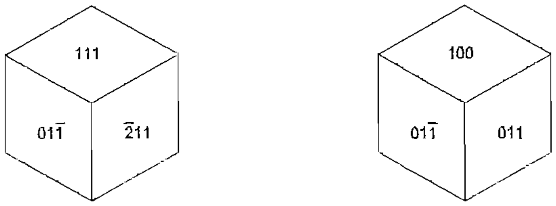

Figure 6.9: Cube orientation used in evaluation of the surface recombination velocity

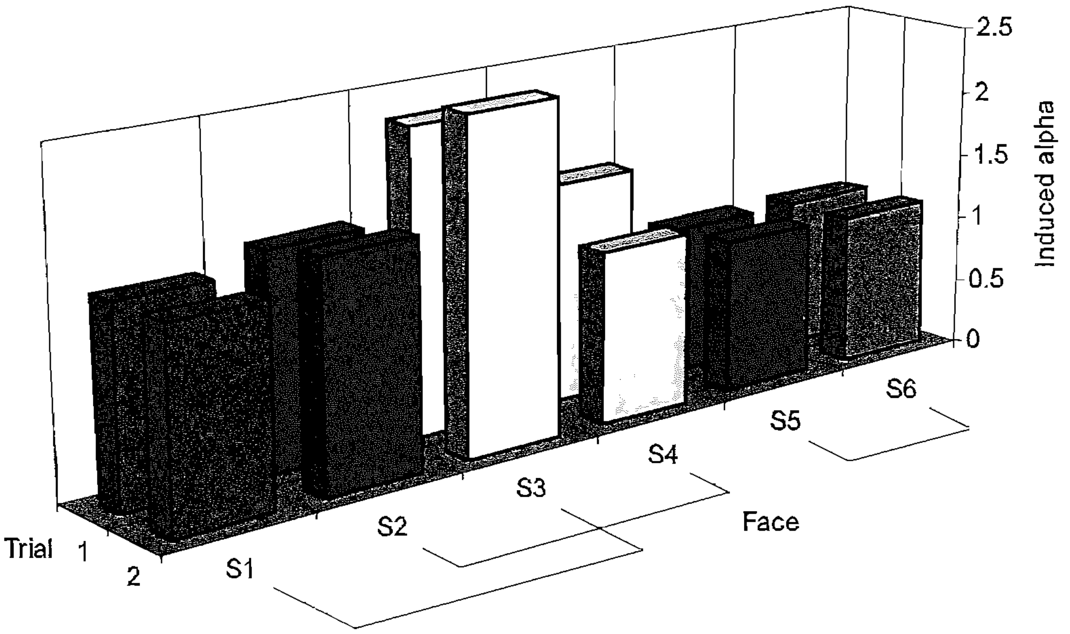

Figure 6.10: Induced absorption coefficient at $10\mu m$ for CP4-etched (100) cube

If significant repeatable differences in surface recombination velocity exist, the results for both trials for a given cube should be equal. The diamond crystal geometry also requires that equivalent (opposite), faces give equal values of induced absorption. Reasonable consistency is seen between the two trials, but the constancy of opposing faces is not shown by these results. In Figure 6.10, S1 and S3 differ significantly, although S2 and S4, and S5 and S6 agree well. In Figure 6.11 all opposite faces differ significantly. In view of the lack of consistent results, Laue orientation to identify S1 to S6 with specific planes was not performed. The most likely explanation for the lack of consistency in

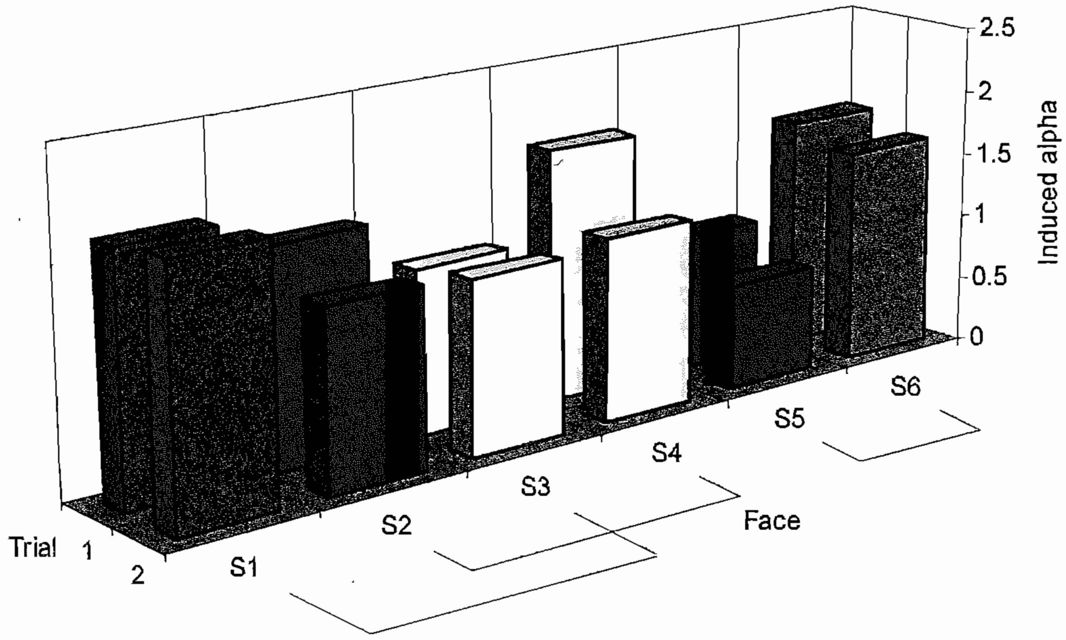

Figure 6.11: Induced absorption coefficient at $10\mu m$ for CP4-etched (111) cube

the results is the presence of patchy surfaces which were seen on some faces after the etch. It is thought that patchy films on particular surfaces after the 10 second etch duration, which is required to maximise the *FOM* on some surfaces, produce films on other surface planes, making simultaneous comparison of the results after one 10 second etch period difficult. Comparison of the results after shorter etch periods, before these films are produced, is unwise as different etch or quench times affect the results. Based also on the known variability of the etch process on a given surface and the difficulty in repeating results, it is concluded that if significant differences exist in surface recombination velocity on the different faces, they are indistinguishable using this technique. Therefore these differences are unlikely to be sufficiently different to offer a benefit to modulator construction.

Results of Film forming etchants

These etchants left noticeable films on the germanium surface after quenching. The experimental procedure was identical to that for the non-film forming etchants: each sample was etched for fixed periods in one etchant. The same (re-polished) optical grade samples were used in these etchants as beforehand to ensure consistent bulk carrier lifetimes for comparison of the *FOM*. The films produced were either white and patchy, or translucent and coloured. Coloured films were found to change colour during the water quench, although acetone and methanol did not affect film colour. The coloured films readily dissolved in H_2O_2. Figure 6.12 represents an etchant which leaves the surface with a coloured film. The coloured film is better at passivating the surface [125] than patchy white films. Patchy misty white films left by etchants C3 and D1 gave reasonable *FOM* results around 0.6 and 0.4 respectively. Etchant D2 gave a poorer maximum *FOM* of 0.2. The patchy-film etchants suggested no promise for a final modulator due to the large variation in results obtained, which were only as good as for the non-film-forming etchants.

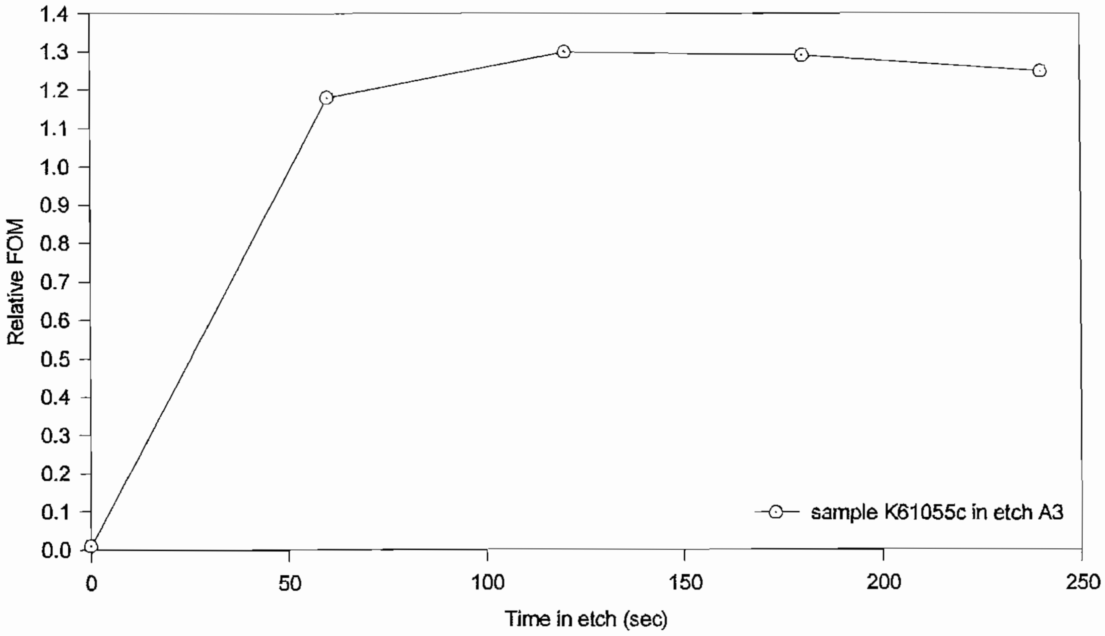

Figure 6.12: Relative *FOM* for Sample K6105-5c in Etch A3 vs etch time

In Figure 6.12 the film produced by etch A3 changed from yellow to blue, gradually becoming darker, with a period of about 5 seconds. Work [125] in 1957 on films with similar characteristics, produced by similar etchants revealed both their passivation behaviour and their antireflection coating property. The passivation behaviour is shown by the much higher *FOM* than for a similar sample etched in non-film-forming etchants. The *FOM* achieved by this etchant was quite steady with repeated etching, reducing slightly with increasing etch time. This suggests the passivating film protects the surface from reaction with air or the quench medium, at least in the short term. The refractive index of this layer is reported as 1.8 for similar films [125]. FTIR spectra of the film showed it effectively provides an AR coating, although difficulty in controlling its rapid growth render this of little use in a final modulator application. Determination of the etch rate using a Taly-step is difficult due to the presence of this film, although the frequency of colour change and estimated refractive index of 1.8 gives a calculated film growth rate of $1.6\mu m\ min^{-1}$.

The coloured-film etchant A3 clearly produced a lower surface recombination velocity than any of the wet chemical etchants considered. It is likely that this was due to significant surface energy band-bending. However, to produce this low surface recombination velocity required a moderate etch time, after which the film had started to form y-shaped cracks which were observed during microscopic inspection. Additionally the complication of depositing essential AR coatings on top of this film would complicate modulator fabrication. The long term (over two years) stability of these films was good, although the compatibility with AR coatings would have to be investigated. This etchant was not pursued for reducing the surface recombination velocity due to these fabrication issues, although further work may show it to be of use in a final modulator.

6.2 Conclusions on etching germanium

Having considered a wide range of etching techniques for increasing the effective carrier lifetime, only wet chemical etchants offered the required significant reduction in surface recombination velocity combined with a damage-free surface. Electrolytic etching may, with the construction of a more complex etch cell involving optical excitation and a rotating cathode [102], offer both these requirements, but requires considerable effort to optimise. RIE was not found to suitably terminate the surface for a low surface recombination velocity, possibly due to the lack of oxide growth with this technique. Wet chemical etchants were the best of those investigated. Among the most successful wet chemical etchants in obtaining a consistent low surface recombination velocity were CP4A [114], and an etch [126] with constituents in the ratios 30% of (50%) HF to 50% of (30%) H_2O_2 to 20% of de-ionised water. The etch times for these processes were four seconds, after which time the etch is quenched by adding flooding amounts of water to the etch container. The etchant was rigorously stirred using a PTFE magnetic follower. All etching equipment was made from PTFE to avoid contamination or chemical-attack. De-ionised water is essential for any etching or washing process. These two etchants were therefore used on all further samples requiring etching.

6.3 Silicon implantation to widen the bandgap

Another means of changing the recombination rate of carriers at the surface but without needing to etch germanium is through widening the germanium bandgap at the surface. This causes optically-generated carriers close to the surface to experience a drift component away from the surface due to the resulting electric field. A wider bandgap at the surface therefore reduces surface carrier recombination by forcing more carriers to recombine in the bulk where a long bulk carrier lifetime exists. The increase in effective lifetime may offer considerable improvement in modulator efficiency. The modulator surfaces would then simply require optical polishing as a final stage prior to the application of AR coatings.

To significantly increase the proportion of carriers recombining in the bulk, the germanium bandgap should be widened over a distance from the surface which is greater than the polish damage depth. In the absence of bandgap-widening, only carriers generated further than a diffusion length from the surface are, to a good approximation, unaffected by the surface. However the presence of different conduction and valence band gradients, or bandgap widening, causes an additional drift current, in this case toward the bulk region. Recombination at the surface is reduced by increasing the drift current away from the surface. The drift current is increased via the electric field, which is maximised by implanting a very shallow silicon layer, creating a large band gap gradient. However, the additional drift component of the total current only exists in the region of the electric field (the implant depth), after which the carriers diffuse away from the surface. A sufficiently high electric field prevents diffusion toward the surface from this point, but if polish damage on an unetched surface still exists in this region, recombination will still take place there via intermediate levels in the bandgap. The position of the recombination in this case has only been shifted slightly away from the surface. To significantly reduce recombination at the surface the electric field (or implant depth) must be significant over the entire damage depth region, which for a high quality commercial polish using $0.05\mu m$ diameter alumina paste, is $0.5\mu m$. Therefore to ensure recombination takes place outside this damaged region, an implant depth of $1\mu m$ was chosen. This takes advantage of the same process as wet chemical etching, which reduces the surface recombination rate by bending the surface energy bands upward over about $1\mu m$ from the surface, causing electrons to drift away from the surface. In both cases the surface damage remains and the mean point at which carriers recombine is shifted away from the surface, although in the implanted case there is also a difference in bandgap gradients.

A convenient means of widening the bandgap is by surface ion-implantation with silicon. If the crystal structure is then regrown by annealing, the resulting surface bandgap is determined by the relative constituents of the two semiconductors. Silicon is a suitable semiconductor although few establishments implant this into germanium. Much of the recent Si:Ge work takes place through epitaxial growth or deposition of high silicon-content Si–Ge onto Si. Silicon's atomic size raises another implantation issue; a relatively deep silicon implant required by this technique needs a high energy ion beam, and this causes significant structural surface damage to the germanium. Annealing re-crystallises much of this lattice damage, but the surface must be lightly polished to remove the amorphous pitted regions of such a high energy implant. The other drawback of bandgap widening by implantation is the possible reduction in bulk carrier lifetime in the immediate vicinity of the implant due to imperfect re-crystallisation. To maintain the long bulk carrier lifetime required for optimising the induced absorption relies on successful re-crystallisation and avoiding contamination by lifetime-reducing impurities at the elevated temperatures required by the annealing process.

The required amount of bandgap widening depends on the thermal energy of conduction-band electrons. The increase in the bandgap should be a few times the room temperature electron thermal energy to prevent thermal excitation of electrons over this surface potential barrier. The surface bandgap must therefore be widened by approximately $4kT$. To increase the bandgap by $4kT$ at room temperature requires [127] approximately 6% of silicon atoms for growth in the [001] direction of the (100) plane. Germanium has 4.42×10^{22} atoms cm^{-3} [42], so to provide 6% silicon atoms over a depth of $1\mu m$ requires 2.65×10^{17} silicon ions per cm^2. The range for a $200keV$ silicon ion in germanium is $0.1884\mu m$ [128], so assuming linear scaling, the energy required for a $1\mu m$ implant is $1.1MeV$. Such a high energy and area implant density would damage the outer surface region beyond repair through annealing. In practice three lower-energy implants were used to generate a stepped implant profile approximating a linear bandgap increase. Thermal diffusion of the silicon into the germanium was considered unwise due to the low diffusion coefficient of silicon in germanium ($\sim 10^{-12} cm^{-2} s^{-1}$ at $800°C$, compared to $5 \times 10^{-5} cm^{-2} s^{-1}$ for copper) and possible permanent damage to bulk carrier lifetime through impurity diffusion at such temperatures for long periods.

A germanium test sample was implanted with 1.34×10^{16} cm^{-2} of $160keV$ Si, followed by 1.95×10^{16} cm^{-2} of $80keV$ Si, followed by 5.39×10^{16} cm^{-2} of $40keV$ Si. This was calculated in order to give 6 *atomic* % of Si to $0.2\mu m$, 4% of Si to $0.4\mu m$ and 2% of Si to $0.6\mu m$. The gaussian implant distribution about these centre distances should give a resulting mean distribution profile which is close to the required triangular potential barrier, reducing away from the surface. Following this implantation the sample should be annealed to enable crystal regrowth. However, the purity of this sample was unknown prior to its implantation. Subsequently, samples from the same batch were found to be of low bulk purity, so any improvement due to the wider bandgap will be small and difficult to distinguish, and so the sample was not annealed. This remains an area for future work.

6.4 Surface coatings

Another means of increasing the modulator's performance and efficiency is by using surface coatings. Antireflection (AR) coatings on the modulator offer three advantages. Aside from increasing the 'on' state transmission in the 8 to $14\mu m$ band to essentially 100%, improving the signal to noise ratio at the detector, the coating can be designed to antireflect the pump laser wavelength, and also protects and preserves the etched low surface recombination surface. The requirement to AR coat the sample at two such widely separated spectral regions is relatively uncommon. Even more uncommon is the requirement to AR coat a sample at a strongly-absorbed wavelength. The pronounced effect of dispersion over these two widely-separated regions must therefore be considered. Usually this is neglected in calculations in the 8 to $14\mu m$ region where dispersion is insignificant. This work has concentrated on the use of a single layer ZnS AR coating designed for the 8 to $14\mu m$ band, and investigated its performance as regards the two subsidiary advantages.

A single layer AR coating is used to reduce optical reflection at the centre design wavelength λ_c and over a moderate bandwidth either side of this. The key aspect of using a single-layer AR coating is that although it introduces angular- and wavelength-dependent reflectivity, the transmission at any wavelength is never worse than with no AR coating at all. Ideally the AR coating should provide 100% transmission of the modulated wavelength band in the 'on' state, and 0% reflection of the pump wavelength, across the entire modulating aperture. The transmission should exist over a range of incidence angles consistent with f2 optics used in the application for the modulated (8 to $14\mu m$ band). The 0% reflection at the pump wavelength should exist over a range that permits optical excitation of the germanium aperture without the optical pump system obscuring the f2 optical transmission of the IR image.

Single layer AR coatings were successfully deposited using an Edwards Auto 306 evaporator to AR coat germanium at design wavelengths close to $10\mu m$. The design constraints and suitability to also AR coating at the pump wavelength ($980nm$) are now discussed. AR coatings accounting for dispersion were designed using a combination of Mathcad simulations and the TFCalc thin film coating design software.

6.4.1 Single-layer antireflection coatings

A single layer antireflection coating requires the optical path difference at normal incidence between reflected rays from the air-coating interface and the coating-germanium interface to be half a wavelength at the design wavelength. At the design wavelength (λ_c) the reflectivity is zero if the coating is perfectly matched to the germanium refractive index. Perfect matching with an external air environment requires that the coating refractive index (n_2) is equal to the square root of the germanium substrate refractive index (n_3). This results [101] from solving the wave equations with their respective boundary conditions, giving the power reflectivity at normal incidence at the design wavelength with incidence medium n_1 as:

$$R = \left(\frac{n_1 n_3 - n_2^2}{n_1 n_3 + n_2^2}\right) \tag{6.3}$$

The reflectivity at the design wavelength therefore becomes zero if this condition is met. In practice, finding a coating with suitable deposition properties, low dispersion and high optical transmission over the required spectral band with an exact refractive index match is difficult, although very good matches are obtained with ZnS and ZnSe. In addition to the reflectivity-minimum at the design wavelength, reflectivity minima also occur at wavelengths λ where the film thickness h satisfies $h = (2n+1)\cdot\lambda/4n_2$, where $n = 0, 1, 2, ...$ and λ_c is the centre design wavelength for the coating. Assuming a germanium refractive index of $n_3 = 4.0$ and a coating refractive index of $n_2 = 2.0$, a coating with a centre design wavelength at $10.0\mu m$ has zero-reflectivity minima at $3.33\mu m$, $2\mu m$, $1.42\mu m$, $1.11\mu m$, $0.909\mu m$ and so on. The problem of dual-wavelength AR coating over such a broad spectral band is now apparent. Although at the design wavelength the fringe separation is slowly varying with wavelength, requiring only moderate accuracy of film deposition thickness, the narrower fringe separation at the shorter pump wavelength ($\sim 980nm$) gives difficult design constraints. This requires an accurate pump wavelength with narrow bandwidth to position within the 6^{th} reflectivity minimum. The success of this single-layer AR coating at the pump wavelength relies on achieving an accurate deposition thickness. The reflectivity is also affected by material dispersion, incidence angle variation and temperature, whose effects are more significant at the shorter pump wavelength. Excitation of the germanium aperture at the pump wavelength requires oblique illumination to avoid the excitation laser obscuring f2 optical transmission in the modulated 8 to 14μm band. The illumination is likely to involve a range of incidence angles if the laser source is uncollimated. This requires modelling of the reflectivity over a range of incidence angles, and accounting for dispersion and temperature variation to determine the constraints and feasibility of such an AR coating at both wavelengths.

The reflectivity is determined as a function of incidence angle and wavelength using the matrix method outlined for the modelling of microwave reflectivity in Section 4.3.2. The characteristic equation for the air-coating-germanium stack shown in Figure 6.13 is given by Equation 6.4.

$$M = \begin{bmatrix} cos\beta_2 & -\frac{j}{p_2}sin\beta_2 \\ -jp_2sin\beta_2 & cos\beta_2 \end{bmatrix} \begin{bmatrix} cos\beta_3 & -\frac{j}{p_3}sin\beta_3 \\ -jp_3sin\beta_3 & cos\beta_3 \end{bmatrix} = \begin{bmatrix} m_{11} & m_{12} \\ m_{21} & m_{22} \end{bmatrix} \tag{6.4}$$

where β_r and p_r are given by Equations 4.51 and 4.52, θ_1 is the incidence angle to the film and θ_2 and θ_3 are determined using Snell's law. The power reflectivity is then given by Equations 4.53 and 4.54.

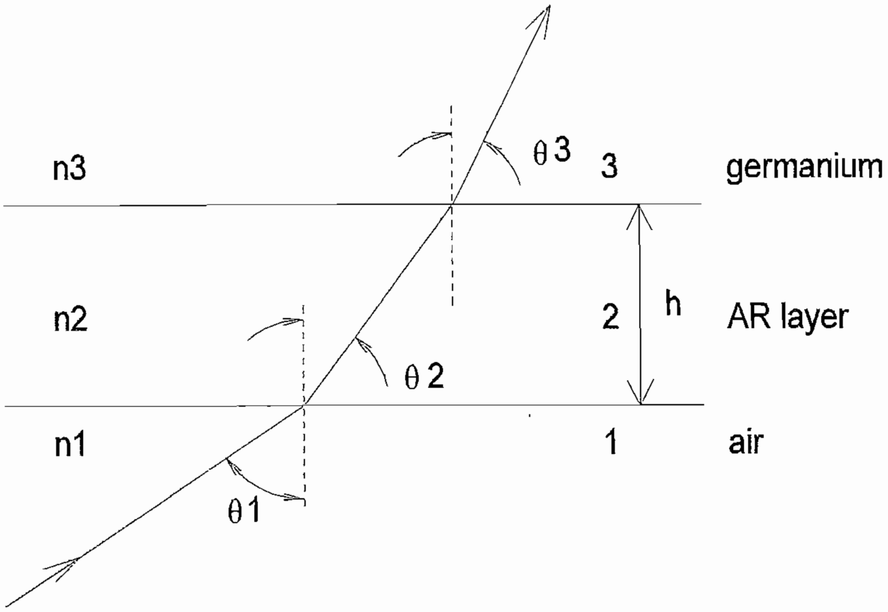

Figure 6.13: Layer configuration used to determine reflectivity of a single layer AR coating

This gives the reflectivity vs incidence angle and wavelength when the dispersion equations for germanium and the coating layer are used. A Mathcad simulation was written using the above equations to determine the reflectivity as a function of incidence angle, temperature and layer thickness.

6.4.2 ZnS as an antireflection coating

Zinc sulphide is an almost perfectly matched AR coating for germanium, and a material in common use. Its refractive index of 2.201 at $10.0\mu m$ means it is very close to perfect matching with germanium of refractive index 4.004 at $10.0\mu m$. This slight offset from the perfect situation gives a maximum transmission at the centre design wavelength (assuming zero film absorption) of 99.1%.

Although other single-layer materials will AR coat germanium reasonably well at this wavelength, such as zinc selenide ($n = 2.406$ at $10.0\mu m$), the ease of deposition of ZnS, its known adherence to germanium and being relatively innocuous determined its choice as the only material of interest. A single-layer quarter-wavelength coating designed for a wavelength λ_c must have an optical thickness of $\lambda_c/4$, requiring a film thickness of $1.136\mu m$ for ZnS. Although the AR coating transmission varies across the 8 to $14\mu m$ band, the fringes at this long wavelength are widely separated, giving an average transmission of 95.6% over this region.

The design of AR coatings at two wavelengths is complicated if either the substrate or AR coating material is dispersive. The wide separation of the two wavelengths requiring AR coating, combined with the fact that both zinc sulphide and germanium are dispersive, means dispersion must be accounted for. At $10.0\mu m$ the refractive indices of ZnS and germanium are 2.201 and 4.004 respectively. By $980nm$ (the desired pump wavelength) these have risen significantly to 2.294 and $4.473 + 0.161i$ (calculated from the Sellmeier [97]) respectively. Generally, dispersion increases the refractive index increases toward shorter wavelength, reducing the fringe-minima separation slightly. To properly model dispersion, the thin film design program TFCalc was used, in which material refractive indices are specified as a function of wavelength. Dispersion also causes a slight shift in the peak transmission from the design wavelength. For example, if the design wavelength is λ_c, then at this point the film thickness $d = \lambda_c/4n_{20}$ where n_{20} is the refractive index at the design wavelength. Equation 6.3 predicts 0% reflectivity (100% transmission in the absence of absorption) at λ_c if the square root of the substrate refractive index, germanium, is equal to the refractive index of the AR film. However with ZnS on germanium the square-root refractive index criteria is not met at the design wavelength, but due to dispersion is more-closely met at slightly longer wavelength, and the transmission maximum moves to longer wavelength. Two competing effects determine the resulting shift in wavelength: the slowly changing reflectivity at the fringe maxima, and the refractive index match. The resulting wavelength shift from the design wavelength is small, but is confusing when looking at the exact values of maximum transmission from a single layer AR film. Typical calculations showed the peak transmission occurs at a few *nm* longer wavelength than the design wavelength, for a design wavelength at around $10\mu m$. Although the dispersion must be modelled, the effect of this latter point on an broadband AR coating at around $10\mu m$ can usually be ignored. This is shown by simulation results below. These results show graphs of polarisation-averaged reflectivity against wavelength for two spectral regions. Detail is shown at the longer wavelength limit for the coating properties in the 8 to $14\mu m$ modulated region. This is shown (where relevant) for normal incidence and for 14° incidence, the latter being the half-cone incidence angle for f2 optics, representing the extremes of reflectivity variation. For the pump wavelength region, normal incidence, 30° degree, 35° degree and 40° degree incidence is considered. Geometrical considerations of exciting of the aperture without obscuring the f2 optical transmission combined with reasonable diode laser excitation parameters, give 30° to 40° as a reasonable spread in incidence angle range for the excitation.

Figures 6.14 to 6.19 show the effects on a $1.173\mu m$ ZnS coating thickness, which has a centre design wavelength of $10.308\mu m$. The thickness was determined by designing a quarter-wavelength coating for a $10\mu m$ centre wavelength, and then changing its thickness slightly until the minimum reflectivity of the 6^{th} fringe occurred at the pump wavelength, $980nm$. The change in fringe position at the shorter wavelength is much more significant than at longer wavelength. The centre wavelength in the wide 8 to $14\mu m$ region is not critical due to the slowly-varying transmission in this region. This resulted in the above film thickness, which is used throughout the analysis. This unconventional approach to coating design means that a small variation in film thickness and a small variation in (longer wavelength) centre design wavelength, is traded for the possibility of simultaneously AR coating at the pump wavelength with a quarter wavelength film.

The importance of accounting for dispersion in the analysis is shown by Figure 6.14, giving the reflectivity variation when dispersion is accounted for, and when dispersion is ignored and the $10\mu m$ refractive indices are used over the entire wavelength range. A slight variation in reflectivity is seen in the longer wavelength region where the reflectivity is not critical. In the shorter wavelength region the effect is much more severe and the 6^{th} fringe minima moves from $980nm$ (accounting for dispersion) to $940nm$. Only at $10\mu m$ do the graphs give the same reflectivity. At the $980nm$ reflectivity minima (accounting for dispersion) the reflectivity becomes 20% if dispersion is not included. Dispersion also changes the amplitude of the fringes as the mismatch between refractive indices of ZnS and Ge changes. If dispersion is not accounted for the fringe pattern has a constant amplitude, and if the film refractive index is perfectly matched to the substrate the reflectivity minima will always be at zero. The stronger effect of any changes at the short wavelength than at longer wavelength is a feature of all the graphs presented.

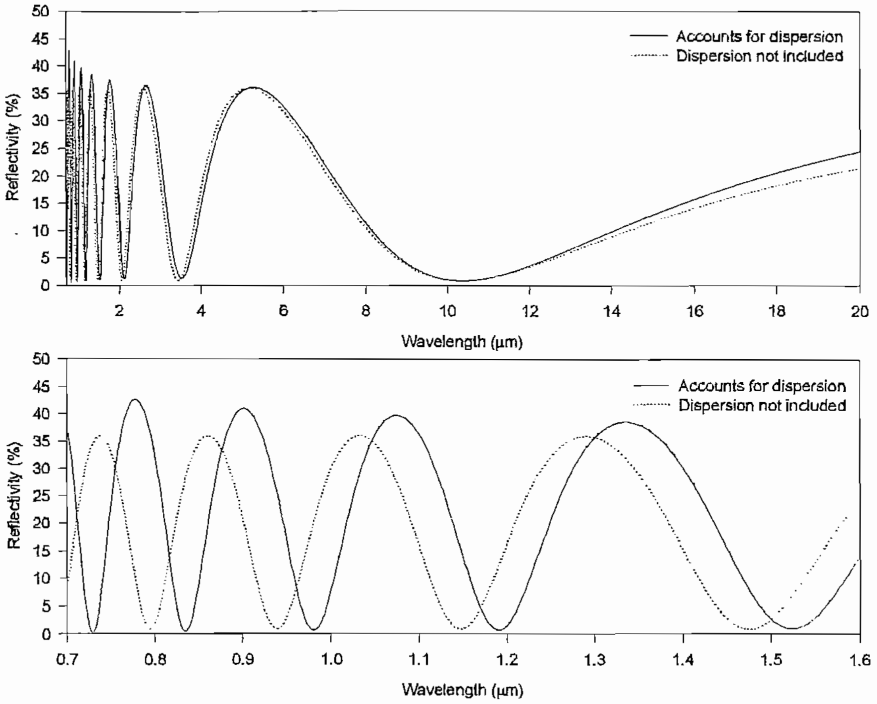

Figure 6.14: Reflectivity variation vs wavelength accounting for dispersion and neglecting dispersion

The effects of dispersion are included in all further graphs. Figure 6.15 shows the effect of a variation in incidence angle. The upper graph shows the reflectivity at the extremes of likely incidence angles in the modulated spectral region. In the centre of the aperture where incidence angles are normal, the reflectivity is slightly lower than at the perimeter of the aperture where incidence will be up to 14° from the f2 optics. The difference in reflectivity at the 8 and $14\mu m$ wavelength extrema is slight; having a maximum difference of 0.5%. The lower graph shows that increasing the incidence angle moves the reflectivity minima toward shorter wavelength. The variation in mean reflectivity at the extremes of 30° and 40° moves the reflectivity minimum from $958nm$ to $943nm$ respectively. The change in reflectivity experienced by a fixed wavelength in this region over this range of incidence angles is no more than 9%.

The effect of temperature variation at normal incidence is shown in Figure 6.16 by using the temperature-dependent Sellmeier equations for the refractive indices of ZnS and Ge over the military temperature range. The graphs almost perfectly overlay,

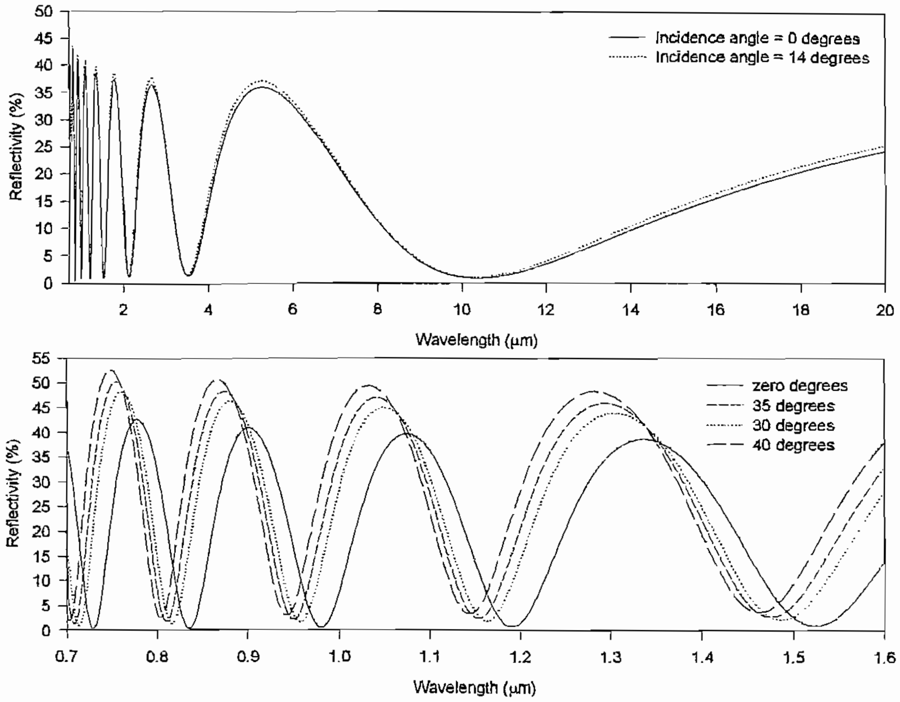

Figure 6.15: Average reflectivity variation vs wavelength for a range of incidence angles

showing negligible change in reflectivity from $-50°C$ to $50°C$.

Finally the thickness tolerance of the film for dual AR coating at $980nm$ and around $10\mu m$ is determined. The tolerance is governed by the shorter pump wavelength region. The effect of AR coating thickness changing by $\pm 10nm$ from the required value of $1.173\mu m$ is shown by Figure 6.17. The solid graph shows a film with a reflectivity minima at $980nm$ for normal incidence, where the average reflectivity is 0.65%. Reducing the film thickness by $10nm$ moves the reflectivity minima to $972.5nm$, and increases the reflectivity at $980nm$ to 2.00%. Increasing the film thickness by $10nm$ moves the reflectivity minima to $987.5nm$, and increases the reflectivity at $980nm$ to 2.1%. Therefore a 1% change in film thickness is seen to cause an absolute change in reflectivity of 2%. This effect on the average reflectivity at the pump wavelength is acceptable due to the absorption-homogenisation effects at high absorption levels, described in Chapter 7.

The above graphs have shown the effects of dispersion, incidence angle variation, temperature and film thickness on the average reflectivity of quarter-wavelength films. The dominant factors affecting success of an AR coating at $980nm$ are i) accounting for dispersion, ii) the variation in incidence angle and iii) achieving accurate film thickness. The film thickness should be accurate to within 1% to maintain an average-reflectivity variation of no more than 1.4%, which is easily attainable using, for example a red

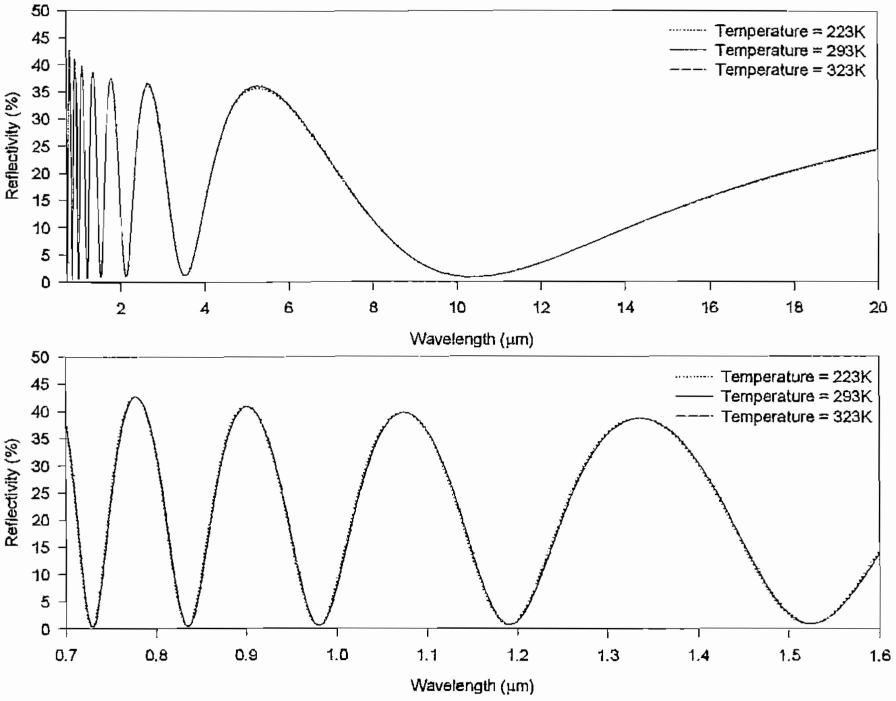

Figure 6.16: Effect of temperature on the position of fringes at long and short wavelength regions

monitor laser diode and counting the fringes during deposition. The tolerance of ±10*nm* is roughly 1/60 wavelength of red light. Minimum reflectivity fringes occur every time the optical path difference is an odd number of quarter wavelengths, giving fringe minima at every odd multiple of approximately $80\mu m$ of ZnS film. Therefore if resolution of 1/10 of a fringe is possible, a deposition tolerance of 1% is relatively easy to attain. The incidence angle variation has shown that over a range of 30 to 40° the average reflectivity at the pump wavelength varies by approximately 9% (±4.5% reflectivity change either side of the mean illumination angle, 35°) over the aperture, assuming uniform aperture illumination. The effects of this can be counteracted if necessary by using a non-uniform excitation illumination pattern.

This has highlighted the dominant parameters of the AR coating, but the excitation in the case considered was that resulting from a circularly-polarised, or random unpolarised source, and only the average reflectivity was determined. To see the effects of a polarised laser source, illumination-modelling software would greatly simplify a very complex task. In the absence of this, the effects of polarisation at the extreme values of variable parameters was considered using the TFCalc software package, which is designed for thin optical film analysis.

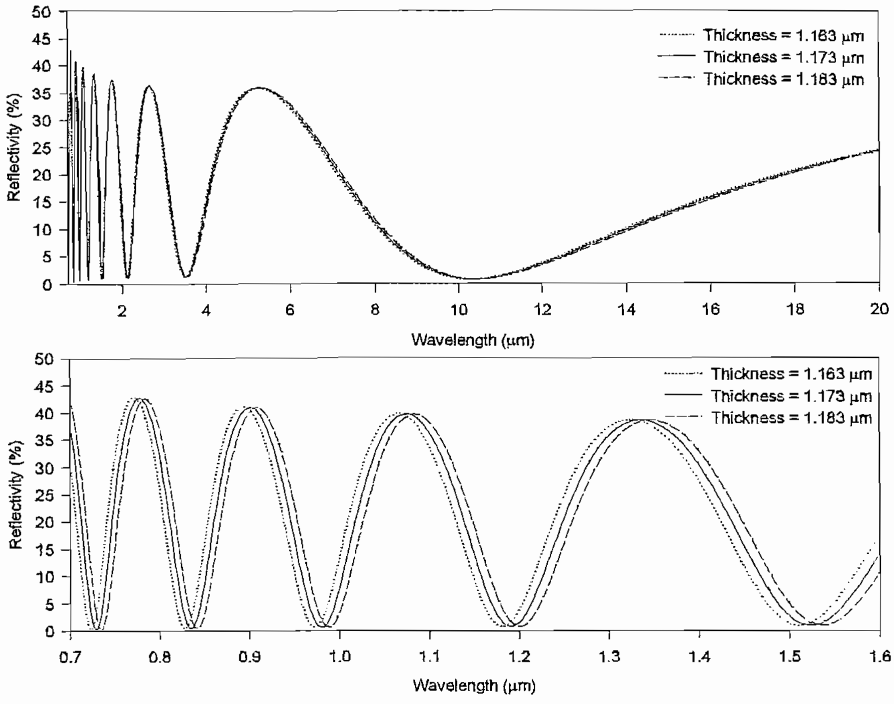

Figure 6.17: Effect of film thickness variation at long and short wavelength regions

The reflectivity vs wavelength for S, P and average polarisation is shown in Figures 6.18 and 6.19 for the longer and shorter wavelength regions respectively, for the same material parameters as above. The polarisation state in this application depends on the specific laser source used. Diode lasers become more linearly polarised [129] as the output power is increased, with the major polarisation axis parallel to the junction plane. If fibre-coupled, the large diameter high power optical fibres likely to be used will be multimode and do not maintain polarisation, giving randomly-polarised illumination. Assuming illumination is incident directly from a diode bar such that the junction plane is perpendicular to the plane of incidence, then the S polarisation dominates and must be considered in the graphs below.

In Figures 6.18 and 6.19, accounting for polarisation does not alter the wavelengths of fringe minima and maxima, although the amplitude and spectral width of the fringes does change. A change in amplitude of the fringes is observed with change in polarisation since this changes the interface reflectivities. In the longer wavelength region, reflectivity is only mildly affected by polarisation. This is due to the smaller angles and narrower range of incidence angles of practical importance in this region. In the shorter wavelength region the effect of polarisation is more pronounced, especially for the S polarisation. At the reflectivity maxima the reflectivity is significantly higher than

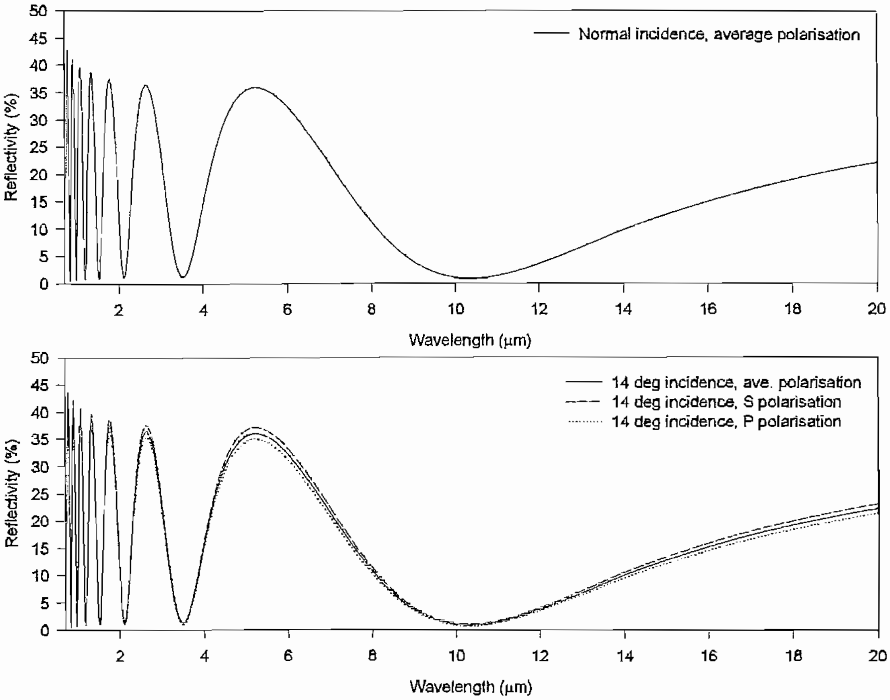

Figure 6.18: Reflectivity vs wavelength for longer wavelength region at normal incidence (upper) and 14° incidence (lower)

the average polarisation reflectivity values previously considered. This increase is larger at larger incidence angles.

However the region of interest for an AR coating is the minimum in reflectivity which differs little over the incidence angle range from the average polarisation case. At $980nm$ the S polarisation minimum reflectivity at 30° and 40° incidence angles is 1.7% and 3.07% respectively. This change in reflectivity is small, although the narrowing spectral width of this fringe is more important. In order to remain within this reflectivity minimum, the tolerance of the source central wavelength should be no greater than $\pm 7nm$. The typical FWHM spectral width of a laser source from diode bar lasers obtained during this work is in the order of $2-3nm$. Using the typical diode laser temperature coefficient of central wavelength of $0.3nm/^{\circ}C$, a $10^{\circ}C$ temperature shift during operation moves the centre wavelength by $3nm$. This gives a practical tolerance of $\pm(3nm + 3nm)/2 = \pm 3nm$. If a spot-wavelength laser diode were obtained, this would fit within the reflectivity minimum as required, from this consideration alone.

If all effects are treated as non-correlating, the maximum change in reflectivity at $980nm$ following uniform illumination of the aperture is 1.3% from incidence angle considerations and $\pm 2\%$ from layer thickness consideration with a tolerance of $\pm 10nm$.

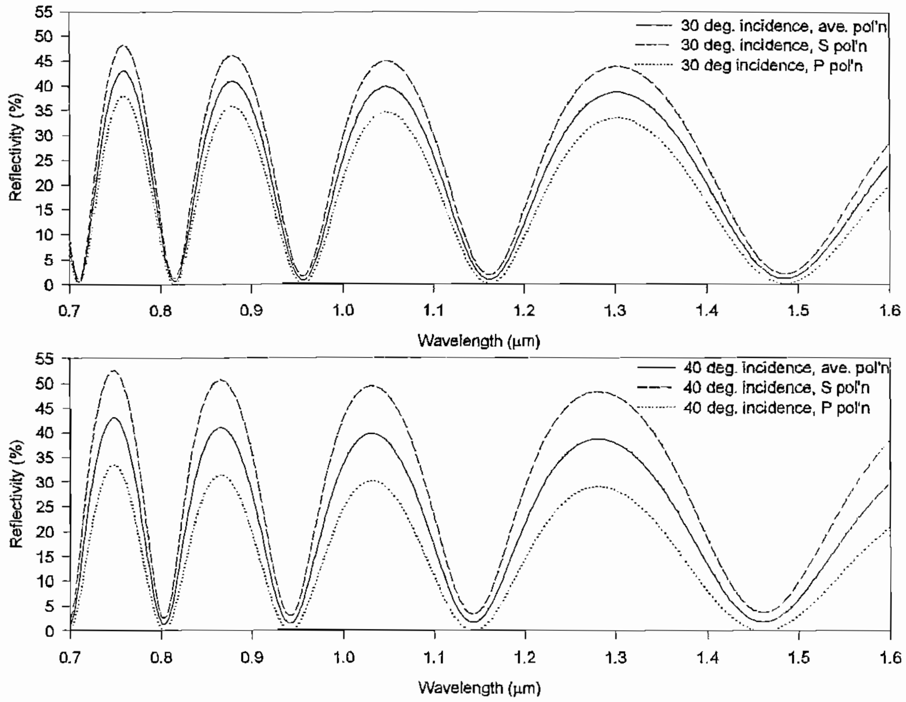

Figure 6.19: Reflectivity vs wavelength for shorter wavelength region at 30° incidence (upper) and 40° incidence (lower)

This few-percent total variation relies on obtaining a spot-wavelength laser diode. This is a difficult and costly task at high power, requiring individual testing of diode lasers due to the temperature-dependence of their centre wavelength. Accurate film deposition thickness with a ±1% tolerance was achieved experimentally using an optical reflectance setup using a red laser diode and counting the fringes during deposition. For the purposes of a demonstration device, a single layer AR film was deposited as accurately as possible, and the effects of reflectivity variations was investigated through testing of the transmission in the excited an unexcited states. For multiple device fabrication, obtaining several diode lasers of such precise wavelength is impractical, therefore a single-layer AR coating suitable for these two wavelength regions simultaneously is unlikely to be used in a final device. The difficulty in procuring spot-wavelength diodes places too much pressure on the position of the 5^{th} or 6^{th} fringe minima. Attempting to do this in a demonstration device does not make things any worse than with no coating at all, since a single-layer AR film only reduces the reflection of the pump wavelength, but could result in a slow variation in absorbed excitation power with incidence angle across the illuminated aperture. The subsequent variation in induced absorption across the aperture may be more than that observed without this type of AR coating, depending on the spectral width and centre wavelength of the laser diode. Therefore in a demonstration device the dual-wavelength quarter-wave AR coating is suitable, although in a final production device a specially designed multilayer coating would be used.

6.4.3 ZnS antireflection coating evaporation

Despite the relatively thick films required by the above calculations, single layer quarter wavelength ZnS films were routinely deposited via evaporation from ZnS in pellet form. No problems with film-adherence were found if, prior to deposition, the sample was heated slightly using a hot air gun prior to evacuation, or during evacuation using a substrate heater. A ZnS layer thickness of $1.173\mu m$ was used so the film AR coated at $\lambda = 10.308\mu m$ (refractive index here = 2.197) and the 6^{th} fringe AR coated at $980nm$.

A typical transmission spectra of a two-surface ZnS-coated germanium sample is shown in Figure 6.20, whose properties are summarised in Table 6.1. Accounting for dispersion, the position of this fringe gives a film thickness of $1.184\mu m$, slightly thicker than the required thickness of $1.173\mu m$. TFCalc was used to determine the properties of the 6^{th} fringe reflection minima using the calculated film thickness.

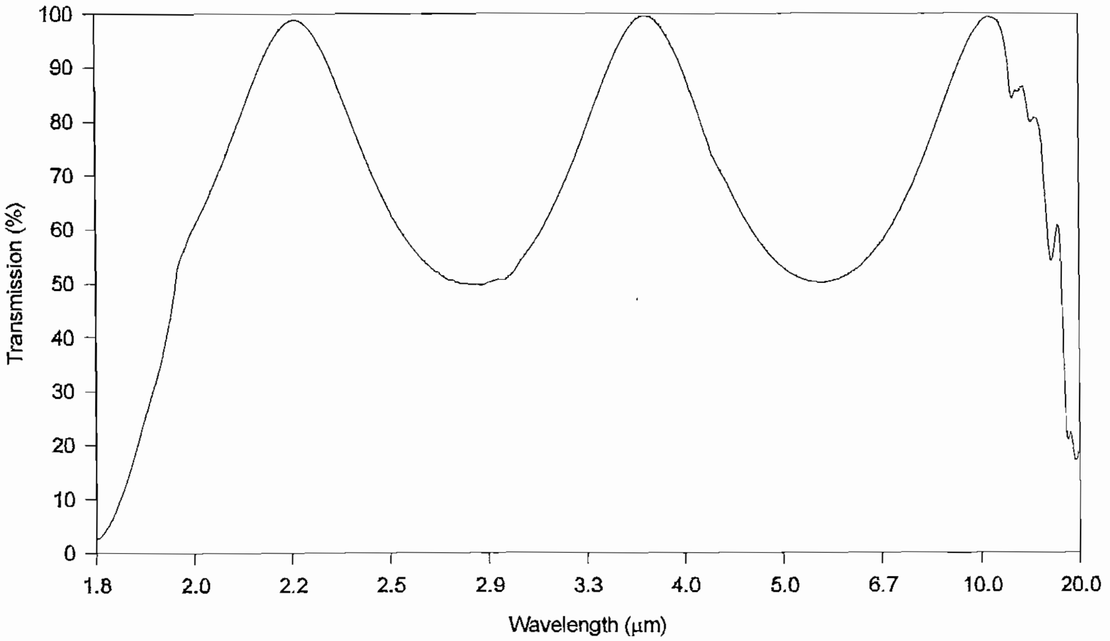

Figure 6.20: Transmission spectra of AR coated germanium sample with centre design wavelength at $10.308\mu m$

	8.0 μm T(%)	**14.0 μm T(%)**	**peak T(%) at λ (μm)**	**6th minima wavelength**	**980nm R (%)**	**film thickness (μm)**
predicted	88.7	90.2	99.1, 10.308	980nm	0.65	1.173
measured	77.0	80.5	99.4, 10.44	988nm	2.09	1.184

Table 6.1: Predicted and measured single-layer AR coating properties

During film deposition the layer thickness was determined using an in-vacuum optical reflectance setup and by counting the reflectivity fringes at 650nm observed during film deposition. A diode laser was directed through the observation window in the evaporation chamber and mirrors directed the beam onto the centre of the sample during deposition, and then out through the window to a detector. A minimum reflectivity in the fringes is seen every time the film optical thickness is an odd multiple of a quarter wavelength of the monitor laser. The expected reflectance vs time graph during deposition of a 1.173μm film is shown by the TFCalc simulation in Figure 6.21.

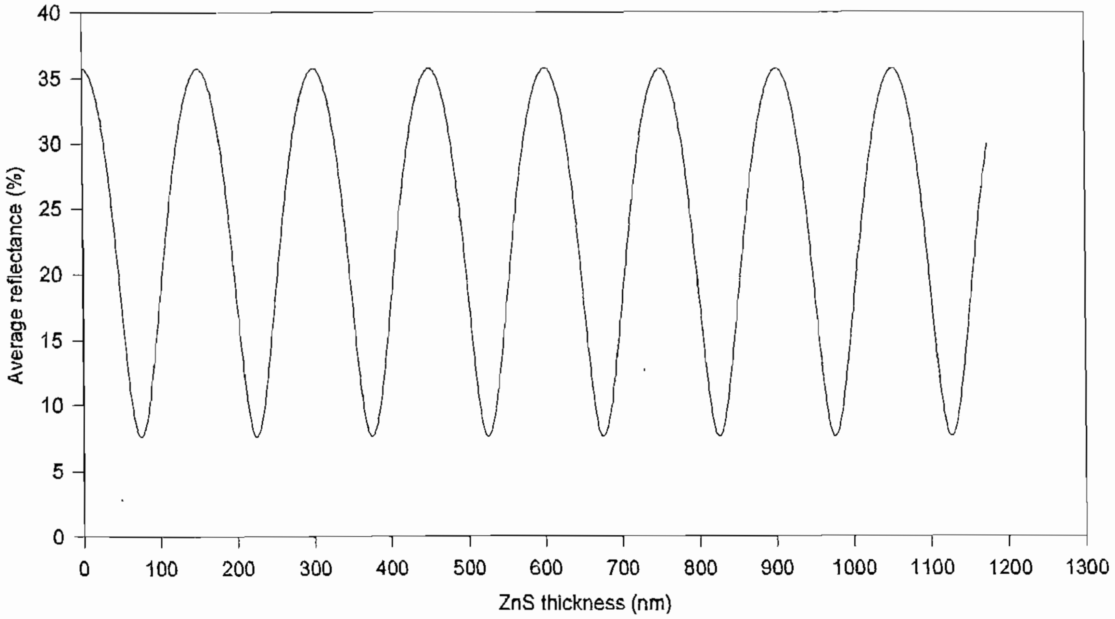

Figure 6.21: Simulation showing reflectance at 650nm vs film thickness for growth of a 1.173μm ZnS film on a germanium substrate

In practice the film deposition rate changes with time due to increased surface contact between ZnS pellet with the evaporation boat or a reduction in pellet size, so uniform fringes are not observed over time. A typical reflectance vs time graph during deposition of ZnS is shown in Figure 6.22. A slow modulation of the amplitude of the required fringe pattern is seen here due to the much slower deposition of ZnS on the mirrors in the evaporation chamber, although this does not affect the shorter period of the fringes caused by faster deposition on the germanium substrate. A slight overshoot of the required thickness was produced due to difficulty in ceasing deposition at a fractional fringe amplitude. The step-up and -down at the start of deposition is due to stray light from the evaporation source as the shutter is opened and closed.

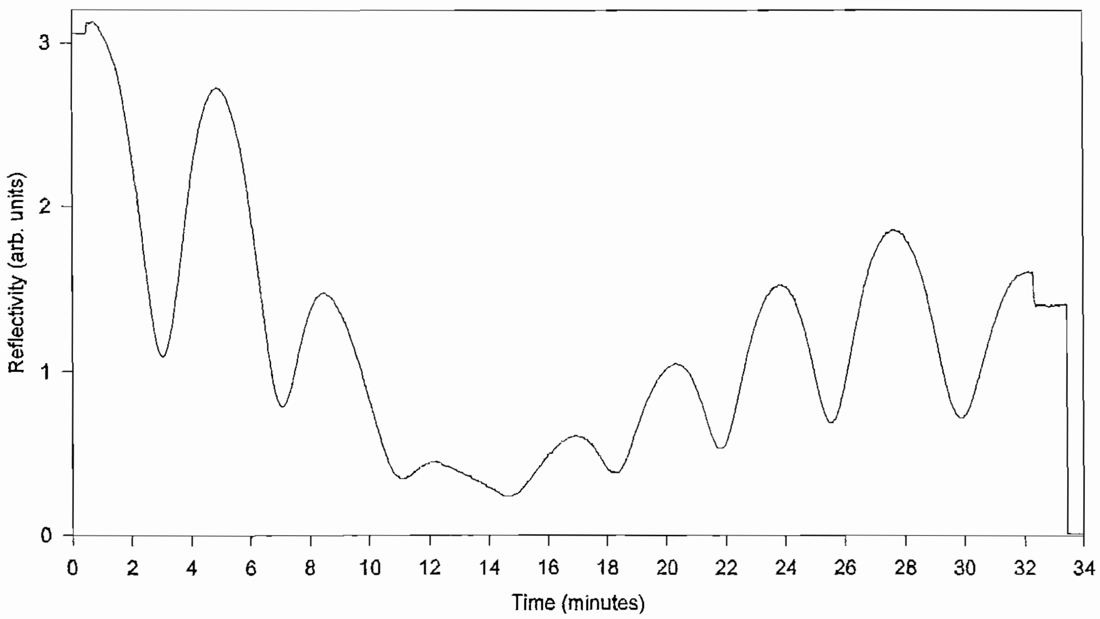

Figure 6.22: Typical variation in reflectance at 650nm with time during film deposition

The design of multilayer AR coatings was not considered by this work. Such an optimised multilayer modulator coating would be designed using a software package to provide the two transmission windows over the required wavelength ranges, and should offer a wider spectral width of low reflectivity around the 980nm pump window and lower reflectivity at the extreme 8 and 14μm regions of the modulated region. This requires a lower centre-wavelength tolerance from the diode laser excitation, easing the necessity to obtain spot-wavelength pump laser diodes. In addition to AR coating a sample, the coating should not degrade the low surface recombination velocity etched surface. A test sample which was etched using the CP4A etchant (Appendix B) and then AR coated using ZnS immediately afterward was found to still have the same depth of modulation after a time in excess of 2 years. This shows that ZnS is compatible with the surface for this purpose.

6.5 Excitation wavelength

Another method of reducing the optical excitation power density required for a given depth of modulation is to use longer-wavelength above-bandgap excitation. This takes advantage of two effects that occur toward longer wavelengths (i) there are more photons in every Watt of optical power since each photon has less energy, and (ii) for above-bandgap wavelengths, the optical absorption coefficient (α_{ill}) is lower. Thus more electron-hole pairs are created per Watt of optical power, and the longer wavelength photons are absorbed deeper into the germanium so electron-hole pairs have to travel further to reach the surfaces. This latter point should increase the effective carrier lifetime (see Equation 3.39).

Two common high power laser diode wavelengths in the excitation wavelength region of interest are reasonably priced: close to $810nm$, and close to $980nm$. Experiments were performed with high power $980nm$ and $813nm$ laser diodes, and a lower power $1480nm$ laser diode. Other than cost, the advantage offered by diodes at $980nm$ and $813nm$ is their ease of availability in $1cm$ diode bar, and stacked-array packages. These offer a convenient, optics-free method of illuminating a germanium aperture in a final working modulator. To date, high power $1480nm$ laser diodes are not available at practicable cost.

By moving the pump wavelength from $813nm$ to $980nm$, A in Equation 3.39 rises by a factor of $980/813 = 1.21$ simply from the 'more photons per Watt' argument. The move also provides an increase in light penetration depth ($1/\alpha_{ill}$) from $0.14\mu m$ to $0.53\mu m$ [91]. Likewise, the move from $813nm$ to $1480nm$ offers an increase in A of a factor $1480/813 = 1.82$ for the same excitation power density, and an optical penetration depth of $2.1\mu m$. To predict the effect of the deeper absorption depth, the steady state carrier distribution model in Section 4.2.2 is used. Figures 6.23 and 6.24 show the modulator's induced absorption (proportional to the area carrier density) in a semi-infinite sample for two values of bulk carrier lifetime, for $S = 1ms^{-1}$ and $S = 5ms^{-1}$ respectively. The induced absorption is normalised to the limiting case of an infinite excitation absorption coefficient, to show the benefit of an increase in excitation absorption depth. The diffusion length is marked L_d.

Figure 6.23 shows that increasing the excitation absorption depth provides an in-

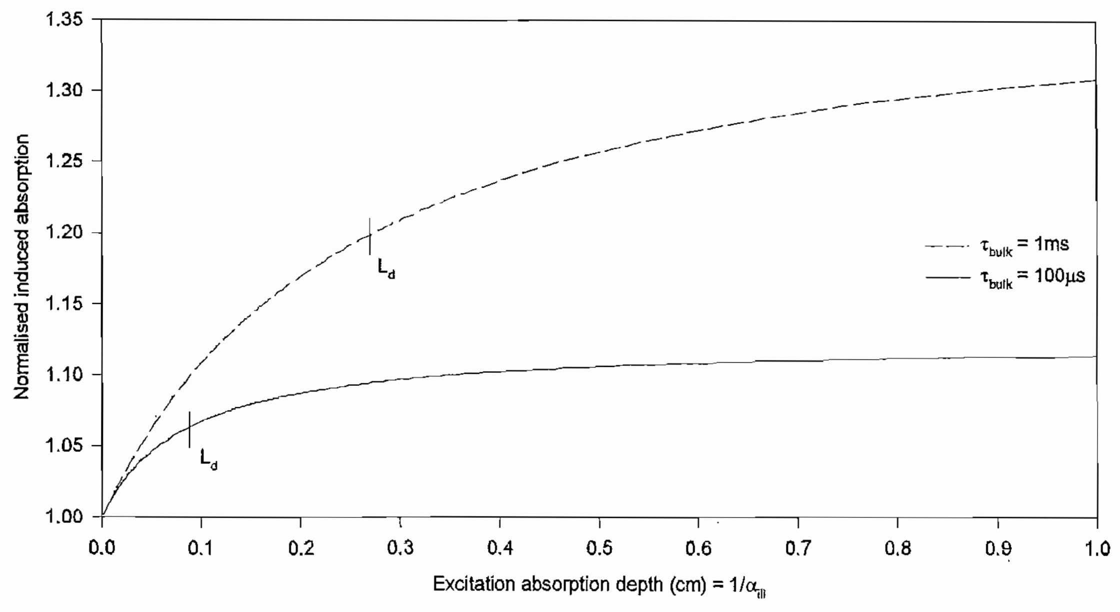

Figure 6.23: Normalised induced absorption vs excitation absorption depth for two values of bulk carrier lifetime and $S = 1ms^{-1}$

crease in induced absorption, although this is only achieved with very deep absorption depths (fractions of $1cm$). The increase in induced absorption only becomes significant when the excitation absorption depth is more than about 10% of the diffusion length in the bulk. Figure 6.24 shows a larger increase in induced absorption with increased excitation absorption depth than Figure 6.23 due to its higher surface recombination velocity, although the dependence on α_{ill} remains the same, and both graphs overlay after a vertical scale change. However, at the micron-absorption depths of the excitation lasers used in the experiments, Table 6.2 shows the longer wavelength lasers offer no significant benefit from this aspect, even in the presence of high S. This table gives the relative absorption, defined as the ratio of the absorption A induced by the given excitation wavelength to that induced by $813nm$ excitation, for the same number of generated electron-hole pairs.

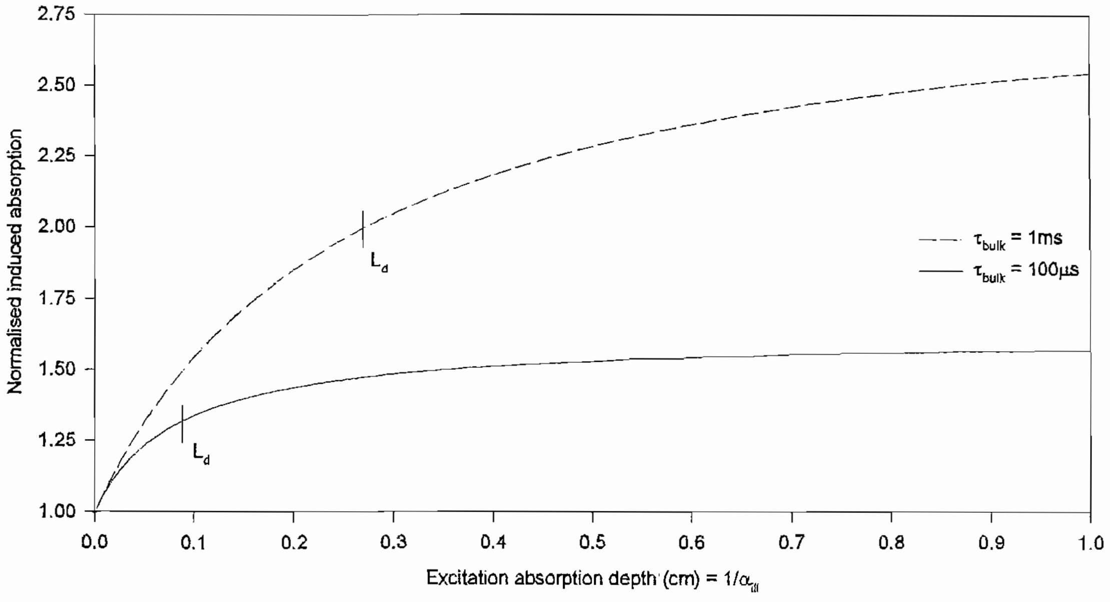

Figure 6.24: Normalised induced absorption vs excitation absorption depth for two values of bulk carrier lifetime and $S = 5ms^{-1}$

6.5.1 Induced absorption dependence on excitation wavelength: experimental results

Experimental validation used a spectrophotometer to determine the induced absorption A at $10.6\mu m$ of various germanium samples when illuminated by equal power densities at $813nm$, $980nm$, and $1480nm$ from laser diode sources. The experimental setup is shown in Figure 6.25. The percentage difference in induced absorption coefficient, $\Delta\alpha$, was determined using the spectrophotometer transmission $T(\%)$, and Equation 6.5, where the excited state transmission is measured at equal power densities.

wavelength (nm)	**absorption depth** (cm)	**relative absorption** $\tau_{bulk} = 1ms$, $S = 1ms^{-1}$	**relative absorption** $\tau_{bulk} = 1ms$, $S = 5ms^{-1}$
813	1.35×10^{-5}	1.0	1.0
980	5.26×10^{-5}	1.000059	1.000296
1480	2.13×10^{-4}	1.000301	1.001507

Table 6.2: Predicted induced absorption at the three laser excitation wavelengths used in the experiments compared to that induced by $813nm$

$$\Delta\alpha = \frac{ln(T\%\, when\, excited\, by\; 980nm\; or\; 1480nm)}{ln(T\%\, when\, excited\, by\; 813nm)} \tag{6.5}$$

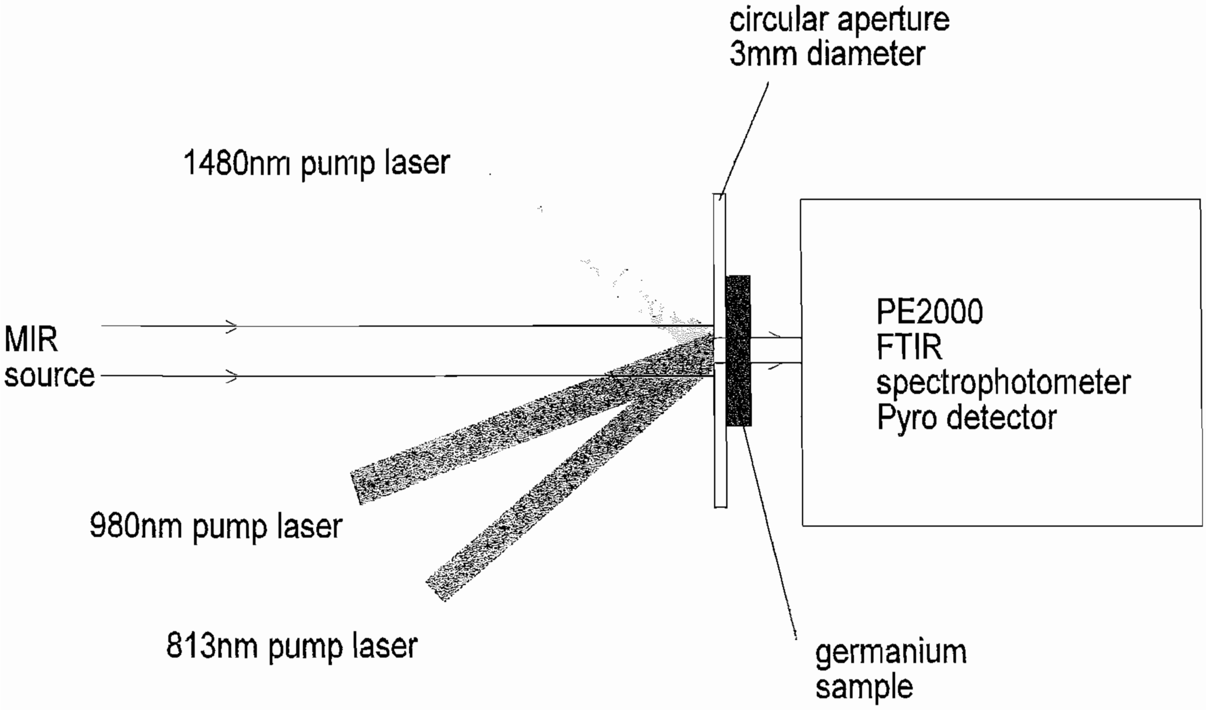

Figure 6.25: Experimental setup to determine the induced absorption during excitation at three laser wavelengths

Equal power densities illuminated the samples by using an aperture to only excite a $3mm$ diameter circle on the sample face. By only using the central region of the exciting laser beams, a reasonably uniform excitation power density was obtained. A power meter situated behind the aperture was used to adjust the laser current to give equal power densities at each wavelength. Snell's law was used to account for changes in Fresnel reflectivity with incidence angle, since oblique illumination was required to position the laser diodes within the spectrophotometer. The complex refractive index [97], incidence angle, laser polarisation and computed absorption at each excitation wavelength are summarised in Table 6.3.

Figures 6.26 and 6.27 show the measured absorption ratio at fixed absorbed power densities for seven samples at $980nm$ compared to $813nm$ and at $1480nm$ compared to $813nm$ respectively. The final column in each stack represents the minimum expected induced absorption ratio, calculated from the ratio of the wavelengths increase in available photons, giving 1.21 and 1.82 respectively. Total instrument-reading error bars are

wavelength *nm*	**refractive index**	**incidence angle°**	**polarisation to incidence plane**	**Absorption** $= (1 - Reflectivity)$
813	$4.674 + 0.4788i$	25	average	0.577
980	$4.473 + 0.1482i$	25	average	0.597
1480	$4.239 + 0.0554i$	40	⊥	0.523

Table 6.3: Wavelength, complex refractive index, incidence angle and power reflectivity in wavelength-dependence experiments

included and although these are small, larger systematic alignment errors exist due to the difficulty in achieving a uniform excitation power density.

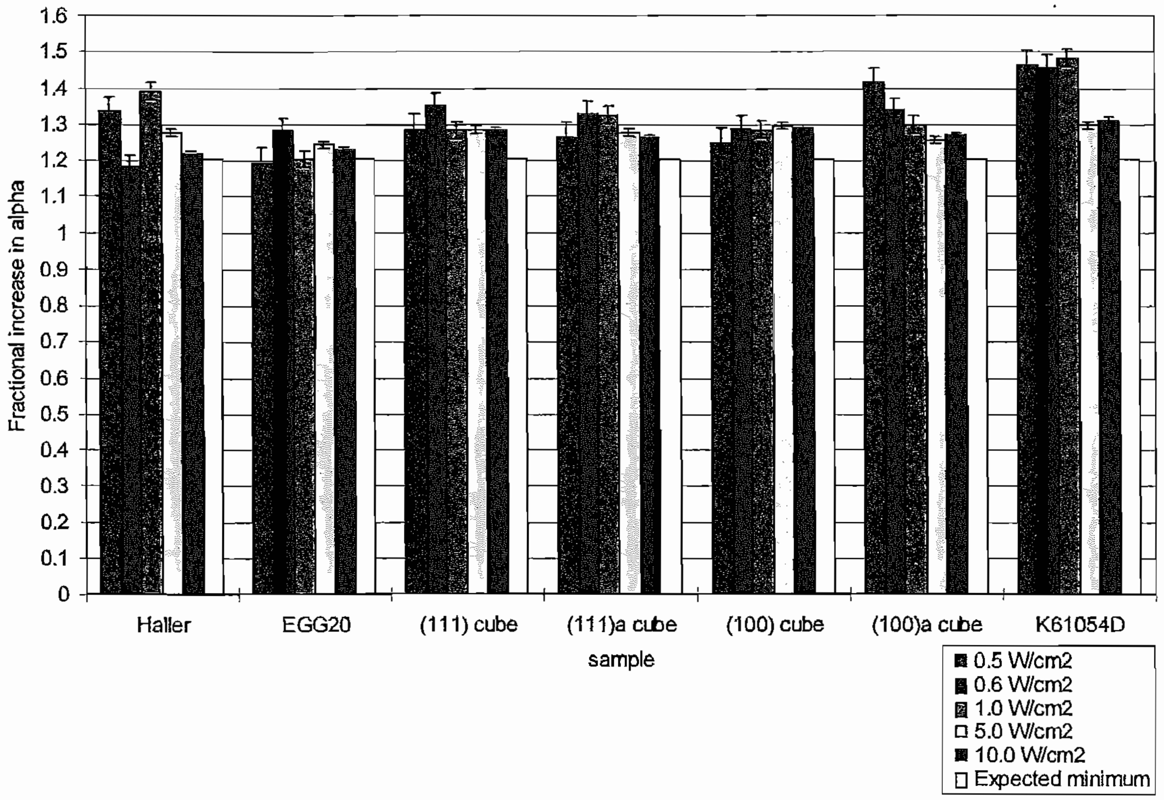

Figure 6.26: Ratio of reflectivity at $980nm$ to reflectivity at $813nm$ with equal absorbed power densities

Within experimental error, Figure 6.26 shows a minimum of the ratio of the wavelengths increase in induced absorption in all samples on moving toward longer wavelength excitation. The average ratio is 1.3. Some readings (K61054D sample) are significantly higher than this. There appears no correlation between measurements at the same power density on different samples, which would indicate different calibration errors at the various excitation currents. In Figure 6.27, a minimum of the ratio of the wavelengths increase in induced absorption is also seen in all samples on moving to the longer wave-

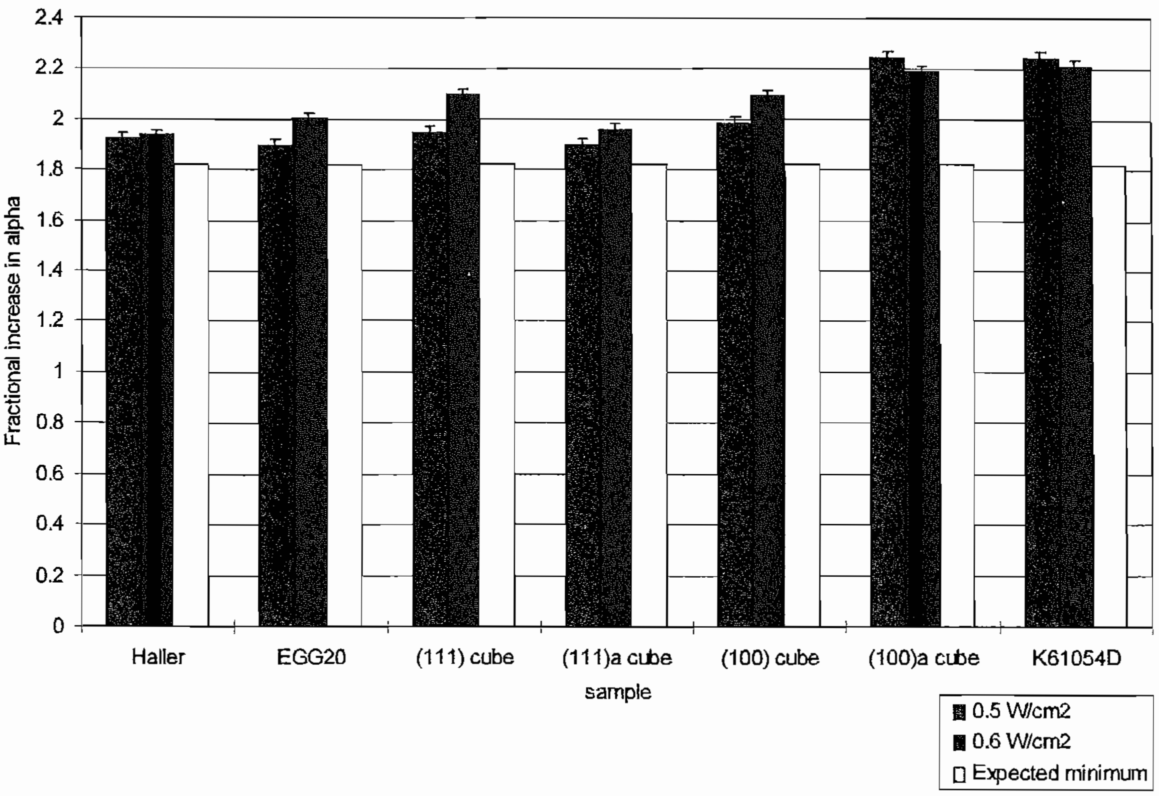

Figure 6.27: Ratio of reflectivity at 1480*nm* to reflectivity at 813*nm* with equal absorbed power densities

length. The average ratio is 2.04. These measurements show much closer agreement for each sample at the two power densities. Comparison between the results of the two above figures shows that consistently higher results are obtained for samples (100)a cube and K61054D. The initial hypothesis that in long bulk carrier lifetime samples where surface recombination is the dominant restriction on the depth of modulation attained, that an increase in excitation absorption depth provided an increase in induced absorption, has been shown by Table 6.2 to be insignificant over the range of wavelengths used in the experiment. The variation in experimental results in Figures 6.26 and 6.27 is therefore attributed to experimental error.

It is concluded, and confirmed by the models in Section 4, that the generation of carriers deeper into the material only renders them less likely to encounter a surface (at which recombination occurs) if they are generated more than $\sim$ 10% of a diffusion length from the surface. In HPGe the diffusion length is several millimetres, the thickness of a modulator element. Corresponding absorption depths in germanium, although achievable through excitation close to the band edge (around $1.8\mu m$), are severely temperature-dependent (see Figure 3.7), and risk the illumination passing straight through the modulator element and onto the detector in the event of a drop in temperature. Thus the significant benefit offered by exciting the modulator at longer wavelengths is solely through the increase in available photons. If high power laser diodes at wavelengths close to $1.5\mu m$ become available in the future, these would offer the benefit of more photons per Watt of optical power without the risk of the excitation passing through the germanium.

Chapter 7

Design and construction of a working demonstration modulator

The purpose of this section is to use the knowledge developed in previous chapters to design and construct a working demonstration modulator. This has been optimised subject to the design constraints placed on the system by the excitation mechanism. In optimising the modulator, several processing considerations must be taken into account. These are considered in this chapter, giving the design path for a working modulator and describing its construction and testing as the first solid state modulator for the 8 to $14\mu m$ thermal image band. The systems, germanium processing and optical excitation tradeoffs and requirements are presented.

7.1 System requirements

The modulator's operation is governed primarily by the tradeoff between switching speed, depth of modulation and system efficiency, until a point where a ceiling of waste heat removal prevents further optimisation. This section gives these systems tradeoffs. Use will be made of Equation 3.39 giving the modulator's total absorption coefficient A. If the unexcited-state modulator transmission is denoted T_0 then the modulator transmission is given by T as:

$$T = T_0 e^{-A\eta} \tag{7.1}$$

In the unexcited state, A is zero providing there is negligible contribution from other processes detailed in Chapter 3. Low-doped 'n' type germanium ($40 - 50\Omega cm$) is sufficient to ensure this, even over the $\pm 50^\circ C$ military temperature range. T_0 is ideally unity within the 8 to $14\mu m$ passband, assuming application of an ideal AR coating. In practice T_0 will be wavelength-dependent as the AR coating will not be perfect. Due to the wide spectral sensitivity of pyroelectric detectors a long-wave pass filter should be included within the modulator system to block the subsidiary-modulated regions around $3.3\mu m$ and around $4.5\mu m$, to avoid misinterpretation of the modulation.

The guideline specification for pyroelectric detector operation was to attain 10% transmission in the 'off' state. Little is gained in detector performance beyond this point and the required power increases rapidly. The excitation efficiency η in Equation 7.1 is the fraction of absorbed excitation power, and depends on the Fresnel reflectivity at the pump wavelength, which is a function of excitation incidence angle. Also, the optical excitation scheme may waste considerable optical power by exciting a larger area than is modulated in attempts to attain greater excitation uniformity. The ideal $\eta = 1$ condition is substantially reduced at the expense of more-uniform excitation. This is considered further in Section 7.3.

In addition to the optical excitation, the waste heat from the diode laser illumination scheme itself must be removed. Currently this is achieved by closed-cycle water-cooling, although a passive heatsink would suffice for short periods.

Finally, the optical illumination involves considerable excitation power (at around $980nm$) reflected by the germanium modulator. To avoid highlighting the camera's position to other IR-sensing systems, and to ensure eye-safety, an absorbing cover is required. This could be simply a piece of AR-coated optical grade germanium, in which no induced absorption (in the 8 to $14\mu m$ region) occurs. This converts incident excitation into heat and also requires heatsinking. A more efficient use of this cover plate is to serve as an additional modulating element, optically in series with the modulator, exploiting reflected excitation power. This is also considered further in section 7.3.

7.1.1 Speed and efficiency tradeoff

The modulator's primary operational tradeoff is that of speed against efficiency. A faster modulator is possible at the cost of a shorter effective carrier lifetime, since this requires faster carrier recombination once optical excitation terminates. This is at the expense of a higher optical excitation power. The effective carrier lifetime results from both bulk and surface recombination. To quantify the speed and efficiency tradeoffs, realistic parameters are now used to model the behaviour of an optically-excited, absorbing, modulator. Typical parameters used in the analysis are given in Table 7.1.

The 8 to $14\mu m$ region 'off' state transmission is given by Equations 3.39 and 7.1 as:

parameter	symbol	value	units
ambipolar diffusion coefficient	D_a	66.04	$cm^2 s^{-1}$
980nm absorption coefficient	α_{ill}	1.9×10^4	cm^{-1}
hole absorption cross section	σ_h	5.33×10^{-16}	cm^2
excitation power	P	1, 2	$W\ cm^{-2}$
excitation wavelength	λ_{exc}	980	nm

Table 7.1: Parameters used in modelling modulator performance

$$T = T_0 e^{-\left(\frac{\tau_{effective} P \lambda_{exc} \sigma_h \eta}{hc}\right)} \tag{7.2}$$

T_0 is assumed unity, as is the absorption efficiency η in all cases. The 'off' state transmission at 10μm must be minimised. This is plotted in Figure 7.1 as a function of effective carrier lifetime and excitation power density, showing the tradeoff between the two parameters. The excited-state transmission is minimised by using high power and a long effective lifetime.

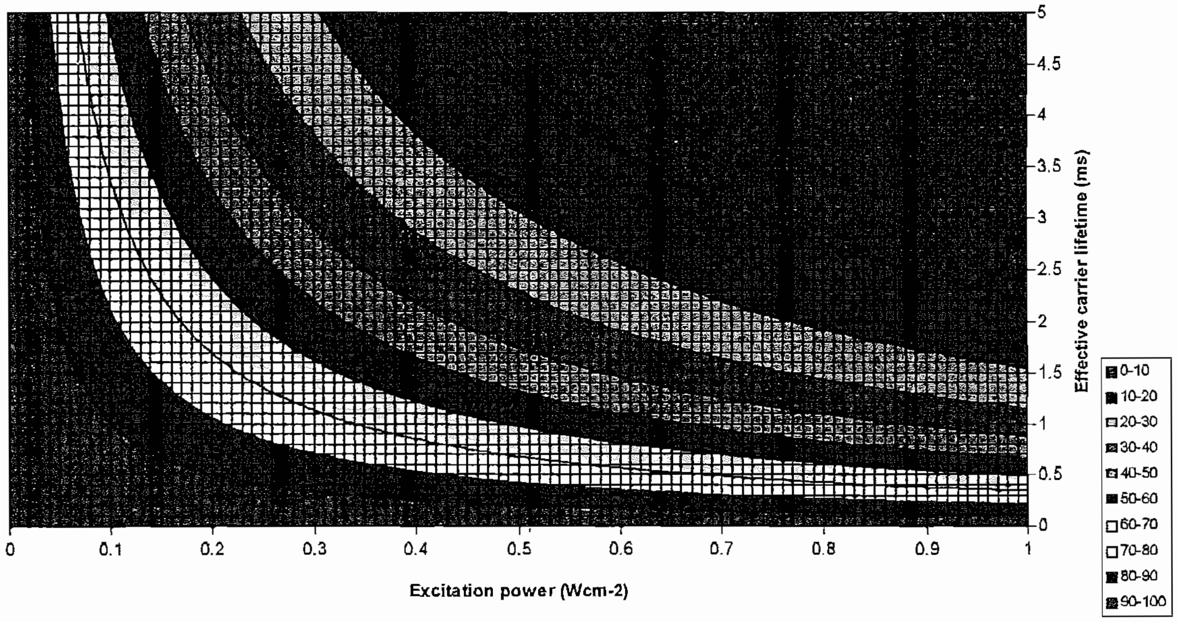

Figure 7.1: Excited-state transmission (%) vs excitation power and effective carrier lifetime

Figure 7.2 shows the excitation power required for the guideline-specification 10% transmission vs effective carrier lifetime, over a wider power range than Figure 7.1.

The modulator's maximum switching frequency is defined by $1/2\pi\tau_{effective}$, and is also plotted in this figure, showing the tradeoff with excitation power.

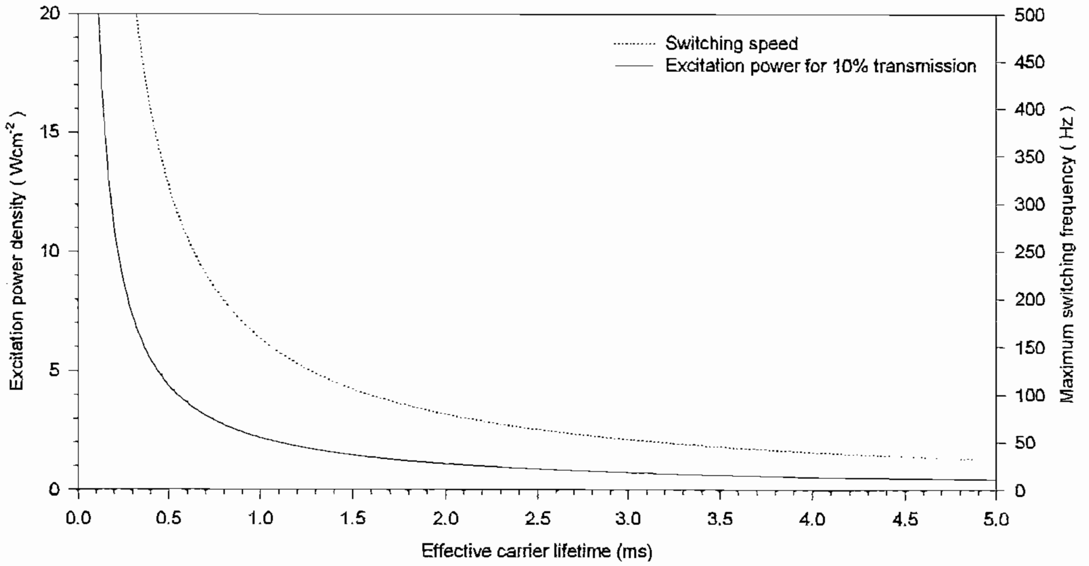

Figure 7.2: Power required for 10% off state transmission and maximum switching frequency vs effective carrier lifetime

In the experimental results reported here, effective carrier lifetimes in the order of $800\mu s$ have been attained (final $\tau_{effective}$ in Table 5.1), showing that a maximum $1/2\pi\tau_{effective}$ switching frequency of $200Hz$ is possible. This requires an absorbed power density of $2.8W\ cm^{-2}$ to reduce the transmission from 100% to 10%.

Figure 7.1 also shows the excitation power uniformity required by the absorbing aperture. Ideally the absorption is the same across the entire aperture so each point on the detector image (after the absorbing aperture) is attenuated by the same factor. However, the optical excitation power density is likely to vary across the modulator's aperture. If the excitation power is $2W\ cm^{-2}$, then an effective carrier lifetime of $\tau_{effective} = 1.1ms$ gives a modulator transmission of 10% (90% absorption). To decrease the transmission to 5% the power must be increased to $2.6W\ cm^{-2}$. Conversely, to increase the transmission to 15% a decrease in excitation power to $1.4W\ cm^{-2}$ is required, for the same effective carrier lifetime. To maintain a transmission of within ±5% absolute of 10% transmission in the absorbing state, the uniformity of excitation power (having implications in Section 7.3) is relaxed to within ±30%. To maintain this uniformity in transmission at higher absolute values of excited-state transmission will however require a smaller tolerance on the excitation power density.

7.1.2 Which etch should be used?

This section summarises the effectiveness of the etchants at reducing the surface recombination velocity. The model in Section 4.2.1 predicting the steady-state area carrier density in a semi-infinite sample is used to analyse the experimental results for S and τ_{bulk} extracted in Chapter 5. Equation 7.3 predicts the ratio of steady state area carrier density in a continually-excited sample with surface recombination velocity S, to the zero S case. Equation 7.3 is plotted in Figure 7.3 for reasonable parameters from Table 7.1, and experimentally-determined values for τ_{bulk} and S obtained by the etch process in Section 5.2.

$$relative\, absorption = \frac{1 - \frac{\alpha_{ill} D_a \tau_{bulk}(S + D_a \alpha_{ill})}{D + S\sqrt{D_a \tau_{bulk}}}}{1 - \alpha_{ill}^2 D_a \tau_{bulk}} \tag{7.3}$$

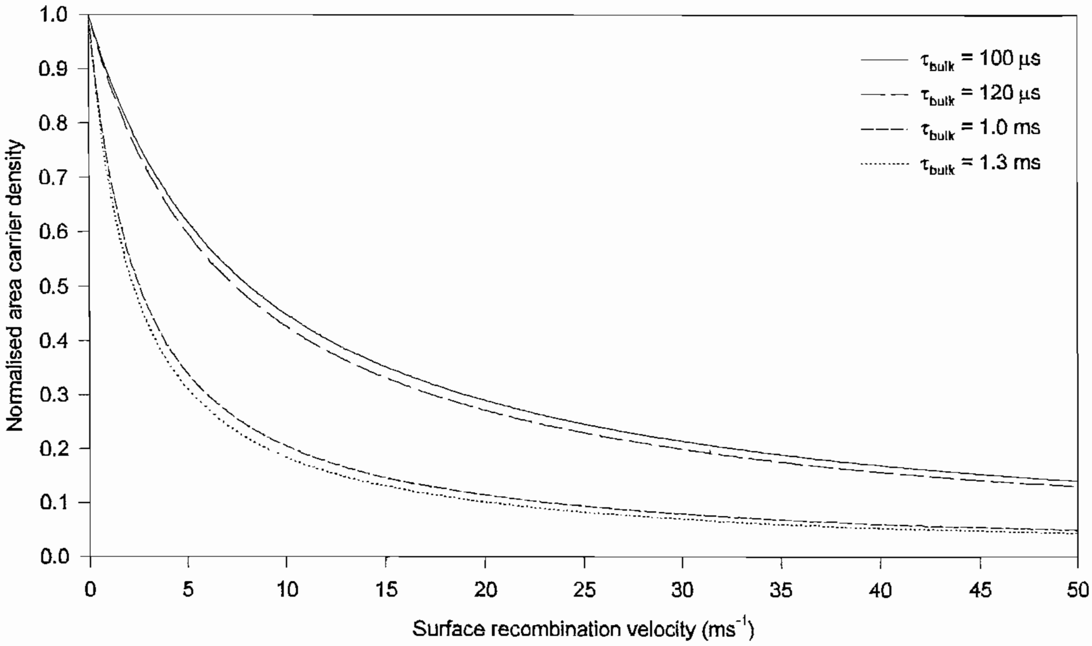

Figure 7.3: Ratio of absorption in presence of surface recombination velocity S to absorption with zero surface recombination for experimentally-determined parameters

The experimental results reported in Section 5.2 gave bulk carrier lifetimes of $1.3ms$, $1.3ms$, and $120\mu s$ in the test samples EGG1, EGG2 and Haller, and corresponding values for the face 1 surface recombination velocity of $2.8ms^{-1}$, $3.0ms^{-1}$ and $2.0ms^{-1}$ were obtained by etching in CP4A (Appendix B). Figure 7.3 shows these carrier parameters have 45%, 43% and 79% of the maximum attainable absorption with their respective bulk carrier lifetimes. For the EGG1 and EGG2 samples these values show that the absorption has been reasonably optimised by the etch. Compared to the unetched case, a great increase in induced absorption has been achieved. Unetched samples invariably show no depth of modulation at these excitation levels. Lower values of S, whilst attainable through etching, and reported in the etching literature, introduce a stronger dependence of induced absorption on S, which is therefore more environmentally-dependent. The post-etch S values measured following etching in CP4A are in a region which gives a low recombination rate in addition to a low dependence on the environment, and are therefore acceptable in the optimisation process.

7.1.3 How thick should a sample be?

In high purity samples with long bulk carrier lifetime, depending on the sample thickness, optically-generated carriers at the front surface may reach the back surface. Even with etched samples a finite surface recombination velocity exists on both surfaces, and carriers could recombine at the back surface. In maximising the effective carrier lifetime in a sample to increase modulator efficiency, it is preferable that carriers recombine in the bulk material where a long carrier lifetime exists, and not at the back surface.

Figure 4.8 predicted that for a practical sample thickness of $5mm$, and typical values of $\tau_{bulk} = 1ms$ and $S = 3ms^{-1}$, the induced absorption was 39% of the maximum that would occur with zero surface recombination for this sample thickness. This value is 85% of the maximum induced absorption that would occur in a semi-infinite sample with the same τ_{bulk} and S values, and corresponds to a sample 1.9 diffusion lengths thick. From the aspect of sample thickness, a $5mm$ sample is therefore sufficient for typical modulator parameters.

For the test samples EGG1, EGG2 and Haller, the post-etch surface recombination velocity results of $2.8ms^{-1}$, $3.0ms^{-1}$ and $2.0ms^{-1}$, and bulk carrier lifetimes of $1.3ms$, $1.3ms$ and $120\mu s$ were extracted respectively in Section 5.2. Graphs of the normalised absorption, given by the ratio of the absorption with surface recombination velocity S and finite thickness, compared to the absorption for a semi-infinite sample with the same S and τ_{bulk} are plotted for these values in Figure 7.4.

In Figure 7.4 the samples EGG1, EGG2 and Haller have thicknesses $5.82mm$, $6.08mm$ and $1.70mm$ respectively. When normalised to the sample's diffusion length, values of

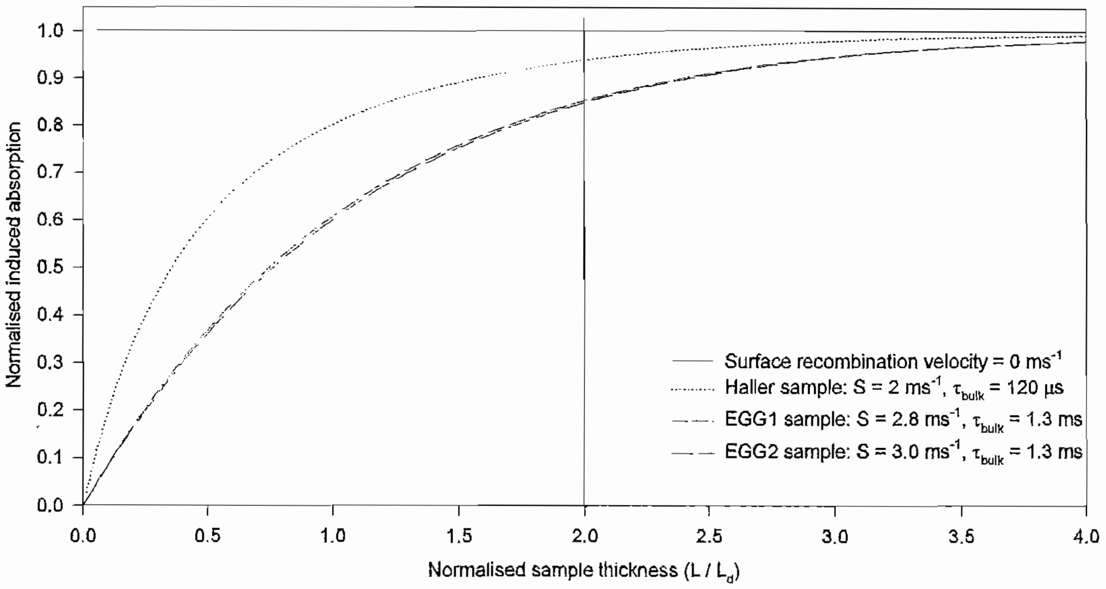

Figure 7.4: Normalised induced absorption vs sample thickness normalised to diffusion length

1.98, 2.06 and 1.90 are found, showing that the normalised induced absorption values are well optimised from the aspect of modulator thickness.

7.2 Germanium processing requirements

The construction stages of a modulator are i) cutting the element to size, ii) polishing to a high optical quality finish, iii) etching to reduce surface recombination velocity iv) fixing the sample into the support and heatsink and finally v) AR coating. All stages have been successfully performed at the University of Southampton.

A primary requirement during these processes is that the germanium does not come into contact with impurities likely to degrade the long carrier lifetime. Such impurities are primarily copper and gold, and to a limited extent, iron and nickel. At elevated temperatures their effects are more severe as their diffusion coefficients increase with temperature, so the germanium should not be unnecessarily heated beyond 150°C, especially when in contact with such impurities. The rate of heating during a process is also important. Thermal shock degrades the long lifetime in high purity samples and should be avoided.

The stages where impurities and heating are encountered in the manufacturing process are during the polishing, etching, AR coating, and fixing of the element to a heatsink. When polishing, etching or washing the sample, deionised water must be used. Care must be taken to ensure the etch constituents have low concentrations of such impurities as any impurities in the etch may adhere to sample surfaces and later diffuse-in upon heating.

The modulator element requires fixing into a heatsink for support and also to remove waste excitation heat, and this may require a moderate temperature. Two methods of obtaining the required good thermal contact were found: conductive epoxy, and low-temperature solder. For research purposes, soldering is more attractive as it offers the possibility of removing the element, and so was used during this work. Low-temperature indium-based solders were obtained from the Indium Corporation of America, in a 'Special joining kit', of which solder number 290 was preferred (97% In, 3% Ag) due to its low liquidus point ($143°C$) and good wettability to germanium.

Soldering the germanium element ($15mm$ square) to the flanged copper heatsink consisted of wetting solder to the germanium edges and heatsink inner edges, placing the germanium into the recess in the heatsink, and then heating the combination, adding solder in the gap around the edge until filled, then allowing to cool. The copper recess was easily wetted by using a flux on freshly-cleaned copper, then contacting the solder wire to the heated copper. The copper was heated using a standard hotplate with an attached thermocouple to prevent overheating the high thermal mass. Wetting solder to germanium was more difficult. A recess was milled into a copper block, into which the germanium was fitted. The block was heated on the hotplate, and then a scrubbing action using a nickel felt pad was used to wet the solder which is run along the edges of the sample simultaneously. Whilst hot, the sample was removed and allowed to cool before placing in the actual modulator heatsink, and re-melting the solder to secure it. During this process the optical window faces the hotplate. Aluminium foil was placed between the heatsink and hotplate to prevent evaporation of hotplate debris onto the optical window.

Once the element is fixed into the heatsink it is AR coated. The AR coating is deposited after the soldering stage to avoid damage during heating. If the sample were glued in place, these two stages can be interchanged for ease of evaporation, and would not require the entire bulky heatsink to be placed into the evaporator for the AR coating stage. The AR coating should ideally be evaporated shortly after the sample is etched. The surface recombination velocity is known to increase slightly with time in the short term before stabilising (Section 6.1.3), so a minimum delay between etching and coating is preferable.

The AR coating was deposited onto the germanium-heatsink arrangement as described in Section 6.3.3. This involves heating the germanium to ensure adherence of the film, although the heatsink with its high thermal mass is heated as opposed to the modulator, and this remained warm enough during the evaporation to ensure an adherent film was produced. At this point, copper may diffuse into the germanium as this is the longest time the germanium spends at elevated temperature. Diffusion of copper into the germanium can be prevented using a metallic barrier, although during this work this was not attempted. Table 7.2 lists the time taken for impurities to attain $10^{10} cm^{-3}$, the same as the HPGe background impurity level, at a depth $100\mu m$ from the surface, assuming infinite-source diffusion at $100°C$, and shows the severity of the heating stage. Data is taken from Table 3.2. Although the copper result seems extraordinary the germanium is not in good contact with the heatsink, due to the indium solder barrier, greatly increasing the allowable heating time. Note that since the diffusion distance $\propto \sqrt{time}$, copper requires 200 seconds diffuse $1mm$.

impurity	copper	nickel	iron	gold	indium
time (seconds)	2	2.4×10^6	3.2×10^9	2.1×10^{23}	4.2×10^{30}

Table 7.2: Impurities that degrade lifetime in germanium and corresponding diffusion times at $100°C$ for $10^{10} cm^{-3}$ at a depth of $100\mu m$

7.3 Optical excitation requirements

This section details the possibilities for optically-exciting the modulator element. Until this point, tests on germanium were performed using fibre-coupled or collimated beams to excite samples over approximately a $3mm$ aperture. In the construction of a working modulator with a $1cm^2$ aperture, the aperture must be illuminated uniformly with high power radiation, giving the same induced absorption across the entire aperture, and stray illumination must be prevented from escaping from the modulator thus drawing attention from other IR sensing systems or posing an eye-hazard.

The required excitation power density is now determined. The transmission of an uncoated element at $10\mu m$ was reduced from 47.1% to 5.2% using $9.6W\ cm^{-2}$ of $980nm$ (Section 1). Extrapolated to an AR coated sample, with 100% unexcited-state transmission, and assuming no AR coating at the pump wavelength, $9.6W\ cm^{-2}$ reduces the transmission from 100% to 11.0%, which is an acceptable depth of modulation for the primary modulator application. The order of this is also supported by predictions in Section 7.1.1 that an absorbed illumination power of $2.8W\ cm^{-2}$ with an typical effective carrier lifetime of $\tau_{effective} = 800\mu s$ gives an 'off' state transmission of 10%. The absence of an AR coating at $980nm$ would approximately require twice this power for the same performance (See Table 6.3).

The spatial uniformity of the illumination considered in Section 7.1.1 required that the power density on the germanium remains within ±30% to maintain 10% ± 5% power transmission through the aperture. This tolerance is widened by the effect of lateral carrier diffusion, which laterally smears-out the carrier density resulting from a non-uniform illumination profile in the presence of a long bulk carrier lifetime and low surface recombination velocity. This was shown by the lateral diffusion models in Section 4.3.2. In this particular design a long effective carrier lifetime is required to maximise efficiency; this widens the lateral excitation uniformity tolerance. Rapid spatial power density fluctuations over less than a diffusion length on the low surface recombination velocity modulator surface will not cause significant lateral variations in absorption during the modulator's off state.

7.3.1 Modulator geometry

Single or dual-surface modulator-excitation schemes shown in Figure 7.5 are possible. The two-sided excitation scheme utilises reflected power that would otherwise be wasted, inherently preventing reflected illumination from escaping. It operates by confining the excitation power, which reflects inside the box until absorbed by the germanium. The one-sided scheme relies on the incident power being in the correct place. Any reflected power is simply turned into heat on the wall of the containing cavity. Whilst the two-sided scheme is more efficient, for the construction of a demonstration modulator (Section 7.4) a one-sided scheme was employed. This simpler scheme offers easier diagnosis of any unexpected effects.

Illumination of the single-absorbing-surface aperture with high power above-bandgap radiation is now considered. A longer wavelength gives more photons per Watt of optical power, and also relaxes the tolerance of the single-layer AR coating thickness (Section 6.3.2). Wavelengths longer than the direct-bandgap wavelength of $1.5\mu m$ are unsuitable due to their temperature-dependence of absorption. A narrow wavelength band is preferable, making AR coating at this pump wavelength easier. Diode lasers, infrared LED's and filtered arc lamp sources are candidates.

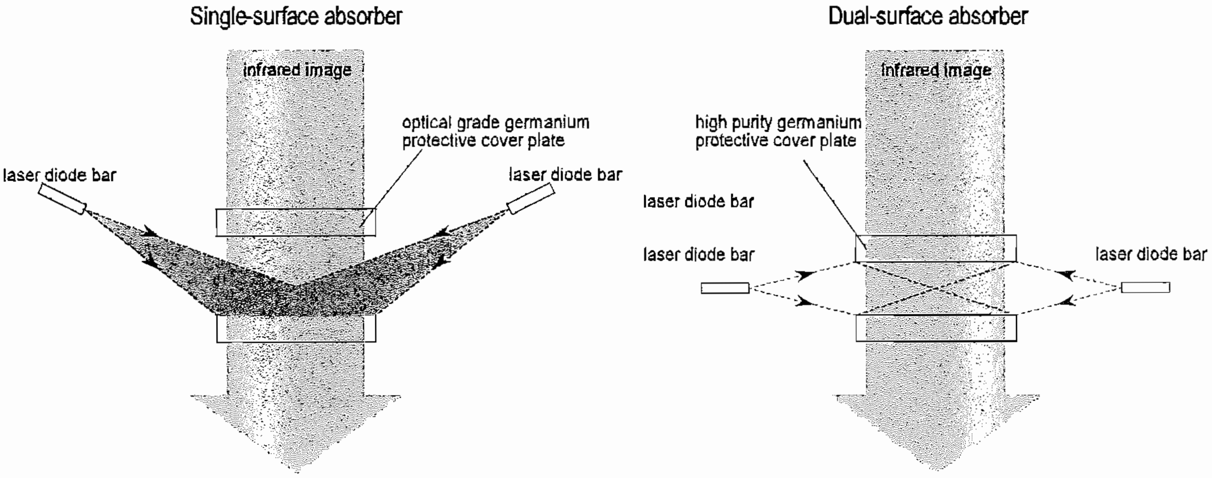

Figure 7.5: One- and two-surface excitation schemes

Diode lasers, offering compactness, portability and fixed wavelength illumination, in contrast to wider spectral-bandwidth LED or (larger) filtered arc lamp sources were chosen as the preferred means of illumination. High power low duty-cycle infrared LED's are currently available in the required spectral region at lower cost, and lower power per device but with a wider spectral bandwidth.

Delivering the high power illumination to the modulating aperture is considered next. Fibre-coupled diode lasers can be remotely-located, reducing the waste heat dissipation close to the absorbing region. Several fibres can be arranged to stare at the aperture to achieve uniform illumination. These often have the disadvantage of high coupling loss to the fibre; with losses of up to 50% being the current state of coupling technology and so require more heatsinking. This is shown in Figure 7.6 (a). Alternatively, several lower power diode-can lasers could be used (b), requiring a more bulky optical illumination head. The idea chosen was to use diode bar lasers (c) with no additional optics. These have recently become widely available at moderate cost and high power.

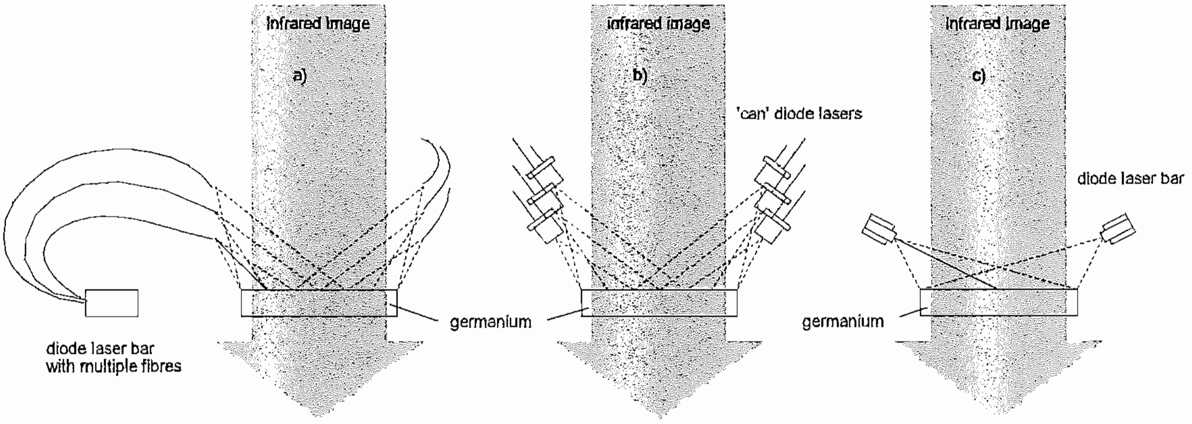

Figure 7.6: Three possible illumination geometries for exciting the aperture

7.3.2 Diode bar lasers as an optical pump source

High power laser diode 'bars' are currently available at $\sim 810nm$ and $\sim 980nm$, offering tens of Watts cw at reasonable cost. In low volume the cost is presently around 800stg (via Laser2000) for a mounted $980nm$ $20W$ bar, and this has fallen sharply over the past two years. In volume, the same unmounted device is presently available at around 150stg (Siemens Microelectronics). Stacked diode bars are also becoming widely available. The efficiency of such bars is $\sim 40\%$ at $20W$ emission, requiring $20A$ at approximately $2V$. Using two such diodes to obtain $40W$ of optical power, pulsed at 50% duty cycle requires an electrical power of $50W$, which is also the waste heat load that must be removed. Standard laser diode bars are a parallel array of emitters, often $100\mu m$ wide on a $200\mu m$ pitch, with an array width of $1cm$. The measured power emission profiles are shown in Figures 7.7 and 7.8 for two particular diode bar lasers, when the sensing CCD is parallel to the emitting face, $3cm$ away.

Manufacturer beam profile measurements are usually only specified in the far-field, and are made by moving a detector in a $1m$ arc around the diode bar. A typical profile from a manufacturer's data sheet is shown in Figure 7.9 for the transverse and lateral distributions.

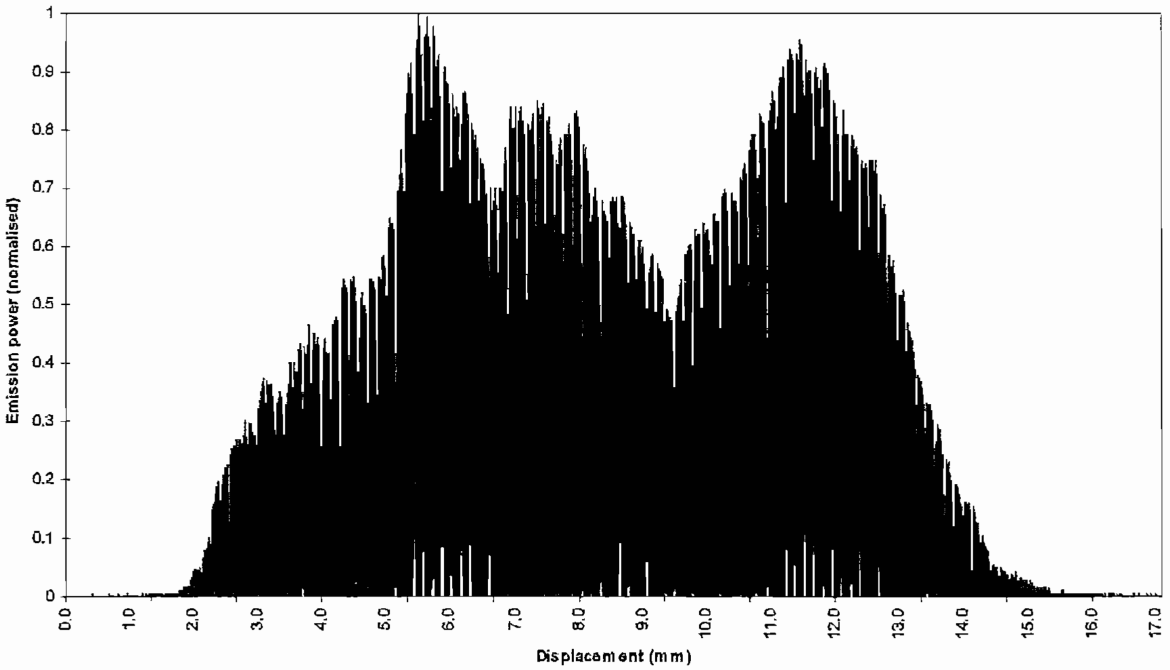

Figure 7.7: Approximately near-field emission profile of reasonable performance $1cm$ $20W$ $980nm$ diode bar

The narrow divergence in the slow axis makes the profile, which in this plane is very roughly a top-hat, suited to unlensed pumping of a $1cm$ aperture with reasonable uniformity. Advantage was taken of this in the demonstration modulator. In practice, the measurements in Figures 7.7 and 7.8 show that whilst the manufacturer's data sheets show roughly gaussian and top hat profiles in the slow and fast axes, these measurements are only valid in the far field, beyond about $10cm$ from the emitting face. After this point all diverging beams in the narrow divergence (12° FWHM) plane from a $1cm$ bar will have overlapped. In the fast axis of wide divergence, the far-field is reached within a few mm of the emitting face. However the power emission profile measured along the slow axis, close to the emitting face, varied wildly on some diode bars. Beam profile measurements using a linear array CCD camera $3cm$ from the emitting face are shown in Figures 7.7 and 7.8 for reasonable and poorer devices respectively.

Although the manufacturer's specified far field profiles are quite uniform and slowly spatially-varying, in the near field these were seen to vary wildly, with some emitters appearing to contribute little power to the total along the slow axis. Often the side emitters emit the least power, with strong nonuniformity across the bar. These results were typical of one manufacturer's diodes (Gateway Photonics, USA), although it is

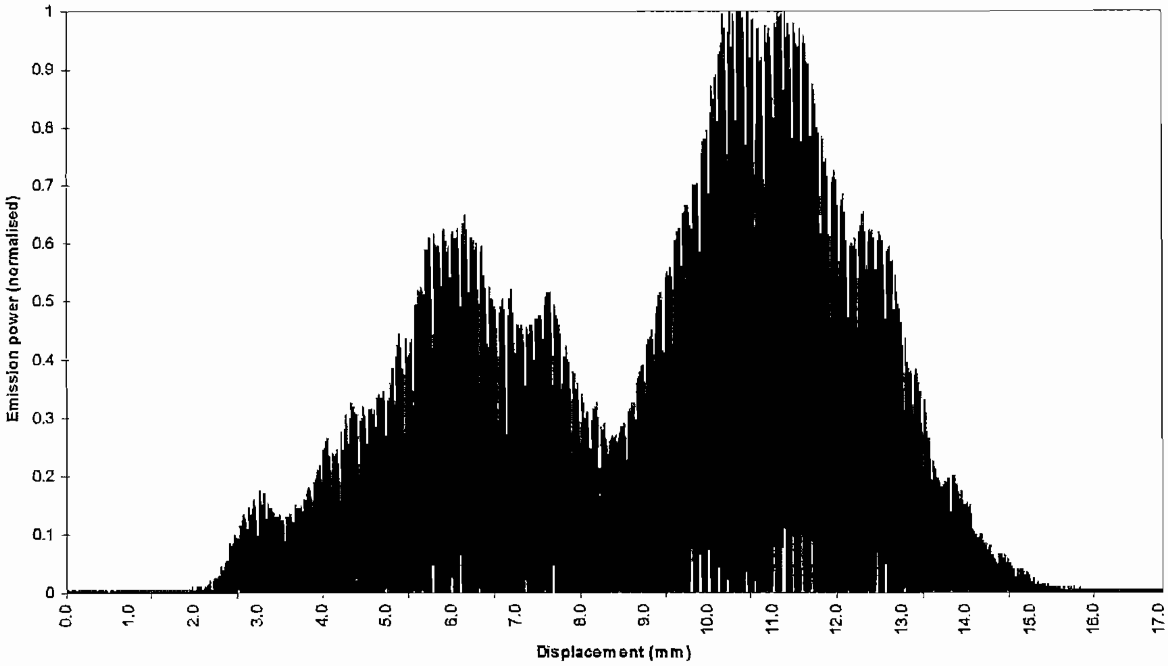

Figure 7.8: Approximately near-field emission profile of poorer performance $1cm$ $20W$ $980nm$ diode bar

unclear how other laser bars might perform. This measurement, approximately in the near-field, is almost never made on the bars, as most users simply specify the centre wavelength, spectral bandwidth, power, far-field beam profile, and efficiency of such a pump source.

In addition to the non-uniformity in laser diode bar emission profile across the aperture, the central wavelength of such devices shifts slightly with drive current. Combined with the difficulty in procuring spot-wavelength laser diodes, this requires the AR coating to have a suitably wide tolerance with low reflectivity over a reasonable incidence angle range at the pump wavelength. Typical FWHM spectral linewidths for the diode laser bars used [130] are 2 to $3nm$. When the junction temperature reaches a steady value, the central wavelength shift of the diode becomes much less significant.

A demonstration modulator was constructed (Section 7.4) based on the manufacturer's far-field data from Figure 7.9, knowing that providing it was operated in a high absorption regime, some fluctuations in power density could be tolerated using the argument in Section 7.1.1, and also smoothed through lateral carrier diffusion in long bulk carrier lifetime material in the presence of a low surface recombination velocity.

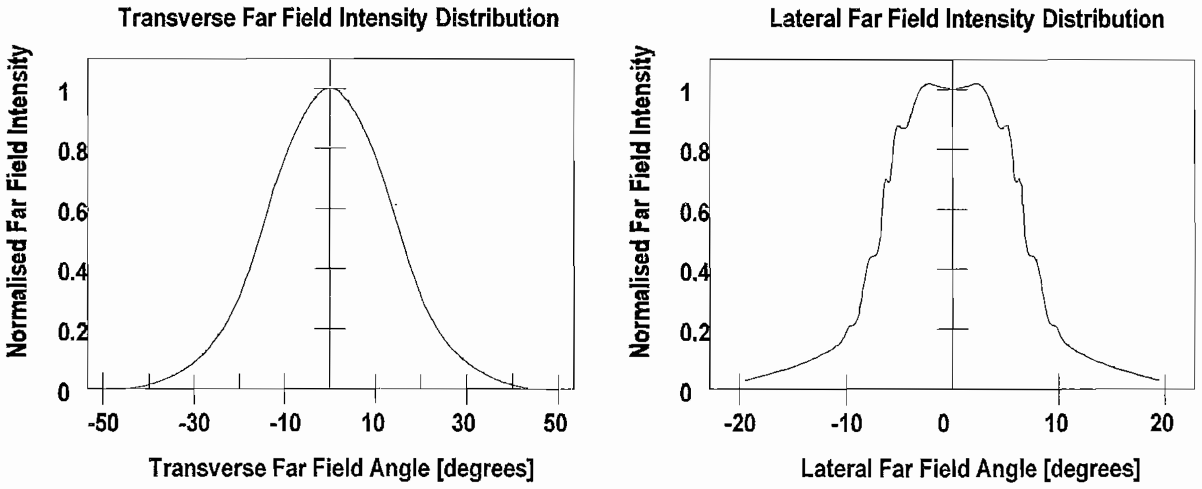

Figure 7.9: Manufacturer data for far-field emission profile for $20W$ diode laser diode bar in fast (left) and slow (right) axes

7.4 Optically-pumped modulator design

This section summarises the design of an optically-pumped modulator, based on the design constraints preceding this section. A summary of the specification for the design of the optically-pumped demonstration modulator is given below:

- Clear aperture $1cm$ square accessible by f2 optics
- On state transmission $> 90\%$ averaged over the 8 to $14\mu m$ band
- Off state transmission $< 10\%$ averaged over the 8 to $14\mu m$ band
- Speed of response time constant $< 3ms$

Based on the preceding arguments, it was decided that an optical power of $10W\ cm^{-2}$ was required to achieve this depth of modulation. Antireflection coatings on the sample would be used to give close to 100% transmission in the 'on' state. A high purity germanium sample $1.5cm$ square was required to permit fixing of the sample around its edges to a support and heatsink arrangement whilst giving at least the required aperture. To minimise carrier recombination at the back surface, a sample thickness of $5mm$ was used (Section 7.1.3). Two side-illuminating $20W$ diode bar lasers provided the optical excitation, and the exclusion of external optics simplified the design. The response speed is within expectations of the bulk carrier lifetime and surface recombination velocity on etched samples. The stray excitation reflected from the modulator element would be contained by an unetched (high surface recombination velocity) optical grade (low bulk carrier lifetime) germanium window, optically in series with the modulator which would not significantly contribute to the induced absorption. The modulator heatsink and support housing would be made from copper. The use of Oxygen Free High Conductivity (OFHC) copper is unnecessary, offering little improvement in thermal conductivity at room temperature over many standard grades.

7.4.1 Optical illumination geometry

It was decided that the required optical excitation power density of $10W\ cm^{-2}$ would be adequately provided by two $20W$ $980nm$ offset diode bar lasers as shown in Figure 7.10.

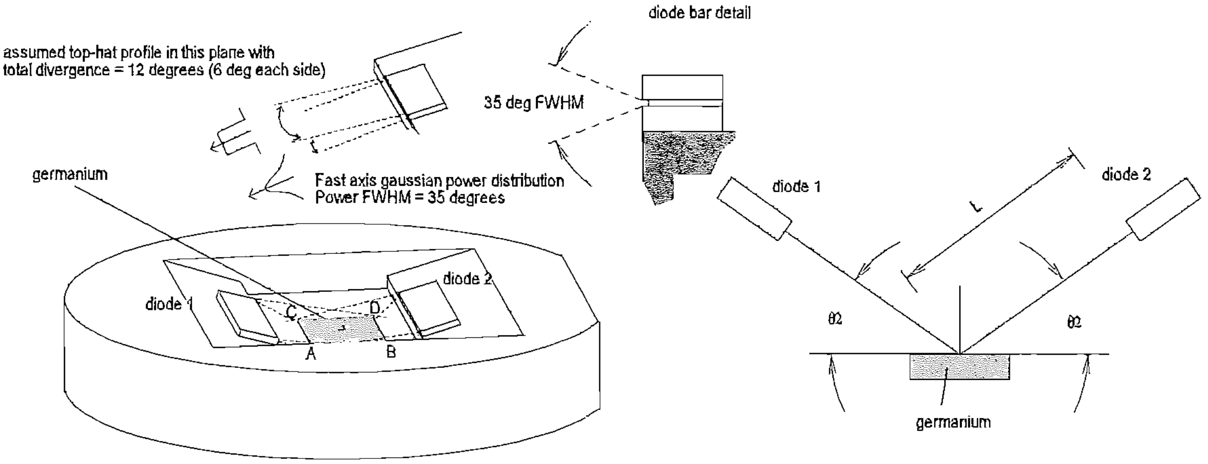

Figure 7.10: Aperture excitation schematic and geometry side profile

The diode profiles have a FWHM power divergence of 35° in the fast axis and a top-hat profile with 12° divergence in the slow axis [130], permitting calculation of the total power profile. These approximations are close to the actual power distribution. The gaussian power profiles in the fast axis from the two diodes sum linearly along plane AB, resulting in a more-rounded-topped distribution in this plane, with the same power density anywhere along a line parallel to AB. Figure 7.11 shows the beam profile modelled along this line.

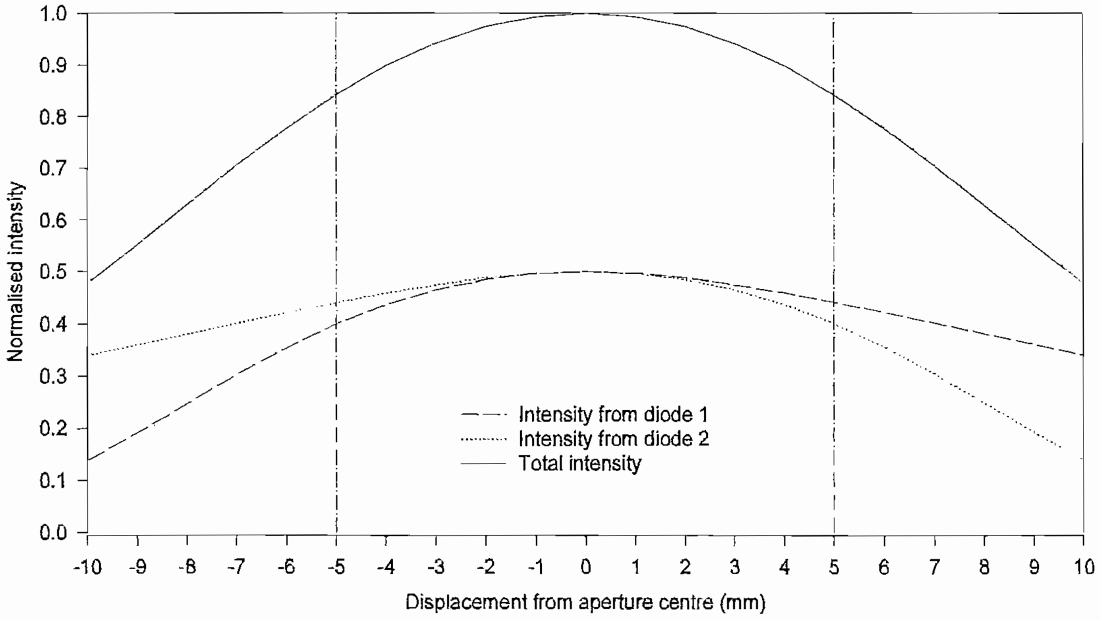

Figure 7.11: Intensity summation along line AB of gaussian profiles from two laser diodes

Optimising this profile involves a tradeoff between illumination uniformity of the power along AB and the efficiency with which the excitation overlaps the modulator element in this plane. The uniformity is defined as the ratio of the maximum to the minimum combined power along AB. The efficiency is defined as the ratio of the area under the total intensity curve along AB to the area assuming unity normalised intensity. These two figures of merit are a function of the excitation incidence angle $(90 - \theta_1)$, and the distance of the source (L) from the centre of the aperture. Optimisation of the efficiency and uniformity showed that it was best to fix θ_1 to a practical value (35°) compatible with the aperture's f2 optical transmission, and to vary L to achieve the desired uniformity and efficiency. These figures of merit are plotted for $\theta_1 = 35°$ in Figure 7.12.

The required uniformity along AB was decided as being 85% based on the wide (±30%) acceptable power illumination tolerance. Figure 7.12 predicts 33% efficiency at a distance $L = 28mm$, which was used in the final design. Along the plane CD the uniformity should be unity, and the FWHM profile width is $16mm$, assuming a top hat profile with 12° divergence from a $1cm$ bar at $28mm$ separation. So approximately $10/16 = 62.5\%$ of the illumination in this plane illuminates the $1cm^2$ aperture. The combined efficiency is therefore roughly $33\% \times 62.5\% = 21\%$. Two $20W$ diode bars

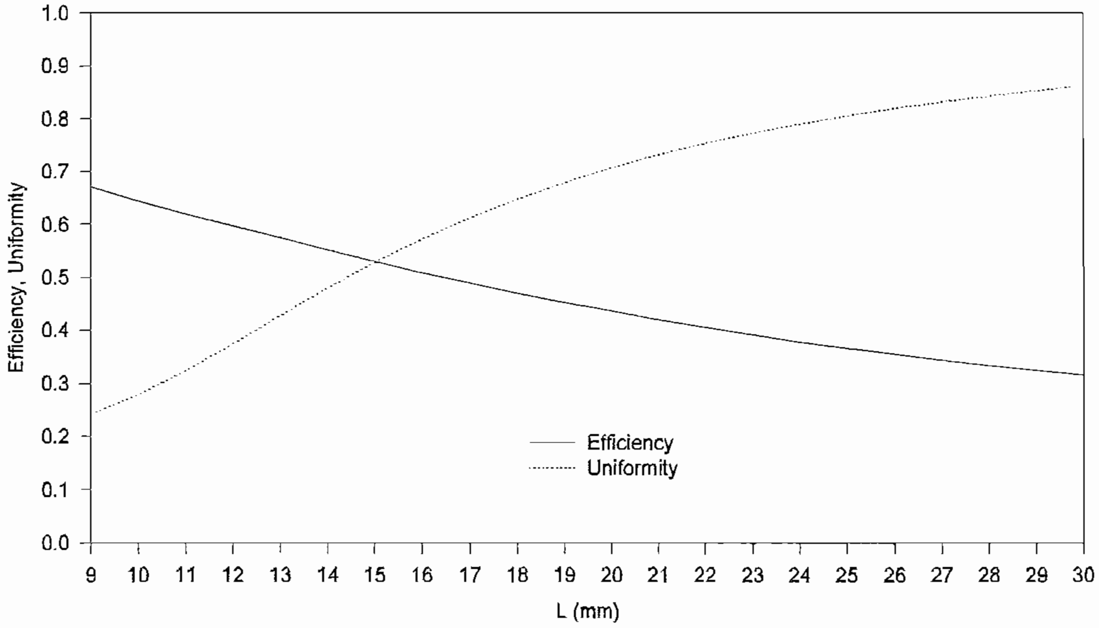

Figure 7.12: Uniformity and efficiency figures of merit for illumination along AB

emitting over a $1cm^2$ aperture, with an illumination efficiency of 21%, give an average power of $8.25W$, which is close to the required average power of $10W\ cm^{-2}$. The AR coating at the pump wavelength is angular- and wavelength-dependent, although it offers an increase in the $8.25W$ absorbed power of up to a factor of 2.5 (See Section 6.3.2).

7.4.2 Copper support and heatsink

The modulator's support and heatsink was made from copper. Water cooling of the germanium element and laser diodes is achieved by integrating the laser diodes into the modulator housing. Technical drawings of this construction are given in Appendix C. The required heat dissipation is $100W$ during cw operation, although during the usual 50% duty cycle operation this halves, and a purpose-built forced-air heat exchanger was employed using a flow rate of approximately $500ml$ per minute. Figures 7.13 and 7.14 show photographs of the construction.

7.4.3 Testing the optically-pumped modulator

Having built the modulator as described above, it was subsequently tested for i) depth of modulation ii) speed of response, and iii) transmission as a function of wavelength.

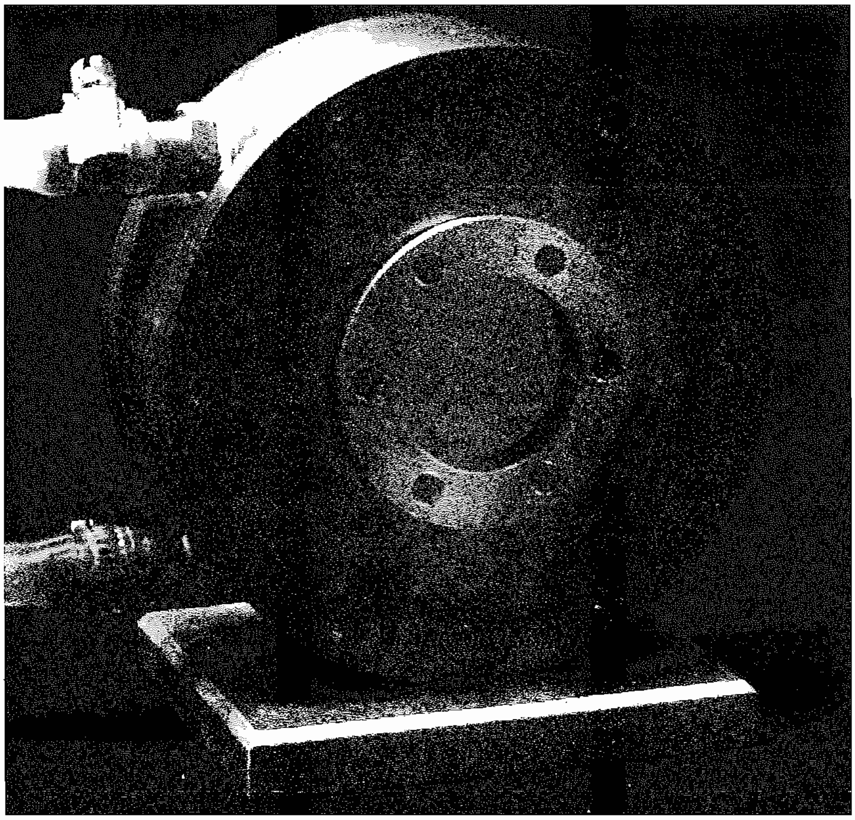

Figure 7.13: Photograph of the optically-pumped modulator

The depth of modulation in the steady-excited state was measured along two perpendicular lines intersecting the central point of the excited region. This was achieved by scanning the black body probe beam across the regions in both the 'on' and 'off' states, giving the average transmission in the 7 to $15\mu m$ region, using the same setup as described in Section 5.3. The laser diodes used in the modulator were the best of nine delivered by the supplier (Gateway Photonics USA). Both suffered from nonuniform emission across the $1cm$ bar, typically as shown in Figures 7.7 and 7.8. Both diodes were driven cw at $18A$, giving a combined optical power of $26.7W$. The results of scanning in the orthogonal directions are seen in Figure 7.15. This plots the ratio of the transmission in both states, along four scan lines detailed in Figure 7.16.

In Figure 7.15 a transmission of 16% is seen in the centre of the aperture in the 'off' state at $10.6\mu m$. The absorption reduces at the edges, and is either due to an increased rate of surface recombination here where the germanium meets the indium solder layer, or due to nonuniform emission from the diode bars at their edges. This is avoidable in a future modulator by using an increased optical power density here to account for the enhanced carrier recombination rate, or a wider unused aperture around the optical aperture, which is also excited but which contains the region where the absorption is not as strong.

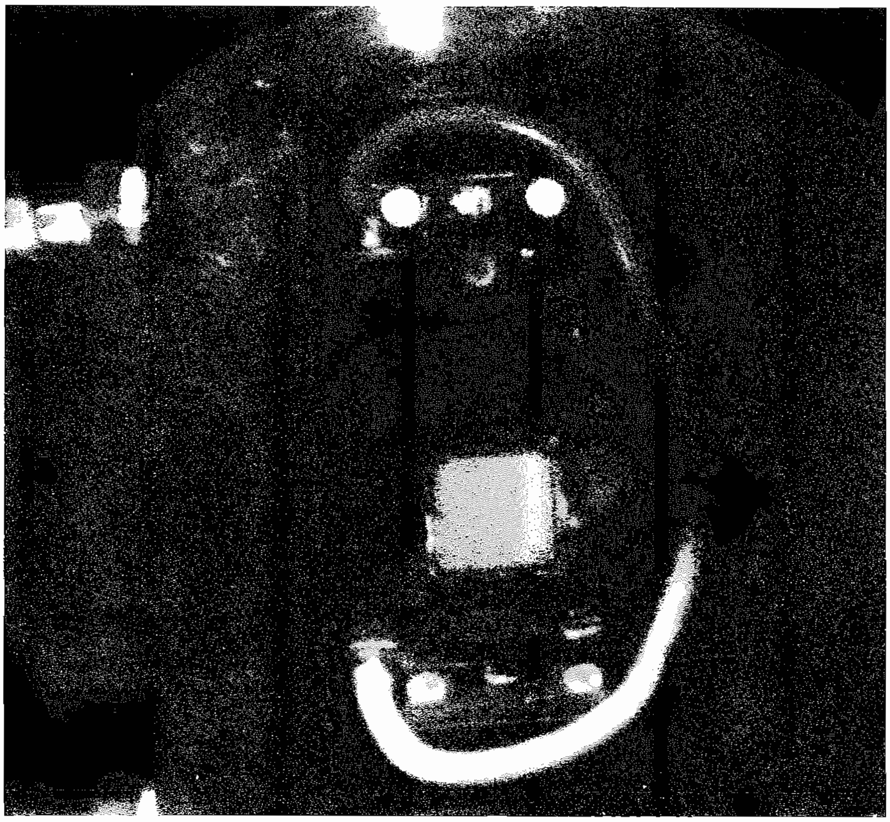

Figure 7.14: Photograph inside the modulator showing laser diode positioning

The parallel scans show a narrower absorbing region than the scans perpendicular to the emitting diode face, despite the same aperture size in the perpendicular planes. This is explained by different levels of excitation in the two planes. The excitation in the perpendicular plane extends for a longer distance since the excitation overlaps more of the area around the germanium. In the parallel plane the excitation only just meets the edge of the aperture. In the parallel plane the germanium is in an intermediary region between near and far field, where the emission is known to differ quite strongly from the ideal model's prediction in Figure 7.11, exhibiting sudden spatial variations in laser power. The illumination in the perpendicular plane (AB direction) is closer to the model's prediction since here the germanium element is in the far field, where the average excitation profile has evened-out rapid spatial power variations. It is known from Figures 7.7 and 7.8 that the emission in the parallel plane along AC is non-uniform, and the effect of this is seen by the narrower absorption profile in Figure 7.11. Inhomogeneities in this plane would be greatly reduced in a future modulator by selecting laser diodes which have more uniform emission profiles in the approximately-near field.

The response speed was measured at $10.6\mu m$ by switching a CO_2 laser probe positioned in the centre of the modulator aperture. Results of this, scaled to 100% transmission using a reference chopper blade, are shown in Figure 7.17, showing the transmission

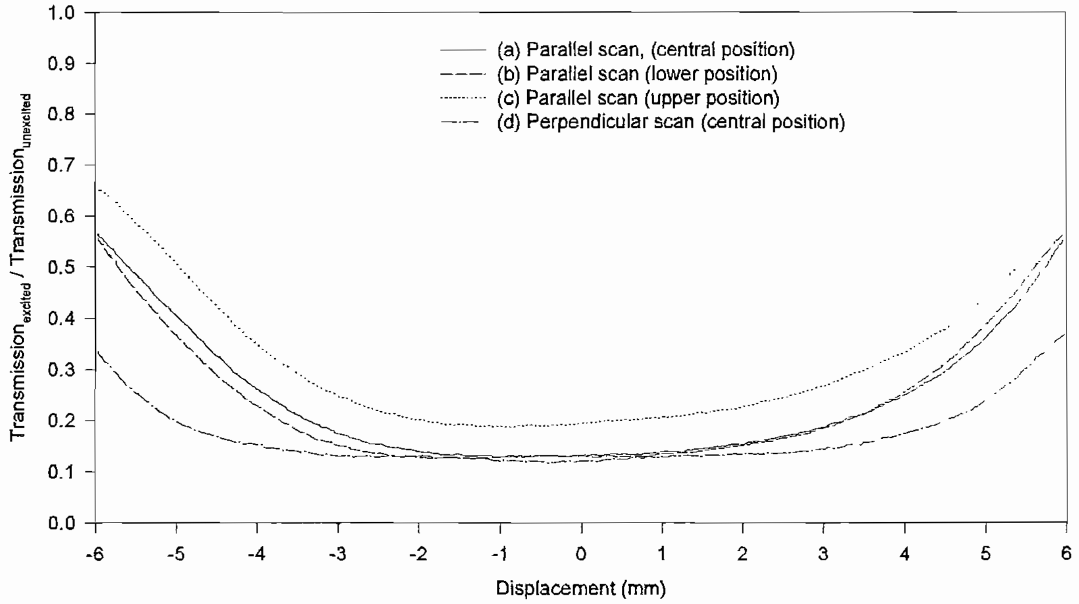

Figure 7.15: Modulator transmission in two intersecting orthogonal directions (a-c) parallel to laser diode bar face (AC direction) (d) perpendicular to bar face (AB direction)

at $10.6\mu m$ switching from 100% to 18% transmission, with a $10-90\%$ risetime of $0.49ms$, and a $10-90\%$ falltime (absorption decay) of $1.73ms$. The minimum transmission in Figure 7.17 is similar to that in Figure 7.15. The latter minimum transmission is slightly higher than that in Figure 7.17 at $10.6\mu m$. In Figure 7.17 the hole absorption cross section is slightly higher than the average spectral absorption cross section in the 6.6 to $15.7\mu m$ region, which determines the absorption in Figure 7.15.

The transmission vs wavelength shown in Figure 7.18 was determined using a spectrophotometer. The modulated transmission within the germanium passband is caused by two sets of fringes with different periods, one from the modulator AR coating (Figure 6.20), the other from the germanium protective cover plate. The highest depth of modulation is seen within thermal imager band, extending from 8 to $14\mu m$, although the subsidiary modulated heavy hole - spin orbit and light hole - spin orbit regions show a significant depth of modulation from 3.3 to $4\mu m$ and in a narrower bandwidth around $5\mu m$ respectively. This figure shows the transmission at $10.6\mu m$ falling from 95.4% to 4.7%, and that at $8.0\mu m$ and $14.0\mu m$ falling from 55.5% to 5.2% and from 68.0% to 1.6% respectively using a total optical power of $26.7W$. These values show a higher level of absorption than observed in Figures 7.15 and 7.17. The difference cannot be accounted

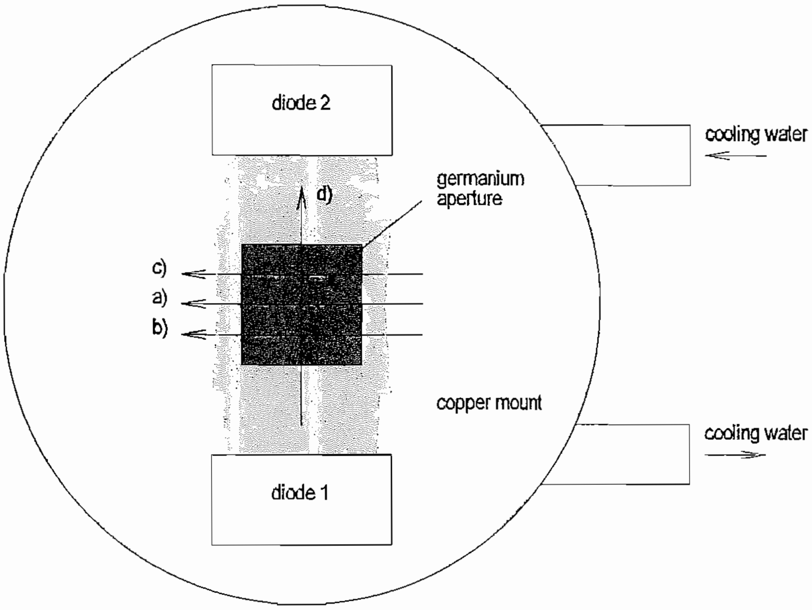

Figure 7.16: Detail of scanning planes in Figure 7.15

for by a moderate temperature shift increasing the free hole density. A moderate sample-temperature increase of 10°C has been calculated to increase the total absorption by an amount 4.45×10^{-3} in a $0.5cm$ sample. Likewise a temperature decrease of 10°C provides a similarly insignificant change in absorption, of -2.72×10^{-3}. These changes are insignificant in a strongly absorbing sample in which $A = 2.3$ (Equation 3.38) is required for 10% transmission. The origin of this discrepancy is likely to be in the decay of the power output from the diode lasers, which were not burnt-in prior to delivery. During the experiments the drive current to the diodes was kept constant, although the results for Figure 7.18 were made before those in Figures 7.15 and 7.17.

The modulator's transmission was also measured by looking at a 30°C black body source situated behind a metal patterned grating of horizontal lines with a pyroelectric-detector thermal imaging camera. Pyroelectric camera frame-grabs in the on and off states are shown in Figures 7.19 and 7.20 respectively. In the absorbing off state the total optical excitation power is approximately $10W$. The darker shading represents lower temperature, such as the cooling water pipes on the left.

These two figures clearly show the modulator absorbing across the aperture. In fact with these particular images only one laser diode was working properly; the faulty diode was only emitting over $2mm$ of the length of the bar during the test.

More recent images with both diodes operational and the modulator situated in the intermediate focal plane of a thermal imaging camera lens are shown in the 'off' and 'on' states respectively in Figures 7.21 and 7.22. The total optical excitation power in the 'off' state power was $28.9W$.

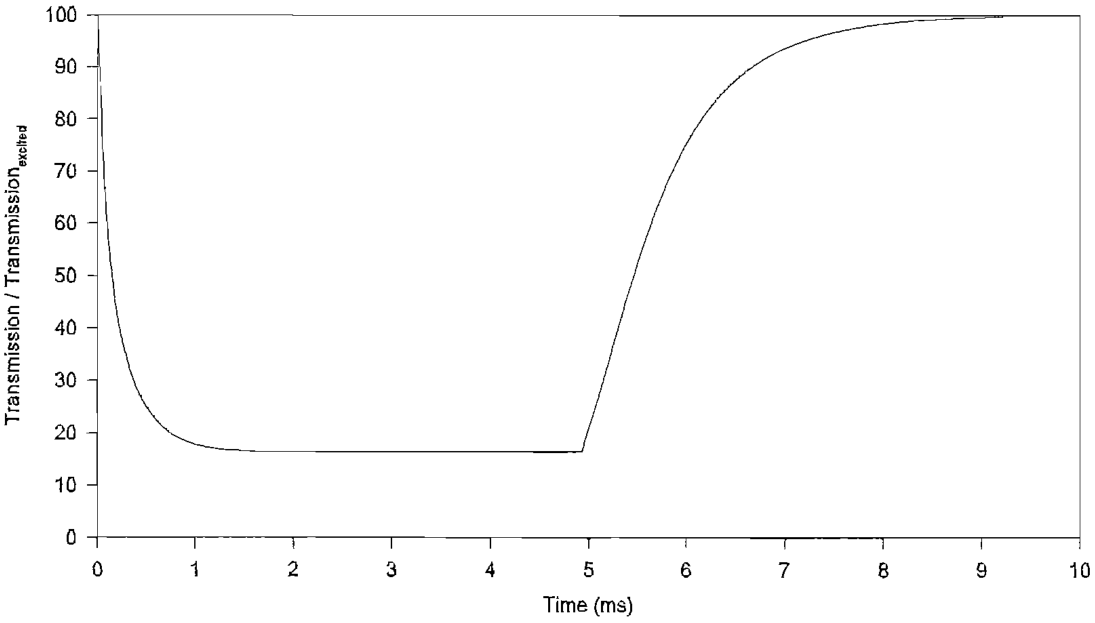

Figure 7.17: Switching response at 10.6μm using a total excitation power of 26.7W

In experiments with no pump-wavelength AR coating, results were extrapolated (Section 7.3) to show the effect of an AR coating at the modulated region only, showing that 9.6W cm^{-2} reduced the transmission from 100% to 11% at 10μm. The experimental results shown in Figure 7.18 for the AR coated sample show a reduction in transmission from 95.4% to 4.7% at 10μm using an average power density of 21% × 26.7W cm^{-2} = 5.6W cm^{-2}. The absorption coefficient transfer functions in the (pump wavelength) uncoated and coated cases are therefore 0.23 per W cm^{-2}, and 0.54 per W cm^{-2} which shows that the absorption of the pump wavelength has increased by a factor of 2.34 as an average over its varying incidence angle. The uncoated reflectivity of germanium at 980nm is 40.3%. If this improvement were offered by the AR coating at 980nm then the mean 980nm reflectivity would have been reduced to (1/2.34) × 40.3% = 17.2%. If the AR coating were perfect, Section 7.4.1 predicted an increase in absorbed pump power of a factor 2.5. The AR coating deposited is therefore close to this ideal case. The difficulty in procuring spot wavelength diodes with uniform emission along the bar length meant that one 980nm and one 960nm laser diode were used. Evidently the reflectivity at 960nm from a quarter wavelength coating designed for 980nm would be considerably different from the zero value desired, so a mean pump-wavelength reflectivity of 17.2% is good. The AR coating therefore works well at the

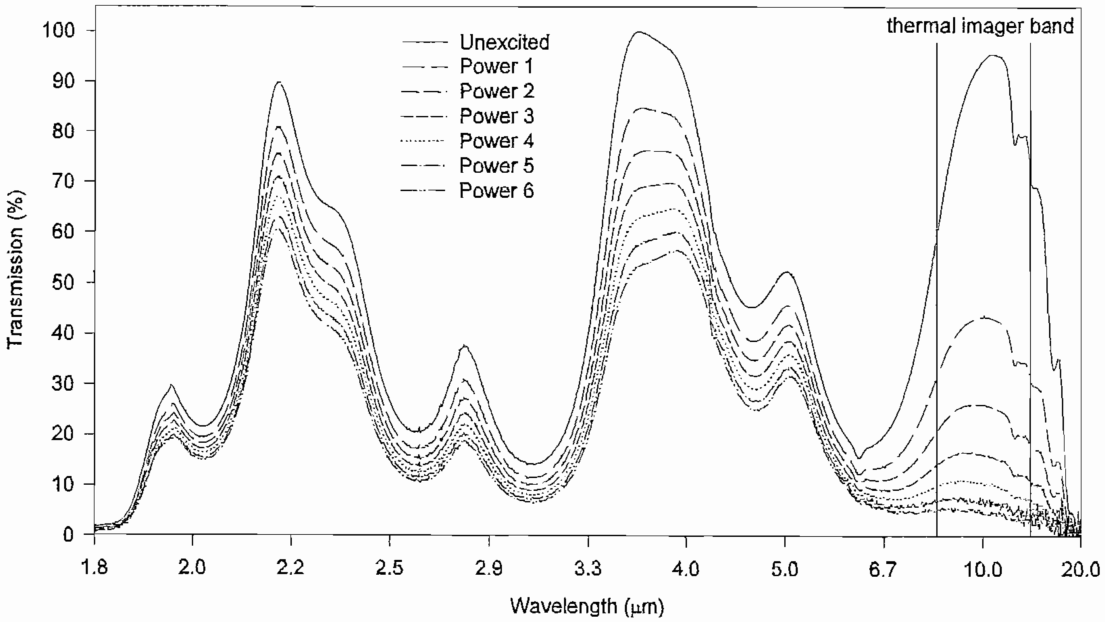

Figure 7.18: Transmission of modulator as a function of wavelength for total optical excitation powers (upper to lower) of 0, 5.4, 9.7, 13.9, 18.2, 22.5, 26.7W

desired 980nm wavelength, although this calculation is based on the assumption of a both a uniform power density on the 1cm^2 aperture, which is not strictly valid, albeit close to the predicted situation, and the assumption of the same surface recombination velocity on the two compared samples, which are cut from the same bulk material. Both samples were etched in the same etchant so this latter assumption is justified.

7.5 Conclusions on the optically-pumped modulator

This has been the first demonstration of a large-area optically-pumped modulator for the 8 to 14μm region. The total optical power used to generate the absorption over a 1cm aperture was 26.7W when operated continuously, and the transmission was reduced from 95.4% to 4.7% at 10.6μm. This is an acceptable depth of modulation for pyroelectric detector operation. The power density used to achieve this was moderate due to the 21% efficiency of the illumination of the aperture in order to achieve more uniform excitation. The uniformity of the modulation was not ideal, and some reduction in depth of modulation is seen at the edges of the aperture. This can be improved through more-uniform excitation or use of a wider aperture, or by using a higher relative excitation

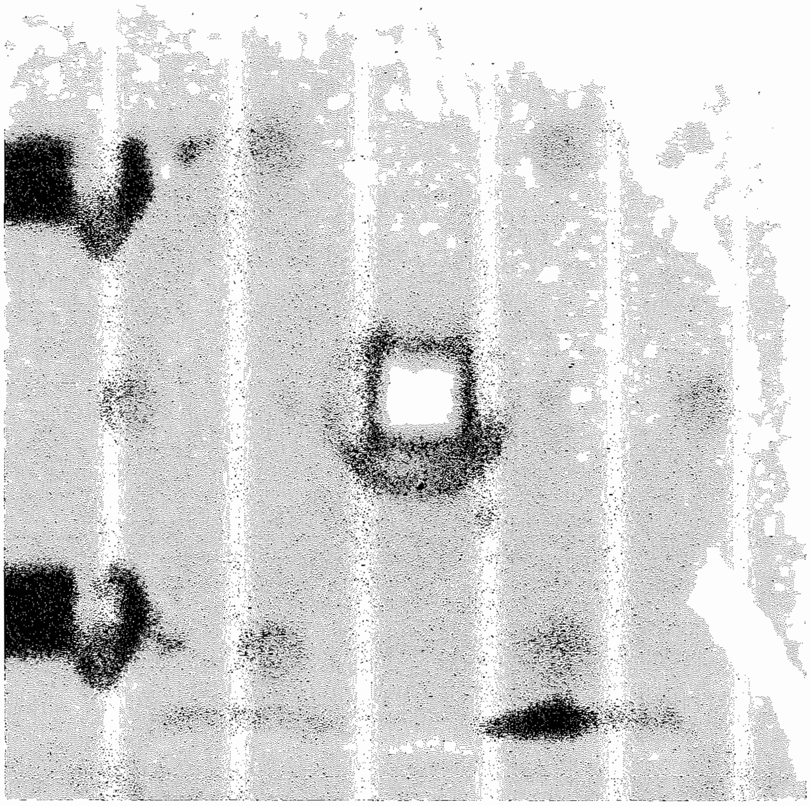

Figure 7.19: Transmission of the modulator in the 'on' state

power at the aperture edges. The response time of the modulator showed a recovery time of $1.7ms$, acceptable for pyroelectric detector operation, and the response time in turning-off the transmission, largely governed by the excitation power, was $0.49ms$. The transmission at the spectral edges of the thermal image band was 77.0% and 80.5% at 8.0 and $14.0\mu m$ respectively in the 'on' state. Ideally these would both be 100% although the actual transmission function is characteristic of the quarter-wavelength AR coating film used. To increase the transmission at the band extrema, a more complex multilayer AR film must be used. The design was achieved using no external optics, which greatly simplified its construction.

The measured depth of modulation is close to that predicted. The illumination nonuniformity of the laser diodes makes absolute comparisons of absorption difficult, but it appears that the AR coating does improve the absorption of the pump wavelength as discussed in Section 7.4.3. The suitability of a single-layer AR coating in providing low reflectivity at the pump wavelength over the wide tolerance of commercially-available laser diode wavelengths was predicted in Section 6.3.2. Ideally the experiment would be repeated using two $980nm$ laser diodes. To further improve the optical system's efficiency, additional optics could be used to 'rescue' some of the wasted 79% excitation power. Optics could be used to collimate the excitation onto the aperture, and laser

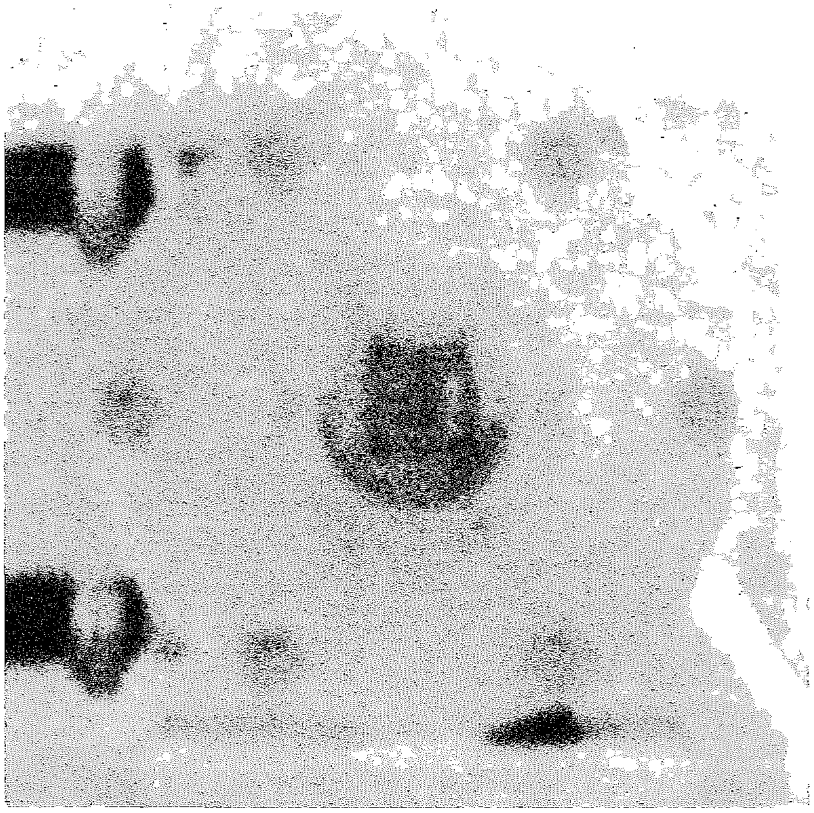

Figure 7.20: Transmission of the modulator in the 'off' state

diode manufacturers are starting to offer custom lenses integrated with the bar faces, which would facilitate this in a small space. It has become clear that laser diodes must be more-extensively tested before use in a final modulator. Standard manufacturer data is inadequate. Diodes should be additionally tested for their uniformity of emission across the bar length and central emission wavelength as a function of drive current for the present system.

A successful area modulator has been constructed, demonstrating the modulator's potential. Other applications include infrared modulation in gas sensing.

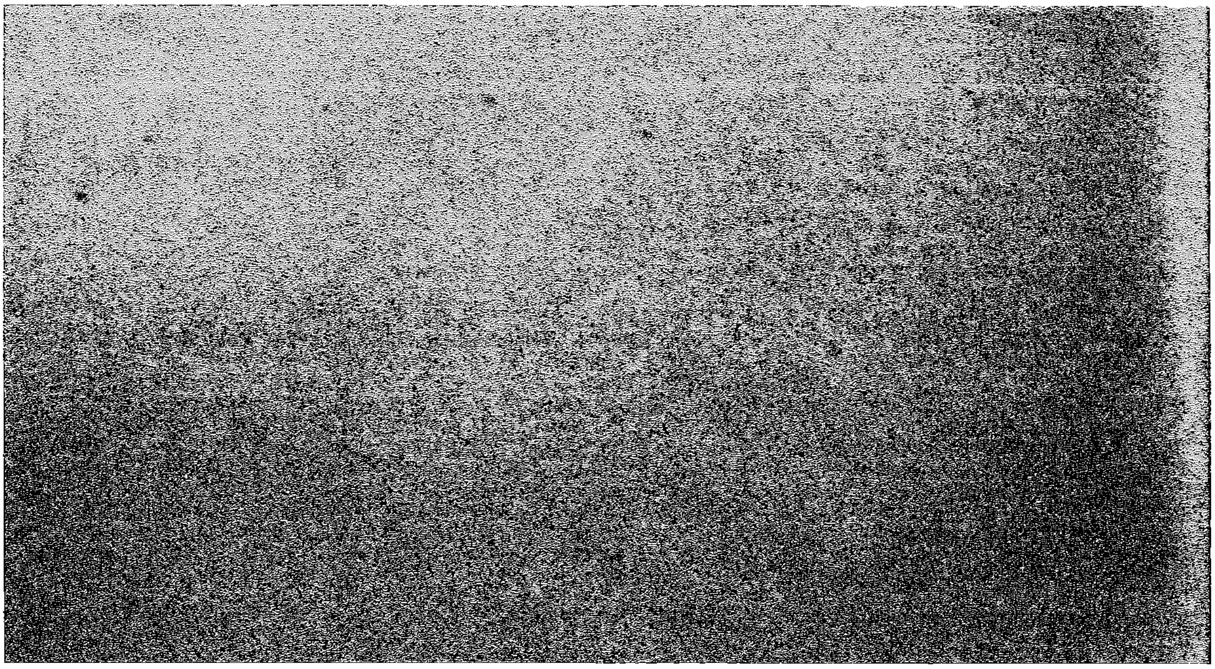

Figure 7.21: Modulator in the 'off' state

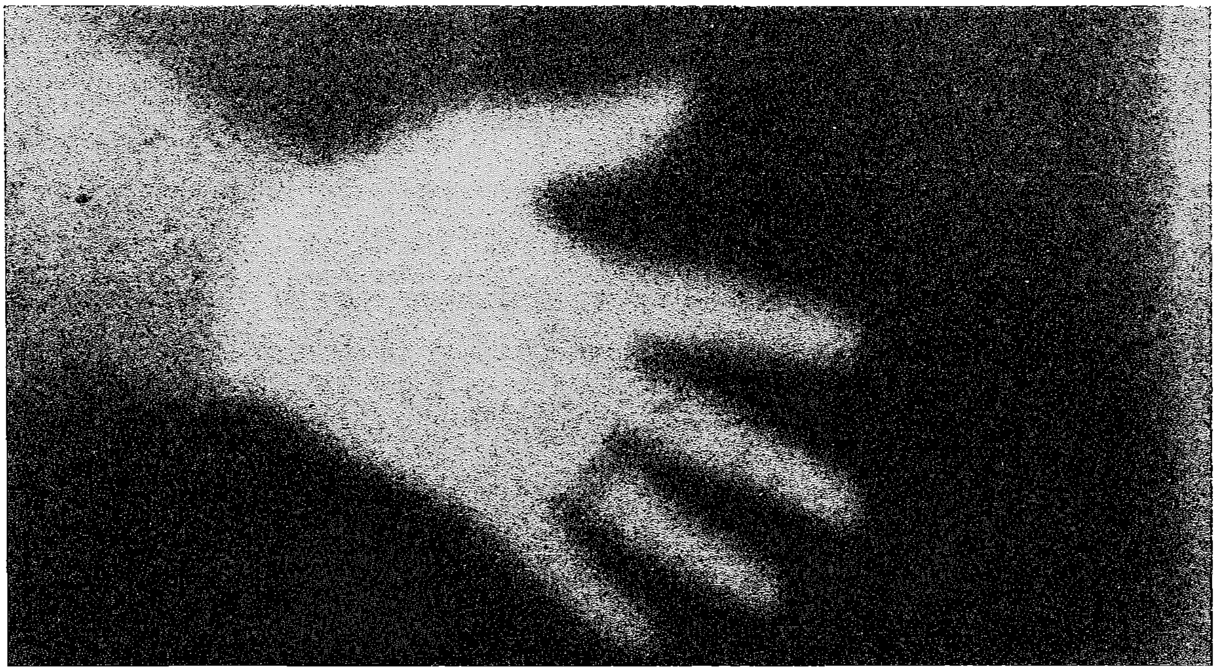

Figure 7.22: Modulator in the 'on' state

Chapter 8

Electrically-pumped modulator

The successful demonstration of an optically-pumped modulator in Chapter 7 raises the question as to whether the holes required for the induced absorption could be electrically-generated. An electrically-pumped modulator has several advantages over the optically-pumped system. These include the reduced number of parts and inherent increased reliability, the improved efficiency due to removal of the 40% efficiency laser diodes, and a more compact system without the need for offset excitation laser diodes. The disadvantages of this pumping scheme arise from the contrasting requirements of a high injection current and a uniformly-absorbing aperture.

Two possibilities exist for injecting carriers into the germanium, i) via carrier injection using a p-i-n type structure and ii) using electron impact excitation. The system requirements and tradeoffs are considered initially, followed by their design. These ideas are developed to the full design of a p-i-n style diode modulator, although time limitations did not permit its construction.

In contrast to the optically-pumped modulator detailed in Chapter 7, the surfaces of the electrically-pumped modulator are not as important with respect to providing a low surface recombination rate. Although surface recombination affects the steady-state excited carrier density in the electron-impact modulator, since carriers in the p-i-n modulator are generated within the bulk material, away from the surfaces, surface recombination is much less important. With the electron-impact system the accelerating voltage of the electrons can be tailored to ensure electron-hole pair generation occurs just beyond the front surface. This reduces slightly the criterion for a low recombination surface when using electron impact excitation, although 'reasonable' electron energies must be used. With the optically-pumped modulator it was found that only when carriers are generated beyond 10% of a diffusion length from the surface were they less dependent on the surface recombination velocity than if they were generated within a few microns of the surface, and the same condition holds for electron impact excitation. With electron-impact excitation, etching therefore increases the modulator's efficiency. Little improvement is expected from etching the surfaces of the p-i-n style modulator and reducing the surface recombination velocity. Both p-i-n and electron-impact modulators still require a long bulk carrier lifetime to maximise modulator efficiency.

The initial design criteria for an electrically-pumped modulator is the current density required to induce an acceptable depth of modulation. Based on the calculation in Section 7.3, that $10W\ cm^{-2}$ at $980nm$ reduces the transmission of an AR coated sample from 100% to 10%, a calculation is made for the electrically-pumped device. Assuming the holes (and electrons) are produced by an electric current, the number of holes required per cm^2 per second is given by Equations 8.1 and 8.2.

$$holes\ (cm^2 s^{-1}) = \frac{P\lambda_{exc}}{hc} \tag{8.1}$$

$$Current\ density\ (A\ cm^{-2}) = holes \cdot q \tag{8.2}$$

Using the above values gives a current density of $7.9A\ cm^{-2}$, which is realistic since p-i-n diode designs are commonplace with current densities in excess of $300A\ cm^{-2}$ [80].

With the electron impact excitation modulator the above current density must be reduced by the ratio of the accelerating voltage to the potential required to generate an electron-hole pair in germanium. This ratio gives the number of electron-hole pairs produced by a high-velocity electron as it passes through the semiconductor. Thus it is possible to tradeoff accelerating voltage against electron beam current and obtain the required depth of modulation by keeping the product of beam current and accelerating voltage constant. In germanium [131] $2.7eV$ is required to generate an electron-hole pair from an electron-impact process. Accelerating voltages of $> 200kV$ are likely to cause crystal damage to many semiconductors [36] (and unacceptable x-ray generation) and a subsequent reduction in the long carrier lifetime in germanium, so much lower voltages than this would be used. In practice the accelerating voltage will be in the order of a few kV. Assuming a $2kV$ accelerating voltage, and $2.7eV$ electron-hole pair generation potential, a current density of $10.7mA\ cm^{-2}$ is required to achieve the above depth of modulation.

8.1 Operational considerations for an electrically-pumped modulator

This section outlines the tradeoffs in the design of an electrically-pumped modulator. General systems are considered by the comparisons. Carrier injection will assume a p-i-n structure with a surface annular electrical contact ring on either side of the p-i-n sandwich. Impact excitation will assume the use of an offset electron source facing the germanium. These generalised structures are shown in Figure 8.1

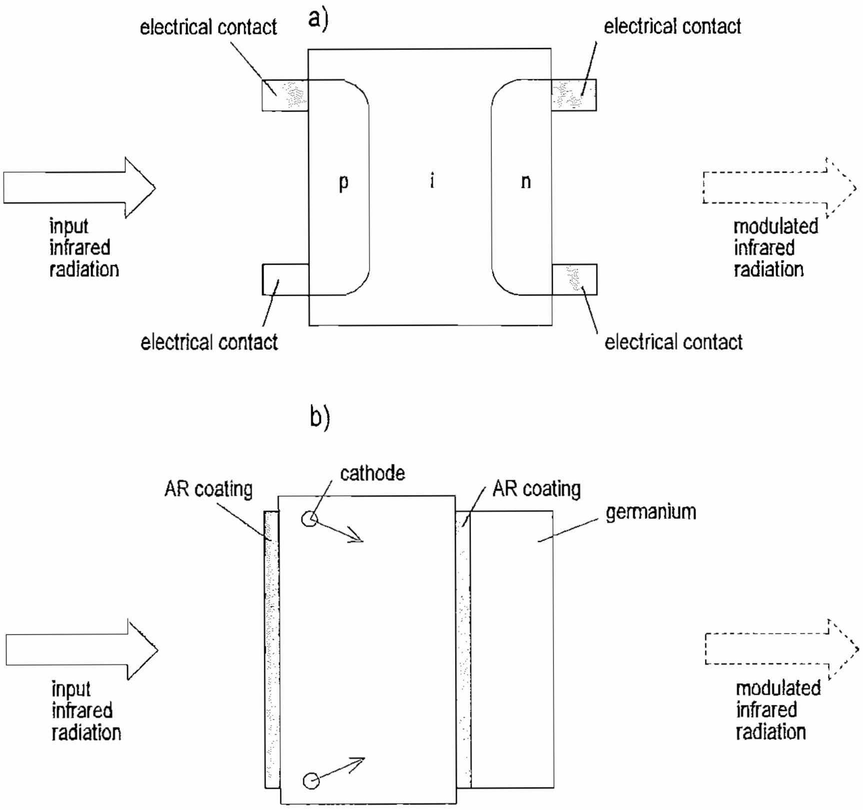

Figure 8.1: Injection (a) and impact excitation (b) modulator structures

8.1.1 Carrier injection requirements

The design of an electrically-modulated carrier-injection device is more complex than the optical-excitation case, requiring an infrared-transparent injecting electrical contact to be made to the germanium. This is achieved using a p-i-n type structure, which has ohmic electrical contacts on the two surfaces to connect it to the driving circuit. The essential modulator requirement of an injecting contact could be achieved using a p-n diode geometry. However, the reduced carrier lifetime associated with significantly doped regions, means it is preferable to have an intrinsic region with long bulk carrier lifetime, within which the induced absorption takes place. An intrinsic region is therefore sandwiched between an injecting 'p' doped region and an injecting 'n' region to create the p-i-n geometry. Both 'p' and 'n' end regions are required on either side of the 'i' region since the electron and hole generation rates must be equal so that a current can flow.

In the following analysis the effects of absorption due to the excess holes in the space charge layers are ignored. Depletion layers exist at the p-i and i-n interfaces, but in order to maintain charge neutrality, equal numbers of holes and electrons must exist either side of each interface. This produces an effective narrowing of each of the p, i, and n layers as far as the number of charge carriers in each layer is concerned. However the charge 'missing' from a layer is in effect in the adjacent layer, and as far as the modulator is concerned, it sees the p-i-n stack as a series optical component, and the area carrier density and hence absorption is unchanged.

In the transmitting 'on' state, the structure in Figure 8.1(a) has no applied bias to the junction. The total transmission is given by the product of the individual transmission of the three ('p', 'i' and 'n') regions, accounting for the antireflection films on the front and back surfaces. The 'on' state transmission is ideally 100%. In the absorbing 'off' state the p-i-n junction is forward-biased, causing the 'p' layer to inject holes into the intrinsic region, and simultaneously electrons are injected into the 'i' region by the 'n' layer. Due to the wide 'i' region, most electrons and holes will recombine here, and carriers both drift and diffuse across this region. The few carriers that have not recombined in the 'i' region, recombine on reaching the opposite end region ('p' or 'n' type). In this forward-bias state the 'i' region with its high hole density becomes strongly absorbing in the 8 to $14 \mu m$ region, and the modulator transmission is again given by the product of the transmission of each of the three layers, accounting for the antireflection coatings. In this state most of the induced absorption occurs via light hole to heavy hole transitions in the 'i' region, although a small contribution to absorption does occur due to holes in the 'n' region which have not yet recombined. By making the 'i' region approximately a diffusion length long the minority hole density in the 'n' doped end region contributes negligible absorption to the total. As with the optically-pumped modulator, the contribution to total absorption from free carrier absorption is insignificant in comparison to that from hole intervalence band transitions.

The considerations in designing the electrically-pumped injection device are i) the form of ohmic contact to the surface of the germanium, ii) the doping levels and iii) the physical widths of the three 'p', 'i' and 'n' regions. These factors affect the switching speed, uniformity of induced absorption, and heat dissipation requirements of a modulator using this geometry, and are considered in the following subsections

8.1.2 Electrical contacts to the germanium

The contacts to the 'p' and 'n' surface layers must be ohmic. Simple barrier theory suggests that in order to destroy the rectifying property of a metal contact on a semiconductor, that the work function of the metal should be higher than that of the semiconductor on a 'p' type surface, and lower than that of the semiconductor on an 'n' type surface. However, this does not follow for a germanium surface [132], on which many common metals will form an injecting contact to some extent. Two methods were used in the past [132] (reference for entire subsection) to suppress the injection; one was to treat the germanium surface prior to contacting the metal and the other was to heavily-dope the surface layer to which the contact was to be made, with the same dopant as was used in the bulk of that region. The former surface treatment consisted of roughening the surface prior to making the contact. This reduces minority carrier injection by killing-off their lifetime close to the contact. The latter heavy-doping (to a few carrier mean-free paths from the surface) increases the potential barrier to minority carriers, greatly reducing their injection into the bulk.

Making contact to the germanium can be achieved through a combination of plating, tinning, or soldering directly onto the surface. The process used depends on the type of surface ('p' or 'n' type) being contacted-to. Plating the germanium with either copper or antimony was often used as a means of providing a more robust contact to the surface. Either copper or antimony, in the form of copper sulphate or antimony trioxide with potassium hydroxide in water, is used as the electrolyte, and a thin layer is deposited on the germanium, surface. To assist uniform deposition of the antimony, copper, which is easier to plate, is often deposited beforehand. In the case of antimony, when the surface is heated by the soldering process, antimony diffuses into the surface and heavily-dopes the surface region, thereby reducing minority carrier injection on an 'n' type surface. In the case of a copper plated layer on the modulator, care would have to be taken to ensure the germanium is not heated afterward, except during a short soldering process, to ensure the copper does not diffuse into the modulation region and degrade the long bulk carrier lifetime there. It would be unwise to use copper plating unless essential. Tinning the germanium surface prior to soldering is only generally used if the surface has been copper-plated. An antimony-plated surface tends to evaporate antimony if a tinning stage is used. Tinning the electrode prior to soldering is, however, more commonly used, and here the same solder is used as for the soldering process.

The process chosen as being the most suitable for the modulator, also requiring a minimum of processing stages, is to solder directly onto the germanium, using a doped-solder. The germanium surface regions requiring contacts are lapped, and then an antimony-bearing solder is used at the 'n' type end, such as 63Pb-35Sn-2Sb (MP = $250^\circ C$), and a 'p' dopant such as gallium or indium is incorporated into the solder at the 'p' type end. Prior to soldering, the electrodes are pre-tinned with the same respective solder. During soldering the solder dopant diffuses into the surface layer, reducing minority carrier injection.

8.1.3 Tradeoffs in the design of a p-i-n modulator

This section assumes the general form of the p-i-n modulator construction as in Figure 8.1(a). All results are given for a $1cm^2$ modulator in this section. The extension to a modulator of any area is given at the end. The most important tradeoff with the p-i-n style modulator concerns the thickness of the 'p', 'i', and 'n' layers, and their doping levels. The AR coating on the front surface will practically eliminate the Fresnel loss at the front 'p' surface, and the same methods of producing this coating as with the optically-pumped device are assumed. The AR coating here need only be designed for the modulated 8 to $14\mu m$ region. In the 'on' state the hole absorption cross section is 16 times higher than that for electrons, so the front layer dominates the absorption. The absorption coefficient of this layer (A in Equation 7.1) is given by the product of the hole volume doping density, 'p', the hole absorption cross section, and the layer thickness x_p.

$$A = p \cdot \sigma_h \cdot x_p \tag{8.3}$$

Since σ_h is constant, the product $p \cdot x_p$ should be minimised to maximise the 'on' state transmission. However, during the 'off' state, the 'p' layer serves as a hole-injecting region. To maintain uniform current injection across the modulator aperture, a low resistance 'p' layer is required so that carriers can be injected from across the entire 'p' aperture, and this requires a high area doping density. The high area doping density conflicts with the requirement for a low absorption in the 'on' state. To compromise, the product of 'p' layer thickness and x_p is reduced, until acceptable absorption and uniformity are obtained. If the doping level is too low, electric field lines emanating from the high resistance 'p' layer will concentrate only in the small volume directly between the metal ring electrodes. Modulation subsequently takes place mainly in this region where the contacts optically obscure the induced-absorption region. This problem of junction breakdown at the edges of contact electrodes is analogous to the emitter-edge-crowding problem in the design of planar transistors [80].

The required width of the 'i' layer requires both optical and electrical analysis, and is compared to the situation of a p-i-n diode [80]. The p-i-n modulator has a geometry defined by Figure 8.2 in the following analysis.

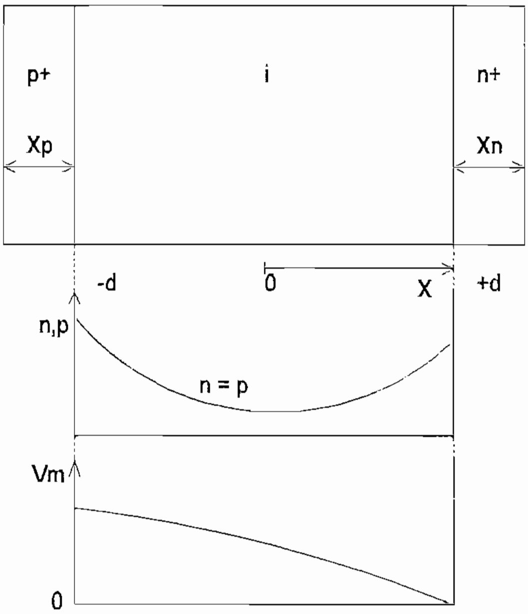

Figure 8.2: $P^{+}in^{+}$ diode geometry, carrier distribution and potential

In Figure 8.2 the upper diagram defines the p-i-n structure, the middle diagram represents the carrier density in the central 'i' region, where electron and hole densities are equal, and the lower diagram represents the potential vs displacement in the 'i' region.

In the 'off' state the electron and hole concentrations are equal in the central intrinsic region, and, if all recombination is assumed to take place within the intrinsic region, are given [95] by Equation 8.4.

$$p(x) = \frac{\tau_a J}{2qL_a} \cdot \left(\frac{cosh(x/L_a)}{sinh(d/L_a)} - B \cdot \frac{sinh(x/L_a)}{cosh(d/L_a)} \right) \tag{8.4}$$

$$L_d = \sqrt{D_a \tau_a} \tag{8.5}$$

$$B = (\mu_n - \mu_p)/(\mu_n + \mu_p) \tag{8.6}$$

This assumes negligible recombination in the heavily-doped end regions where a lower lifetime exists. J is the current density, L_a is the ambipolar diffusion length, the base region thickness is $2d$, and B is a mobility scaling parameter. Integrating $p(x)$

over displacement x gives the hole area carrier density $p_1(cm^{-2})$ in the intrinsic region, Equation 8.7.

$$p_1(cm^{-2}) = \frac{\tau_a \cdot J(A \cdot cm^{-2})}{q} \tag{8.7}$$

Interestingly the total area hole density is independent of the intrinsic region length, and depends only on the current density passing through the region, and the ambipolar carrier lifetime, which is fixed by the material purity.

If an ambipolar lifetime of $500\mu s$ is assumed, Equation 8.7 gives the modulator's area hole density as $p_1 = 3.12 \times 10^{15}$ per $A\ cm^{-2}$. Equation 8.3 is used to validate the current density required for a given depth of modulation, which was predicted at the start of Chapter 8. The transmission of the intrinsic layer in the 'off' state is, Equation 8.8:

$$T = e^{-A} = T_0 e^{-\sigma_h p_1} \tag{8.8}$$

Where $\sigma_h = 5.33 \times 10^{-16} cm^2$ is the hole absorption cross section. Hence for an ambipolar lifetime of $500\mu s$ and a current density of $7.9A\ cm^{-2}$ (start of Chapter 8) and assuming 100% transmission from an AR coating ($T_0 = 1$), a transmission of e^{-13} is attained in the excited state. Although this appears unreasonably low, it is indicative of the high rate of carrier loss in the optically-excited device. A calculation using a bulk carrier lifetime of $100\mu s$ in the p-i-n type device (a closer approximation to the optical device, in which the surfaces greatly reduced the effective carrier lifetime) and the same current density as that predicted from operation of the optical device gives an 'off' state transmission of 7.2%. This agrees more closely with that predicted (10%) from the optical device operation at this current. This calculation shows the large benefit offered by using a p-i-n type electrically excited structure, which makes full use of the long bulk carrier lifetime. The design constraints based on the above assumptions are now determined. The transmission in the 'on' and absorbing 'off' states are given respectively by:

$$T_{on} = T_0 \cdot e^{-A} = T_0 \cdot e^{-\sigma_h \cdot [p \cdot x_p]} \tag{8.9}$$

$$T_{off} = T_0 \cdot e^{-\sigma_h \cdot [p \cdot x_p]} \cdot e^{-\sigma_h \cdot p_1(cm^{-2})} \tag{8.10}$$

p is the 'p' layer doping density (cm^{-3}), x_p is the 'p' layer width, and p_1 is the area carrier density in the intrinsic region during forward injection, and is given by Equation 8.7. A graph of 'on' state transmission from Equation 8.9 against 'p' dopant area density ($p \cdot x_p$) is given in Figure 8.3. This shows the significant reduction in 'on' state transmission caused by only a moderate hole doping density. The area carrier density at which the 'on' state transmission is 90% and 50% is 1.98×10^{14} and 1.3×10^{15} respectively.

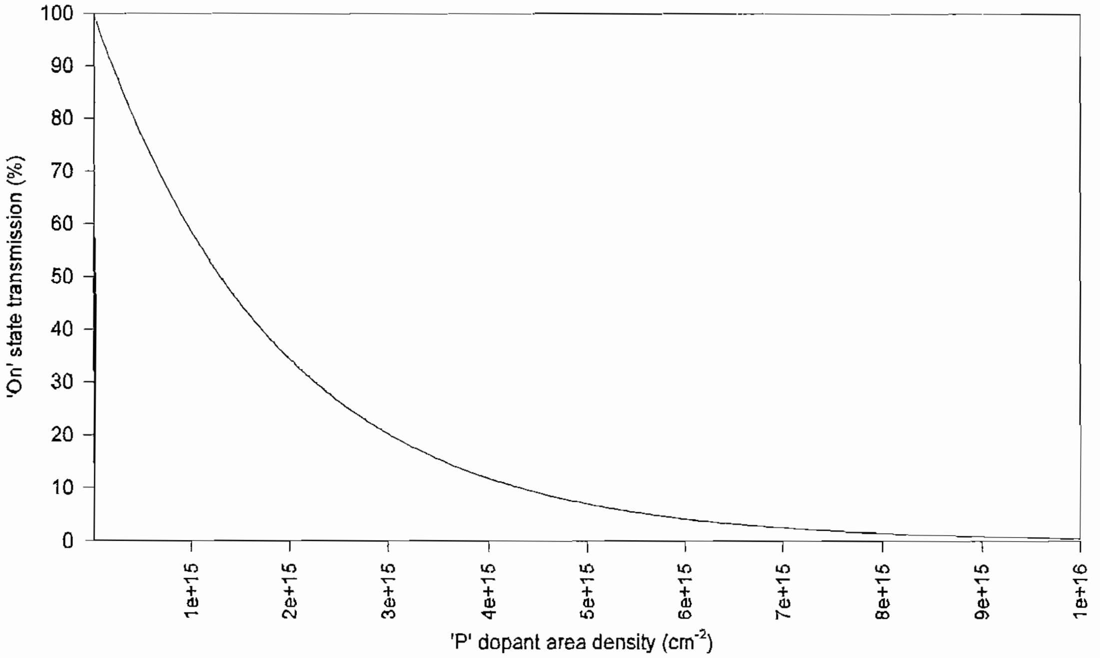

Figure 8.3: 'On' state device transmission vs 'p' dopant area density assuming zero 'n' layer absorption from Equation 8.9

Considering now the effect of the bulk (or ambipolar) carrier lifetime on the induced absorption in the 'off' state. Figure 8.4 plots the 'off' state transmission from Equation 8.10 against current density, based on an acceptable 'on' state transmission of 90% (due to p layer absorption) for a range of bulk carrier lifetimes. This shows that an increased bulk carrier lifetime produces a higher level of induced absorption for a given current density.

The current-voltage characteristic of the p-i-n diode is now determined for use in Section 8.1.4 in determining the uniformity of absorption across the aperture. The total voltage drop across the p-i-n device is given by the sum of the voltage drops across the p-i injection region, the 'i' region, and that across the i-n region. The voltage drops across the outer p-i and i-n regions will each be roughly equal to the voltage drop across two forward biased diodes, each being in the order of $0.4V$ based on usual germanium diode turn-on voltages. The voltage drop across the central intrinsic region is dependent

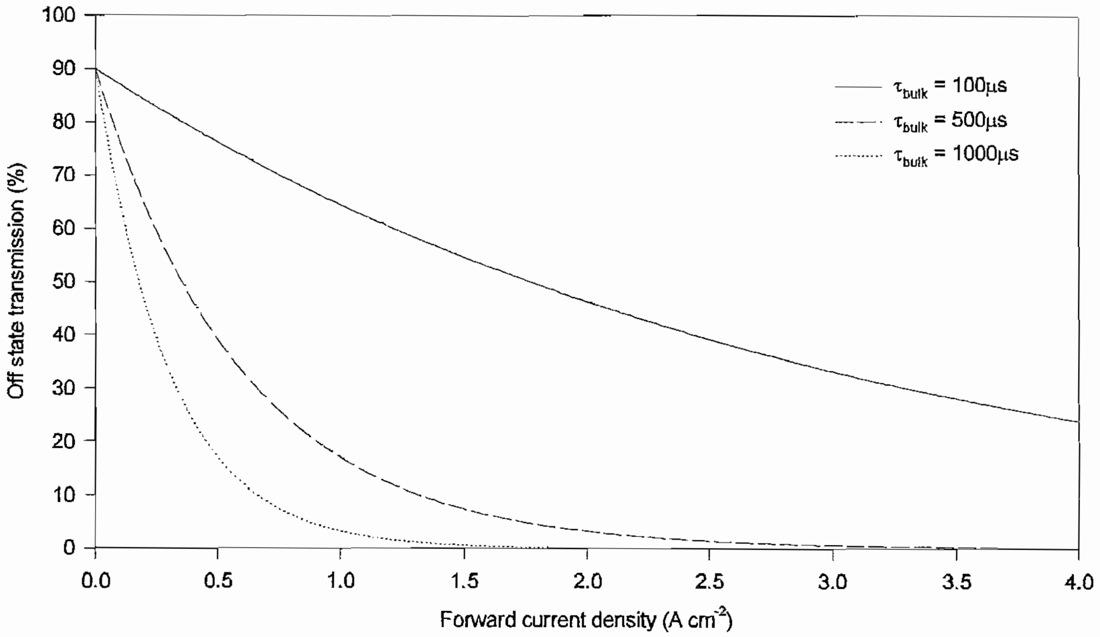

Figure 8.4: 'Off' state device transmission vs current density for various carrier lifetimes assuming zero 'n' layer absorption

on its width, $2d$, and is given [95] by Equation 8.11.

$$V_m = \frac{kT}{q} \cdot \left[\left[\frac{8b}{(b+1)^2} \cdot \frac{sinh(d/L_a)}{\sqrt{1 - B^2 tanh^2(d/L_a)}} \cdot arctan\left(\sqrt{1 - B^2 tanh^2(d/L_a)} \cdot sinh(d/L_a)\right)\right] + B \cdot ln\left[\frac{1 + B \cdot tanh^2(d/L_a)}{1 - B \cdot tanh^2(d/L_a)}\right]\right] \tag{8.11}$$

where $b = \mu_n/\mu_p$. The parameters in Equation 8.11 have the same meaning as in Equations 8.4 to 8.6, and V_m is plotted against 'i' layer width normalised to diffusion length $(2d/L_a)$ in Figure 8.5. Thus at $2d/L_a$ = unity, the intrinsic region length equals the ambipolar diffusion length.

Figure 8.5 shows that the forward voltage drop across the intrinsic region should be insignificant in comparison to the total device forward voltage ($\sim 2 \times 0.4V$), until a point where the intrinsic region is a few diffusion lengths long. Until this point the electrical power dissipated in the intrinsic region is very low. This shows that the penalty for making the intrinsic region too long is that of increased heat dissipation in this region due to an increased V_m. The assumption made here is that all the recombination takes place in the intrinsic region. If this is made much shorter than a diffusion length the recom-

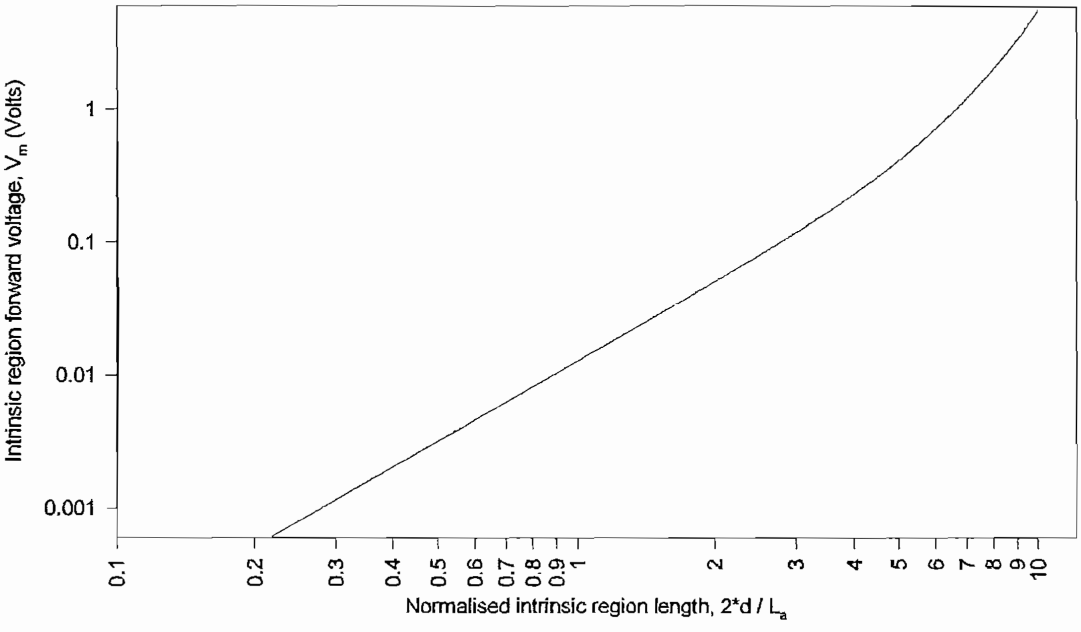

Figure 8.5: Graph of p-i-n diode forward voltage drop against normalised intrinsic region length

bination in the more-heavily doped end regions increases [133] and the current drops due to the increased proportion of carriers recombining there with a shorter lifetime. One design criteria is therefore to make the intrinsic region length equal to a diffusion length, requiring an intrinsic region length of $1.8mm$ in $500\mu s$ lifetime germanium. At this thickness the forward voltage drop across the intrinsic region is $V_m = 0.013V$.

If the intrinsic region length is made equal to a diffusion length, then assuming the 'p' and 'n' end regions have the same volume doping density and minority carrier lifetimes, then to a good approximation, all the current flow is due to that injected into the 'i' region, and negligible contribution is provided by minority carrier injection into the doped end regions. This assumes unity injection efficiency. Under these conditions, the error introduced to the total diode current is small, and the forward-conduction diode current is given by:

$$J_f = 2q \cdot \frac{D_a n_i}{d} \cdot F\left[\frac{d}{L_a}\right] \cdot e^{\frac{qV_A}{2kT}} \tag{8.12}$$

$$F\left[\frac{d}{L_a}\right] = [(d/L_a) \cdot tanh(d/L_a)] \cdot [1 - B^2 tanh^4(d/L_a)]^{-1/2} \cdot e^{-\frac{qV_m}{2kT}} \tag{8.13}$$

B is given by Equation 8.6 and V_m is given by Equation 8.11. The forward current density J_f is plotted vs applied diode voltage V_A in Figure 8.6.

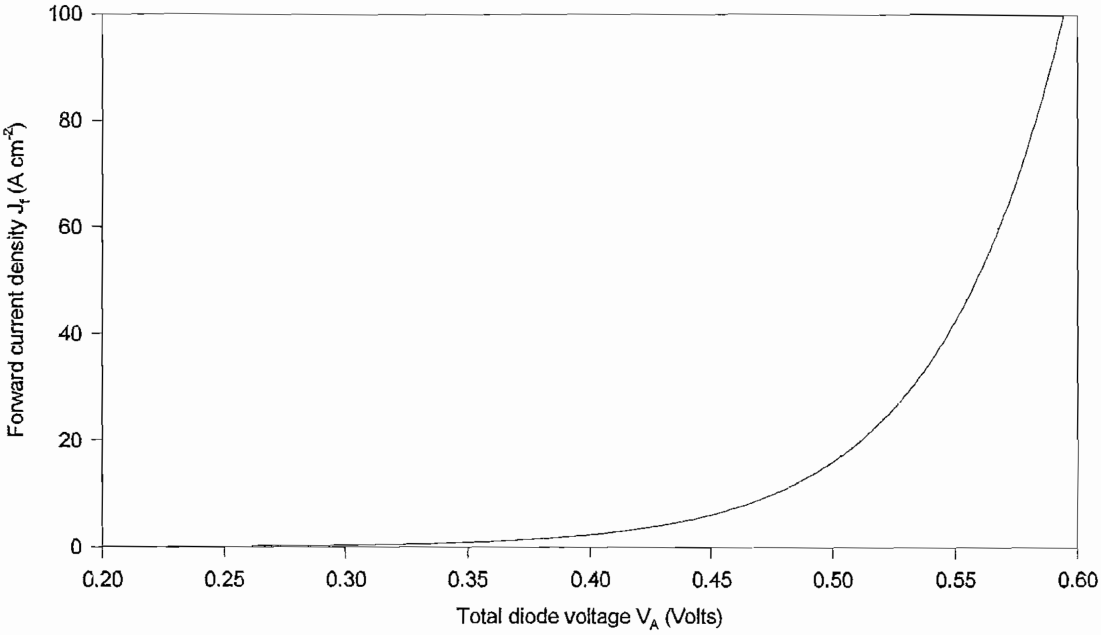

Figure 8.6: P-i-n diode forward current density vs total applied diode voltage V_A

Figure 8.6 shows the p-i-n diode current-voltage characteristic with $\tau_{bulk} = 500\mu s$ and $2d/L_a = 1$. On the above scale the turn-on voltage of approximately $0.5V$ is much lower than was predicted earlier. Initially it was thought that the forward voltage would be that due to two forward-biased germanium diodes, plus the (small) voltage drop across the intrinsic region, V_m, giving a turn-on voltage of $\sim 0.8V$. However, the device dimensions are more typical of a high current diode, having a 'knee' current density in the order of $\sim 500A\ cm^{-2}$. The current required for reasonable levels of absorption in the modulator is up to $10A\ cm^{-2}$, where the forward voltage (seen in Figure 8.6) is much lower. The modulator therefore operates in a region of fairly low injection, and although for the plotted current scale it appears the device has turned-on by $0.5V$, the device is well below the 'knee' turnon-current density, which is in the order of $\sim 500A\ cm^{-2}$ for this structure. At the 'knee' the diode forward voltage is $\sim 0.8V$, closer to that predicted earlier.

As with the optically-pumped modulator, the switching rate of the p-i-n modulator is different for switching-on and switching-off the absorption. When switching-on the absorption the generation of electron-hole pairs is limited only by the ability of the driving circuit to supply the stored charge, and can be made very fast. Although it will take an ambipolar lifetime for the carriers to reach an equilibrium distribution, the holes still absorb the infrared if they are at the edge of the 'i' region and diffusing into their equilibrium distribution in the 'i' region. As with the optically-pumped modulator, the switching rate of a p-i-n diode which simply has its current switched off, is determined by the hole decay time, and in the p-i-n diode this is given by the ambipolar lifetime. Thus the minimum switching frequency observed by the switching of the p-i-n modulator is dominated by the transmission recovery, and is given by $1/2\pi\tau_{ambipolar}$. This is plotted in Figure 8.7. If instead of simply turning-off the diode current, a small reverse-bias voltage were applied to the diode during the intended transmitting state, carriers would be swept-out from the intrinsic region at a faster rate, reducing the recovery time. Figure 8.7 also shows the normalised 'i' layer induced absorption, defined as $(1 - T/T_0)$ at fixed current density as a function of the bulk carrier lifetime. As with the optically excited modulator, a higher switching speed is available at the expense of a shorter bulk carrier lifetime, but achieving the same level of absorption with a reduced carrier lifetime requires a higher current density. Figure 8.7 does not account for using a reverse bias in the 'off' state to switch the device faster, which requires further modelling.

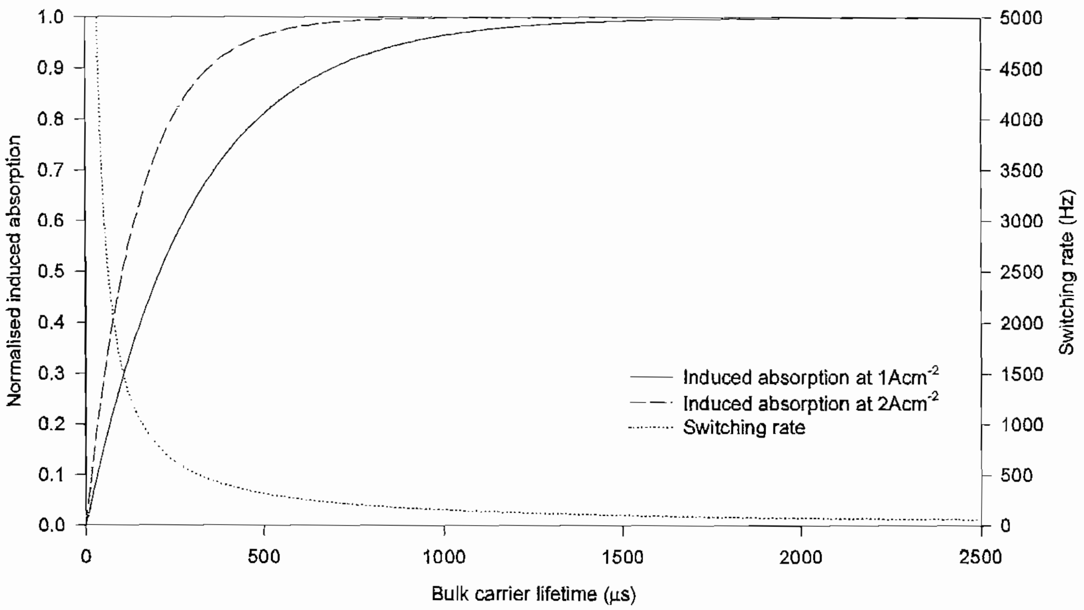

Figure 8.7: Intrinsic layer normalised 'off' state absorption and switching speed vs carrier lifetime for a given uniform current density assuming zero 'p' layer absorption

During switching of p-i-n diodes, voltage transients are seen on pulsing the device current. These often exceed (by $30V$ or more [95]) the forward and reverse voltages pulsed to the diode, occurring at the initial stage of turn-on when carriers are injected into the 'i region and during the decay stage when a reverse bias is applied to the device to draw carriers out of the intrinsic region. Before significant carrier injection takes place, the overshoot potential occurs across the high impedance intrinsic region. After significant carrier injection its subsequent drop in resistance causes the turn-on overshoot to terminate. This overshoot has implications for the electronic circuitry pulsing the p-i-n diode.

In contrast to the optically-pumped modulator, with the p-i-n style modulator there is no stringent requirement to have a low surface recombination velocity. The electric field across the 'i' layer draws carriers into the sample, so the induced absorption in the 'off' state takes place in the 'i' region, and high carrier densities to not appear close to the sample surfaces. From the aspect of carrier loss through surface recombination, no benefit is expected from etching the optical surfaces. There is however a benefit of etching the side faces of the modulator to reduce surface leakage currents.

8.1.4 Design requirements of a p-i-n modulator

Considering the above arguments, some p-i-n modulator design criteria for the length and doping of the 'p', 'i' and 'n' regions are determined. The 'p' layer must be sufficiently doped that carrier injection uniformity is achieved across the entire aperture, but not so highly doped that its contribution to hole absorption in the 'on' state is too significant. The compromise here sets the minimum acceptable 'on' state transmission for this layer, and the doping density and layer thickness are calculated to achieve this. Using Equation 8.8, and setting the Fresnel loss at this layer to be zero ($T_0 = 1$) by assuming a perfect AR coating, requires that for a maximum transmission T of 95%, a maximum absorption $\sigma_h p = -ln(0.95) = 0.05$ is required. This requires a hole area density of $p = 9.6 \times 10^{13} cm^{-2}$. If these are in a $1\mu m$ ($10^{-4} cm$) layer, the corresponding doping density is $9.6 \times 10^{17} cm^{-3}$. A high volume doping density in the p layer degrades the mobility. Carrier-carrier scattering in practical devices starts to degrade the mobility at doping densities above $\sim 10^{16} cm^{-3}$ [134] [80], so longer 'p' and 'n' region lengths are preferable in obtaining the required area doping density with a lower volume doping density. Figure 8.8 shows the required thickness of this 'p' layer against 'p' layer doping density (cm^{-3}) for 95% 'on' state 'p' layer transmission.

To obtain low resistance layers, very thick 'p' and 'n' layer widths of approximately

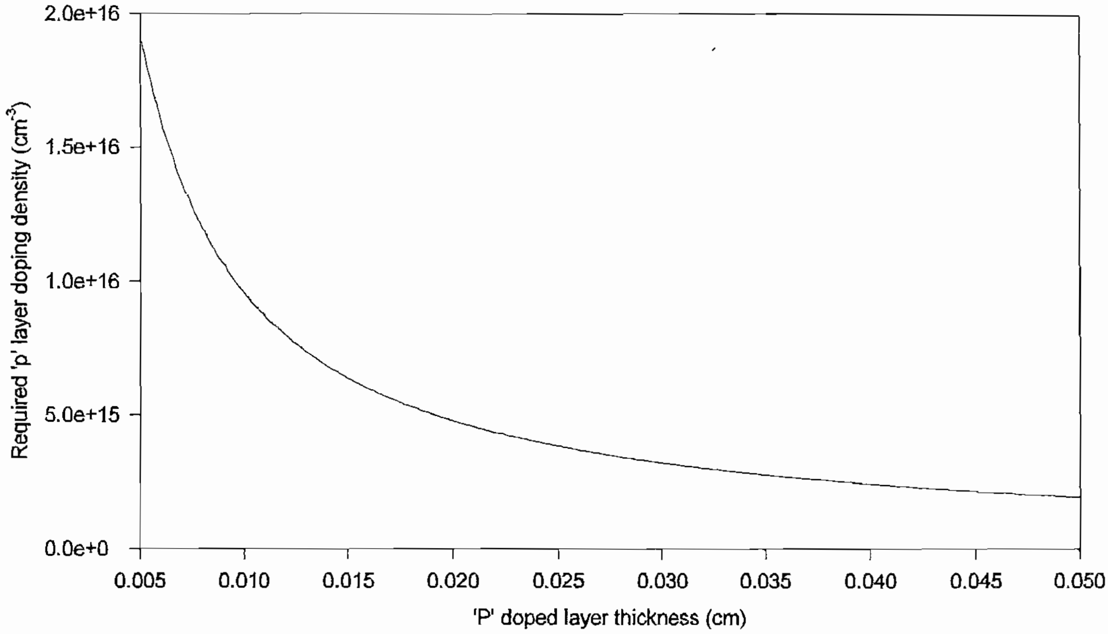

Figure 8.8: 'p' layer thickness vs doping density for 95% 'p' layer transmission in the 'on' state

$100\mu m$ are required to preserve the high mobility. Such diffusion lengths are impractical, requiring an excessive diffusion time ($\sim 5500h$ for indium at $850°C$), although if the layer is made $10\mu m$ thick a small reduction in mobility [134] ($\sim$ 35% lower) is traded for a acceptable diffusion time ($\sim 66h$ for indium at $850°C$). The 95% transmission calculated above is a close approximation to the modulator's 'on' state transmission, making the reasonable assumption of negligible contribution to absorption from the 'n' and intrinsic layers. Some reduction in 'on' state transmission is essential to achieve more uniform modulation across the aperture.

Having considered the transmission resulting from the 'p' layer area doping density, the lateral resistance of the 'p' layer is determined. The lateral resistance affects uniformity of carrier injection and hence the induced absorption across the aperture. A lower resistance gives more uniform injection.

The injection uniformity across the aperture depends on the thickness and doping density of the 'p' doped layer. A complex 3-dimensional analysis is required to properly see the tradeoff between the layer thickness and injection uniformity. However rough approximations of the required layer thickness and doping density are made by assuming the situation illustrated by Figure 8.9. This simplified model assumes a current I passing laterally through a narrow conducting ring of radius a on the surface of the (shaded) 'p' layer causes 50% of the total current through the device to flow within the inner region of radius $0.71a$, which is 50% of the modulator's total aperture area. This represents uniform absorption across the aperture if there is zero lateral voltage drop ΔV_L between the two circumferences (between $r = a$ and $r = 0.71a$). This lateral voltage drop cannot be zero due to the finite 'p' layer resistance, but providing it is not too large, approximates uniform absorption across the aperture. The lateral voltage drop is given by the product of the average current passing through this section of the 'p' doped layer and the lateral resistance of the 'p' layer between $r = a$ and $r = 0.71a$. When this voltage drop is too large there will be different level of current injection at $r = a$ and $r = 0.71a$, and at this value of ΔV_L , injection uniformity across the aperture ceases to be maintained.

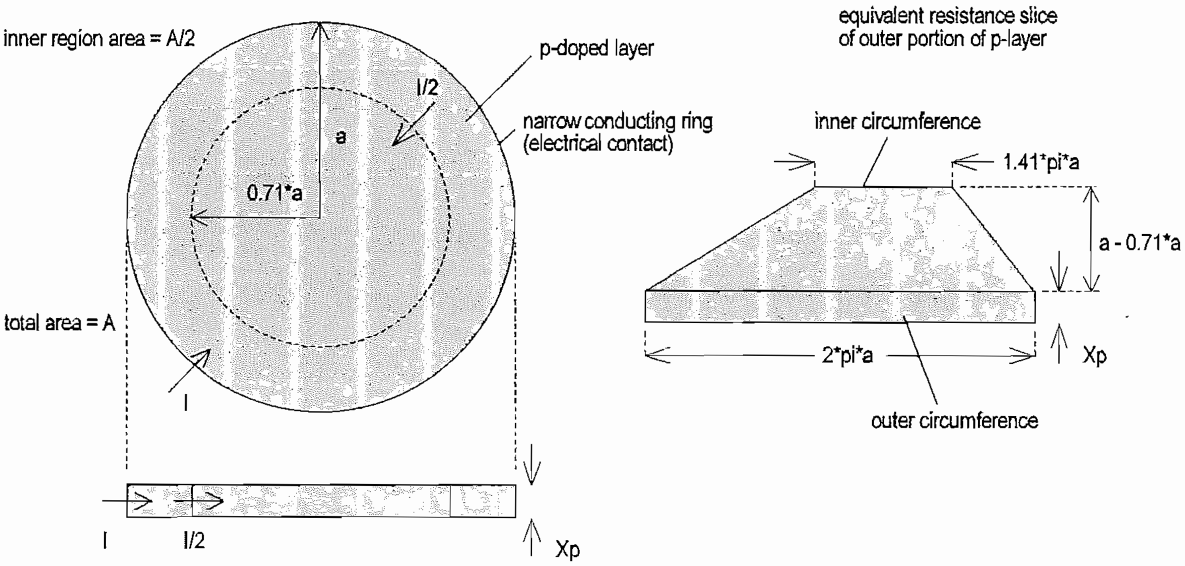

Figure 8.9: P layer injection model from infinitely-narrow ring of radius a

At low current I the absorption at $r = a$ and $r = 0.71a$ will be equal, but the induced absorption is low. At higher current the absorption at $r = a$ and at $r = 0.71a$ rises, but at a certain current, the lateral voltage drop between $r = a$ and $r = 0.71a$ will become too large to inject similar current at the two points. The value of ΔV_L and device current at which this occurs are now determined. Assuming the above model, an average resistance for the outer region of the 'p' layer is calculated as R_{av} where ρ_p is the resistivity of the 'p' layer film, and x_p is its thickness, giving:

$$R_{av} = \rho_p \cdot \frac{\Delta a}{cross\ section\ area} = \rho_p \cdot \frac{(1 - 1/\sqrt{2})}{\pi(1 + 1/\sqrt{2})x_p} \tag{8.14}$$

$$\rho_p = 1/[p(cm^{-3}) \cdot q \cdot \mu_p] \tag{8.15}$$

Interestingly Equations 8.14 and 8.15 show that with this relatively simple model, the resistance of the 'p' layer that affects uniform injection depends on the product of p and x_p, the area doping density (cm^{-2}) in the 'p' layer. There is no optimal 'p' layer thickness as regards injection uniformity, and nothing is gained by making the 'p' layer thin. This permits calculation of the lateral voltage drop across the 'p' region between $r = a$ and $r = 0.71a$ for a $1cm^2$ modulated aperture, which is given by the product of the mean current flowing through the outer region of the 'p' layer and the resistance, R_{av}. To achieve uniform injection, half the total device current must pass through half the modulator's area. The inner half of the modulator's area occurs inside the boundary $r = 0.71a$, across which half the total device current must flow. The mean current in the outer portion of the p-layer (right diagram in Figure 8.9) is therefore 75% of the total device current.

$$\Delta V_L = 0.75 \times R_{av}(per\ Amp) \tag{8.16}$$

Re-writing the total device forward current in Equation 8.12 as

$$J_f = J_0 \cdot e^{\frac{qV_A}{2kT}} \tag{8.17}$$

$$J_0 = 2q\frac{D_a n_i}{d} \cdot F\left[\frac{d}{L_a}\right] \tag{8.18}$$

The reverse saturation current, J_0 , is $1.01mA\ cm^{-2}$ using typical parameters of $d = L_a/2$ and $\tau = 500\mu s$. This appears high, but is due to design of the diode in a non-standard way with low doping densities, long carrier lifetime and subsequent high diffusion length. In standard diodes, values for these parameters may differ considerably on account of high switching rate requirements. Combining Equations 8.7 and 8.10 gives the 'off' state transmission as:

$$T = T_0 \cdot e^{-A} = T_0 \cdot e^{-\sigma_h \cdot [p \cdot x_p]} \cdot e^{-\sigma_h \tau_a \frac{J_f}{q}} \tag{8.19}$$

where J_f is given in Equation 8.17 and is an exponential function of V_A. The dependence of transmission on the diode's surface voltage V_A means small (lateral) fluctuations in V_A (denoted ΔV_A) affect the 'off' state transmission very strongly. The first exponential in Equation 8.19 gives the 'p' layer transmission, the second gives the 'i' layer transmission as a function of radially-varying potential V_A on the aperture face. The 'i' layer transmission is shown as a function of V_A in Figure 8.10 using the above d, τ_a and J_0 values.

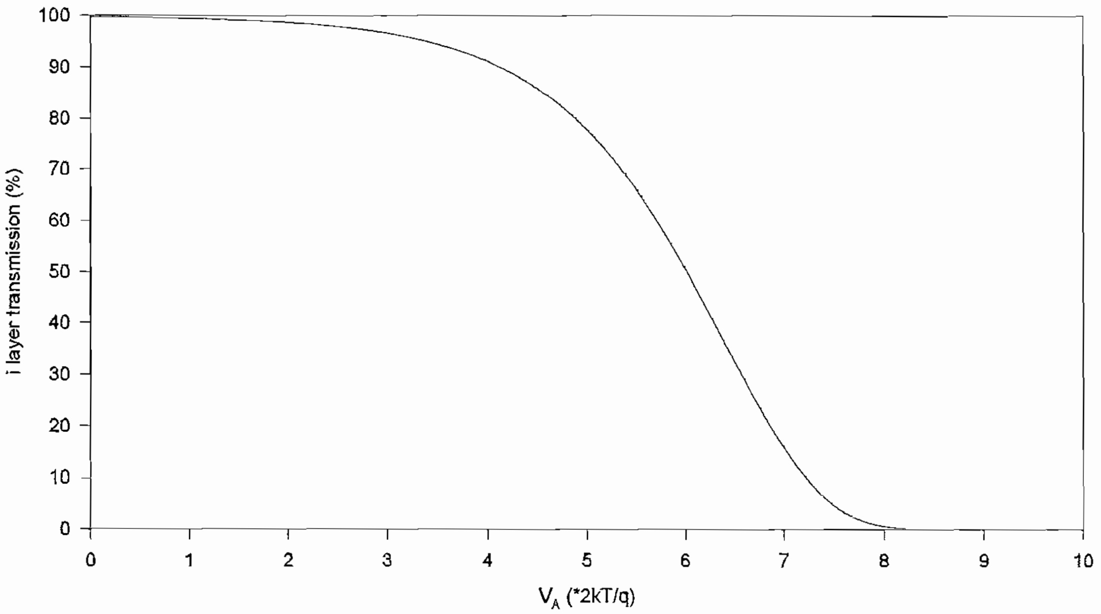

Figure 8.10: i layer transmission as a function of potential on the aperture

Figure 8.10 shows that if the potential at the contact ($r = a$) is say $6 \cdot (2kT/q)$, giving an i layer transmission of 50.78%, then if the diode current were such that the potential at the inner radius ($r = a/\sqrt{2}$) caused a lateral potential drop of $0.2 \cdot (2kT/q)$ across the p layer ($V_A = 5.8 \cdot 2kT/q$ at the inner radius), the transmission at the inner radius would be 57.41%. The criterion of $\Delta V_L = 0.2 \cdot 2kT/q$ therefore provides a reasonable test of uniformity of transmission at the two points on the surface of the diode aperture. For different contact potentials there is a few % difference in transmission at the two points between which $\Delta V_A = 0.2 \cdot 2kT/q$. From Figure 8.10 it might be inferred that it is beneficial to make V_A as large as possible at the contact, thus for $V_A = 10 \cdot (2kT/q)$ the transmission saturates and a small ΔV_A causes insignificant change in transmission between the contact ring and inner ring. However this is incorrect, as ΔV_A depends on the product of the current flowing and the layer resistance, and at the saturation current, ΔV_A is much greater than $0.2 \cdot 2kT/q$.

Using the condition $\Delta V_L = \Delta V_A$ a graph is plotted of the total device current at which the transmission at a point at radius $r = a$ on the aperture above, and that at $r = 0.71a$ start to become significantly different, following the condition above. This is given for a $1cm^2$ circular aperture by $I_{max}(A\ cm^{-2})$ in Equation 8.20, found by equating Equation 8.14, 8.15 and 8.16 with ΔV_A above.

$$I_{max} = \frac{8}{15} kT\mu_h\pi \left[\frac{1 + 1/\sqrt{2}}{1 - 1/\sqrt{2}}\right] \cdot [px_p] \tag{8.20}$$

After a current I_{max} , uniformity in 'off' state transmission across the aperture ceases to be maintained. I_{max} is plotted against 'p' dopant area density ($= p \cdot x_p$) in Figure 8.11.

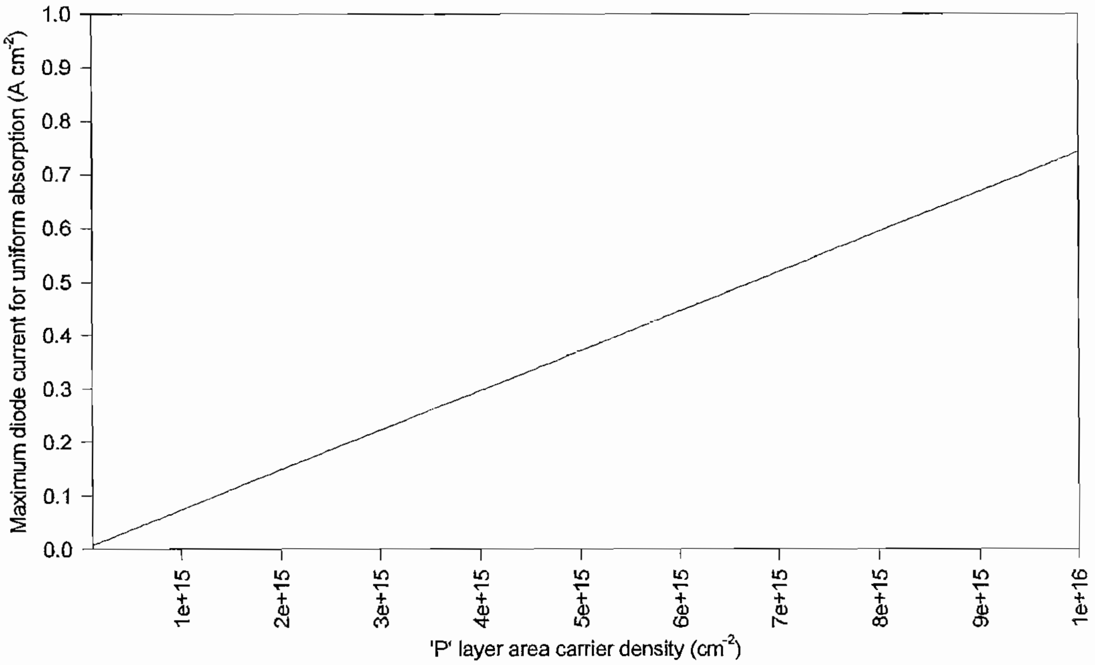

Figure 8.11: Graph of maximum device current for uniform 'off' state transmission vs 'p' layer dopant area density for a $1cm^2$ circular aperture

Figure 8.11 shows that a higher 'p' layer area carrier density reduces its lateral resistance, giving a higher tolerable current I_{max} before the surface voltage drop becomes too large to maintain uniform carrier injection. However, whilst providing a lower lateral resistance, this increase in hole area density reduces the 'on' state transmission. This is shown in Figure 8.12, giving the 'on' state transmission, limited by the 'p' layer absorption, and the minimum transmission at which uniform injection is still maintained, based on a device current I_{max} calculated above, as a function of 'p' dopant area density

$p \cdot x_p$. This is plotted for a range of bulk carrier lifetimes in Figure 8.12.

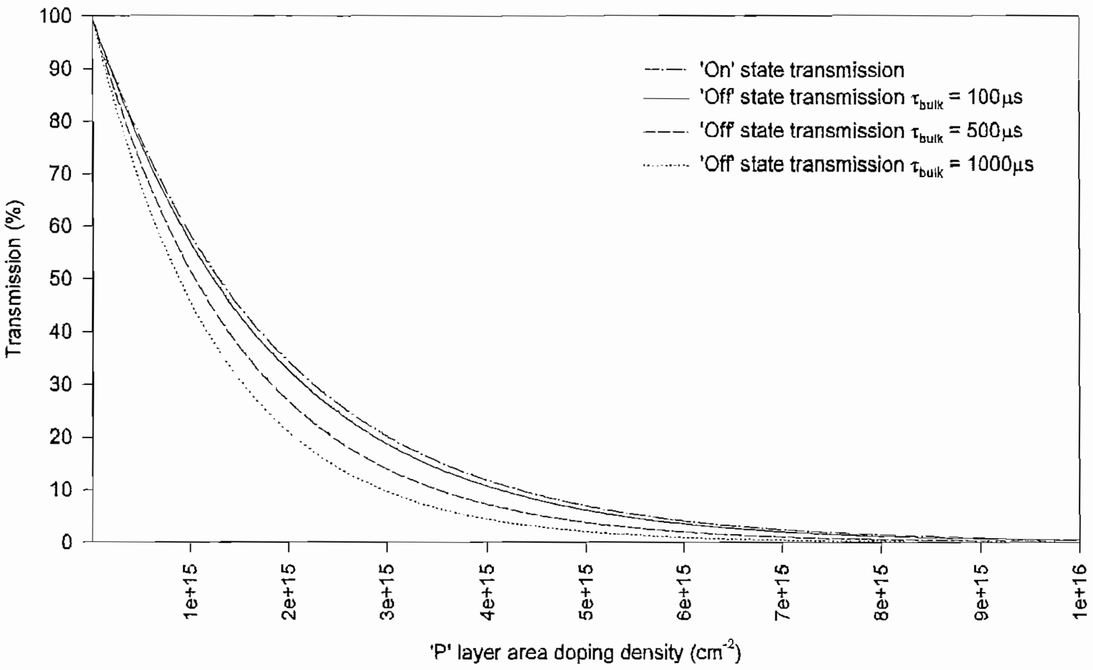

Figure 8.12: 'On' state transmission and minimum 'off' state transmission at which uniform absorption is maintained for a $1cm^2$ circular aperture

Figure 8.12 shows that for a low 'p' dopant area density the 'p' layer lateral resistance is too high for current to spread far laterally. Uniform 'off' state transmission across the aperture rapidly ceases to be maintained with increasing current as voltage is quickly dropped across the high resistance layer. At high 'p' dopant area density the lateral resistance of the 'p' layer is lower, but the 'on' state transmission is severely limited by absorption in the 'p' layer. A significant reduction in absolute transmission requires a much larger increase in current when starting at this reduced value of transmission. This large current increase again drops a large lateral voltage across the 'p' layer and uniformity quickly ceases to be maintained.

Figure 8.13 plots the difference between on state transmission in Figure 8.12 and the minimum in uniform-absorption 'off' state transmission from Figure 8.13 as a function of 'p' dopant area density. This shows the absolute % depth of modulation to which uniform absorption will be seen across the entire aperture.

Figure 8.13 shows that a compromise value of 'p' layer doping exists at around $p \cdot x_p = 2 \times 10^{15} cm^{-2}$ at which point the benefit of reduced 'p' layer resistance balances the expense of the reduction in transmission. This offers the biggest absolute % change

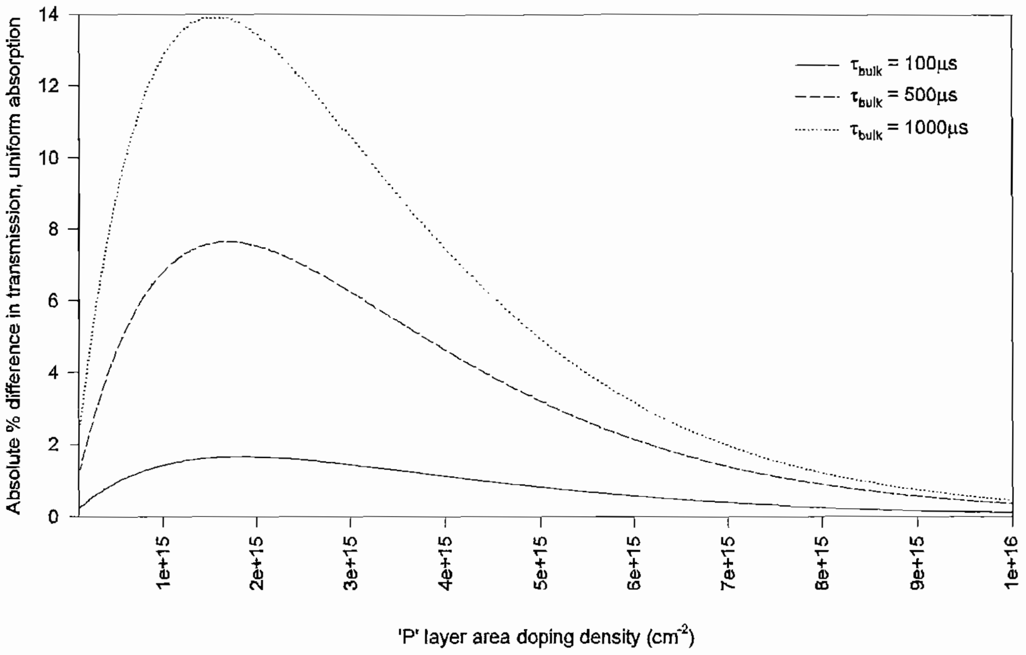

Figure 8.13: Depth of modulation for uniform absorption vs 'p' dopant area density for a $1cm^2$ circular aperture

in transmission between 'on' and 'off' states whilst still giving uniform absorption. The disadvantage of this area carrier density is a low 'on' state transmission of 34.4%. In practice it would be better to accept a slightly lower maximum depth of uniform modulation, in favour of a higher 'on' state transmission by using a hole area density of $p \cdot x_p = 1 \times 10^{15} cm^{-2}$, which would provide an 'on' state transmission of 58.7%.

Figure 8.13 does not represent the maximum depth of modulation at any point on the aperture, it gives the depth of modulation to which uniform absorption will exist across the aperture. Further increase in diode current reduces the transmission in the region close to the conducting ring, but does not further reduce the transmission close to the centre of the aperture, which saturates at the values in Figure 8.12, for the given 'p' dopant area density.

The implication of this is that uniform absorption across the $1cm^2$ aperture is only attainable for low depths of modulation with this planar injection geometry. The loss in transmission with increasing 'p' layer area doping density occurs too rapidly for the subsequent reduction of lateral resistance to be of benefit in maintaining uniform injection. This means that an alternative form of current injection is required to assist lateral current spreading without too high a drop in lateral voltage. Alternative methods of achieving this are considered in Section 6.1.4.

Although the above conclusions assumed a $1cm^2$ aperture, the situation improves considerably if this is reduced. As the modulated area is reduced the resistance of the outer p-doped ring in Equation 8.14 remains constant. The effective length of this resistor $(a - 0.71a)$ and cross sectional area $(2\pi a x_p)$ increase both increase proportionately with the ring radius a. However if the modulated area is halved, then the current required for a given absorption must also halve. The maximum current at which injection uniformity breaks down (I_{max} in Equation 8.20) assumed a $1cm^2$ area, and must therefore be divided by the area (in cm^2). Graphs of the depth of modulation for uniform absorption for various device areas are given in Figures 8.14 to 8.16 for different bulk carrier lifetimes, showing the increased depth of modulation available.

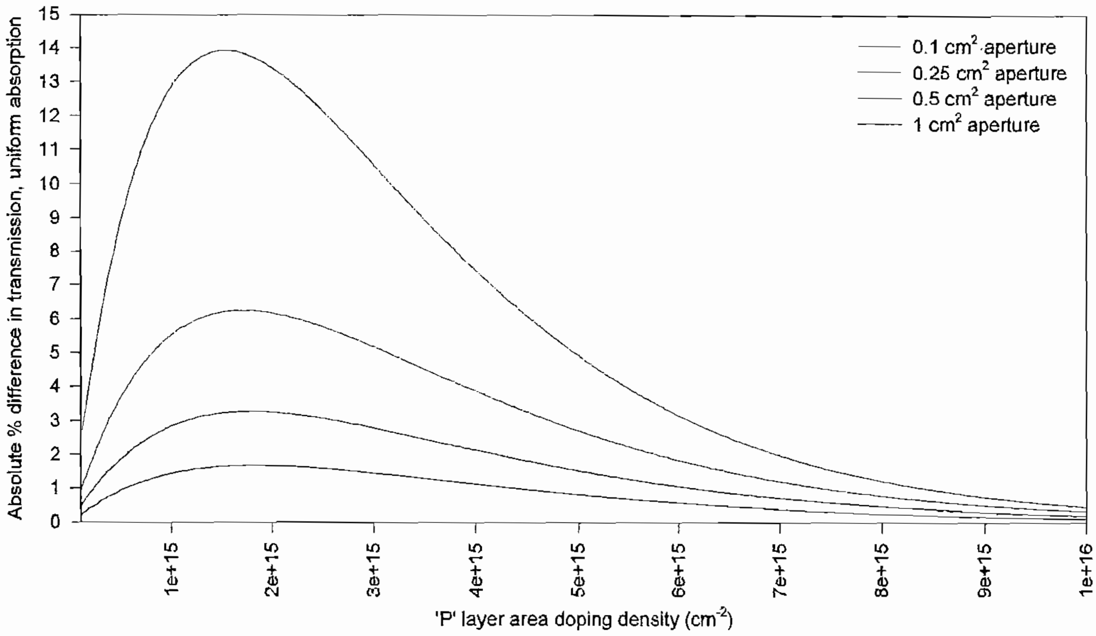

Figure 8.14: Depth of modulation for uniform absorption vs 'p' dopant area density for various aperture areas and $\tau_{bulk} = 100\mu s$

These figures show the considerable increase in depth of uniform modulation offered through use of a smaller modulated area. A reduced modulator aperture could be utilised through use of further optics in the application, although this is undesirable due to the increased system size. Whilst the model presented gives an idea as to the required level of uniformity achieved during operation, a full 3-d diffusion equation analysis would provide further insight into the depth and uniformity of modulation attained. However

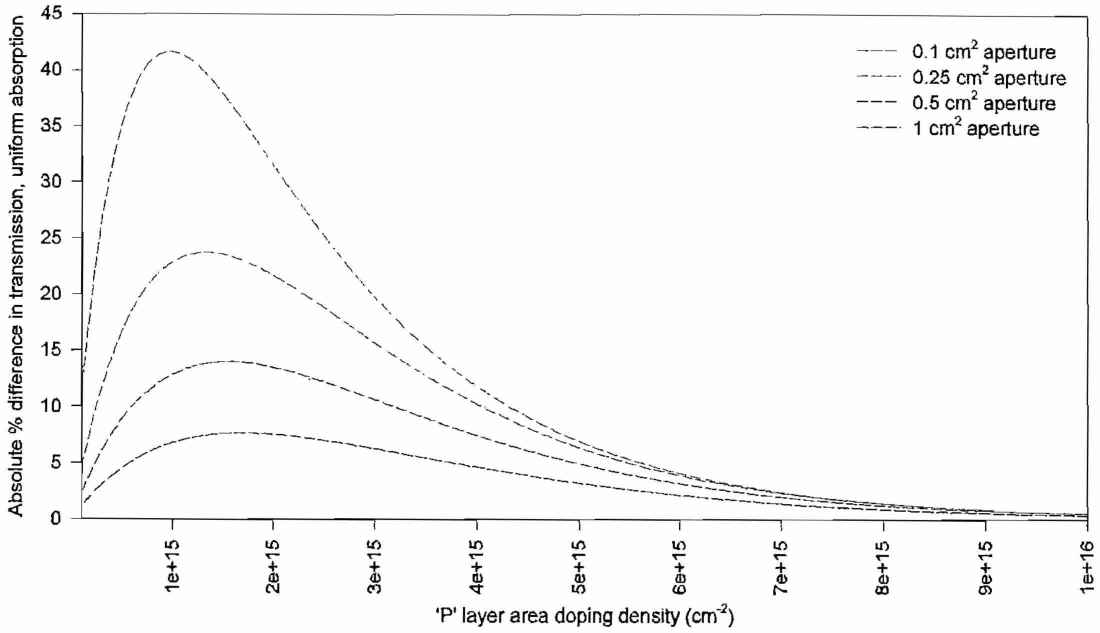

Figure 8.15: Depth of modulation for uniform absorption vs 'p' dopant area density for various aperture areas and $\tau_{bulk} = 500\mu s$

it has been shown that unless only a low depth of modulation is required by the $1cm^2$ p-i-n device, a change in transmission of up to 10%, an alternative form of laterally spreading the injected current across the entire aperture is required by the modulator, or a smaller aperture area must be used.

The thickness of the 'n' layer is the least important parameter discussed so far. However, the absorption resulting from its doping should be low to avoid reducing the 'on' state transmission. Since the electron absorption cross section is $1/16^{th}$ of that for holes, minimising the 'n' layer absorption presents little problem. In the 'off' state the 'n' layer injects electrons to the intrinsic region, and the rate of electron injection at the 'n' doped end must equal the rate of hole injection at the 'p' doped end. Unequal doping concentrations at the 'p' type and 'n' type ends results in the diode compensating for this by dropping a larger voltage across the lower-doped region to equalise the injection rates. However, to achieve uniform injection across the aperture, the resistance of the 'n' doped layer should be the same as that of the 'p' doped layer, to mirror its carrier injection. In germanium, since the ratio of electron to hole mobility is $3900/1900 = 2.05$, the 'n' layer can have this fraction of the 'p' layer area doping density. At this limit the absorption is $1/(2.05 \times 16) = 3\%$ of that in the 'p' layer. So if the 'p' layer alone

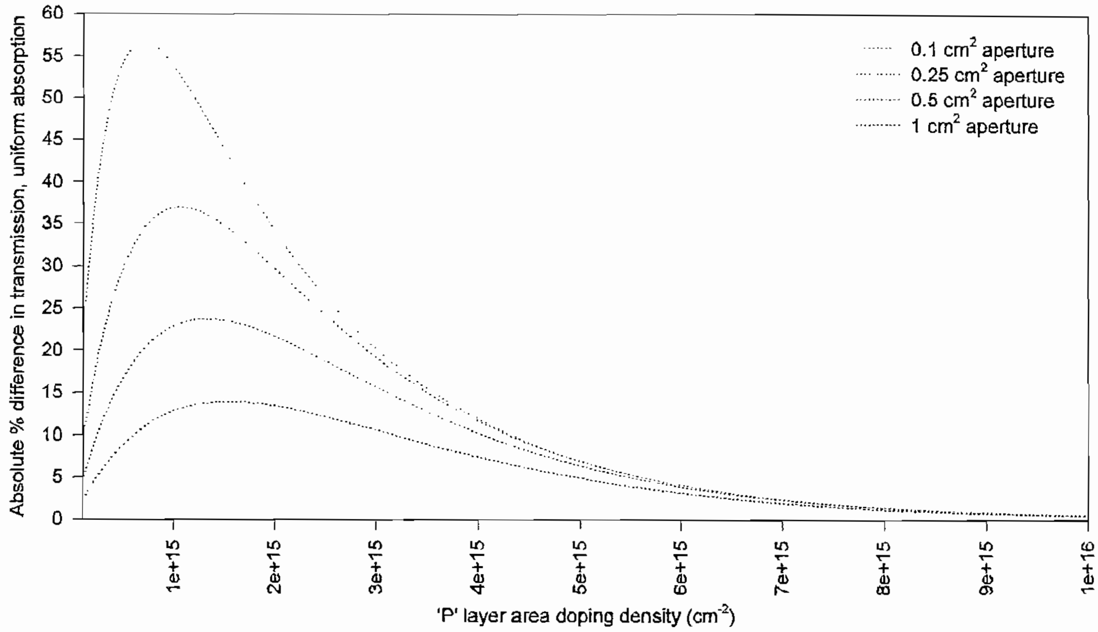

Figure 8.16: Depth of modulation for uniform absorption vs 'p' dopant area density for various aperture areas and $\tau_{bulk} = 1ms$

gave 90% transmission, the 'n' layer gives 99.7% transmission. In practice it would be advantageous to use a higher 'n' layer area carrier density than this so that injected holes travel on a trajectory pointing slightly toward the centre of the aperture, thus improving the uniformity.

In practice, doping germanium would probably involve over-doping the region and polishing the surfaces until the required 'on' state transmission (or surface resistivity) is achieved. A typical maximum layer thickness for the 'n' or 'p' region is in the order of $0.5\mu m$ for ion implantation, and a few μm for a diffused layer. To obtain the required area doping density of $\sim 10^{15} cm^{-2}$ (from Figures 8.14 to 8.16) a 'p' or 'n' layer thickness in the order of $100\mu m$ is required to give a volume doping density of $10^{17} cm^{-3}$ to avoid significant reduction in layer mobility. For a thermally-diffused 'p' type layer, both indium and gallium have impractically low thermal diffusion coefficients. Boron has a much higher diffusion coefficient so might be of use following ion implantation. For the 'n' type diffusion, either arsenic or phosphorus could be used. For the arsenic and phosphorus an intermediary compound containing the dopant would be deposited on the surface prior to thermal diffusion.

The requirement for two such deep diffused layers is made easier in the presence of equal, or very different diffusion coefficients for the two dopants. For example at $850°C$ the diffusion coefficient [30] of arsenic is 35 times that of boron and requires a diffusion time of $\sim 4.5h$ to give a concentration $10^{17}cm^{-3}$ at a depth of $100\mu m$. In this case the arsenic diffusion would be preceded by the boron diffusion which takes $\sim 140h$ at $850°C$ for the same depth and concentration. These figures are approximate, and assume infinite-source diffusion giving an $erfc$ diffused profile. Alternatively, epitaxial growth is routinely used to grow layers of $50\mu m$ [95]. This offers a much faster process with more abrupt doping profiles, which could be used, providing the layer mobility remains high.

A quantitative design for 23% depth of modulation is now outlined. If the modulator has a circular aperture of $0.25cm^2$, and a 'p' layer doping density of $10^{15}cm^{-2}$ (Figure 8.15), then 'p' and 'n' layer widths of $100\mu m$ have volume doping densities of $10^{17}cm^{-3}$, giving only a slight reduction in layer mobility. The intrinsic layer thickness is set by 'off' state operation to be equal to the diffusion length L_a. If the germanium has a bulk carrier lifetime of $500\mu s$, an intrinsic layer width of $1.82mm$ is required (Equation 8.5). If this 'intrinsic' region were very slightly 'n' doped (ν doped), the reduced room temperature hole density reduces the hole-dominated increase in absorption arising from thermal electron-hole pair generation, and hence reduces the temperature-sensitivity of the 'on' state transmission. Making the intrinsic region ν doped with resistivity of $40\Omega cm$ using a doping density of $3.1 \times 10^{13}cm^{-3}$ would assist this via hole-density suppression but not serve to significantly alter the injection efficiencies from the higher doping density end regions. Under these assumptions the 'on' state transmission is 58.7% and the 'off' state transmission at which uniformity of absorption across the aperture ceases to be maintained, is $58.7\% - 22.9\% = 35.8\%$. In practice, uniformity would no longer be attained at a slightly higher transmission due to the assumption of negligible drop in mobility. This is reported to drop [95] from its intrinsic value by a factor of 2.5 at a doping density of $10^{17}cm^{-3}$. When this is accounted for the transmission in the 'on' and 'off' states is 58.7% and $58.7\% - 10.5\% = 48.2\%$ respectively, highlighting the requirement for even thicker 'p' and 'n' layers. The 'off' state transmission for this device immediately adjacent to the contact is given vs total device current in Figure 8.17. This device has a maximum $1/2\pi\tau_{ambipolar}$ switching frequency of $318Hz$.

8.1.5 Possible design alternatives for a p-i-n modulator

This section reviews some variations in the design of the p-i-n type modulator. The p-i-n structure remains the same, although different injection methods that offer more

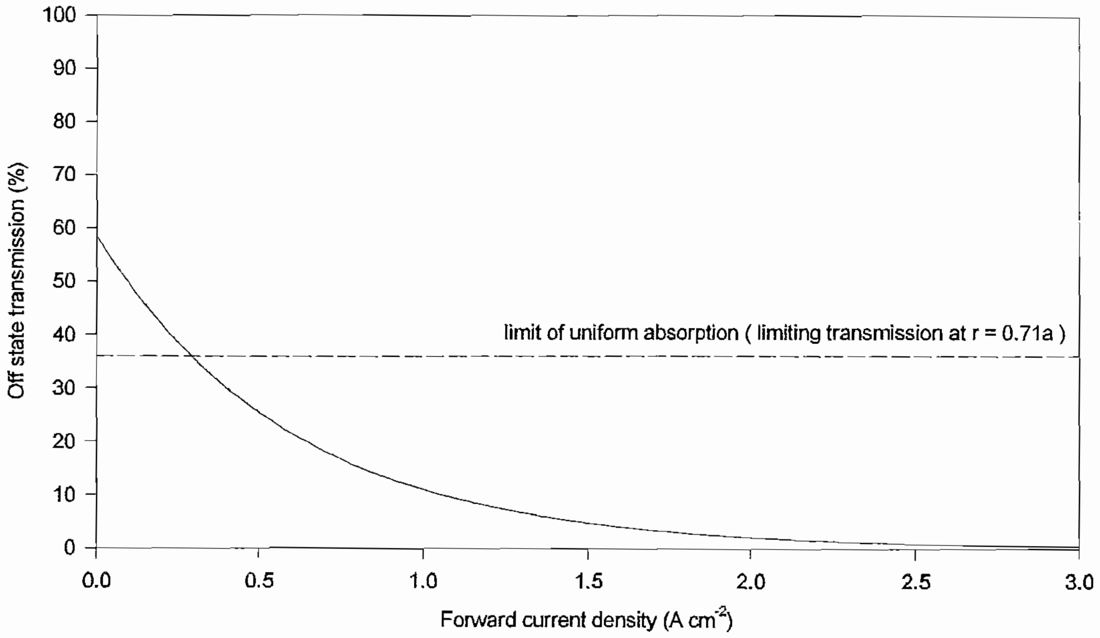

Figure 8.17: 'Off' state p-i-n modulator transmission vs current density immediately adjacent to electrical contact only

uniform hole injection across the aperture are considered.

Figure 8.18(a) shows the p-i-n structure considered thus far. Figure 8.18(b) shows a p-i-n structure with a grid of electrical connections on the surface. The same injection process is used as with (a) except this offers the possibility of controlling the uniformity of current injection by spreading the current distribution over the aperture using the deposited metal grid. This also offers the possibility of spatially varying the absorption by turning on and off individual regions of the aperture. This structure requires 3-dimensional modelling to determine the effect on the modulation transfer function of the deposited grid, and what grid pattern offers optimal performance. Figure 8.18(c) shows a p-i-n structure but with a heavier-doped 'p' type regions diffused into the 'p' layer. This offers the benefits of (b) but without a surface metallisation layer. In some of these solutions a similar injection structure would be applied to the 'n' side if required.

8.2 Electron impact excitation requirements

If electron impact excitation were used to generate the holes required for the induced absorption, an electron source with accelerating voltage in the order of $2kV$, and possi-

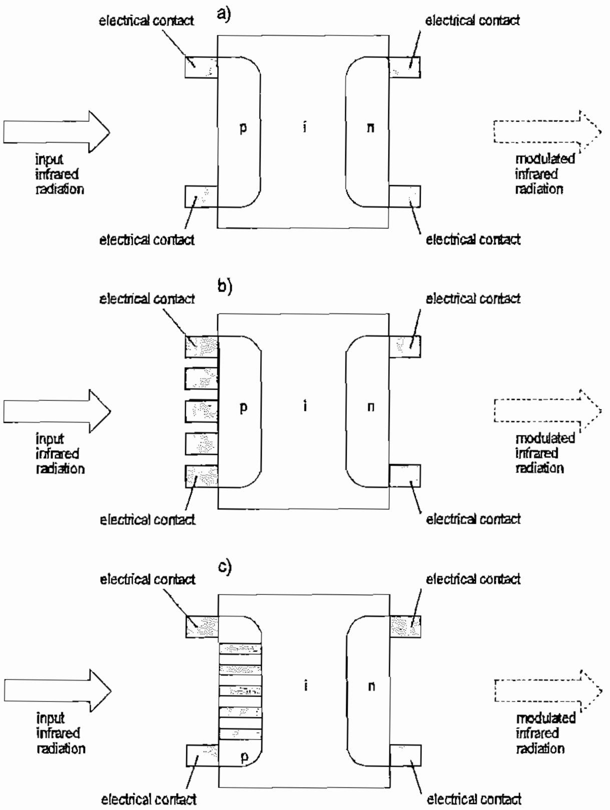

Figure 8.18: Possible p-i-n type structures for electrically-pumped modulator

bly a coil to generate a steering magnetic field would be required. The electron beam can operate at higher voltage and lower current, since a higher accelerating voltage produces more electron-hole pairs in the germanium as calculated at the start of Section 6. The main limitations on the voltage are the generation of x-rays and the practicality of high voltages. Ideally, electrons should be generated in the germanium just away from the front surface at which recombination occurs. Generation of carriers more than 10% of a diffusion length from the front surface reduces the effect of surface recombination but requires immense accelerating voltages that are likely to permanently damage the crystal structure. There is little advantage in terms of reduced sensitivity to surface recombination gained by generating carriers a few microns further from the surface, and the only disadvantage of moderate-range carrier generation is the requirement for a higher accelerating voltage. As with the optically-excited modulator the surfaces of the electron-impact modulator should be etched in order to reduce the rate of surface recombination. Earlier in this section it was calculated that an accelerating voltage of $2kV$ with a current density of $10.7mA\ cm^{-2}$ was required to achieve 100% to 10% depth of modulation. This did not account for attenuation of the electron beam by the AR coating. Electron beam damage to single-crystal ZnS layers has been reported at $100keV$ [135], setting an upper limit to the accelerating voltage. CRT monitor displays with ZnS-based phosphor pixels currently use voltages in excess of $15kV$, which is therefore unlikely to damage the coating. However, electron penetration depths at voltages of $5keV$ and $20keV$ of $\sim 0.1\mu m$ and $\sim 1\mu m$ have been reported [136] in ZnS, and the required AR coating thickness (Section 6.5.2) is $1.1\mu m$. The required accelerating voltage is therefore in the order of $80keV$, or a Fresnel loss at the front air-germanium interface must be accepted. The electron acceleration unit faces the image-side of an AR coated piece of long bulk carrier lifetime germanium, and the germanium transmission is modulated in response to changes in electron beam current.

8.2.1 Possible design structures for an electron-impact modulator

This section outlines various modulator structures which could be used in the design of the electron-impact modulator.

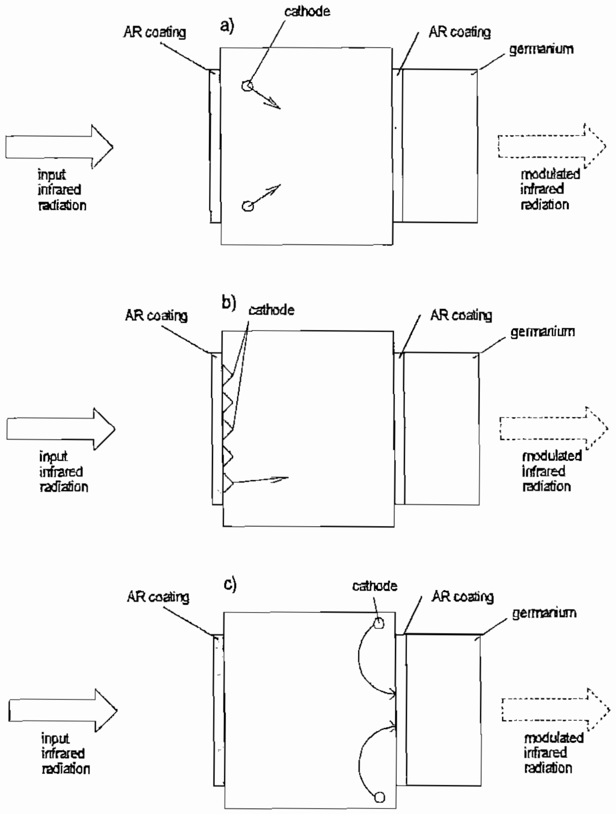

Figure 8.19: Possible structures for the electron-impact electrically-pumped modulator

Figure 8.19 shows three possible injection geometries for electron-impact excitation of the germanium. The central box is a vacuum tube, within which the high velocity electron generation takes place. Antireflection coatings are used on external surfaces to essentially give 100% transmission in the 'on' state. Figure 8.19(a) shows electrons from a cathode being accelerated across a vacuum region before impinging on the germanium element. A photocathode or field emission cathode is preferable to a thermal cathode as the infrared emission from a hot cathode would simply pass through to the detector. Figure 8.19(b) shows a similar arrangement to (a) except with an array of micromachined sharp points acting as field emitters, mounted on the infrared transparent cathode. Figure 8.19(c) uses a thermal emission cathode to generate electrons, which are directed onto the germanium using electric or magnetic fields. The latter arrangement permits shielding of the detector from infrared radiation from the hot cathode. The design of these structures requires attention to uniform electron beam generation, and minimising waste heat from the process, which would simply be seen as a background signal on the detector. Using the electron-impact technique, as with the optically-excited modulator (in contrast with the electrically-excited device) avoids the tradeoff between reduced 'on' state transmission and more uniform excitation.

8.3 Demonstration of modulation via carrier injection into a p-n junction

As a first stage to demonstrate the potential of electrically-based hole injection, a high power germanium p-n diode was reconfigured for use as a small-area modulator. The diode (GD30R49123), supplied by Germanium Power Devices Corporation USA was opened and the germanium die de-soldered. The die was then soldered to two wires and set in epoxy resin. The combination was polished to provide two optical flats on parallel chords of the die, through which a probe beam was passed. The transmission of the combination was monitored using a cw $10.6\mu m$ CO_2 probe beam and MCT detector while the device current was pulsed. Coherent detection using a phase sensitive detector (PSD) ensured baseline-transmission-shift effects, possibly of thermal origin, were not measured by the setup, unless these were coherent with the electrical modulation. The MCT detector was required to detect the low-intensity probe beam passing through the sample. The test device construction is shown in Figure 8.20.

The induced depth of modulation at $191Hz$ was measured as a function of peak pulsed current. These readings were normalised to the zero-current transmission, which was determined using a reference mechanical chopper, to give the % depth of modulation. The absolute transmission of the region probed by the diode is not known. The depth of modulation is shown in Figure 8.21 and the transmission was extinguished by a current of $1200mA$.

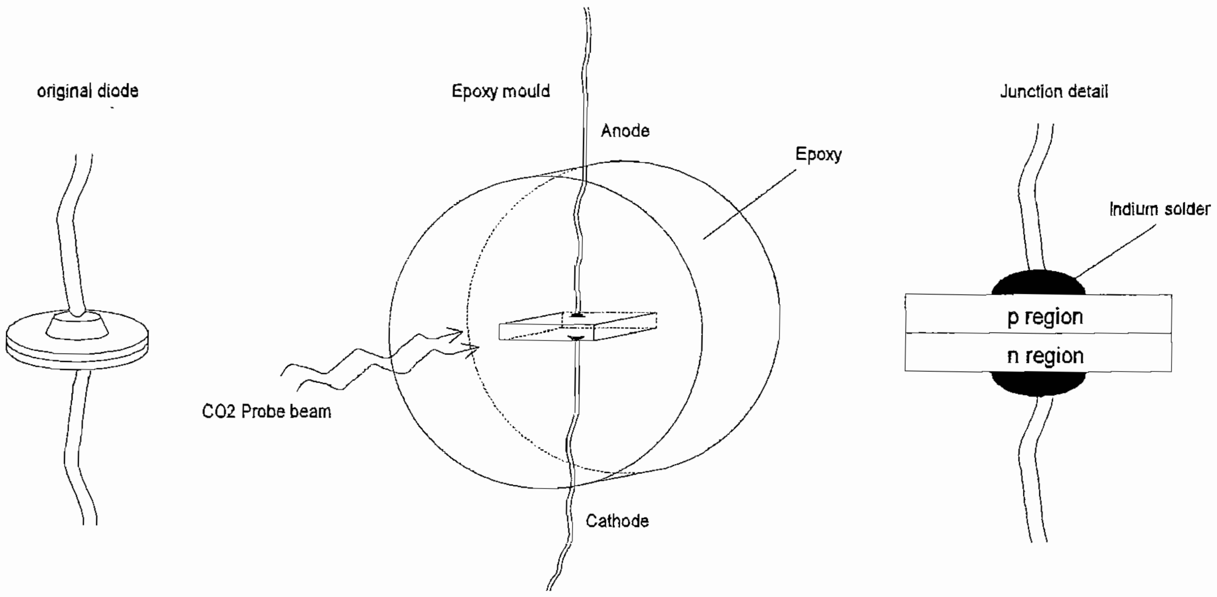

Figure 8.20: Test device reconfigured from a high power germanium diode

Figure 8.21 shows that for low current the depth of modulation (upper curve) increases as the negative exponential of the peak current. The absorption coefficient (lower curve) is proportional to the hole density, which is proportional to the peak drive current. At low peak pulsed current the device transmission reduces as $e^{-constant \cdot current}$. The rise and fall times of the modulation were verified as being $< 100\mu s$; too fast for significant contribution to the modulation from thermal effects. At higher currents ($> 800mA$) the deviation from linearity in induced alpha is due to another contribution to absorption, and the depth of modulation deviates from the single-exponential as it approaches 100%. This is unlikely to be thermal in origin since the thermal time constant of the device with its good thermal-insulation is much longer than that observable at the modulation frequency used. The deviation from linearity with current density is unlikely to be present in a real modulator.

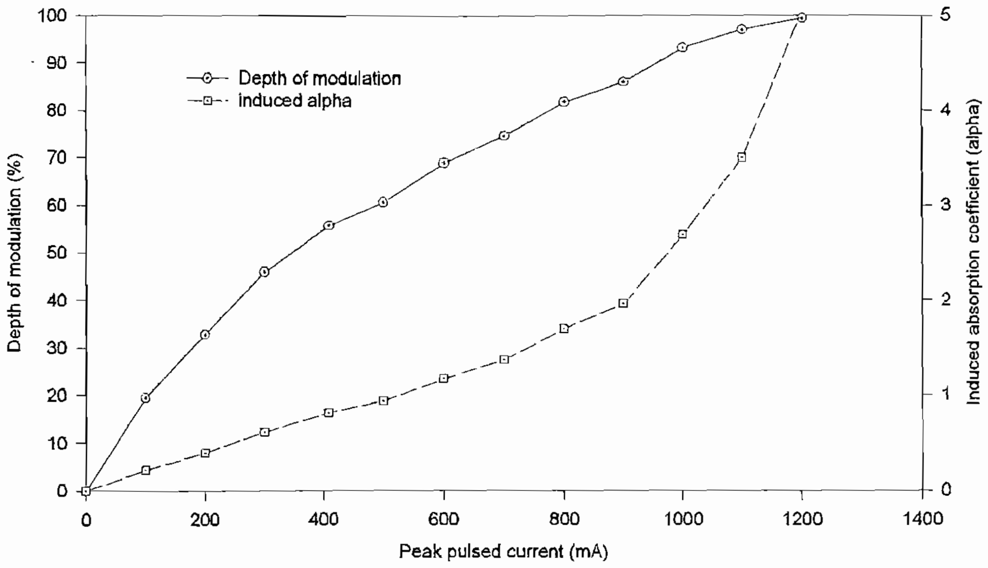

Figure 8.21: Depth of modulation of modified germanium diode parallel to junction plane

8.4 Conclusions on the electrically-pumped modulator

This section has considered the primary design constraints involved in the design of an electrically-pumped modulator. This has been from the aspects of p-i-n and electron-impact excitation geometries.

With the p-i-n style geometry, carrier generation is remote from the surfaces. This, combined with the electric field across the device during forward conduction, keeps carriers away from the surfaces so they decay with their bulk carrier lifetime. The maximisation of available carrier lifetime offers high modulator efficiency without needing to etch the germanium surfaces. A relatively low current density is therefore required to obtain a high depth of modulation within the aperture. During the transmitting 'on' state, nearly all the absorption occurs in the 'p' doped layer. The tradeoff between maximising the 'on' state transmission of this layer and obtaining uniform absorption across the aperture in the 'off' state has been demonstrated by a simplified model. The tradeoff depends on the resistance of the 'p' type layer, which depends on the doping density in this region. A higher area doping density provides more-uniform absorption across the aperture in the 'off' state but a higher level of residual absorption in the 'on' state. Volume doping densities above $\sim 10^{17} cm^{-3}$ are impractical due to the reduced layer mobility and subsequent increase in layer resistance. The simplified model has shown that a simple planar-injection p-i-n device is only capable of providing uniform induced absorption across the entire aperture for depths of modulation of a few tens of percent in absolute transmission if the aperture is reduced considerably. This is also at the expense of a considerable reduction in 'on' state transmission. The 'p' and 'n' layer widths for such a structure were necessarily wide to reduce the volume doping density, and although achievable via long thermal diffusion times could alternatively be provided by epitaxial growth. More exact determination of the uniformity would be provided by a full 3-dimensional carrier injection model, showing the extent of this tradeoff, and how alternative, non-planar or surface current-spreading, injection geometries could be used to improve 'off' state uniformity without such cost to the 'on' state transmission. Some possible geometries of achieving this have been reviewed.

The required excitation current for a reasonable depth of modulation via electron-impact excitation has been predicted, and different geometries which achieve this have been considered. One of the more attractive ideas uses a magnetic field to steer the electron beam onto the germanium. This permits shielding of the detector from the electron source, which will be hot if a thermal cathode is used. The next stage in this area of work involves the generation of an electron beam with uniform current density over the aperture.

A demonstration has shown the operation of an electrically-pumped modulator using a reconfigured p-n junction diode. This gave a high depth of modulation, departing from a linear increase in absorption only at high current density. The 'on' state transmission of the junction was not determined, although this was low. This simple yet effective demonstration of modulation of a beam perpendicular to the junction has shown the potential for an electrically-pumped modulator.

Chapter 9

Conclusions and future work

9.1 Conclusions

The work presented in this thesis has described the development, operation and optimisation of the light to heavy hole inter-valence band absorption process in a practical modulator. This offers solid state modulation in the infrared thermal imager band, extending the applications of pyroelectric array based cameras through the removal of the rotating chopper blade. No other modulator offers comparable performance in terms of polarisation-insensitive broad optical bandwidth modulation over a large aperture and low f-number at the power density required for its operation.

Chapter 2 reviewed methods of inducing absorption in the infrared, showing that the light to heavy hole transition process offered the highest potential for the modulator. In the more common materials, germanium was the only material to possess the required properties and was therefore the only material of interest in this work. Chapter 3 analysed the electrical and optical properties of germanium relevant to the modulator's operation, forming the basis of the modelling in Chapter 4. The effective carrier lifetime is of utmost importance in determining modulator's efficiency, and this depends on the bulk and surface contributions to recombination. This analysis showed that the bulk carrier lifetime and surface recombination velocity could be treated as constants at the excess carrier densities typically encountered during the modulator's operation. Bulk recombination in high purity germanium proceeds almost entirely through Shockley-Read-Hall processes involving one or more energy levels within the bandgap. Trapping at room temperature in HPGe is negligible, and Auger processes only become significant (compared to a $1ms$ lifetime from other processes) at carrier densities above $\sim 10^{17} cm^{-3}$. The surface recombination velocity strongly affects the carrier density in the modulator's 'off' state, reducing the modulator's efficiency. This is due to the presence of a polish-damaged surface layer and lack of a uniform oxide. Etching removes some of the damage but primarily it increases the surface energy band bending which greatly reduces the surface recombination velocity. Consideration of the diffusion of the carrier plasma generated by optical excitation showed that it could be treated as having a homogeneous ambipolar diffusion coefficient, since it is electrically neutral over the Debye length, which (at the carrier densities encountered) is much less than a diffusion length. The mobility was treated as a constant at fixed temperature in this chapter since the carriers were not degenerate. In order to be an effective modulator, slightly n-type germanium is the optimal material as the reduced hole density provides high 'on' state transmission.

The constant bulk carrier lifetime, surface recombination velocity and diffusion coefficient parameters were used throughout Chapter 4 to model carrier diffusion following their generation by a laser source. One-dimensional modelling showed that optimisation of the induced absorption for a given bulk carrier lifetime required a surface recombination velocity of $\sim 3ms^{-1}$. A long bulk carrier lifetime offers more efficient operation, and this primarily determines the modulator's switching speed. The application requires modulation at a few $100Hz$, for which a bulk carrier lifetime of $1ms$ is sufficient. Faster modulation is achievable through higher rates of bulk and surface recombination, at the expense of a higher power density for a given level of absorption. The assumptions that the diffusion coefficient and bulk carrier lifetime were independent of the excess carrier densities encountered during usual modulator operation were justified using 1-D diffusion model simulations.

The one-dimensional diffusion model was extended to model the microwave reflectance of excited samples. This enabled the extraction of the bulk and surface carrier parameters, the effects of which are more easily separated from reflectance measurements at microwave wavelengths. At the $10GHz$ frequency used in later experiments, absorption by the plasma dip was negligible, and the total reflectance is dependent on the interference between contributions from back and front surfaces. The contributions depend non-linearly on the volume carrier density of the distributed plasma, as opposed to the linear dependence of the absorption coefficient on the area carrier density which is measured via infrared transmission experiments. The solutions to the diffusion equations predicting the carrier distribution were extended to those for gaussian and square-edge shaped illumination functions, limited in one and two dimensions, and later used in experiments validating predictions of the required values for these parameters. When diffusion is accounted for in more dimensions, the extent of lateral diffusion is reduced in any given direction due to the extra directional freedom, and the effective carrier lifetime seen by a probe pulse in the centre of the excited region is also reduced. These predictions were observed experimentally. Extra directional freedom increases the modulator's switching rate, and increases the definition of a sharp absorbing edge generated on the aperture compared to simple diffusion-length approximations.

Chapter 5 detailed the experimental results which validated the models and parameter assumptions of Chapters 3 and 4. Results were given for three samples, to enable their comparison. The temporal carrier decay, measured via the transmission of a $10.6\mu m$ CO_2 laser probe beam was used with the one-dimensional diffusion equation model in Chapter 3 to extract the S and τ_{bulk} carrier parameters based on examination of the initial and final decay constants. Blackbody probe experiments were used to measure the transmission of an optically-excited region, and revealed a shorter lateral diffusion length than predicted by modelling. A reduced lateral diffusion coefficient was postulated, and supported by literature which showed that this occurs in the presence of practical levels of surface energy band bending due to enhanced surface scattering and carrier confinement in the surface potential well. The measured lateral diffusion coefficient was found to be in the order of $1/2$ of that in bulk (non-degenerate) material. The microwave reflectance results were used in combination with the model's predictions to extract carrier parameters. Practical difficulties in uniformly illuminating the germanium are likely to have introduced experimental errors in these experiments. The results from the three techniques for the same samples were compared, showing that spatially-restricted optical excitation of samples gave a reduction in apparent lateral diffusion coefficient, and this explained the discrepancy seen in the blackbody probe measurements. Results from the microwave reflectance and CO_2 laser probe experiments gave results which are likely to have been complicated by the presence of finite samples, thermal effects and nonuniform excitation, although the technique remains accurate and valid. When samples in the blackbody probe experiments were excited with half the power density used to obtain the reported results, nonlinear carrier recombination processes such as Auger recombination were not evident or at the carrier densities incurred, any effect was in a saturation regime. No evidence was found from the temporal CO_2 laser probe decay experiments at different excitation power densities to suggest that Auger recombination or trapping processes were significant. The carrier parameters extracted from these experiments showed that the desired few ms^{-1} surface recombination velocity had been attained by etching.

The demonstration of an optically-pumped area modulator in Chapter 7 combined the theory of its operation with its optimisation in the areas addressed in Chapter 6. The modulator was optimised by maximising the effective carrier lifetime, increasing the 'on' state transmission to effectively 100% through use of AR coatings, increasing the fraction of absorbed excitation power, and increasing the excitation wavelength. The use of etched HPGe ensured a sufficiently long effective carrier lifetime for modulation at a few $100Hz$, whilst giving a reasonable response time. Long bulk carrier lifetime HPGe is readily available due to its use in nuclear detectors. Two successful etchants were identified which provide both a low rate of surface recombination and a planar surface.

Optical excitation of the modulator currently favours use of $980nm$ laser diodes, which are moderately priced due to other pumping applications. The optical power required by the modulator was not optimised; instead uniformity of excitation was aimed-for to produce uniform induced absorption. The uniformity was not as ideal as that predicted due to the discrepancy between the power emission profiles of 'ideal' diodes and those of real devices. It appears that uniformity in diode bar emission is a technology problem, and that a future modulator would do better by not relying on obtaining ideal diodes, but in using profile 'scrambling' optics or another illumination geometry to excite the germanium uniformly, such as an array of optic fibres emanating from one laser bar. Zinc sulphide quarter-wavelength antireflection coatings were deposited on the modulator, with the aim of AR coating at both the modulated 8 to $14\mu m$ and pump regions. These operated successfully in the modulated region, but, as predicted in Chapter 6, success at the pump region relied on obtaining spot wavelength laser diodes. Spot wavelength devices were not obtained, although calculations of the induced absorption showed these were also successful at the pump wavelength. Film adherence posed no problem, and the coatings did not degrade the depth of modulation with time. This type of single-layer AR coating is however not well-suited to dual AR coating at such a distant pump wavelength due to the narrow spectral separation of fringes at this shorter wavelength, and the dependence of reflectivity on incidence angle. The required accuracy in film deposition is attainable but the variation in reflectivity over a reasonable range of incidence angles produced by such films, combined with the difficulty in procuring spot-wavelength laser diodes at a given drive current, makes this type of film unsuitable for this latter purpose. In order to AR coat over these two spectral bands and over a suitable range of incidence angles, a custom multilayer coating is required, and methods of achieving this are in the literature. The optically-pumped modulator is currently a commercial viability. Ideally the systems designers would prefer a lower total power consumption for portable devices, whilst for many applications the power budget is acceptable.

The design constraints affecting construction of an electrically modulated p-i-n style modulator have been reviewed, and a design for an electrically-pumped area modulator has been outlined. With the p-i-n modulator, holes decay with the bulk carrier lifetime since their densities are low at the germanium surfaces. Full use is made of the long bulk carrier lifetime in high purity germanium without the need for etching. The independence of the effective carrier lifetime on the surface lifetime in this type of device offers increased efficiency. The strong tradeoff between 'on' state transmission and uniformity of absorption across the aperture has been revealed by a simplified model. This showed that a simple $1cm^2$ planar injection p-i-n modulator is only capable of providing uniform absorption across the entire aperture for a few % depth of modulation. Further increase in device current beyond this limit reduces the transmission in the immediate vicinity of the contact electrode, whilst that in the centre of the aperture effectively saturates. A significant increase in depth of uniform modulation can be attained by reducing the modulator area, although the optics in the application must be modified to accept this. The p-i-n device also requires very thick doped regions in the order of $100\mu m$ to avoid degrading the carrier mobility and subsequently increasing the layer resistance. Thus to provide uniform absorption across the entire aperture for reasonable depths of modulation, alternative methods of laterally spreading the current over the aperture must be investigated. Some methods of achieving this have been discussed.

The operation of an electrically-pumped modulator has been demonstrated using a reconfigured high power germanium diode, in which the transmission parallel to the junction plane was virtually extinguished with a moderate current. This proof of principle offers considerable hope in producing a functional area-based modulator. Several structures for this purpose, achieving modulation perpendicular to the junction plane, have been suggested, although time did not permit their construction. A current density of $7.9A\ cm^{-2}$ was predicted for 100% to 10% transmission switching. This was based on an optically-pumped sample in which surface recombination was present so the actual current density will be much lower. This current density is not unreasonable, and although an optically-pumped device is attractive, an electrically-pumped device offers improved efficiency, and a simpler system design.

9.2 Future work

Continuation of this work is divided into the optically-pumped and electrically-pumped areas, with some overlap. With the optical device, system efficiency can be improved through the optical excitation mechanism. This will use a custom-designed optic-fibre bundle to uniformly illuminate the aperture, or lensed laser diode bars to maintain excitation uniformity whilst only exciting the germanium aperture. A full polarisation analysis is required using an optical design package to properly predict the resulting spatial illumination. Equally, a double-surface absorbing modulator is attractive. This ensures high illumination efficiency, without the power loss associated with coupling an optic fibre to a laser diode package.

Although surface recombination has been controlled through etching the germanium, the possibility of generating a wider surface bandgap through silicon implantation to achieve the same effect should be investigated further. The omission of the etching stage offers a more controlled process than is presently used, and may reduce the environmental dependence of the surface recombination velocity. Ideally an excitation wavelength longer than $980nm$ will be used in the modulator to increase the excitation efficiency, although these are currently expensive and of limited availability.

Another area of interest is the pressure-dependence of the hole absorption cross section. The aim is to see if an increase in hole absorption cross section in the thermal imager band can be achieved by applying pressure along a particular direction. This requires calculation of the resulting average absorption cross section over all crystal directions, and determining the benefit offered to the modulator. A practical approach involves cutting germanium cubes with particular crystal orientations and using a steel mould which would be heated and used to compress the cubes along particular crystal directions. The relative induced absorption of the stressed crystals would then be compared. If the starting material were 'p' type germanium, comparison of the transmission spectra before and after stressing would determine the relative change in absorption cross section and any spectral shift of the heavy hole to light hole absorption band. Birefringence will be introduced at high stress levels.

Work in the area of the electrically-pumped modulator requires further modelling of the excitation geometries outlined by this thesis. Much background research on its electrical operation is available from the design of high power diodes, although this application's requirements are made more difficult by the need for an infrared-transmitting 'p' type layer. The use of a deposited patterned metal grid on the germanium surface to assist lateral spreading of the injected current will be important in generating the absorption across the large aperture. This requires modelling of the injected-carrier profiles, the absorption, and thermal analysis. The deposition of electrodes on the surface requires an analysis of the modulation transfer function regarding its suitability to the application. Initially much insight into this area of work would be obtained by building a trial device and thus revealing the dominant aspects of its design. This promises to be an interesting development in the germanium modulator.

Appendix A

The solution to the continuity equation for a temporally square pulse of laser excitation is given here. The time-dependent continuity equation for carrier diffusion is given by:

$$\frac{\partial n(x,t)}{\partial t} = D_a \frac{\partial^2 n(x,t)}{\partial x^2} - \frac{n(x,t)}{\tau_{bulk}} \tag{A.1}$$

where n is the excess carrier density, and x and t represent displacement and time variables following Figure A.1.

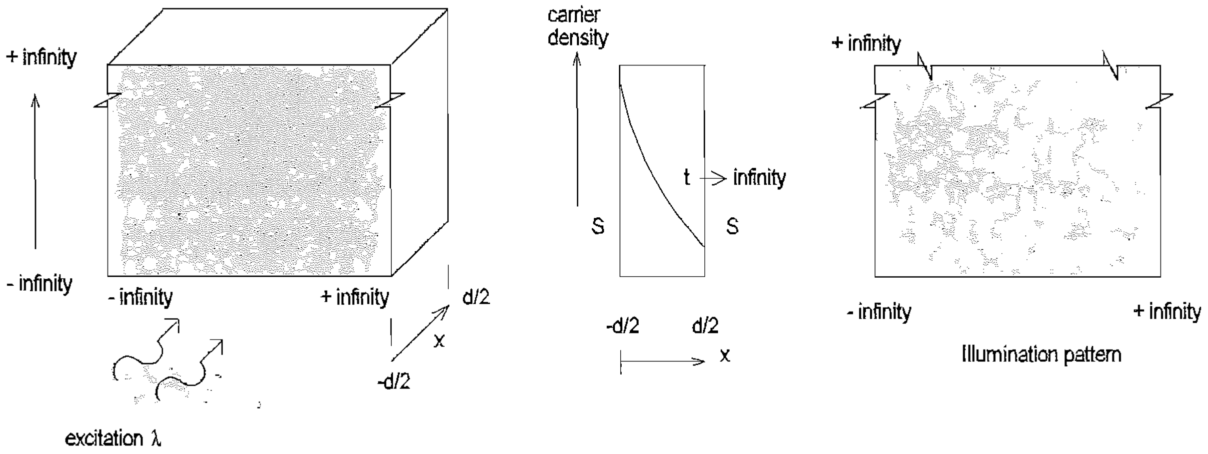

Figure A.1: Excitation geometry for a finite length germanium sample

The carrier generation term from the laser excitation does not appear in Equation A.1, and is instead assumed to be an impulse function which is used as an initial condition. Solution of Equation A.1 therefore gives the impulse response. The response to a temporally square illumination pulse, as required by the physical situation, is found by convolving the impulse response $n_i(x,t)$ with a square pulse function. Initially the impulse response is determined. The generation term is:

$$G_i(x,t) = N_0 e^{-\alpha_{ill}\cdot\left(x+\frac{d}{2}\right)} \cdot \delta(t) \tag{A.2}$$

and the initial carrier distribution is given by:

$$n(x,t=0) = N_0 e^{-\alpha_{ill}\cdot\left(x+\frac{d}{2}\right)} \tag{A.3}$$

$$N_0 = \frac{\alpha_{ill} P_{Excabs} \lambda_{exc}}{hc} \tag{A.4}$$

P_{Excabs} is the absorbed excitation power density, λ_{exc} is the excitation wavelength, h is Planck's constant and c is the speed of light. N_0 represents the carrier generation rate at the surface in cm^2s^{-1}.

The boundary conditions represent the continuity equation between the surface recombination velocity and carrier density gradient at the two surfaces, and are given by:

$$D_a \frac{dn}{dx}\bigg|_{x=-\frac{d}{2}} = S \cdot n\left(x = -\frac{d}{2}\right) \tag{A.5}$$

$$D_a \frac{dn}{dx}\bigg|_{x=\frac{d}{2}} = -S \cdot n\left(x = \frac{d}{2}\right) \tag{A.6}$$

Solution Equation A.1 is given by the separation of variables method, for example [99], [100]. If the solution is assumed to be of the form:

$$n(x,t) = X(x) \cdot T(t) \tag{A.7}$$

Then substitution into Equation 4.21 gives:

$$\frac{1}{T}\frac{dT}{dt} + \frac{1}{\tau_{bulk}} = \frac{D}{X}\frac{d^2X}{dx^2} = \psi \tag{A.8}$$

in which ψ must be a constant, giving the following separated differential equations:

$$D\frac{d^2X}{dx^2} - \psi X = 0 \tag{A.9}$$

$$\frac{dT}{dt} = T\left(\frac{1}{\tau_{bulk}} - \psi\right) = 0 \tag{A.10}$$

From Equations A.9 and A.10, one such solution is:

$$n(x,t) = e^{-\frac{t}{\tau_{bulk}}} \cdot [Ae^{-D_a\alpha_1^2 t}cos(\alpha_1 x) + Be^{-D_a\beta_1^2 t}sin(\beta_1 x)] \tag{A.11}$$

thus a linear superposition of such solutions also satisfies the diffusion equation, and is needed to satisfy the boundary conditions. This is given by:

$$n(x,t) = e^{-\frac{t}{\tau_{bulk}}} \sum_n \cdot [A_n e^{-D_a\alpha_n^2 t}cos(\alpha_n x) + B_n e^{-D_a\beta_n^2 t}sin(\beta_n x)] \tag{A.12}$$

The separate substitution of the n^{th} sine and cosine terms in Equation A.5 solves for the α_n and β_n coefficients respectively, given by the periodic series:

$$cot\left(\frac{\alpha_n d}{2}\right) = \frac{D_a \alpha_n}{S} \tag{A.13}$$

$$tan\left(\frac{\beta_n d}{2}\right) = -\frac{D_a \beta_n}{S} \tag{A.14}$$

which also satisfy the second boundary condition, Equation A.6. The roots of Equations A.13 and A.14 are given graphically in Figure A.2.

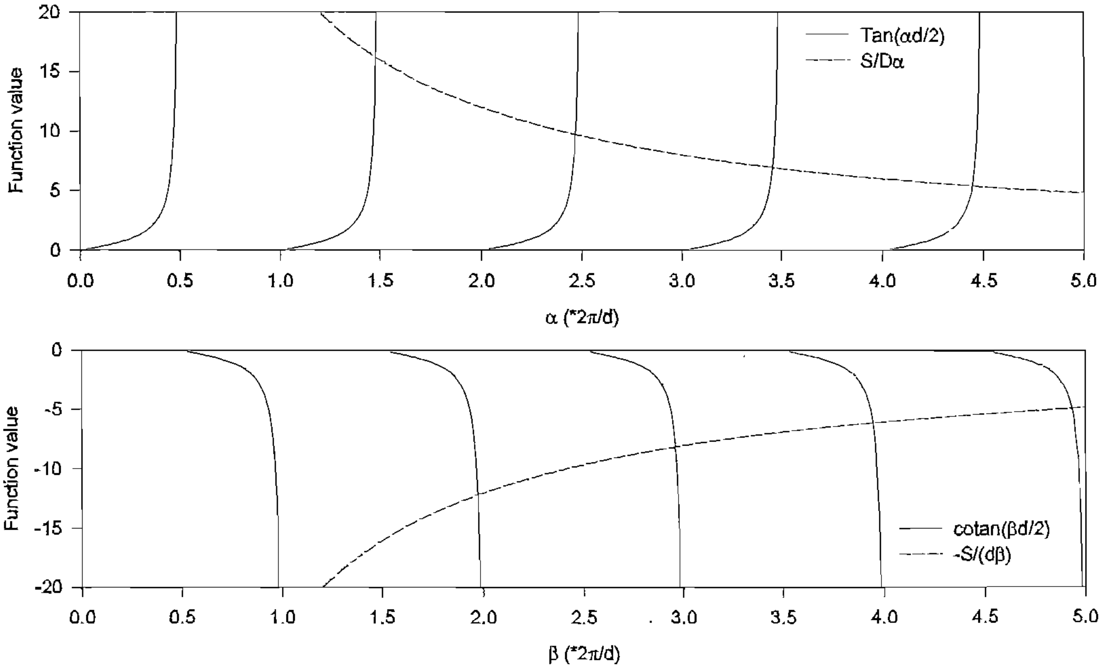

Figure A.2: Graphical solution of α_n and β_n roots

The A_n and B_n coefficients are determined by substitution of the initial condition Equation 4.23 into Equation 4.28, giving:

$$A_n = \frac{2N_0\alpha_{ill}\alpha_n}{(\alpha_n d + sin(\alpha_n d))(\alpha_{ill}^2 + \alpha_n^2)} \cdot \left[\alpha_{ill} cos\left(\frac{\alpha_n d}{2}\right) \cdot (1 - e^{-\alpha_{ill} d}) + \alpha_n sin\left(\frac{\alpha_n d}{2}\right) \cdot (1 + e^{-\alpha_{ill} d})\right] \tag{A.15}$$

$$B_n = \frac{2N_0\alpha_{ill}\beta_n}{(\beta_n d - sin(\beta_n d))(\alpha_{ill}^2 + \beta_n^2)} \cdot \left[\beta_n cos\left(\frac{\beta_n d}{2}\right) \cdot (1 - e^{-\alpha_{ill} d}) - \alpha_{ill} sin\left(\frac{\beta_n d}{2}\right) \cdot (1 + e^{-\alpha_{ill} d})\right] \tag{A.16}$$

which, with Equations A.12, Equations A.13, and Equations A.14 give the solution for impulse excitation. To determine the effect of square pulse excitation (or any shape pulse), the impulse response must be convolved with the excitation pulse function. For a square pulse of period T this gives two solutions, one for the duration of the optical pulse, and one for the decay. These are given by:

$$\begin{aligned} n(x,t) = \frac{1}{T}\sum_n \quad & \Big[\frac{A_n \cdot cos(\alpha_n x)}{(D_a\alpha_n^2 + \frac{1}{\tau_{bulk}})} \cdot \Big(1 - exp\Big[-(D_a\alpha_n^2 + \frac{1}{\tau_{bulk}})t\Big]\Big) + \\ & \frac{B_n \cdot sin(\beta_n x)}{(D_a\beta_n^2 + \frac{1}{\tau_{bulk}})} \cdot \Big(1 - exp\Big[-(D_a\beta_n^2 + \frac{1}{\tau_{bulk}})t)\Big]\Big)\Big] \end{aligned} \tag{A.17}$$

$$\begin{aligned} n(x,t) = \frac{1}{T}\sum_n \quad & \Big[\frac{A_n \cdot cos(\alpha_n x)}{(D_a\alpha_n^2 + \frac{1}{\tau_{bulk}})} \cdot \Big[exp\Big(-\Big[D_a\alpha_n^2 + \frac{1}{\tau_{bulk}}\Big]t\Big)\Big]\Big[exp\Big[D_a\alpha_n^2 + \frac{1}{\tau_{bulk}}\Big]T - 1\Big] + \\ & \frac{B_n \cdot sin(\beta_n x)}{(D_a\beta_n^2 + \frac{1}{\tau_{bulk}})} \cdot \Big[exp\Big(-\Big[D_a\beta_n^2 + \frac{1}{\tau_{bulk}}\Big]t\Big)\Big]\Big[exp\Big[D_a\beta_n^2 + \frac{1}{\tau_{bulk}}\Big]T - 1\Big]\Big] \end{aligned} \tag{A.18}$$

Appendix B

Etchants investigated for reducing S

Type A etchants: HF - H_2O_2 - H_2O
References [118] [137] [138] [139] [121] [140].

A1 Volume parts 30% of (50%) HF : 50% of (30%) H_2O_2 : 20% of H_2O
Etch for 10 seconds at a time (9.7μm per minute) for 3 minutes max. or until no further improvement.

A2 Volume parts: 4% of (50%) HF : 6% of (30%) H_2O_2 : 90% of H_2O
Etch for 2 minutes at a time (0.5μm per minute) for 60 minutes max. or until no further improvement.

A3 No. 5 etch: Volume parts: 58% of (50%) HF : 7% of (30%) H_2O_2 : 35% of H_2O
Etch until pale yellow or blue film appears first time (about 10μm per minute) for 3 minute max. Require uniform 5^{th} order blue or pale yellow film for low surface recombination velocity. Thick oxide on top of amorphous surface structure.

A4 Use etch A1 to remove damaged layer for 3 minutes then A3 for film production time to passivate.

A5 Superoxyl Etch: Volume parts: 17% of (50%) HF : 17% of (30%) H_2O_2 : 66% of H_2O. Etch for 30 seconds at a time for a maximum of 5 minutes or until no further improvement.

A6 Hydrogen peroxide: etch in (30%) H_2O_2 at room temperature.

Type B etchants: CP4 variations References [137] [123] [119] [120] [113] [116] [138].

B1 CP-4: Volume parts 75ml Nitric Acid (69%) : 45ml Hydrofluoric Acid : 45ml Acetic Acid : 0.9ml Bromine (6 drops). Remove every 20 seconds (possible 15 second induction time) for a max. of 3 minutes. 1.5 minutes should remove the damaged layer.

B2 CP4 (variant) Volume parts 50ml fuming Nitric acid : 30ml Nitric Acid (69%) : 20ml Hydrofluoric acid (40%) : 80ml Galacial Acetic acid. Remove every 20 seconds (possible induction time) for a max. of 3minute. Uniform corrosion rate over 18 to 53°C temperature range.

B3 CP4-A (also known as CP6) Volume parts 75ml Nitric Acid (69%) : 45ml Hydrofluoric Acid : 45ml Acetic Acid. Remove every 1 minute; etch for a maximum of 20 minutes. Etch rate is about an order of magnitude slower than CP4.

Type C etchants: Nitric acid-X etchants References [139] [125] [138]

C1) Volume parts 50% of 48% HF : 50% of 69% HNO_3. Etch for 20 secs at a time for 3 minute max. or until no further improvement. Etch pits on (111) planes.

C2 No. 3 Etch. Volume parts are 5 of 48% HF : 5 of 69% HNO_3 : 1 of H_2O

Etch for 10 seconds at a time to a maximum of 3 minutes or until no further improvement. Possible passivation layer with erratic etch rate results.

C3 Volume parts are 1 of 69% HNO_3 : 1 of 1.19 vol. HCl. Etch for 10 seconds at a time for 3 minutes max. or until no further improvement.

C4 Volume parts are 1 part 48% HF : 2 parts 69% HNO_3
Etch until the etchant begins to turn brown. Rapidly transfer to distilled water wash and agitate vigorously. Dip in Methanol then blow dry in N_2.

Type D etchants: Miscellaneous etchants

D1 CP-I: HF - HNO_3 - CH_3COOH - I 50ml HNO_3 : 50ml HF : 100ml CH_3COOH

containing 2*g* of iodine Etch for 20 seconds at a time for 5 minutes max. or until no further improvement.

D2 WAg: H_2O - HF - HNO_3 - $AgNO_3$ 4g of $AgNO_3$ dissolved into 80ml H_2O : 80ml HF : 40ml HNO_3 (69%) Etch for 20 secs at a time for 4 minute max. or until no further improvement. Deep pits represent dislocations, background of shallower pits evident

.

D3 H_2O_2 - HF in volume parts ratio 1:10
20ml H_2O_2 (30%) : 200ml HF (48%) Remove sample when homogeneous film appears. Wash in methanol. Dry in N_2.

Type E etchants: Electrolytic etchants

E1 H_2O - Oxalic Acid (HO_2CCO_2H) 100cc H_2O (dist.) : 20g Oxalic acid (dissolved) Etch for 10 seconds at a time for 1 minute max. or until no further improvement. Anodic Ge is at 4V to 6V. May reveal grain boundaries. Monitor I vs V to ensure operation in linear section of graph.

E2 HF - Galacial Acetic Acid
50cc 48% HF : 50cc Galacial CH_3COOH Etch for up to 15 minute. with anodic Ge at approx. 10V and current of approx. 25mA for K6 samples. Remove samples every 10 seconds. No passivation behaviour at high current density. Bubbling of electrolyte. Monitor I vs V to ensure operation in linear section of graph. Ratio of etchants suggested as non-critical.

E3 Potassium Hydroxide

450cc H_2O : 1cc 45 wt% KOH in H_2O solution. Current density likely to be approx. 120mA for K6 samples. Monitor I vs V to ensure operation in linear section of graph. Remove sample every 30 seconds.

E4 Antimony Oxychloride. Add Antimony Trichloride to 100ml distilled H_2O to form a saturated solution. Reaction may be violent with water. Remove sample every 30 seconds for a maximum of 3 minutes.

Appendix C

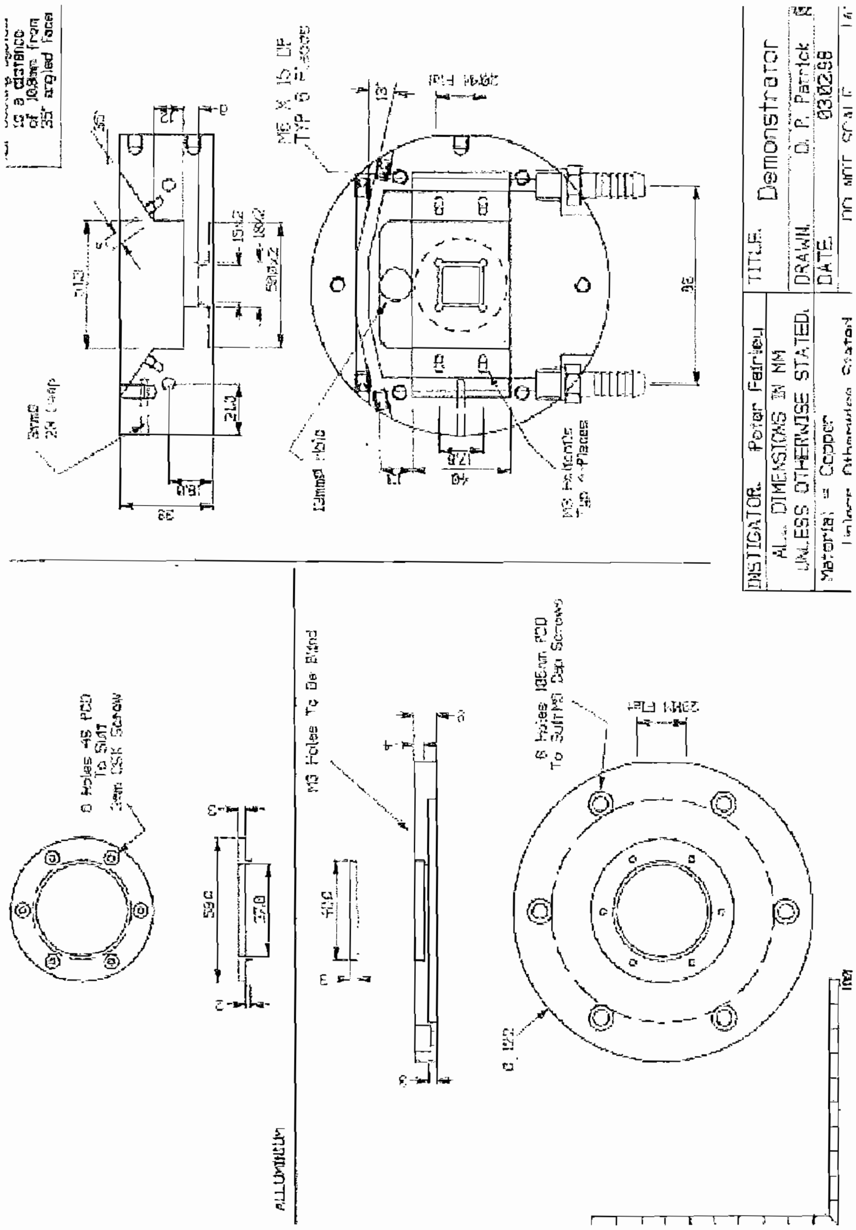

Figure C.1: Technical drawing for demonstration modulator (1 of 2)

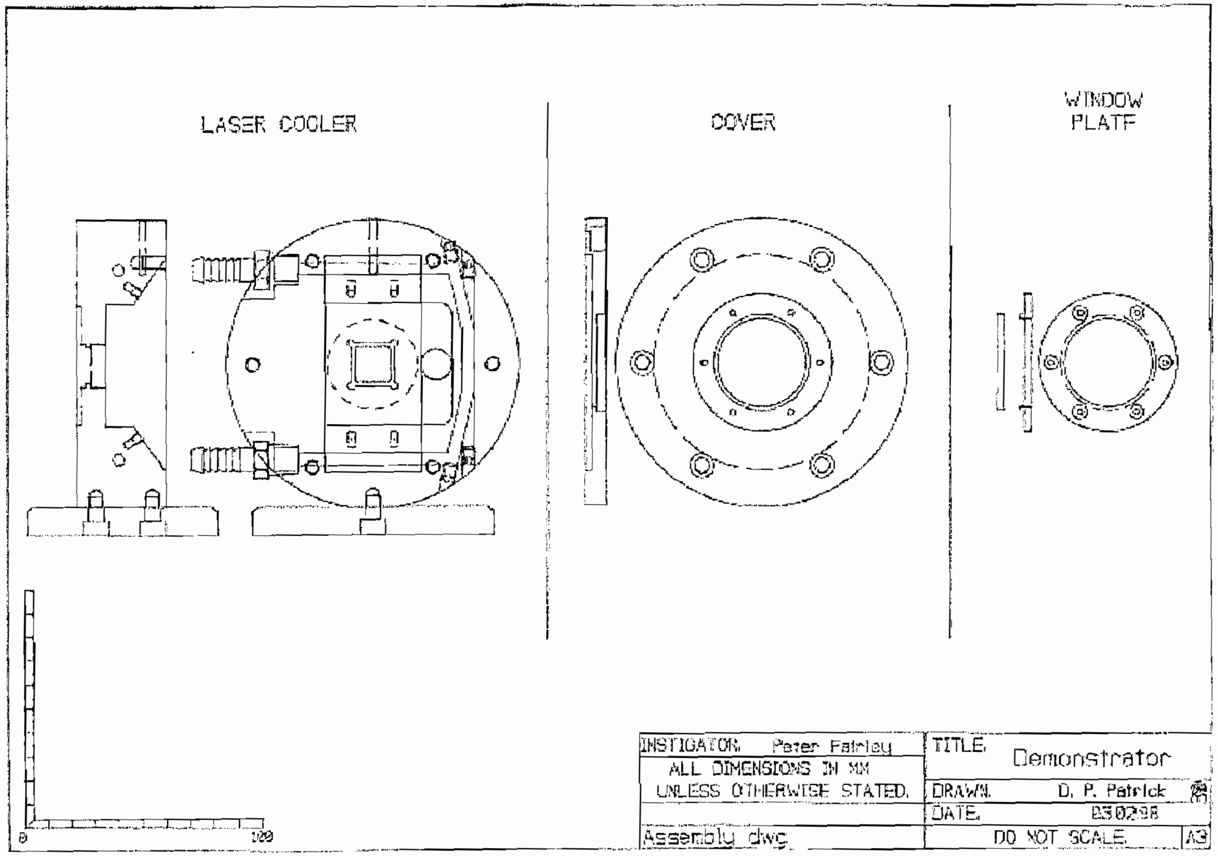

Figure C.2: Technical drawing for demonstration modulator (2 of 2)

Appendix D

Publications

A Novel Gas Concentration Monitor using a Solid State Modulator
P. D. Fairley, H. N. Rutt, *submitted to Sensors and Actuators*, June 2000

Microwave PCD technique applied to extraction of carrier parameters in a germanium IR modulator
P. D. Fairley, H. N. Rutt, *submitted to Semiconductor Science and Technology*, June 2000

Novel Germanium Infrared Modulator
P. D. Fairley, H. N. Rutt, *submitted to Journal of Physics D (Applied Physics)*, June 2000

Conference presentations

A Solid State Modulator for Thermal Imaging Applications
P. A. Manning, P. D. Fairley and H. N. Rutt, *to be presented at SPIE Conference: Infrared Technologies and Applications*, San Diego, July 2000

Solid State Modulator for the Infrared
P. D. Fairley, H. N. Rutt, *Mid-infrared Optoelectronics Materials and devices*, Prague, March 1998

The Germanium Modulator
P. D. Fairley, H. N. Rutt, *Semiconductor and Integrated Optoelectronics*, University of Cardiff, March 1997

Germanium Infrared Absorption Chopper
P. D. Fairley, H. N. Rutt, *Mid-infrared Optoelectronics Materials and Devices*, University of Lancaster, September 1996

Bibliography

[1] L. J. Denes, M. S. Gottlieb, B. Kaminsky. Acousto-optic filters in imaging applications. *Optical Engineering*, 37(4):1262–1267, 1998.

[2] J. Sapriel. Cinnabar (α HgS), a promising acousto-optical material. *Applied Physics Letters*, 19(12):533–535, 1971.

[3] D. R. Suhre, E. Villa. Imaging spectroradiometer for the 8-12 micron region with a 3cm^{-1} passband acousto-optic tunable filter. *Applied Optics*, 37(12):2340–2345, 1998.

[4] A. B. Seddon, M. J. Laine. A review of amorphous chalcogenides as materials for infrared bulk acousto-optic devices. *Physics and applications of non-crystalline semiconductors in optoelectronics*, 36:327–336, 1997.

[5] T. E. Walsh. Gallium-arsenide electro-optic modulators. *RCA Review*, 27(1):323–335, 1966.

[6] L. F. Champagne, F. O'Neill, W. T. Whitney. A large aperture pockels cell for CO_2 lasers. *Optics Communications*, 13(3):282–285, 1975.

[7] C. J. Johnson. Electrooptic effect in CdTe at 23.35 and 27.95 microns. *Proceedings of the IEEE*, 56(10):1719–1720, 1968.

[8] I. P. Kaminow. Measurement of the electrooptic effect in CdS, ZnTe and GaAs at 10.6 microns. *IEEE Journal of Quantum Electronics*, QE4(1):23–26, 1968.

[9] J. F. Figueira E. J. McLellan. Ultrafast pockels cells for the infrared. *Review of Scientific Instrumentation*, 50(10):1213–1217, 1979.

[10] D. J. James A. J. Alcock, P. B. Corkum. Laser controlled optical switching in semiconductors. US Patent 4190811, Feb. 1980.

[11] A. J. Alcock, P. B. Corkum, D. J. James. A fast scalable switching technique for high power CO_2 laser radiation. *Applied Physics Letters*, 27(12):680–682, 1975.

[12] P. B. Corkum, A. J. Alcock, D. J. James, K. J. Andrews, K. E. Leopold, D. F. Rollin, J. C. Samson. *Recent developments in high power CO_2 laser mode-locking and pulse selection*, volume 4A, pages 143–160. Plenum Publishing Corporation, 1977.

[13] S. A. Jamison, A. V. Nurmikko, H. J. Gerritsen. Fast laser spectroscopy of the free carrier plasma edge in Ge. *Applied Physics Letters*, 29(10):640–643, Nov. 1976.

[14] S. A. Jamison, A. V. Nurmikko. Generation of picosecond pulses of variable duration at 10.6 microns. *Applied Physics Letters*, 33(7):598–600, 1978.

[15] H. Alius, G. Dodel. Far infrared modulation techniques based on optical excitation of semiconductors. *Infrared Physics Technology*, 35(1):73–78, 1994.

[16] A. J. Alcock, P. B. Corkum, D. J. James, K. E. Leopold, J. C. Samson. Selection of single, mode-locked CO_2 laser pulses by semiconductor switching. *Optics Communications*, 18(4):543–545, 1976.

[17] R. S. Taylor, B. K. Garside, E. A. Ballik. Passive mode-locking of CO_2 lasers employing a germanium saturable absorber. *IEEE Journal of Quantum Electronics*, QE14(7):532–543, 1978.

[18] A. J. Alcock, P. B. Corkum. Ultra-fast switching of infrared radiation by laser-produced carriers in semiconductors. *Canadian Journal of Physics*, 57:1280–1290, 1979.

[19] K. Yoshino J. Kobayashi, M. Kinoshita, J-Ichi Kita. The IR modulator utilizing light scattering effect with ferroelectric liquid crystal for gas analysis. *International Journal of Infrared and Millimeter waves*, 17(7):1149–1163, 1996.

[20] K. Yoshino, . M. Ozaki. New electro-optic effect of microsecond response utilizing transient light scattering in ferroelectric liquid crystal. *Japanese Journal of Applied Physics*, 23(6):L385 – L387, 1984.

[21] H. N. Rutt. Effect of visible and near-infrared illumination on the mid-infrared transmission of silicon and germanium. *Window and dome technologies and materials 4*, 2286(Ch. 55):100–107, 1994.

[22] H. N. Rutt, P. A. Manning, P. P. Donohue. Infrared radiation modulating device. International Patent, PCT/GB96/02221, Sept. 1996.

[23] H. B. Briggs, R. C. Fletcher. New infrared absorption bands in p-type germanium. *Physical Review*, 87:1130–1131, 1952.

[24] W. Kaiser, R. J. Collins, H. Y. Fan. Infrared absorption in p-type germanium. *Physical Review*, 91(6):1380–1381, 1953.

[25] A. H. Kahn. Theory of the infrared absorption of carriers in germanium and silicon. *Physical Review*, 97(6):1647–1652, March 1955.

[26] E. O. Kane. Energy band structure in p-type germanium and silicon. *Journal of the Physical Chemistry of Solids*, 1:82–99, 1956.

[27] P. J. Bishop, A. F. Gibson. Absorption coefficient of germanium at 10.6 microns. *Applied Optics*, 12(11):2549–2550, Nov. 1973.

[28] C. J. Hutchinson, C. Lewis, J. A. Savage, A. Pitt. Surface and bulk absorption in germanium at $10.6\mu m$. *Applied Optics*, 21(8):1490–1495, 1982.

[29] A. N. Pikhtin, D. A. Yaskov. Infrared absorption in gallium phosphide. *Physica Status Solidus*, 34:815–824, 1969.

[30] N. B. Hannay. *Semiconductors*. Reinhold publishing corporation, 2nd edition, 1960.

[31] E. M. Conwell. Properties of silicon and germanium II. *Proceedings of the IRE*, 46:1281 – 1300, 1958.

[32] R. J. Elliott. Intensity of optical absorption by excitons. *Physical Review*, 108(6):1384 – 1389, 1957.

[33] G. G. Macfarlane, T. P. McLean, J. E. Quarrington, V. Roberts. Fine structure in the absorption-edge of Ge. *Physical Review*, 108(6):1377 – 1383, 1957.

[34] W. G. Spitzer, M. Gershenzon, C. J. Frosch, D. F. Gibbs. Optical absorption in n-type gallium phosphide. *The Physics and Chemistry of solids*, 11:339–341, 1959.

[35] H. F. Wolf. *Semiconductors*. Wiley-interscience, 1971.

[36] J. I. Pankove. *Optical processes in semiconductors*. Dover Publications, 1975.

[37] E. Burstein. Anomolous optical absorption limit in InSb. *Physical Review*, 93:632–633, 1954.

[38] A. V. Nurmikko, G. W. Pratt. Fast infrared optical shutter. *Applied Physics Letters*, 27(2):83–84, 1975.

[39] T. S. Moss. *Optical properties of semi-conductors.* New York Academic Press, 1959.

[40] J. F. Young, H. M. van Driel. Ambipolar diffusion of high-density electrons and holes in Ge, Si, and GaAs: Many body effects. *Physical Review B*, 26(4):2147–2158, Aug. 1982.

[41] J. M. Goldey, S. C. Brown. Microwave determination of the average masses of electrons and holes in germanium. *Physical Review*, 98(6):1761–1763, 1955.

[42] S. M. Sze. *Physics of semiconductor devices.* John Wiley and sons, 1981.

[43] S. Yamada, T. Urisu, Y. Mizushima. High speed infra-red modulator with multi-layered pn junctions. *Electronics Letters*, 19(22):940–941, 1983.

[44] S. Kaneda, Y. Fujusawa, K. Kikuiri. Infra-red light modulator of ridge-type optical waveguide structure using effect of free carrier absorption. *Electronics Letters*, 22(17):922–923, 1986.

[45] J. Steins, M. Kuijk, R. Vounckx, G. Borghs. New modulator for far-infrared light: integrated mirror optical switch. *Applied Physics Letters*, 59(25):3210–3212, 1991.

[46] G. V. Treyz, P. G. May, J. M. Halbout. Silicon optical modulators at 1.3μm based on free carrier absorption. *IEEE Electron Device Letters*, 12(6):276–278, 1991.

[47] K. Seeger. *Semiconductor Physics.* Springer-Verlag, 5th edition, 1991.

[48] S. M. Ryvkin. Indirect optical tranaitions induced by carrier interaction in semi-conductors. *Physica Status Solidus*, 11:285–295, 1965.

[49] H. P. M. Pellemans, P. C. M. Planken. Effect of nonequilibrium LO phonons and hot electrons on far-infrared intraband absorption in n-type gaas. *Physical Review B*, 57(8):R4222–R4225, 1998.

[50] R. B. James, D. L. Smith. Theoretical description of intervalence-band photoconductivity of p-Ge at 10.6μm. *Physical Review B*, 23(8):4049–4053, 1981.

[51] R. B. James, D. L. Smith. Laser-induced changes in the dispersion properties of p-Ge due to intervalence band transitions. *Physical Review B*, 23(8):4044–4048, 1981.

[52] M. Woerner, T. Elsaesser, W. Kaiser. Inter-valence band scattering and cooling of hot holes in p-type germanium studied by picosecond infrared pulses. *Physical Review B*, 41(8):5463–5466, 1990.

[53] J. Paduano. *Infrared Nude Photography: A Guide to Black and White Infrared and Advanced Technique.* Amherst Media, 1994.

[54] W. M. Becker, A. K. Ramdas, H. Y. Fan. Energy band structure of gallium antimonide. *Journal of Applied Physics*, 32(10):2094–2102, 1961.

[55] P. Klocek, editor. *Handbook of infrared optical materials.* Marcel Dekker Inc, 1991.

[56] S. W. Kurnick, J. M. Powell. Optical absorption in pure single crystal InSb at 298K and 78K. *Physical Review*, 116(3):597–604, 1959.

[57] G. W. Gobeli, H. Y. Fan. Infrared absorption and valence band in aluminium antimonide. *Physical Review*, 119(2):613–620, 1960.

[58] F. Matossi, F. Stern. Temperature dependence of optical absorption in p-type indium arsenide. *Physical Review*, 111(2):472–475, 1958.

[59] F. Stern, R. M. Talley. Optical absorption in p-type Indium Arsenide. *Physical Review*, page 158, 1957.

[60] W. J. Turner, W. E. Reese. Infrared absorption in n-type aluminium antimonide. *Physical Review*, 117(4):1003–1004, 1960.

[61] R. F. Blunt, H. P. R. Frederiske, J. H. Becker, W. R. Hosler. Electrical and optical properties of intermetallic compounds III: Aluminium antimonide. *Physical Review*, 96(3):578–580, 1954.

[62] E. D. Palik. *Handbook of optical constants of solids II.* Academic Press, 1991.

[63] W. Spitzer, H. Y. fan. Infrared absorption in n-type silicon. *Physical Review*, 108(2):268–271, 1957.

[64] D. A. Kleinman, W. G. Spitzer. Infrared lattice absorption of GaP. *Physical Review*, 118(1):110–117, 1960.

[65] M. A. Afromowitz, M. DiDomico Jr. Measurement of the free-carrier lifetimes in GaP by photoinduced modulation of infrared absorption. *Journal of Applied Physics*, 42(8):3205–3208, 1971.

[66] C. A. Huber, A. V. Nurmikko. Strong photoinduced infrared absorption in GaP. *Journal of Applied Physics*, 54(1):326–328, 1983.

[67] H. Y. Fan, W. Spitzer, R. J. Collins. Infrared absorption in n-type germanium. *Physical Review*, 101(2):566–572, 1956.

[68] W. C. Dash, R. Newman. Intrinsic optical absorption in single crystal germanium and silicon at 77K and 300K. *Physical Review*, 99(4):1151–1155, 1955.

[69] L. S. Darken, C. E. Cox. *Semiconductors and Semimetals Volume 43*, chapter 2, pages 23–83. Academic Press, 1995.

[70] R. N. Hall, T. J. Soltys. High purity germanium for nuclear detector fabrication. *IEEE Transactions on Nuclear Science*, 18(1):160–165, 1971.

[71] J. A. Savage. Evolution of a procurement specification for optical germanium. *Proceedings of the Society of Photo-Optical Instrumentation Engineers*, 274:175–179, 1981.

[72] J. R. Haynes. New radiation resulting from recombination of holes and electrons in germanium. *Physical Review*, 98:1866–1868, 1955.

[73] P. T. Landsberg. *Recombination in Semiconductors.* Cambridge University Press, 1991.

[74] W. Shockley, W. T. Read. Statistics of the recombinations of holes and electrons. *Physical Review*, 87(5):835–842, 1952.

[75] A. F. Gibson, editor. *Progress in Semiconductors 3*, pages 119–151. London Heywood and Co., 1958.

[76] F. J. Biondi, H. E. Bridgers, J. H. Scaff, J. N. Shive, editor. *Transistor Technology*, volume I-III. Van Nostrand, 1958.

[77] F. J. Biondi, editor. *Transistor Technology*, volume 3. D. Van Nostrand, 1958.

[78] J. A. Burton, G. W. Hull, F. J. Morin, J. C. Severiens. Effect of nickel and copper impurities on the recombination of holes and electrons in germanium. *Physical Review*, 57:853–859, Nov. 1953.

[79] F. J. Biondi, editor. *Transistor Technology*, volume 2. D. Van Nostrand, 1958.

[80] B. J. Baliga. *Modern Power Devices.* Number ISBN 0471819867. J. Wiley and Sons, 1987.

[81] H. Y. Fan, D. Navon, H. Gebbie. Recombination and trapping of carriers in germanium. *Physica*, 20:855–872, 1954.

[82] L. Huldt. Auger recombination in germanium. *Physica Status Solidus A*, 24:221–229, 1974.

[83] I. V. Karpova, V. I. Perel', S. M. Syrovegin. Auger recombination in heavily doped germanium. *Soviet Physics: Semiconductors*, 23(5):518–521, 1989.

[84] D. H. Auston, C. V. Shan, P. LeFur. Picosecond optical measurements of band-to-band Auger recombination of high density plasmas in germanium. *Physical Review Letters*, 35(15):1022–1025, 1975.

[85] R. Conradt, J. Aengenheister. Minority carrier lifetime in highly doped Ge. *Solid State Communications*, 10:321–323, 1972.

[86] J. F. Battey, R. M. Baum. Carrier capture probabilties in nickel doped germanium. *Physical Review*, 100(6):1634 – 1637, 1955.

[87] E. M. Pell. Reverse current and carrier lifetime as a function of temperature in germanium junction diodes. *Journal of Applied Physics*, 26(6):658 – 665, 1954.

[88] R. N. Hall. Electron-hole recombination in germanium. *Physical Review*, 87:387, 1952.

[89] D. T. Stevenson, R. J. Keys. Measurement of the recombination velocity at germanium surfaces. *Physica*, 20(11):1041–1046, 1954.

[90] A. Many, D. Gerlach. Distribution and cross section of fast states on germanium surfaces in different gaseous ambients. *Physical Review*, 107(2):404–411, 1957.

[91] S. M. Sze. *Semiconductor devices: Physics and technology.* John Wiley and sons, 1985.

[92] M. Wautelet, J. A. Van Vechten. Carrier diffusion in semiconductors subject to large gradients of excited carrier density. *Physical Review B*, 23(10):5551 – 5554, 1981.

[93] H. M. Van Driel, J. S Preston, M. I Gallant. Confinement of laser-generated carriers in semiconductors by induced lattice temperature gradients. *Applied Physics Letters*, 40(5):385 – 387, 1982.

[94] D. H. Auston, C. V. Shank. Picosecond ellipsometry of transient electron-hole plasmas in germanium. *Physical Review Letters*, 32(20):1120–1123, 1974.

[95] S. K. Ghandhi. *Semiconductor Power Devices.* J. Wiley and Sons, 1977. pp 93-140.

[96] F. J. Morin, J. P. Maita. Conductivity and hall effect in the intrinsic range of germanium. *Physical Review*, 94(6):1525–1529, 1954.

[97] E. D. Palik. *Handbook of optical constants of solids.* Orlando Academic Press, 1984.

[98] J. R. Haynes, H. B. Briggs. Radiation produced in germanium and silicon by electron-hole recombination. *Physical Review*, 86:647, 1952.

[99] W. Shockley. *Electrons and holes in semiconductors.* D. van Nostrand company, 8th edition, 1950.

[100] E. Kreyszig. *Advanced Engineering Mathematics.* J. Wiley and Sons, 6th edition, 1988.

[101] M. Born, E. Wolf. *Principles of optics : electromagnetic theory of propagation, interference and diffraction of light.* Oxford : Pergamon Press, 5th edition, 1975.

[102] P. J. Holmes, editor. *The electrochemisty of semiconductors.* Academic Press London and New York, 1962.

[103] J. R. Schrieffer. Effective carrier mobility in surface-space charge layers. *Physical Review*, 97(3):641 – 646, 1955.

[104] W. H. Brattain, J. Bardeen. Surface properties of germanium. *The Bell System Technical Journal*, 32(1):1 – 41, 1953.

[105] J. N. Zemel, R. L. Petritz. Magnetosurface effects. *Bulletin of the American Physical Society*, 2:131, 1957.

[106] R. Missman, P. Handler. Hall mobility of a cleaned germanium surface. *Journal of the Physical Chemistry of Solids*, 8:109–111, 1959.

[107] M. B. Das. Physical limitations of MOS structures. *Solid State Electronics*, 12:305–306, 1969.

[108] J. Linnros, V. Grivickas. Carrier-diffusion measurements in silicon with a Fourier-transient grating method. *Physical Review B*, 50(23):16943–55, 1994.

[109] L. B. Valdes. Measurement of minority carrier lifetime in germanium. *Proceedings of the IRE*, 40:1420–1423, 1952.

[110] N. J. Harrick. Use of infrared absorption in germanium to determine carrier distributions for injection and extraction. *Physical Review*, 103(5):1173–1181, 1956.

[111] E. Yablonovitch, D. L. Allara, C. C. Chang, T. Gmitter, T. B. Bright. Unusually low surface recombination velocity on silicon and germanium slices. *Physical Review Letters*, 57(2):249–252, 1986.

[112] R. H. Kingston. Review of germanium surface phenomena. *Journal of Applied Physics*, 27(2):101–114, 1956.

[113] B. W. Batterman. Hillocks, pits and etch rate in germanium crystals. *Journal of Applied Physics*, 28(11):1236–1241, Nov. 1957.

[114] G. Petzow. *Metallographic etching.* Number ISBN 0871700026. American society for metals, 6th edition, 1978.

[115] I. A. Lesk, R. E. Gonzalez. Selective electrolytic etching of germanium and silicon junction transistor structures. *Journal of the Electrochemical society*, 105(8):469–472, Aug. 1958.

[116] T. M. Buck, W. H. Brattain. Investigations of surface recombination velocities on germanium by the photoelectromagnetic effect. *Journal of the Electrochemical society*, 102(11):636–640, Nov. 1955.

[117] R. D. Heidenreich, N. J. Madison. Surface treatment of germanium circuit elements. US Patent 2619414, May 1950.

[118] J. Bloem, J. C. van Vessem. Etching germanium with mixtures of HF-H_2O_2-H_2O. *Journal of the Electrochemical society*, 1:33–36, 1962.

[119] B. Schwartz, H. Robbins. Chemical etching of germanium in HF, HNO_3, H_2O and $HC_2H_3O_2$. *Journal of the Electrochemical society*, 111(2):196–201, Feb. 1964.

[120] A. F. Bogenschutz, W. Krusemark, K. H. Locherer, W. Mussinger. Activation energies in the chemical etching of semiconductors in HNO_3-HF-CH_3COOH. *Journal of the Electrochemical society: Solid State science*, 114(9):970–973, Sept. 1967.

[121] B. Schwartz. Chemical etching of germanium in the system HF-H_2O_2-H_2O. *Journal of the Electrochemical society: Solid State science*, 114(3):285–292, March 1967.

[122] W. Primak, R. Kampwirth. Peroxide etching of germanium. *Journal of the Electrochemical society: Solid State science*, 114(1):88–91, Jan. 1967.

[123] E. N. Pugh, L. E. Samuels. Etching of abraded germanium surfaces with CP-4 reagent. *Journal of the Electrochemical society*, 109(5):409–412, May 1962.

[124] P. R. Camp. A study of the etching rate of single crystal germanium. *Journal of the Electrochemical society*, 102(10):586–593, Oct. 1955.

[125] S. G. Ellis. Surface studies on single-crystal germanium. *Journal of Applied Physics*, 28(11):1262–1269, Nov. 1957.

[126] B. O. Kolbesen, C. Claeys, P. Stallhofer, editor. *Analytical techniques for semiconductor materials and process characterisation II*, volume 95. ESSDERC 95, 1995.

[127] E. Kasper, editor. *Properties of strained and relaxed silicon germanium.* Number ISBN 0852968264. IEE Inspec, 1995.

[128] R. Elliman. Private communication. University of Canberra, Australia.

[129] J. Hecht. *The Laser guidebook, 2nd Edition.* Mc Graw-Hill, 1992.

[130] Gateway Photonics USA. 980nm 20w diode laser bar data sheet, 1999.

[131] C. A. Klein. Bandgap dependence and related features of radiation ionisation energies in semiconductors. *Journal of Applied Physics*, 39(4):2029–2038, 1968.

[132] H.E. Bridgers, J. H. Scaff, J. N. Shive, editor. *Transistor Technology*, volume 1. D. Van Nostrand Company Inc, 1958.

[133] H. Schlangenotto, W. Gerlach. On the lifetime in p-s-n rectifiers at high injection levels. *Solid State Electronics*, 12:267–275, 1969.

[134] N. H. Fletcher. The high current limit for semiconductor junction devices. *Proceedings of the IRE*, 45:862–872, 1957.

[135] Y. Y. Loginov, P. D. Brown, N. Thompson. TEM study of sub-threshold electron irradiation damage in II-VI compounds. *Physica Status Solidus A*, 126:63 – 83, 1991.

[136] Y. V. Voronov. Proceedings of the P. N. Lebedev Physics Institute. In D. V. Skobel'tsyn, editor, *Radiative recombination in semiconducting crystals*, volume 68, 1975.

[137] P. J. Holmes. The use of etchants in assessment of semiconductor crystal properties. *IEE*, (Paper No. 2941E):861–865, 1959.

[138] G. Petzow. *Metallographic etching.* Number ISBN 0871700026. American society for metals, 6th edition, 1978.

[139] V. Grivickas, J. Linnros, A. Vigelis, J. Seckus, J. A. Tellefsen. A study of carrier lifetime in silicon by laser-induced absorption: a perpendicular geometry measurement. *Solid State Electronics*, 35(3):299–310, 1992.

[140] P. Balk, E. L. Peterson. Properties of HF-H_2O_2 treated germanium surfaces. *Journal of the Electrochemical society*, 110(12):1245–1252, Dec. 1963.